**Mathew John Haskew, BSc Chemistry, MSc Chemistry (By Research)**

**Computational and experimental study on silk fibroin and silk fibroin polymer electrolyte for application in transient energy storage devices**

**Lancaster University**

**Department of Engineering and Department of Chemistry**

**November 2022**

**Declaration**

This thesis has been composed solely by myself and the work submitted is my own, except where corresponding references or acknowledgements state otherwise. No portion of the work referred to this thesis has been submitted in support of an application for another degree qualification for this or any other university or institute of learning.

**Acknowledgments**

**Table of Contents**

**Table of acronyms**

| | |
|---|---|
| [Ch][NO$_3$] | Choline nitrate |
| 2-D | Two-dimensional |
| 3-D | Three-dimensional |
| α-C | Alpha carbon |
| Å | Ångströms |
| AC | Alternating current |
| Ag-AgCl | Silver-silver chloride |
| Al | Aluminium |
| Ala | Alanine |
| Alg | Alginate |
| AMBER | Assisted model building with energy refinement |
| Au | Gold |
| *B. mori* | *Bombyx mori* |
| C | Carbon |
| CAD | Computed aided design |
| Cd | Cadmium |
| Cd(OH)$_2$ | Cadmium hydroxide |
| CHARMM | Chemistry at Harvard macromolecular mechanics |
| Cl | Chlorine |
| COMPASS | Condensed-phase optimised molecular potentials for atomistic simulation studies |
| CP | Conductive polymers |
| CP-MAS | Cross-polarisation magic angle spinning |
| cPPA | Cyclic PPA |
| Cu | Copper |
| CV | Cyclic voltammetry |
| $D_0$ | Maximal diffusivity |
| $D$ | Diffusivity |
| DC | Direct current |
| DEMS | Differential electrochemical mass spectroscopy |
| DFT | Density functional theory |

| | |
|---|---|
| DP | Degree of polymerisation |
| ECG | Electrocardiogram |
| EDL | Electrical double layer |
| EIS | Electrical impedance spectroscopy |
| EMF | Electromotive force |
| EPA | Environmental protection agency |
| E-waste | Electronic waste |
| FDA | Food and drug administration |
| Fe | Iron |
| FET | Field effect transistors |
| FTIR | Fourier-transform infrared spectroscopy |
| Ge | Germanium |
| Gly | Glycine |
| H | Hydrogen |
| HA | Hydroxyapatite |
| HC | Heavy chain |
| HCl | Hydrochloric acid |
| HER | Hydrogen evolution reaction |
| His | Histamine |
| IL | Ionic liquid |
| ISO | International organisation for standardisation |
| kDa | Kilodalton |
| LC | Light chain |
| LED | Light emitting diode |
| Li | Lithium |
| Li-MDX | Lithium-manganese dioxide |
| LSV | Linear sweep voltammetry |
| mAh | MilliAmpere-hour |
| MBTT | 2-(4-methoxystyryl)-4,6-bis(trichloromethyl)-1,3,5-triazine |
| MD | Molecular dynamics |
| Mg | Magnesium |
| Mg AZ31 | 96 % magnesium, 3 % aluminium and 1 % zinc alloy |
| $Mg(OH)_2$ | Magnesium hydroxide |

| | |
|---|---|
| Mn | Manganese |
| $MnO_2$ | Manganese dioxide |
| Mo | Molybdenum |
| $MoO_3$ | Molybdenum trioxide |
| MSD | Mean squared displacement |
| $M_w$ | Molecular weight |
| MWCO | Molecular weight cut-off |
| $n$ | Excited electrons |
| N | Nitrogen |
| Na | Sodium |
| Ni | Nickel |
| $NiO(OH)_2$ | Nickel oxide hydroxide |
| NMR | Nuclear magnetic resonance |
| NPT | Isothermal-isobaric ensemble |
| NVE | Microcanonical ensemble |
| NVT | Canonical ensemble |
| O | Oxygen |
| OCV | Open-circuit voltage |
| OPLS-AA | All-atom optimised potentials for liquid simulations |
| OPLS | Optimised potentials for liquid simulations |
| ORR | Oxygen reduction reaction |
| $p$ | Holes |
| PA | Polyamide |
| PBS | Phosphate buffered saline |
| PCL | Polycaprolactone |
| PDB | Protein database bank |
| PE | Polymer electrolyte |
| PEE | Polyethylene |
| PEIS | Potentiostatic electrical impedance spectroscopy |
| Phi | φ |
| PLA | Polylactic acid |
| PLGA | Poly(lactic-co-glycolic acid) |
| PPA | Poly(phthalaldehyde) |

| | |
|---|---|
| PPy-pTS | Polypyrrole−*para*(toluene sulfonic acid) |
| Psi | ψ |
| Pt | Platinum |
| PVA | Poly(vinyl alcohol) |
| REDOR | Rotational echo double resonance |
| Redox | Reduction-oxidation |
| Ser | Serine |
| SF | Silk fibroin |
| SHE | Standard hydrogen electrode |
| Si | Silicon |
| SI | Supplementary information |
| SPME | Smooth particle mesh Ewald |
| ssNMR | Solid-state nuclear magnetic resonance |
| TGA | Thermogravimetric analysis |
| Thr | Threonine |
| Ti | Titanium |
| TIMB | Transient implantable medical bionics |
| TIP3P | Three-site transferable intermolecular potential |
| Tyr | Tyrosine |
| UV | Ultraviolet |
| Val | Valine |
| VdW | Van der Waals |
| VMD | Visual molecular dynamics |
| W | Tungsten |
| XRD | X-ray diffraction |
| Zn | Zinc |
| ZnO | Zinc oxide |

**Table of figures**

| | |
|---|---|
| **Figure 19** | (a) Ramachandran plot at 298 K of the non-hydrated $(Ala-Gly)_{1024}$ SF crystal. (b) Ramachandran plot at 298 K of the hydrated $(Ala-Gly)_{1024}$ SF crystal |
| **Figure 20** | (a) Ramachandran contour plot at 298 K of the non-hydrated $(Ala-Gly)_{128}$ SF crystal. (b) Ramachandran contour plot at 298 K of the hydrated $(Ala-Gly)_{128}$ SF crystal |
| **Figure 21** | (a) Ramachandran contour plot at 298 K of the non-hydrated $(Ala-Gly)_{1024}$ SF crystal. (b) Ramachandran contour plot at 298 K of the hydrated $(Ala-Gly)_{1024}$ SF crystal |
| **Figure 22** | MSD of the oxygen ions from the water molecules (in $Å^2$) in the hydrated SF crystal model $(Ala-Gly)_{1024}$ |
| **Figure 23** | Arrhenius plot of the hydrated $(Ala-Gly)_{1024}$ SF crystal at the temperature range of 273 to 310 K |
| **Figure 24** | A VESTA visualisation of the water trajectory of the hydrated $(Ala-Gly)_{1024}$ SF crystal at 298 K over 1 ns |
| **Figure 25** | The directional MSD of the oxygen ions from the water molecules (in $Å^2$) in the hydrated SF crystal model $(Ala-Gly)_{1024}$ at 298 K |
| **Figure 26** | Pictures of the prototype battery |
| **Figure 27** | OCV of the prototype battery using an Ag-AgCl leak-free electrode as the reference electrode |
| **Figure 28** | Linear sweep voltammogram of the prototype battery where the working electrode is the Mg AZ31 alloy, reference electrode the Ag-AgCl and counter electrode the coiled Au wire |
| **Figure 29** | Prototype Mg-air battery's current versus power density |
| **Figure 30** | (a) FTIR spectroscopy of the $[Ch][NO_3]$ IL solution (b) FTIR spectroscopy of the *B. mori* SF film |
| **Figure 31** | (a) FTIR spectroscopy of the 1:1 wt ratio of SF:IL PE film (b) FTIR spectroscopy of the 1:3 wt ratio of SF:IL PE film |
| **Figure 32** | (a) XRD of the 1:1 SF:IL PE in the liquid state (b) XRD of the 1:1 SF:IL PE in the solid (film) state |
| **Figure 33** | (a) XRD of the 1:3 SF:IL PE in the liquid state (b) XRD of the 1:3 SF:IL PE in the solid (film) state |
| **Figure 34** | Averaged TGA curves for the PE 1:1 and 1:3 films |

## Abstract

Transient implantable medical bionics (TIMBs), such as, degradable and biocompatible batteries that disappear after their operation, are gaining attention because they potentially facilitate the deployment of novel instructive biomaterials for regenerative medicine. In the wider context, the generation of degradable electronics potentially addresses problems associated with electronic waste (E-waste) and these materials can influence biological processes in a controllable manner, (e.g. tissue regeneration and drug delivery via electrical stimulation). Implantable degradable and biocompatible batteries may be capable of satisfying the power requirements of some biomedical devices and then harmlessly degrading.[1] Therefore, these batteries are of great interest and a number of different battery designs have been reported in the literature. In this work, Mg and Zn primary air batteries utilising a degradable and biocompatible polymer electrolyte (PE) (silk fibroin [SF] and choline nitrate [Ch]NO$_3$] ionic liquid [IL]) is reported. The batteries detailed in this work offer up to 7.18 Wh L$^{-1}$ and 3.89 Wh L$^{-1}$, respectively, which is sufficient to power ultralow power devices (e.g. 10 to 1000 µW pacemakers).[5] However, the chemistry that underpins the interactions and performance of the materials utilised in the batteries reported in the literature has yet to be fully explored. Therefore, classical molecular dynamics (MD) simulations have been employed to investigate the interactions between SF and water molecules which are essential to the functionality of the batteries detailed in this work.[1] An alanine-glycine (Ala-Gly) crystal model is implemented to represent the SF[11, 68] with 7.5 % water by weight, which is analogous to regenerated SF films.[1, 116] The silk crystal structure, reported in this work, is in the silk I form (i.e. repeated β-turn type II conformation), because β-sheets are not the predominant secondary structure (ca. 26 %), instead, the 3$_{10}$-helix is the predominant secondary structure (ca. 37 %). Furthermore, the trajectory of water diffusion is reported to be anisotropic (diffusion is prominent along the X-axis of the crystal model) with a diffusivity calculated at 1.60x10$^{-6}$ cm$^2$ s$^{-1}$ at 298 K. Similar results were observed for experimentally determined water diffusivity in SF films at 5.79x10$^{-6}$ cm$^2$ s$^{-1}$ at 298 K, possessing 36 % β-sheet content. By drawing inspiration from experimental studies on degradable and biocompatible batteries in the literature and producing an appropriate computational model to represent the pertinent materials theoretically (and experimental validation of them), should result in an improved understanding of the science underpinning the interactions and performance of these devices. Thus, a greater control over these devices should be achieved and potentially enable new applications of transient energy storage devices.

## 1. Introduction

Transient technology is an emerging field that requires materials, devices, and systems to be capable of disappearing with minimal or non-traceable remains over a period of stable operation. Transient technology has developed fast since it was first proposed in 2012.[2] In recent years, transient technology has been extended to biomedical applications, bioelectronics and environmental monitoring systems, as well as, devices for energy harvesting and storage.[3] Although the concept is relatively new, this emerging technology will enable numerous real world applications. Here, TIMBs will be examined, particularly, degradable and biocompatible batteries because few studies to date have attempted to fabricate these transient devices. In addition, further exploring and understanding the science behind the degradation of these batteries will inevitably increase their controllability and usefulness, resulting in improved targeted application and potentially development of a prototype device.

If well-designed, degradable batteries are potentially eco-friendly because there will be no E-waste. Currently, E-waste accumulates at a rate of ca. 50 million tons a year, which is potentially environmentally harmful and difficult or expensive to dispose of appropriately.[4] As a result, transient technology and degradable batteries offer potentially significant economic, environmental and societal benefits, for a progressive society. Furthermore, the biocompatibility of degradable batteries is greatly desired, for instance, they could be coupled with other implantable medical bionics and provide sufficient voltage, current and power requirements for ultralow power devices (e.g. 10 to 1000 μW for pacemakers).[5] These TIMBs will therefore, eliminate the need for a second surgical procedure to remove the device if it degrades naturally and harmlessly, thus, reducing the risk of infection from surgery and inflammatory responses (immune system responding to the foreign device) and reducing hospital costs (i.e. it becomes more socio-economically viable).

Biocompatibility is usually determined by *in vitro* and *in vivo* testing, involving the interaction of the material with biological fluids and cells and is measured in terms of its effects (e.g. tissue reactions). In addition, for implantable objects, a materials' effect on tissue and bone may also be observed. The international organisation for standardisation (IOS or ISO internationally) describes the following biocompatibility tests: cytotoxicity, sensitisation, irritation, acute systemic toxicity, subchronic toxicity, genotoxicity, implantation, chronic toxicity, and carcinogenicity.[6] In most cases, *in vitro* cytotoxicity tests may yield a good guideline for biocompatibility, because it tests a materials' quality of being toxic to cells by observing the cell growth, reproduction and morphological effects.

The research on degradable materials for electronics can be categorised as fully degradable or partially degradable. Although materials capable of full degradation have been proposed (e.g. a biodegradable thin-film magnesium primary battery using SF-IL PE)[1] and various functional devices have been demonstrated, further materials studies are necessary for optimal and practical application. For instance, this should include extensive investigation of a material's biocompatibility/compostability and interactions with active species during functional operation. Early attempts have focused on organic materials including natural or synthetised degradable polymers (e.g. SF and food and drug administration (FDA) approved polycaprolactone (PCL)). SF is of particular interest in this work because it is a naturally occurring biodegradable and biocompatible protein, making it a promising candidate for *in vivo* applications. Moreover, partially degradable devices have been fabricated and reported successful application (e.g. organic thin-film transistor on poly(lactic-co-glycolic acid) (PLGA) substrates).[7]

In order to achieve both stable operation for a certain period of time and then degradation once the pre-determined functionality had been achieved (transience), encapsulation materials (to impart a degree of protection from degradation) are critically important.[7] The degradation time and permeability of materials/encapsulation materials and thickness of the active electronic components mostly define the functional lifetime of TIMBs. Therefore, degradable and transient electronic materials require extensive investigation of their chemistry and electrochemistry, materials-biology interface, and associated biocompatibility. Thus, device designs and architectures based on these degradable and transient electronic materials should be improved to achieve the electrical performance that meets practical and clinical standards, while remaining capable of benign degradation after the specified functionality had been carried out (e.g. drug delivery systems in 2 to 4 days and sensing systems in a few weeks).[1, 7]

By adopting a combination of computational and experimental approaches offers an interdisciplinary view that can benefit almost/if not all areas of science. In this case, it will be employed to enhance our understanding of the underlying science of degradable batteries/devices, that can assist in the practical application of these (or similar) designs. More specifically, classical MD will be employed to investigate the structure and interactions with water of a degradable and biocompatible material (e.g. SF) where its utilisation is essential to the function of TIMB devices (e.g. degradable and biocompatible primary air batteries) for protection from degradation (e.g. encapsulation) or ionically conductive separating membrane (e.g. PE). Electrochemical experimentation of the batteries will verify performance capabilities and thus potential applications. The combination of the information gathered from the separate techniques would elucidate the chemistry and interactions involved in the design of the

devices, resulting in an improved understanding and perhaps a tuneable/controllable characteristic. Hereby, the objectives for this study are as follows: fabrication of an appropriate (justified by experimental validation and comparison with the literature) SF crystal structure model, evaluation of the SF secondary structure and water diffusion at various temperatures with water content akin to experimentally reproduced SF films, fabrication of a unique primary air battery utilising biocompatible materials (e.g. SF and [Ch]NO$_3$] IL PE) to allow for implantable biomedical applications, and evaluation of the fabricated battery's performance capabilities with various experimental parameters (e.g. PE content ratio and different cathode material Mg and Zn) which are experimentally validated and with comparison to the literature. The objectives, mentioned previously, are detailed and discussed in the following chapters *Results and discussion: Computational studies* and *Results and discussion: Experimental studies*, respectively.

## 2. Literature review

### 2.1 Transient technology

With the rapid development of technology, large amounts of electronics have been developed and discarded. E-waste has become a huge 21$^{st}$ century issue causing great environmental burdens.[3] To combat the aforementioned issue, the concept of transient technology has gained traction in recent years. The utilisation of transient technology would enable electronics to degrade into the surrounding environment with minimal/no impact, and as a result, minimises E-waste; these electronics have also been named "green electronics". These transient electronics are required to be degradable with the resulting products being environmentally friendly. In addition, transient electronics may acquire a biocompatible characteristic; therefore, they have a variety of applications including TIMB devices. A degradable and biocompatible battery is a TIMB device that could power other biomedical devices, such as drug delivery devices or tissue scaffolds where electrical stimulation initiates drug release or stimulates the cells in contact with it. As a result, this could eliminate the need for a secondary surgical procedure to remove an implanted device because the battery should degrade harmlessly in the body. Although, stable operation of the battery is necessary before transience has occurred, the stable operation depends upon a reliable performance for a specified period i.e. transience ideally occurs after the functional assignment of the device is fulfilled. Encapsulation materials (e.g. SF) can be vital for protecting a transient device, like a degradable and biocompatible battery, from premature degradation or controlling the transient characteristic of the device when first exposed to a stimulus (e.g. enzymatic aqueous solution).[1, 3] The transient behaviours of these devices, as well as their encapsulations, are greatly influenced by factors that include the material's properties, device

structure/design, and system integrations. In addition to these intrinsic factors, the external stimulus is another important factor that determines the transient behaviour of these devices. Transient triggers come in a variety of formats, such as, solutions, light, temperature and even mechanical forces.[13, 14]

Transient materials (e.g. metals, polymers and semiconductor materials) are a type of material that can fulfil a functional role for a specified period and are therefore essential for transient technology. When transience is triggered, (e.g. exposure to a solution), a device will either physically or chemically disappear totally or partially in a controlled manner. Transient systems triggered via solution seem to be the only category, reported thus far, that can realise fully transient electronics.[3] Therefore, transient electronics can be divided into two classes: fully transient electronics (the device completely degrades) and partially transient electronics (the device partially degrades with some material left behind, such as bioinert gold [Au] or platinum [Pt]).

In electronics, conductive materials serve as electrodes and connections. Compared to conductive polymers (CPs), metals are more attractive because of their high electrical conductivity, stable properties, and established roles in commercial devices. Recently, magnesium (Mg), zinc (Zn), iron (Fe), tungsten (W), and molybdenum (Mo) has been reported as dissolvable metals for transient electronics. Each of these metals are important to biological functions and can be used in biomedical implants.[15] For example, Mg, Mg alloys, and Fe have been used in the design of bioresorbable implants, such as vascular stents, due to their suitable biocompatibility and favourable mechanical properties.[3]

Water-soluble polymers cover a wide range of materials with various applications (e.g. paints, textiles, paper and coatings) and have the capability to be degradable. These degradable polymers are substituted or incorporated with some hydrophilic groups into their backbone so that they can dissolve, disperse, or swell in water. Typical water-soluble polymers include poly(vinyl alcohol) (PVA), PLGA and PCL. PLGA has been applied into transient electronics through organic thin-film transistors.[7] In 2014, PVA (ca. molecular weight ($M_w$) 31,000 or 31 kilodalton (kDa)) was reported and used as a substrate for transient single-walled carbon nanotube field effect transistors (FETs).[16] Furthermore, as previously mentioned, a controllable degradation is critical to the systematic design of transient electronics. An effort to control this degradation can involve the modification of the components involved within the transient electronic device. For instance, the solubility of PVA in water relies on the degree of polymerisation (DP) and temperature of solution.[3] The dissolution rate of PVA in water can be easily adjusted by simply adding gelatin or sucrose to the PVA polymer matrix, sucrose increases the rate of dissolution, whereas, gelatin has the opposite effect.[17] Moreover, PLGA is a copolymer of

lactic acid and glycolic acid, thus, degradation is tuneable on the adjustment of the $M_w$ and ratio of these monomers.[3]

Most transient devices are designed for biocompatible applications and are capable of degrading in buffered solutions (e.g. via hydrolysis, enzymatic degradation, or cellular activity). Therefore, the design of water-soluble materials (both metal and polymer) has been extensively studied for buffered and neutral solutions.[3] However, acidic conditions can cause degradation, increasing the potential applications of transient electronic devices (electronic devices that do not require biocompatibility but need to disappear entirely or require a complete destruction of the electronic components). Poly(phthalaldehyde) (PPA) has been utilised as a substrate material in transient electronics to support Mg electrodes. Ultra-violet (UV) light triggered polymer 2-(4-methoxystyryl)-4,6-bis(trichloromethyl)-1,3,5-triazine (MBTT) was used as a photoacid generator and linked with the backbone of cyclic PPA (cPPA). When exposed to 379 nm UV-light, the MBTT additive generates a highly reactive chlorine (Cl) radical that captures a H from its surroundings to form hydrochloric acid (HCl). When in the presence of HCl, cPPA undergoes rapid depolymerisation that leads to the disintegration of the polymer substrate and the destruction of the electronics on the substrate. In addition to the disintegration of PPA substrate, HCl also degrades the Mg electrodes.[13]

PVA and PLGA are examples of synthetic degradable polymers utilised in transient electronics, in addition, natural degradable polymers such as, silk and cellulose, have great potential as non-toxic degradable materials for transient electronic devices/systems. Silk proteins have been utilised as a degradable thin-film substrate to integrate with silicon (Si) semiconductors to fabricate electronics such as, capacitors, inductors, diodes and transistors.[18] Furthermore, cellulose nanofibril paper has been utilised as a flexible substrate for green flexile electronics.[19] In addition, these materials could act as encapsulation materials for TIMB devices like a biodegradable and biocompatible battery, therefore, introducing a degree of degradation control. Since these materials are degradable, biocompatible and low cost, it demonstrates a great potential for large scale fabrication of electronics in an eco-friendly way. This further demonstrates how transient technology can battle the crisis of E-waste, while providing unique and useful applications for the scientific and clinical community.

Electronic properties can sometimes be altered in a controllable manner by doping. Doping is the intentional introduction of impurities into a semiconductor to modulate its electrical, optical and structural properties. Intrinsic semiconductors are un-doped semiconductors where the charge carriers, excited electrons ($n$) and holes ($p$), are equal $n=p$. However, $n=p$ can still be achieved even after doping, as long as the semiconductor is doped equally with both electron donors and acceptors.

When a semiconductor has been doped and $n$ is not equal to $p$, it is now referred to as an extrinsic semiconductor. There can be two types of extrinsic semiconductors, depending on the doping agent; these are $n$-type semiconductors and $p$-type semiconductors. An $n$-type semiconductor has been doped with an electron donor atom and now the majority of charge carriers in the crystal are negative electrons. Whereas, a $p$-type semiconductor has been doped with an electron acceptor atom and the majority of charge carriers in the crystal are electron vacancies a.k.a. positively charged holes, which can move through the crystal.

Semiconducting materials are crucial to the development of electronics. Among the various available semiconductor materials, Si is one of the most widely used semiconductor materials for the electronics industry.[3] Since Si can dissolve in water within a certain time by hydrolysis, it can be easily applied into transient technology. For instance, monocrystalline Si nanomembranes have served as semiconductors in circuits, and Si oxide has been applied in transistor devices like inverters and gates.[20] The morphology of Si is tuneable, which is critical to the material's performance as well as the dissolution evolution. The dissolution mechanism of single-crystalline Si nanomembranes demonstrated uniform hydrolysis of the Si nanomembranes, and a wide range of aqueous solutions with different pH values can control the dissolution rate. Moreover, the dissolution rate varies among semiconductors with different dopant types and dopant concentrations. Typically, the dissolution rates of these semiconductor materials at physiological temperature (37 °C) are higher than those at room temperature.[20]

To summarise, transient technology addresses an important issue for the 21st century, E-waste, while providing practical commercial/industrial and clinical applications. Transient materials involve a wide array of designs and applications, from substrate or encapsulation materials, different transient triggers, biocompatibility and different functional roles. Because these materials can be vital for electronic systems/components, it is therefore important to systematically study and understand their transient behaviour and chemistry i.e. the interactions within a system. Therefore, there are plentiful opportunities available with transient technology and the science surrounding the technology is yet to be fully explored. In the next section we explore the application of the transient technology.

## 2.2 Batteries

A battery is a connection of one or more electrochemical cells and possesses three components: an anode, a cathode, and the electrolyte. In addition, the anode and cathode would typically be connected to an electrical circuit/external load. Oxidation occurs at the anode whereas reduction occurs at the cathode. In a galvanic cell the anode is the negative terminal, and it supplies the electrons to the

external circuit to which the battery is connected. Therefore, an electron build-up is initiated at the anode that causes a potential difference between the two electrodes (anode vs cathode). The electrons would naturally try to redistribute themselves, but this is prevented by the electrolyte, when the electrical circuit is connected to the electrodes it provides a clear path for the electrons to move from the anode to the cathode thereby powering the circuit to which it is connected, demonstrated in **Figure 1**. Furthermore, the electrolyte can be a salt bridge or porous membrane allowing for the movement of ions between the electrodes, as demonstrated by **Figure 2**.
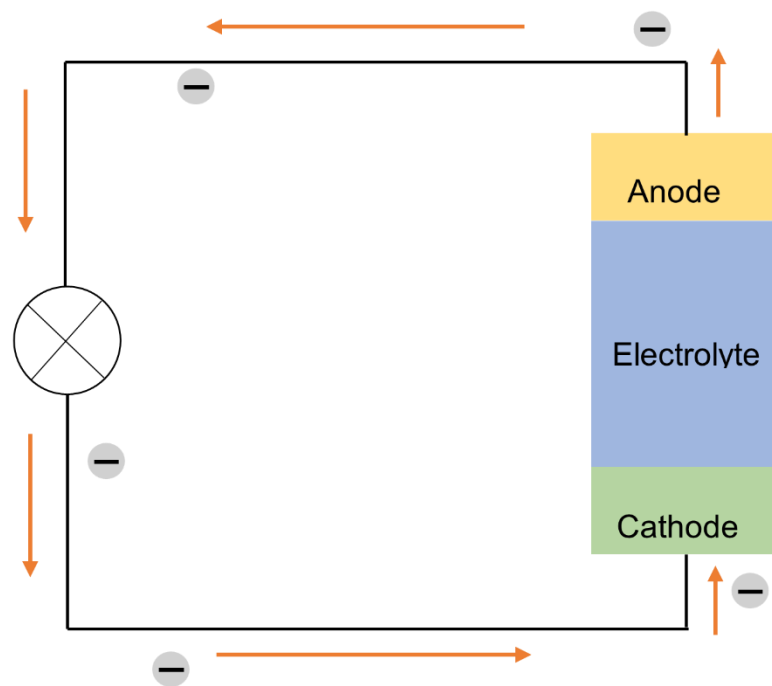


**Figure 1.** Diagram depicting how a battery can power a lightbulb. Orange arrows represents the electron flow in the external circuit.

Anode

Half-cell equation:

$Zn_{(s)} \rightarrow Zn^{2+}_{(aq)} + 2e^-$

Cathode

Half-cell equation:

$Cu^{2+}_{(aq)} + 2e^- \rightarrow Cu_{(s)}$
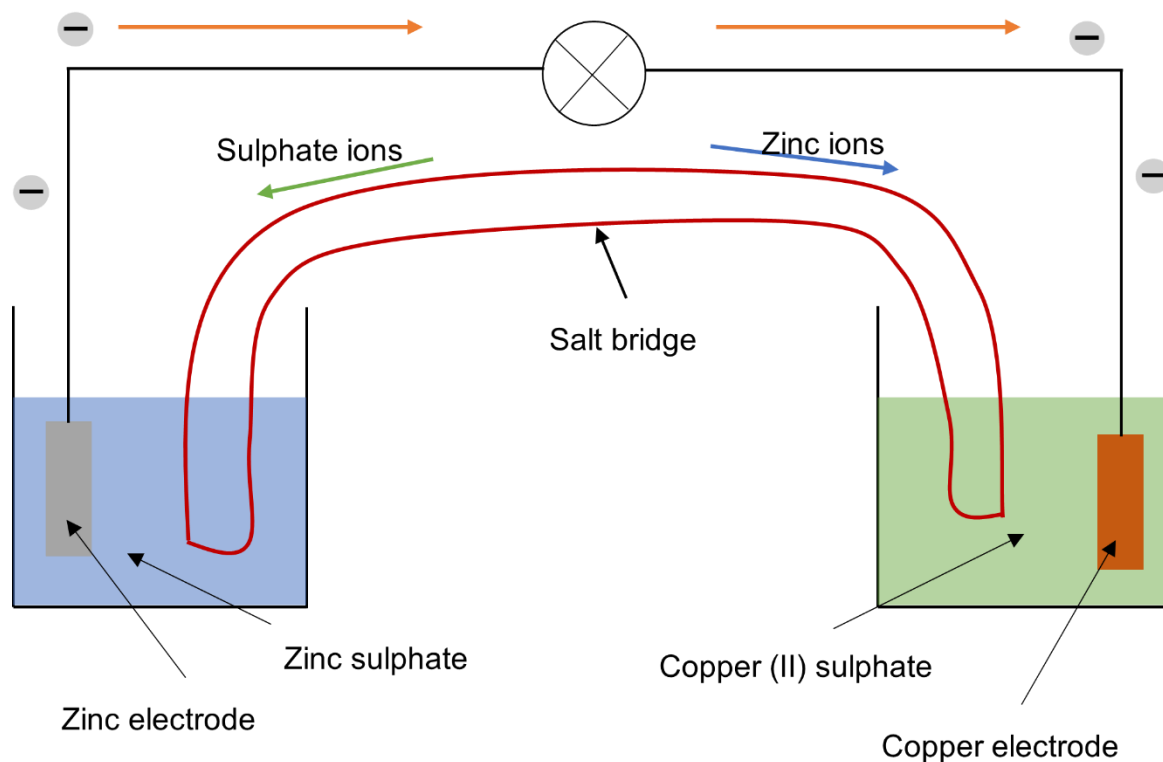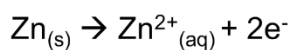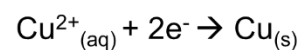
**Figure 2.** Representation of a Daniell cell powering a lightbulb. Orange arrows represents the electron flow in the external circuit.

The total reaction equation (combination of both half-cell equations, anode and cathode) from **Figure 2** is:

$$Zn_{(s)} + Cu^{2+}_{(aq)} \rightarrow Zn^{2+}_{(aq)} + Cu_{(s)}$$
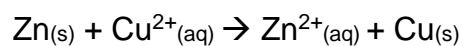
An electrochemical cell is a device capable of either generating electrical energy from chemical reactions (**Figure 2** is an example of this type of electrochemical cell) or using electrical energy to cause chemical reactions. The electrochemical cells that generate an electric current are called voltaic cells or galvanic cells and those that generate chemical reactions via electrolysis, are called electrolytic

cells. The fundamental difference between a galvanic cell and electrolytic cell is what drives them. For an electrolytic cell, a non-spontaneous reduction-oxidation (redox) reaction is driven by the application of electrical energy, hence, they are typically used to induce the decomposition/synthesis of chemical compounds via electricity. Whereas a spontaneous redox reaction takes place within a galvanic cell and electrical energy is derived from this spontaneous redox reaction.

Furthermore, primary and secondary cells are systems that incorporate aspects of the aforementioned electrochemical cells. A primary cell is essentially a galvanic battery that is designed to be used once, therefore, the electrochemical reactions within a primary cell are not reversible. During the primary cell's functional use, chemical reactions within the battery use up the available chemicals/material to produce electrical energy. After the chemical reactions have reached completion, i.e. equilibrium or there are no chemical reactants left, the battery will stop producing electricity and will no longer be useful. This will then require disposal of this type of battery as E-waste. However, for degradable and biocompatible primary batteries, they can degrade harmlessly into their environment (e.g. soil or human body), thus making them attractive alternatives which does not contribute to E-waste. On the other hand, a secondary cell which is commonly referred to as a rechargeable battery can be run as both a galvanic cell or as an electrolytic cell. In contrast, the electrochemical reaction can be reversed by running a current into the cell with a battery charger to recharge it, regenerating the chemical reactants. Therefore, secondary batteries are not typically thrown away after their first discharge and tend to have a longer functional lifetime overall versus primary batteries. Nevertheless, secondary batteries have a charge cycle lifetime and seldom achieve 100 % efficiency, resulting in the eventual discarding of the battery, thus, contributing to E-waste. However, a biodegradable sodium ion secondary battery has been reported with its capacity at ca. 0.12 mAh $cm^{-2}$ and with a ca. 80 % efficiency after 50 cycles.[247] Although, the reported capacity is lower than that of reported degradable and biocompatible primary batteries[1, 5, 26, 32] and without the added benefits of biocompatibility, as discussed later in the *Transient batteries* chapter. In addition to the previously discussed electrochemical cells, there are also fuel cells. In fuel cells, the chemical energy from a fuel is converted into electrical energy (e.g. electrochemical reaction of hydrogen fuel with oxygen or another oxidising agent).[21] They differentiate from primary or secondary batteries because unlike batteries, fuel cells require a continuous source of fuel and oxygen to sustain their chemical reactions.

Electrochemical cells incorporate two half-cell reactions, as depicted in **Figure 2**. Each half-cell consists of an electrode (either anode or cathode) and an electrolyte, they may use the same electrolyte or different electrolytes. Furthermore, they may also involve external substances, such as hydrogen gas as a reactant in fuel cells, mentioned previously. In a complete electrochemical cell, a

species from one half-cell will lose electrons to their electrode, while species from the other half-cell will gain electrons to their electrode. This explains the term of "redox", which describes what is occurring at each electrode (i.e. the gain of electrons at the electrode means reduction is occurring whereas the opposite will be happening at the other electrode, thus, oxidation should be occurring). Each half-cell has a characteristic voltage (e.g. $Cu^{2+}_{(aq)} + 2e^- \rightarrow Cu_{(s)}$ has a standard potential of 0.34 V and $Zn_{(s)} \rightarrow Zn^{2+}_{(aq)} + 2e^-$ has a standard potential of 0.76 V). The half-cell potentials are defined relative to a reduction standard hydrogen electrode (SHE) in water at 25 °C which possess a potential of ca. 0 V. The difference in voltage between the half-cell electrode potentials provides a prediction for the cell potential. Thus, the electrochemical cell potential can be predicted through the use of electrode potentials of each half-cell. For instance, in **Figure 2** is a Daniell cell, typically at standard state conditions (1 M, 1 atm at 25 °C) the standard cell potential is 1.10 V,[22] this value can be obtained by using equation (1):

$$E^0_{cell} = E^0_{red} + E^0_{ox} \qquad (1)$$

where, $E^0_{cell}$ is the cell potential at standard state conditions and $E^0_{red}$ and $E^0_{ox}$ are the standard reduction and oxidation half-cell potentials (0.34 and 0.76 V), respectively. As the SHE provides the $E^0_{red}$ value, to obtain the relevant $E^0_{ox}$ value the relationship as follows is defined by equation (2):

$$E^0_{ox} = -E^0_{red} \qquad (2)$$

essentially, the $E^0_{red}$ can be obtained, based on the SHE, and by reversing the sign will provide the $E^0_{ox}$.

The cell potential depends on the concentration of chemical reactants and their type, because as the cell is discharged the concentration of reactants will decrease, as will the cell potential. Furthermore, if conditions are not at standard state the cell potential is not as easily determined and is now defined by using the Nernst equation (3):

$$E_{cell} = E^0_{cell} - \frac{RT}{nF} \ln Q \qquad (3)$$

where, $E_{cell}$ is the cell potential under non-standard state conditions, $R$ is the universal gas constant (8.314 J K$^{-1}$ mol$^{-1}$), $T$ the temperature in Kelvin, $F$ the Faraday's constant (96,485 C mol$^{-1}$), $n$ is the number of moles of electrons transferred in the balanced equation for the electrochemical cell reaction, and $Q$ reaction quotient as defined by equation (4):

$$Q = \frac{1}{P[RED^+]^n \times [OX^-]^n} \qquad (4)$$

where, $P$ is the pressure of the system in atm, $[RED^+]^n$ and $[OX^-]^n$ is the concentration of the reduced and oxidised substances (respectively) raised to the power of however many electrons are being transferred.

In addition, the difference in electrical potential between two terminals (e.g. the electrodes in a battery), when disconnected from any external circuit is referred to as the open-circuit voltage (OCV). The OCV can also be referred to as the electromotive force (EMF), which is the maximum potential difference when there is no current and the circuit is not closed. Alternatively, the OCV may be thought of as the voltage that must be applied to a battery to stop the current. In general, voltage is the difference in potential, current the rate of which the potential is flowing and resistance the materials tendency to resist the potentials flow. The relationship between voltage, current and resistance is represented by the Ohm's law equation (5):

$$V = I \times R \qquad (5)$$

where, V is the potential difference between two points which include a resistance $R$, and $I$ is the current flowing through the resistance.

Currently, commercial batteries are easily accessible for a consumer's day-to-day usage and can come in a variety of different forms (e.g. size or whether it is rechargeable or not), to fulfil a specific function. Furthermore, an on-going argument between the use of secondary batteries over primary batteries is prevalent and both have their advantages and disadvantages. For instance, a secondary battery would have less of an impact on the environment in the form of E-waste compared to a primary battery, due

to its rechargeability, therefore, would not be discarded or recycled after its functional use like a primary battery. However, secondary batteries do have a limited cycle count and would require a certain degree of battery maintenance to maintain optimal battery function, meaning that secondary batteries will be discarded/recycled, eventually. Therefore, to minimise E-waste a degradable battery is ideal. Furthermore, the largest users of primary batteries are the military and specialty emergency services.[23] This is generally due to a primary battery possessing a higher energy density with longer storage life and operational readiness. As an example, a lithium (Li) primary battery used in cameras possesses more than three times the energy of a Li-ion secondary battery of the same size.[23] Although, within the last ten years there have been a great shift of focus toward secondary batteries due to the improvements in battery technology, charging methods and accessibility to power outlets. In addition, secondary batteries eventually become more economical despite being more expensive initially to produce and to purchase commercially. For instance, an AA sized 1.5 V alkaline primary battery would cost ca. £ 91.90 to produce 1 kWh, whereas, a 6 cell 7.2 V nickel-cadmium (Ni-Cd) secondary battery would cost ca. £ 44.23 to produce 1 kWh.[23] However, this secondary battery is considerably larger than the primary battery and the size difference between these batteries could be a factor to also consider. **Figures 3** and **4** demonstrate examples of commercially available primary and secondary batteries.

Manganese dioxide cathode and positive connection

Outer protective casing

Zinc anode with potassium hydroxide (electrolyte)

Ion conducting separator

Current collector for anode and negative connection

Protective and separating cap

Anode

Half-cell equation:

$Zn_{(s)} + 2OH^-_{(aq)} \rightarrow ZnO_{(s)} + H_2O_{(l)} + 2e^-$

Oxidation

Cathode

Half-cell equation:

$2MnO_{2(s)} + H_2O_{(l)} + 2e^- \rightarrow Mn_2O_{3(s)} + 2OH^-_{(aq)}$
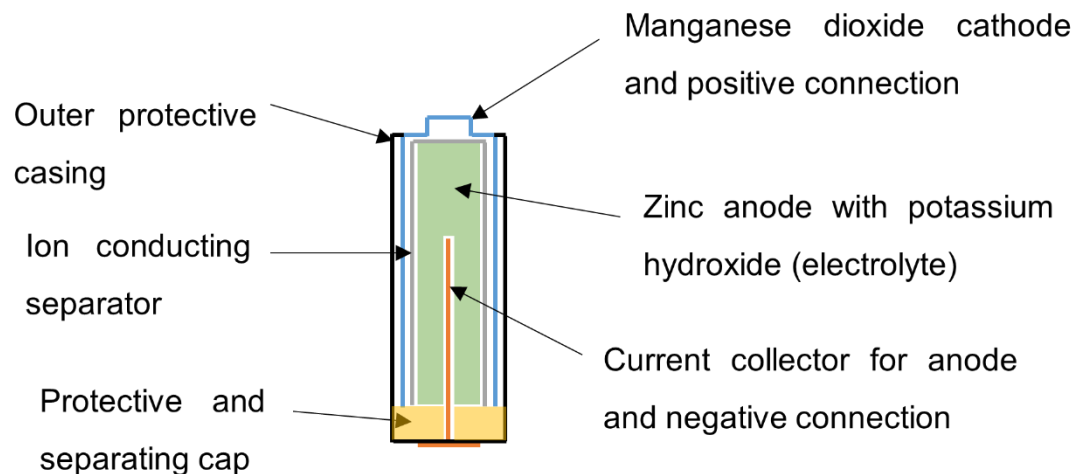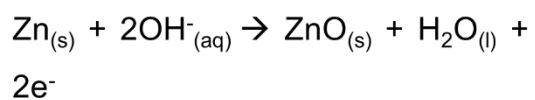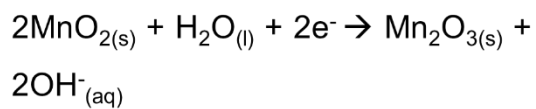
Reduction

**Figure 3.** Diagram for a commercially available 1.5 V alkaline primary battery.

The overall electrochemical cell reaction of the battery in **Figure 3** is:

$$Zn_{(s)} + 2MnO_{2(s)} \rightarrow ZnO_{(s)} + Mn_2O_{3(s)}$$

Ion conducting separator

Nickel oxide-hydroxide cathode and positive connection

Outer protective casing

Cadmium anode with potassium hydroxide (electrolyte) and negative connection

Anode

Half-cell equation:

$Cd_{(s)} + 2OH^-_{(aq)} \rightarrow Cd(OH)_{2(s)} + 2e^-$

Oxidation

Cathode

Half-cell equation:

$2NiO(OH)_{(s)} + 2H_2O_{(l)} + 2e^- \rightarrow 2Ni(OH)_{2(s)} + 2OH^-_{(aq)}$
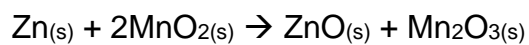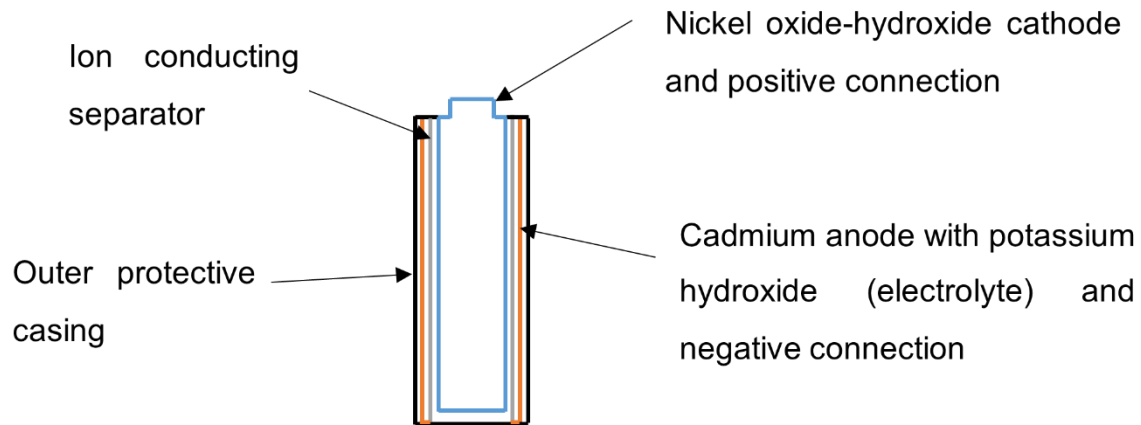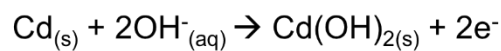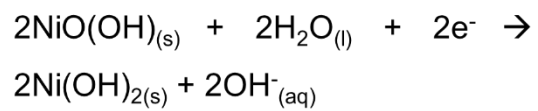
Reduction

**Figure 4.** Diagram for a commercially available 1.2 V Ni-Cd secondary battery.

During discharge, the overall electrochemical cell reaction of the battery in **Figure 4** is:

$$2NiO(OH)_{(s)} + Cd_{(s)} + 2H_2O_{(l)} \rightarrow 2Ni(OH)_{2(s)} + Cd(OH)_{2(s)}$$
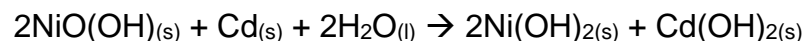
during recharge, under an applied current, the above reaction is reversed.

In summary, the design and choice of material for each half-cell electrode, electrolyte and the conditions of a battery, will give varied current and potential difference values. As a result, this will be a factor in determining the practical applications for a battery. In addition, battery capacity is a measure (typically in Amp-hr) of the charge stored by the battery and is determined by the mass/concentration of active material within the battery. This battery capacity represents the maximum amount of energy that can be extracted from the battery under certain specified conditions. Since batteries are thought of as storing energy; the capacity is how much energy it can store. Therefore, batteries with larger

milliAmpere-hour (mAh) generally last longer than those with smaller mAh values, assuming that the batteries are subjected to the same conditions of use. Furthermore, each redox reaction will spontaneously approach equilibrium between the different oxidation states of the ions, when equilibrium is reached a battery can no longer provide further voltage. Thus, a battery at equilibrium (or without chemical reactants) is a dead battery or is no longer useful. The voltage can be thought of as the cause for a battery to work (i.e. it is out of equilibrium), and the current is the effect of establishing equilibrium. Moreover, when a battery is connected to an external circuit a function can be powered (e.g. a lightbulb can be operated), as depicted in **Figure 1**, **2**, **3** and **4**. However, the extent of useful applications available do not end with operating lightbulbs, a battery is a ubiquitous device in the 21$^{st}$ century and new designs are being developed (e.g. degradable and biocompatible batteries).

## 2.3 Transient batteries

Batteries fulfil a significant role in powering our technology, they are also as important when applied in transient electronic technologies. Since these energy storage devices are commonly used in a variety of different electronic devices, it is therefore crucial to improve and develop their potency (i.e. being practical with low-cost, high energy density and safe for the environment). To date, battery technology (e.g. akin to that depicted in **Figure 1**, **2**, **3** and **4)** has been mostly successful, attributed by how common they are in our day-to-day lifestyle. According to the environmental protection agency (EPA), the populace of the United States of America discards more than 3 billion batteries each year,[24] by factoring in the estimated total population of the United States of America in 2018 (327.2 million), would suggest each person had potentially used 9 batteries, at least. Therefore, the success has ultimately led to the accumulation of E-waste, ca. 50 million tons a year.[4] An additional motivation for a transient design in energy storage is by tackling the E-waste issue. Hereby, a degradable battery possesses the highlight feature that enable them to power potential and current transient electronic devices, such as TIMBs to achieve full transiency, because they may degrade harmlessly into their environment.

Consumer market aside, research and development continue to develop and design new energy storage devices with transiency. Recently, a fully degradable battery has been reported capable of driving typical ultralow power implantable electronics with robust functions. Demonstrated operations included a light emitting diode (LED), a calculator, and the amplifier of an electrocardiogram (ECG) signal detector. The battery also exhibited a desirable biocompatibility both *in vitro* and *in vivo*. The battery can potentially be used as an on-board power source to achieve self-powered therapeutic systems for tissue regeneration, pre-surgery, or post-surgery monitoring over extended periods, which

would otherwise be impossible due to the limitations of currently available power tools.[5] **Figure 5** demonstrates the design of this degradable and biocompatible battery.
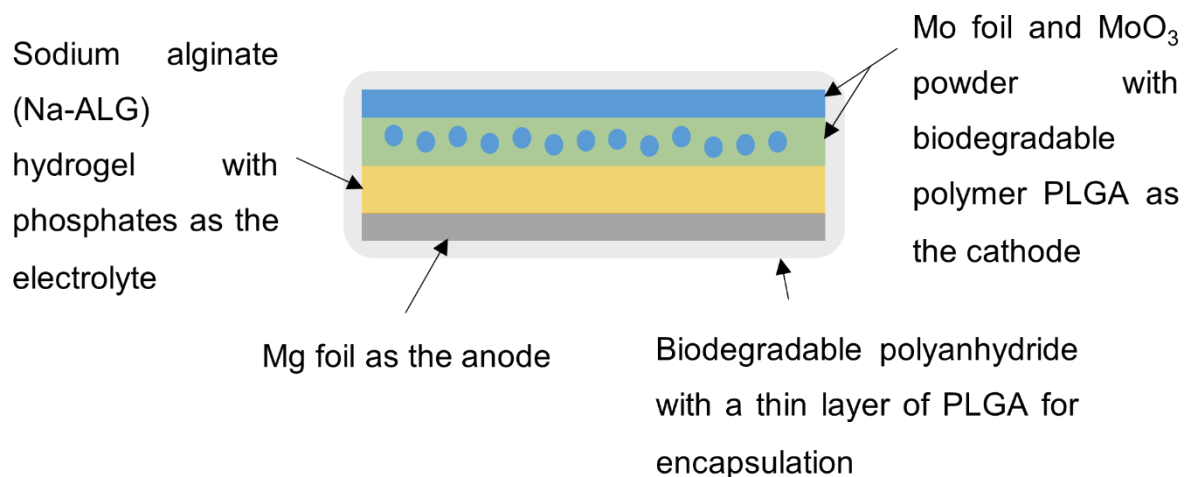


**Figure 5.** Schematic of the degradable and biocompatible Mg-MoO₃ battery. The battery was assembled by stacking the layers of electrodes and electrolyte. In addition, an encapsulation procedure was carried out for protection and rigidity. A degradable UV curable polyanhydride with a thin layer of PLGA encapsulated the battery.

The materials strategies and fabrication scheme represented in **Figure 5** enable a functional, fully degradable battery. The degradation rates of biopolymers depend on their specific chemistry, molecular weight and terminal groups, for instance, partially oxidised alginate losses 70 % of molecular weight within 5 days, PLGA (65:35) losses 50 % of mass after ca. 18 days,[5] while polyanhydride fully degrades within 48 hours in moisturised environments.[5] Although $MoO_3$ is expected to dissolve quickly in aqueous solutions, due to its high solubility (ca. 1 g $L^{-1}$), its degradation rate is modulated by the PLGA binder and encapsulation layers. The observed degradation rates of the battery materials (e.g. metallic films, alginate and polyanhydride) are comparable with the reported results in the literature, while PLGA dissolves faster likely due to the thin-film formats of the layer (< 20 µm).[5]

The introduction of $MoO_3$ to the cathode material increased the output voltage by a factor of three compared to that of a Mg-Mo battery.[5] This increase was reported to be due to the reduction of Mo(VI) at the cathode site, as well as the 3-D network structure.[5] The discharge reactions of the Mg-MoO₃ battery at the Mg anode are reported as follows:

$$Mg_{(s)} \rightarrow Mg^{2+}_{(aq)} + 2e^-$$
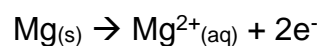
with a side reaction with aqueous electrolyte

$$Mg_{(s)} + 2H_2O_{(l)} \rightarrow Mg(OH)_{2(s)} + H_{2(g)}$$

whereas for the $MoO_3$ cathode, the discharge reactions are supposed to be either hydrogen evolution or oxygen reduction, reported as follows:

$$2H_2O_{(l)} + 2e^- \rightarrow H_{2(g)} + 2OH^-_{(aq)}$$

$$O_{2(g)} + 2H_2O_{(l)} + 4e^- \rightarrow 4OH^-_{(aq)}$$
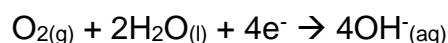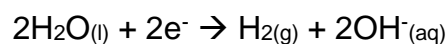
in addition, at the $MoO_3$ cathode, in the analogy to Li-ion battery, the reaction was speculated to be the reduction of Mo(IV)[25]

$$MoO_3 + xM^{n+} + nxe^- \rightarrow M_xMoO_3$$
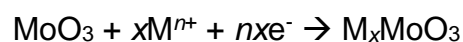
furthermore, the active component $MoO_3$ at the cathode gradually dissolves as the battery discharges which is considered another side reaction. As the $MoO_3$ material is being consumed, the performance of the battery transits to the behaviour of a Mg-Mo battery.[5]

The single cell battery represented in **Figure 5** possessed a stable voltage (~ 1.5 V at a current density of 0.15 mA cm$^{-2}$ for over 5 hours), current capability (12.5 to 150 µA cm$^{-2}$) and capacity (6.5 mWh cm$^{-2}$). This is promising to satisfy the voltage, current and power requirements for most representative ultralow power devices designed for implantable applications.[5] Furthermore, the battery possessed ca. 100 % living cell viability over 5 days *in vitro* and showed no clear visual damage *in vivo*, even after complete degradation within 4 weeks, when implanted subcutaneously in a small mammal (e.g. rats).

In addition, a different degradable battery has been documented in that of a microfabricated PCL-encapsulated Mg-Fe battery with physiological fluid, phosphate buffered saline (PBS) as electrolyte. The battery was documented to meet the power requirements necessary to operate a pacemaker for 4 days.[26] Furthermore, the aim of the study was to demonstrate a degradable battery with improved discharge performance and examine Mg-based battery chemistries to support future efforts in developing degradable batteries. **Figure 6** depicts the design of this degradable battery.
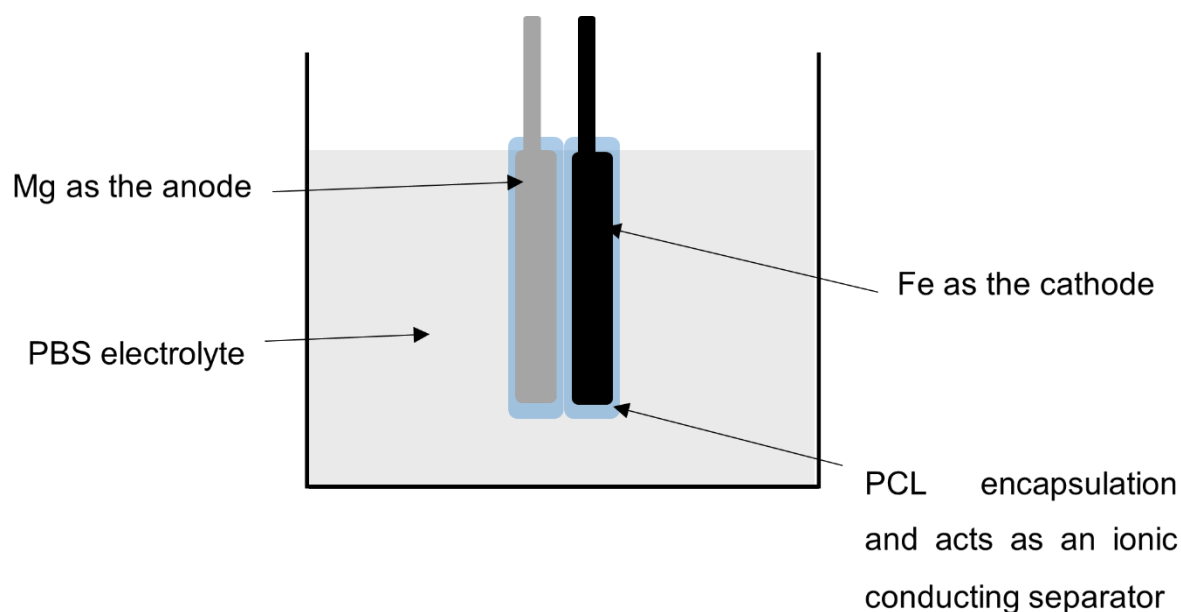


**Figure 6.** Diagram depicting the degradable PCL-encapsulated Mg-Fe battery. The Mg electrode was fabricated via electrodeposition under a nitrogen atmosphere and the Fe electrode via micromachining Fe foil. The assembly of the battery required both electrodes to be dip-coated with a PCL solution and laminated together.

In **Figure 6**, a PCL-encapsulated Mg-Fe battery was shown suspended in a PBS electrolyte, because the ionic constituents of PBS are similarly found within the human body.[27, 28] Although, PBS was used for *in vitro* experiments, it was also reported that this degradable battery can use the body's physiological solution as the electrolyte. Therefore, this battery has promising potential to power TIMB devices (e.g. drug delivery scaffolds and pacemakers) because it also possesses biocompatible materials, such as, Mg, PCL and Fe. More specifically, PCL being FDA approved and both Mg and Fe have confirmed biocompatibility *in vivo* having been used as degradable structural implants, like bone screws or fixation plates.[29, 30, 31] In addition, $Mg^{2+}$ is the fourth most abundant cation found in the body and is an essential mineral nutrient.[32]

The discharge reactions of the Mg-Fe battery depicted in **Figure 6** are reported as follows:

$$Anode\ half\text{-}cell:\ Mg_{(s)} + 2OH^-_{(aq)} \rightarrow Mg(OH)_{2(s)} + 2e^-$$

$$Cathodic\ half\text{-}cell:\ 2H_2O_{(l)} + 2e^- \rightarrow H_{2(g)} + 2OH^-_{(aq)}$$

$$Overall:\ Mg_{(s)} + 2H_2O_{(l)} \rightarrow Mg(OH)_{2(s)} + H_{2(g)}$$
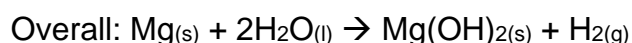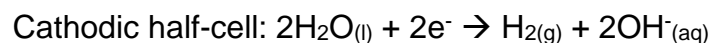
the oxidation of Mg takes place on the anode surface and reduction of either water or hydrogen occurs at the cathode surface. As seen from the overall discharge reaction, magnesium hydroxide and hydrogen gas are generated. However, additional reactions may occur involving electrolyte constituents and should be considered because the by-products of these reactions may have an increased effect on Mg anode corrosion rate[32] which may lower the overall lifetime and performance of the Mg-based battery. In addition, the *in vivo* implantation of Mg implants may have an adverse impact on biological systems due to the evolution of hydrogen gas as has been observed in rats.[33] It has been documented that the gas cavity produced by the hydrogen evolution, from sintered Mg powders, spreads from muscle to more loose subcutaneous tissues causing massive subcutaneous emphysema in the rat's body (ca. 10 to 30 $cm^2$ gas cavity area).[33] The persistent presence of the gas cavity causes prolonged discomfort and disturbs the balance of blood cell parameters which can decrease the rat's survival rate.

Moreover, the battery possessed a discharge time of 99 hours with an average discharge potential (0.7 V), a capacity (1060 mAh $g^{-1}$) and power (29 µW). After 20 days in 37 °C PBS solution, the PCL encapsulation and Mg anode had essentially disintegrated and only the Fe cathode remained. In addition, this battery was reported to possess an energy density of 694 Wh $kg^{-1}$, four times greater than that of non-degradable lithium-manganese dioxide (Li-MDX) batteries, reported to possess 149 Wh $kg^{-1}$.[32] Thus, the effectiveness of this battery was demonstrated, despite the Fe cathode remaining after the 20 day degradation test, meaning the degradation test did not capture the full biodegradation profile of this particular battery.

Furthermore, a silk-based compact encapsulated Mg-air battery made entirely of degradable and biocompatible materials has been documented recently.[1] In addition, the battery utilised a PE

composite, consisting of SF from the *Bombyx mori* (*B. mori*) silkworm and IL ([Ch][NO$_3$]) at a weight ratio of 1:3, respectively. The SF-[Ch][NO$_3$] PE possessed an ionic conductivity of 3.4 mS cm$^{-1}$ and had a two-day degradation profile when immersed in a concentrated buffered protease solution. Since Mg and its alloys possess a high theoretical capacity (ca. 3833 mAh cm$^{-3}$),[34] acceptable dissolution rate and favourable biocompatibility, the Mg alloy 96 % Mg, 3 % aluminium (Al) and 1 % Zn (AZ31) was used as the anode. Furthermore, as a bioinert noble metal and catalyst toward oxygen reduction reaction (ORR), Au was used as the cathode.[1] The design of this battery is represented in **Figure 7**.
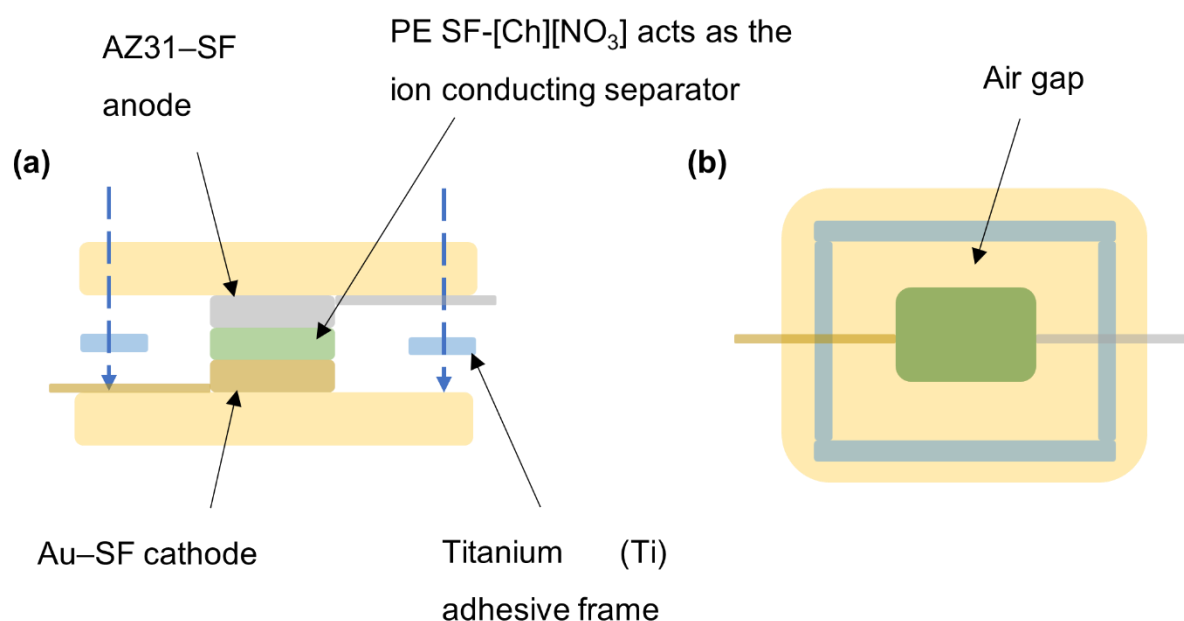


**Figure 7.** Schematic of the degradable and biocompatible thin-film Mg-air battery. a) Cross-section of the Mg-air battery. b) Over head view of the Mg-air battery. The blue dashed arrows demonstrate the edge lamination of the battery utilising a thermal process (120 °C and 130 Psi for 30 s) to achieve complete encapsulation of the battery. Both AZ31 and Au was magnetron sputtered onto a crystallised SF film.

The Mg-air battery system demonstrated in **Figure 7** possesses a reported electrochemical cell notation as follows:

AZ31|SF-[Ch][NO$_3$]|Au-SF

furthermore, the main discharge reactions involved are as follows:

$$\text{Anode half-cell: } 2Mg_{(s)} + 4OH^-_{(aq)} \rightarrow 2Mg(OH)_{2(s)} + 4e^-$$

$$\text{Cathode half-cell: } O_{2(g)} + 2H_2O_{(l)} + 4e^- \rightarrow 4OH^-_{(aq)}$$

$$\text{Overall: } 2Mg_{(s)} + O_{2(g)} + 2H_2O_{(l)} \rightarrow 2Mg(OH)_{2(s)}$$
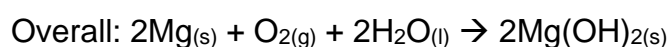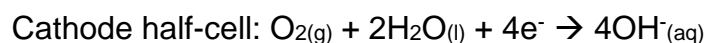
in addition, the anion in the PE may also participate in the reaction with AZ31 forming magnesium nitrate and can result in a decreased conductivity after discharge.[1]

The battery represented in **Figure 7** (with ca. 500 nm AZ31 anode) can deliver a specific capacity of 0.06 mAh cm$^{-2}$ at a current density of 10 µA cm$^{-2}$. The discharge performance was evaluated at the current density of 10 µA cm$^{-2}$ maintained a stable voltage of ~ 1.0 V for 180 minutes. It was also reported that the unsealed version of this battery utilising an AZ31 foil, delivered a specific capacity of 1.43 mAh cm$^{-2}$ with the same current density and for longer discharge times. It was stated that the reduced AZ31 material and limited oxygen availability in the encapsulated battery (as depicted in **Figure 7**), may be the reason for this discrepancy.[1] Nevertheless, the power offered (8.7 µW cm$^{-2}$) may fulfil the requirements for average consumption of published wireless implantable sensing systems (< 0.5 V, < 0.5 µW).[35] In addition, the encapsulated design provides an air preloaded battery strategy, being advantageous when implanted in sites where oxygen is limited. Moreover, SF was utilised because it is a naturally occurring degradable protein. It possesses the capability to entrap or stabilise chemical or biologically active molecules, allowing for the addition of a new function. Hence, the combination of the SF and IL created the PE composite membrane suitable for the Mg-air battery. Specifically, it is both degradable and biocompatible while providing a suitable and stable electrochemical potential window (up to 2.3 V) and ionic conductivity (3.4 mS cm$^{-1}$, mentioned previously). The degradation test for the battery had shown a complete disintegration within 45 days when incubated in buffered protease solution at 37 °C.[1]

To note, the OCV for the encapsulated Mg-air battery in air and when submerged in PBS solution was also recorded. It was documented that when in air the battery had shown a stable OCV (1.21 V) with 11 % self-discharge loss after 180 minutes. Whereas, when exposed to PBS solution had instead shown a two-stage transient behaviour. The OCV was stable at 1.21 V for 64 minutes i.e. the same discharge profile as in air, but rapidly degraded in function within the next 22 minutes.[1] In addition, it was also reported that the discharge profile can be lengthened with additional silk layers for increased protection. For instance, with an additional silk layer, the OCV results showed the same discharge profile as the battery in air for 125 minutes before degrading in function within 50 minutes.[1] The utilisation of SF from the *B. mori* silkworm was observed to be key in tuning the device's transience. Hereby, demonstrating a tuneable characteristic for this battery, granting a greater degree of controllability.

The importance of SF in the previously mentioned device's functionality is undeniable, SF is a biopolymer that can be processed into materials with attractive properties for use in a multitude of technical and medical applications (including textiles, sutures, drug delivery devices, tissue scaffolds, etc.) [11, 37, 38, 39, 40, 41] Natural silk fibres are semi-crystalline materials containing a mixture of secondary structures (e.g. β-sheets, helices, β-turns and random coils) dependent on the species creating them.[42, 43] *B. mori* SF can assume two distinct structures in the solid state,[11] silk I and silk II (before and after spinning, respectively). Silk I is a β-turn type II conformation-rich structure, whereas, silk II is an antiparallel β-sheet-rich structure.[11] A common challenge when analysing silk via XRD or electron diffraction studies, is the potential for the silk to convert from silk I to silk II.[43] Other experimental techniques have also been applied, such as, solid-state nuclear magnetic resonance (ssNMR), which is advantageous as the silk I form can be analysed without reorientation or crystallisation (and simultaneous conversion into silk II).[43] Further detail has been obtained using atomistic simulations on SF structures derived from nuclear magnetic resonance (NMR) methods, such as, two-dimensional (2-D) spin diffusion NMR, rotational echo double resonance (REDOR) and $^{13}$C chemical shift data, as well as, XRD data of a poly(Ala-Gly) sample.[11] The *B. mori* SF macromolecule is comprised of three segments (heavy chain [HC] ca. 350 kDa, light chain [LC] ca. 26 kDa and P25 ca. 25 kDa) in a ratio of 6:6:1.[44, 45] The HC is connected to the LC via a single disulphide link, while the P25 gene has non-covalent interactions with the HC and LC.[46] Furthermore, the HC is made up of 5,263 residues where glycine (Gly) is present in 45.9 %, alanine (Ala) in 30.3 %, serine (Ser) in 12.1 %, tyrosine (Tyr) in 5.3 %, valine (Val) in 1.8 % and 4.7 % of the other amino acids.[47] The HC possesses twelve repetitive domains that are Gly rich forming the crystalline regions, separated by short linker domains (42 to 43 residues). The short linker domains are non-repetitive and form amorphous regions.[43] Whereas, the

repetitive domain is predominantly formed of Gly-X repeats (ca. 94 % of the repetitive domain), where X is Ala (64 %), Ser (22 %), Tyr (10 %), Val (3 %), threonine (Thr) (1.3 %).[46, 47]

Ultimately, information such as that discussed above, can assist in the design of future degradable and biocompatible batteries which may lead to the overall development and improvement of transient electronic technology and their potency. Future work may provide additional avenues for applications using transient on-board energy storage systems to support the next generation of transient electronics and TIMBs, for example, systems required for tissue regeneration or drug delivering scaffolds. All the while, protecting the environment from E-waste.

## 2.4 Molecular dynamics

Since the 1970s, MD has been widely used to study the structure and dynamics of macromolecules, like proteins. There are two main echelons of MD methods which can be distinguished according to the model and the resulting mathematical formalism chosen to represent a physical system.[48] The classical approach to MD simulations treats molecules as classical objects, resembling a ball and stick model. The laws of classical mechanics define the dynamics of the system. The quantum approach to MD simulations considers the quantum nature of the chemical bond. The electron density function for the valence electrons that determine the bonding in the system are computed using quantum equations, whereas the dynamics of ions are followed classically.[48] Therefore, quantum MD simulations represent an improvement over the classical approach, however, they require more computational resources. Currently, classical MD simulations are practical for larger molecular systems comprising many thousands or millions of atoms over longer timescales (e.g. microseconds).[49, 50] To note, it is intuitively clear that computational approximations inevitably become less accurate with the growing complexity of a system. Thus, bridging the gap between experiment and theory is difficult and requires the use of realistic but practical models to represent 'real' systems, or as close to reality as currently achievable.

MD studies can be described as a computer simulation method used for the study of the physical movements of atoms and molecules, and can examine aspects that are not easily measured experimentally (e.g. specific bond interactions, conformational probability, and energies of interactions and chemical structures).[8] An MD simulation experiment requires a setup process, like laboratory-based experiments (e.g. wet laboratories). For instance, classical all-atom MD simulations employ Newtonian's laws of motion to evolve a system of atoms in time. These simulations simply require the user to provide a set of initial atomic coordinates and a potential model to describe the interactions present. The atoms and molecules are allowed to evolve in time, providing a view of the dynamic

evolution of the system. The method was originally developed within the field of theoretical physics in the late 1950s but has since seen application in chemical physics, materials science and the modelling of biomolecules.[9, 10, 11]

The coordinates required for an MD simulation can be obtained from experimental structures, or from models, or some combination thereof.[8] Such experimental structures and information can be derived from X-ray diffraction (XRD) studies, which is a technique used for determining the atomic and molecular structure of a crystal. The crystalline structure causes a beam of incident X-rays to diffract into many specific directions. By measuring the angles and intensities of these diffracted beams, a crystallographer can produce a three-dimensional (3-D) picture of the density of electrons within the crystal. From this electron density, the mean positions of the atoms in the crystal can be determined, as well as their chemical bonds, their crystallographic disorder, and various other information. These structures are then stored in easily accessible databases, such as the protein database bank (PDB), that allow researchers to download the information required to create an MD simulation. The information contained in these PDB files are necessary to run certain MD simulations, specifically, the atom records: atom name (N, C, Ca), residue name (ALA, HIS), residue id (integer), coordinates (x, y, z), occupancy (0.0 to 1.0) etc. However, PDB files for compounds do not contain their hydrogen (H) atoms, so they should be added manually after download but before running MD simulations. In addition, if the simulation requires a compound/structure not available on the PDB, this then will require the building of a representative structural model, which can be very complex.

An MD simulation also requires the definition of a potential function, or a description of the terms by which the particles in the simulation will interact. This can be referred to as a force field and can be defined at different levels of physical accuracy; those most used in chemistry are based on molecular mechanics and embody a classical mechanics treatment of particle-particle interactions that can reproduce structural and conformational changes, but usually cannot reproduce chemical reactions.[12] With respect to high molecular weight components (e.g. proteins and polymers) they can consist of a vast number of atoms, rendering it difficult to determine all the properties of such complex systems due to the expensive computational cost. However, MD simulations can circumvent this problem by using numerical methods. Long MD simulations can be mathematically ill-conditioned, generating cumulative errors in numerical integration, yet they can be minimised with the proper selection of algorithms and parameters (although potentially not entirely eliminated). Another aspect to consider when conducting MD simulations is the timescale of the experiment; these depend on the interactions desired to probe in the simulation, including bond vibrations (femtoseconds) and protein folding (microseconds to seconds). Furthermore, the MD system parameters can be carefully controlled (e.g.

its temperature and pressure) which is advantageous since the MD simulations can be directly linked to experimental observations because you can perform the simulations within the standard thermodynamic ensembles used in statistical mechanics. Thus, as a general principle, the simulation length and model should be as close to reality and the biological event as possible.

With the necessary information acquired, MD simulations can be run with ease and the data collected and analysed without the use of expensive consumables or generation of waste. Therefore, simulations provide a cheaper/safer (and quick) method to improve the understanding of the science underpinning TIMBs, by predicting the behaviour of the device, and thereby enhancing device controllability. In summary, computational simulation is a tool used to improve the understanding of physical and chemical properties. In addition, it can provide information not easily accessible from experimental study.

### 2.5 Molecular dynamics of transient materials

A better understanding of transient materials could lead to the development and improvement of transient electronics, like degradable and biocompatible batteries, as previously discussed. Therefore, further investigation on the science behind the transient characteristic is required and laboratory-based *in vitro* tests currently do not provide sufficient information. MD simulations on the materials involved within a transient electronic device could elucidate the transient process (e.g. water diffusivity, ion interactions and alterations to secondary structures). MD simulation experiments using test models for transient materials (e.g. degradable polymers), may explain how/why degradation (during a degradation experimental test) occurs and could lead to theoretical predictions for future investigations. This could ultimately introduce a degree of control over the transience of a material and to a more tailored application for a transient electronic device. Moreover, there is a complex network of chemical entities and interactions within a system that can evolve dynamically at a molecular level, and the challenge arises from utilising a representative model for describing a process. For example, polymers and proteins fold (adopting specific structure consistent with their function), ions transported through membranes and enzymes triggering a cascade of chemical reactions (protease increasing the degradation rate of the Mg-air battery depicted in **Figure 7**). With faster and more powerful computers larger and more complex systems may be explored using computer modelling or computer simulations.[48]

A study conducted in 2008 utilised MD simulations to investigate hydroxyapatite (HA)/biopolymer interface interactions in composites for biomedical applications (e.g. bioceramics).[65] The binding energies between HA and three different polymers: polyethylene (PEE), polyamide (PA) and polylactic

acid (PLA) were analysed on HA crystallographic planes (001), (100) and (110). The results demonstrated that HA (110) had the highest binding energy (at least a 20 % increase in binding energy in Kcal mol$^{-1}$) with the three polymers due to a reported higher planar atom density over HA (001), and (100). Furthermore, the binding energies of PA/HA and PLA/HA were much higher than that of PE/HA (ca. 4 times magnitude), which was attributed to the greater degree of polar groups in PA and PLA chains over PE.[65] The MD simulation results reported from this paper provided further insight into the design of polymer/HA composites by investigating the binding energies, the high binding energy indicates a high adhesive strength between the polymer and HA surfaces. This study is of particular interest because PLA is a degradable and biocompatible polymer that has been used in transient electronic devices, in the form of water-soluble organic thin-film transistors, mentioned previously. The computational model for the discussed PLA and HA is depicted in **Figure 8**.
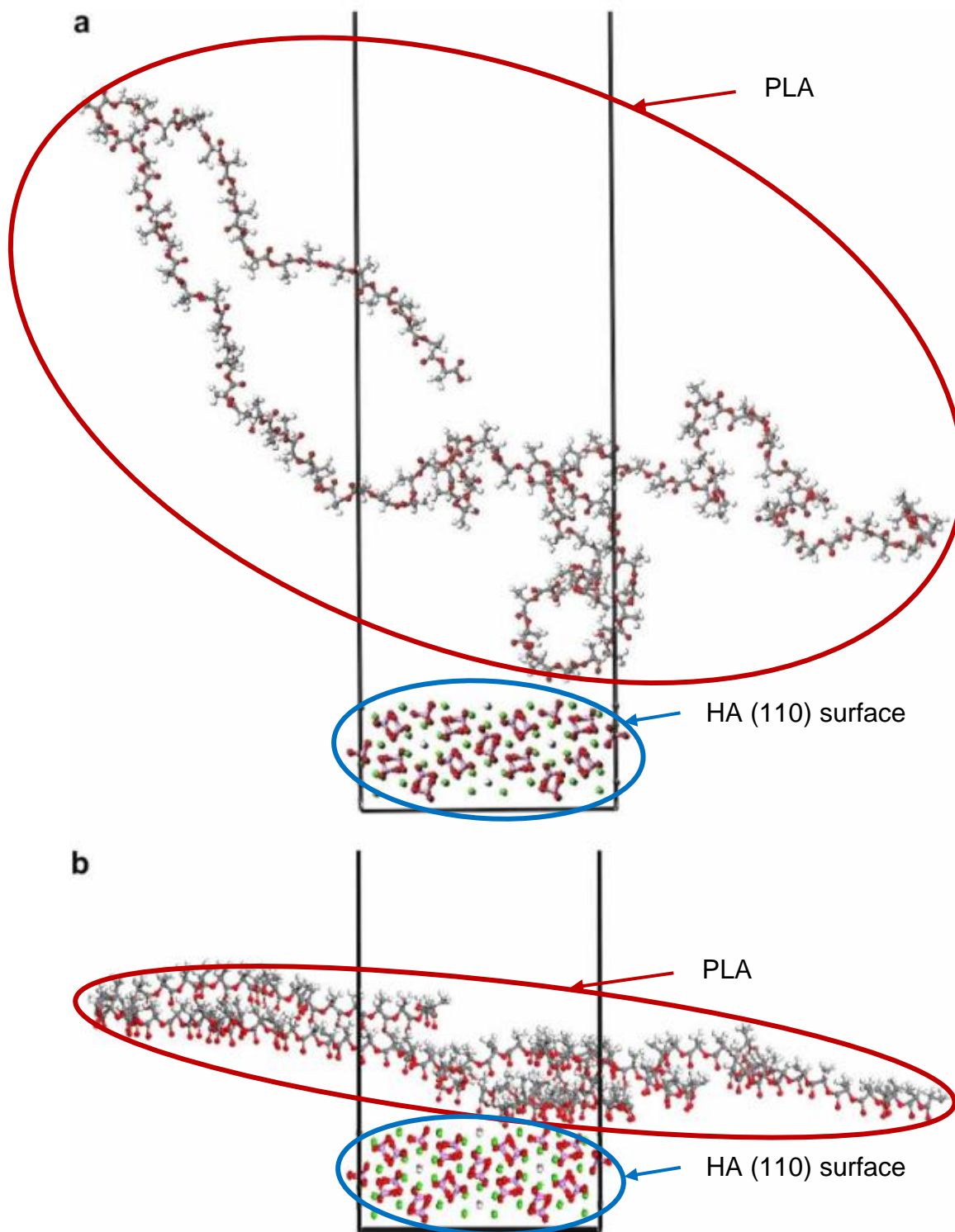
**Figure 8.** Edited screenshot taken from the literature[65] representing PLA on the HA (110) surface pre (a) and post (b) MD simulation. The dark grey ball and sticks depict carbon atoms, white the hydrogen atoms and red the oxygen atoms for PLA. The white ball and sticks depict the hydrogen atoms, green the calcium atoms, red the oxygen atoms and purple the phosphorous atoms for HA (110).

The simulation was conducted using condensed-phase optimised molecular potentials for atomistic simulation studies (COMPASS) force field. The COMPASS force field is a general all-atom force field for atomistic simulation, developed by state-of-the-art *ab initio* and empirical parameterisation techniques and has been proven to be applicable to both organic and inorganic materials.[65] The polymer chains used for the MD simulation were built with an amorphous characteristic (lack of periodicity) and with densities that match commercially available versions of each polymer. For instance, PE (190 monomers) 0.94 g cm$^{-3}$, PA (30 monomers) 1.15 g cm$^{-3}$ and PLA (120 monomers) 1.2 g cm$^{-3}$. In addition, each polymer system was optimised using MD calculations to obtain a stable configuration for 50 ps at 300 K under the NVT ensemble.

Yamane *et al.* conducted MD simulations to investigate the conformational change of silk I to silk II of SF from the *B. mori* silkworm to elucidate the characterisation of the conformational structure (specifically silk I form).[11] It was reported from this study that the conformational change of silk I to silk II occurred by stretching the chain within the MD simulation, but the change occurs under temperatures as high as 1000 K with great tensile stress (1.0 Gpa) in a vacuum. Although, it was also documented that this change can be easily facilitated by considering several external factors. Such factors include the application of shear and tensile stresses to the chain simultaneously and with water molecules present around the silk chains. It was reported that a system at 298 K with shear stress ca. 0.5 Gpa and tensile stress fixed at 0.1 Gpa, with 229 water molecules in the periodic cell, the conformational change of silk I to silk II can be achieved. The 229 water molecules correspond to about 30 w/v %, which is analogous to what can be observed for the concentration of SF in the middle of silk glands.[66] In addition to PLA previously discussed, SF is another example of a degradable and biocompatible material that has been applied in transient electronic devices. For instance, SF has been used as an encapsulation material for the degradable and biocompatible battery depicted in **Figure 7**. The computational model used to represent the initial silk structure (in silk I conformation) was a repeat of four type II β-turn (Ala-Gly)$_4$ structures, represented in **Figure 9**.
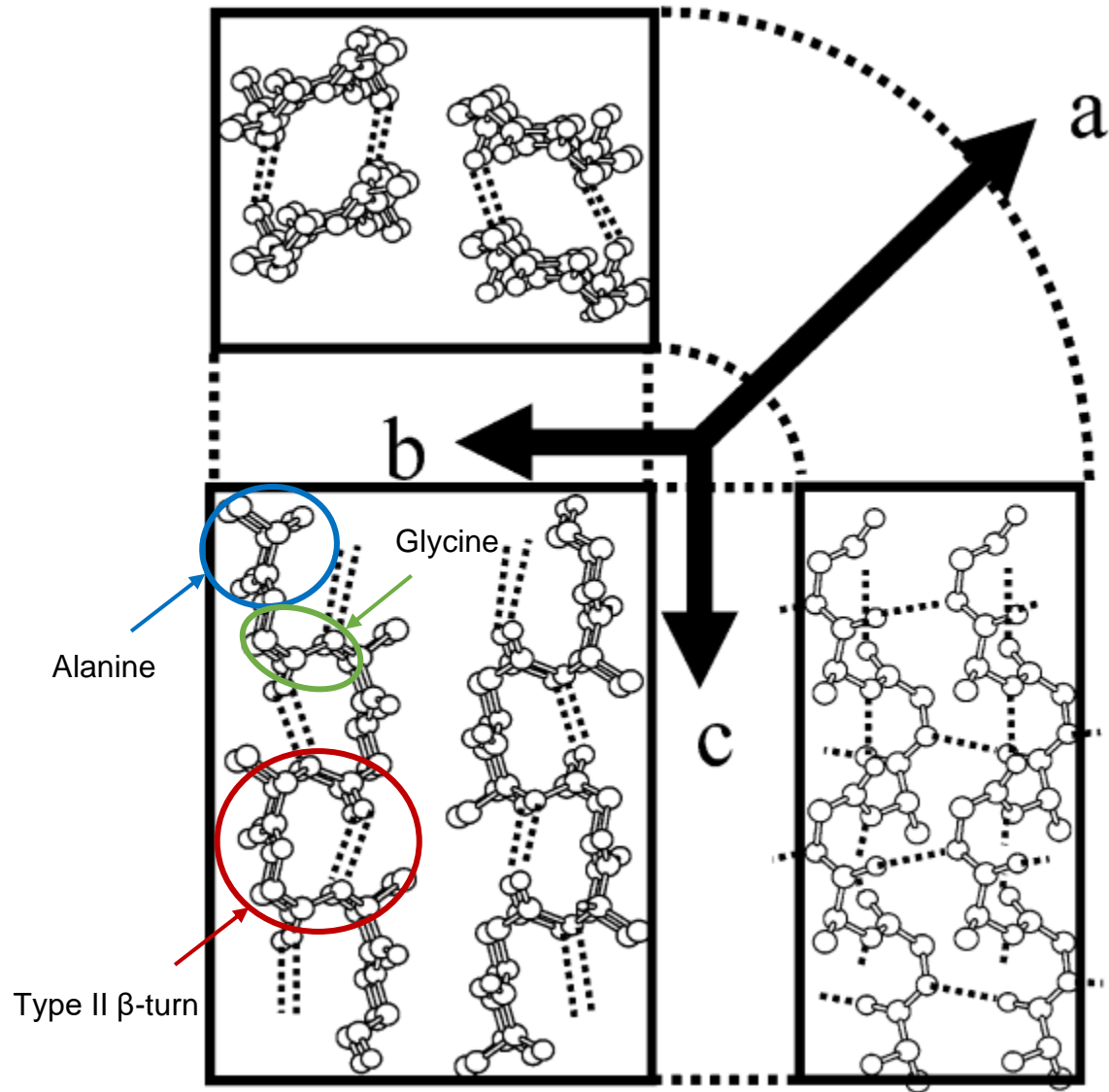
**Figure 9.** Edited screenshot taken from the literature[11] depicting the initial crystal structure of *B. mori.* SF in a silk I conformation. The type II β-turn structure is stabilised by 4 → 1 intramolecular hydrogen bond interactions, depicted by the dashed lines between polymer chains. The thick black box represents the periodic boundary.

The initial silk structure model for the MD simulations were equilibrated (with no stress conditions), both in vacuum and in the presence of water molecules. Once the equilibrium state had been obtained, the Parrinello and Rahman method was used for the MD simulations under external stress such as tensile and/or shear stress. With this method, the cell vectors ($a$, $b$, $c$) determine the cell shape and size and are introduced as a degree of freedom in the system.[11] Then, the Lagrangians of the system

at the $n$th time step in a simulation are modified based on before an $(n-1)$th time step with a term representing the kinetic energy of the cell as follows in equation (6):

$$L_n = \frac{1}{2}\sum_{i=1}^{N} m_i \dot{s}'_{i,n} G_n \dot{s}_{i,n} - \sum_{i}^{N}\sum_{j}^{N} \phi(|r_{i,n} - rj, n|) + \frac{1}{2}WTr(h'_n h_n) - p(\Omega_n - \Omega_{n-1})$$

$$+ \Omega_{n-1} Tr(\sigma - p)\epsilon_n \qquad (6)$$

Here, $m_i$, $\dot{s}_{i,n}/\dot{s}'_{i,n}$ are mass and positional parameters for the $i$th atom in the cell at the $n$th time step. The $h_n = \{a_n, b_n, c_n\}$ is the cell vector matrix at the $n$th time step, $G_n = h'_n h_n$, $r_{i,n} = h_n s_{i,n}$, $\phi$ is the interaction potential, and $W$ is an arbitrary variable which can be defined by the user, in this study it was maintained at the default value. The $p$ and $\Omega_n$ are the pressure and volume of the cell, respectively. Furthermore, $\sigma$ and $\epsilon$ are the stress and strain tensors, respectively. To note, it was reported that the different tensile stresses were performed parallel to the silk fibre's axis, defined as the Z-axis of the Cartesian coordinate of the system. In addition, in both vacuum and water systems, the velocity Verlet algorithm[51] was used to integrate Newton's equation of motion (with a time step of 1.0 fs) and the temperature was controlled using the Andersen method.[67]

The conformational probability was calculated at the equilibrium stage and after MD calculations under external forces. The backbone torsion angles of each residue were extracted from the trajectory of each simulation, then used for the calculation required for the fabrication of the histograms of conformations.[11] Hereby, the conformational probability of the residues of the structural model were calculated using the following equation (7):

$$P(\phi, \psi) = \frac{N(\phi \pm 10°, \psi \pm 10°)}{N_{total}} \qquad (7)$$

Where $N_{total}$ depicts the total number of configurations in the trajectory. The conformational probabilities $P(\phi, \psi)$ would typically be plotted against the torsion angles, $\phi$ and $\psi$.

As previously mentioned, the torsion angles for residues were extracted from the trajectory of the MD simulation. The overall planar sheets were held together by a number of intermolecular hydrogen bond interactions, involving a central amide bond of the β-turn, perpendicular to intramolecular interactions. This would represent the SF in the silk I form and would comprise the periodic cell unit, as shown in **Figure 9** (the water molecules could then be added, as mentioned previously). The periodic boundary condition used was where N- and C-terminals are connected to mirror images of themselves. It has been documented via X-ray and electron diffraction studies that *B. mori* SF and periodic copolypeptide L-Ala-Gly, show similar unit cell dimensions and crystal structure.[68] Since Ala-Gly is a highly repetitive sequence of the *B. mori* silkworm's SF,[69] the use of this structural model is relatively justified, albeit, vastly simplifies the overall structure of *B. mori* silkworm's SF. However, it is easier and more convenient to run computational MD simulations on the Ala-Gly structural model compared with the entirety of *B. mori* silkworm's SF crystal structure. Furthermore, upon achieving the silk II form, the water molecules were removed and the fraction % of β-sheet and β-turn Ala-Gly residue chains were extracted. The results from the MD simulation experiments were compared with ^{13}C ssNMR experimental studies of the natural fibre of *B. mori* silkworm SF, in the silk II form. Both computer simulation and experimental results demonstrate silk II as a heterogenous structure, possessing a mixture of β-sheet (parallel and anti-parallel) and distorted β-turn configurations. More specifically, the MD simulation experiment at 298 K, ca. 0.5 Gpa shear and 0.1 Gpa tensile stress with water molecules present, achieved 74.9 % β-sheet and 25.1 % β-turn content. Comparatively, the ^{13}C ssNMR experimental study reported that SF possessed 73 % β-sheet and 27 % β-turn content.[11] Thus, the heterogeneous structure determined from the ^{13}C ssNMR spectrum could be reproduced from MD simulation experiments. Hereby, representing an important example of bridging two different methods, experimental and theoretical, at tackling new challenges.

MD simulations can provide a key insight into the structural dynamics of proteins and, by implication, also their function. However, reliability of structural predictions derived from MD simulations depends on the accuracy of the underlying force field. Despite formidable progress in the development of accurate all-atom MD force fields in the past decade,[70] MD force fields can struggle to accurately reproduce conformational dynamics of intrinsic amino acid residues and unfolded short peptides.[59] Specifically, the affinity of most amino acid residues (e.g. Ala) to adopt the polyproline II conformation is typically underestimated, whereas the helical content is overestimated.[71] However, repetitive fibrous proteins, like that of the HC of *B. mori* SF, can be polymorphic and may possess an insoluble/poorly soluble crystallisable block and a soluble amorphous block and the dominant secondary structure of the silk may change, depending on the environment of the protein.[72] This is attributed to the high Gly

content of the silk allowing for greater conformational variability than that of most proteins.[72] In addition, while the threefold polyglycine II helix, twofold antiparallel β-pleated sheets, and the poorly characterised structure of silk I have been observed, the conformational freedom provided by the Gly residues do not prohibit other conformations (e.g. intermediate helices) in the extended chain conformational region between the threefold polyglycine II conformation and the twofold β-sheet. Furthermore, a silk III form has also been observed in films prepared from aqueous SF solutions using the Langmuir Blodgett technique. The SF films obtained from the air water interface without compression adopt a different orientation, with the helical axes lying roughly in the plane of the film. The orientation of the fibroin chain axis in the plane of the interfacial film for uncompressed samples is consistent with the amphiphilic behaviour previously postulated to drive the formation of the threefold helical silk III conformation.[73] This polymorphism, notably the ability to induce a transition from a water-soluble silk I form to an intractable β-sheet silk II form, provide attractive options for processing these protein materials for useful biomedical applications (e.g. transient devices).[74] On the other hand, the presence and possibility of a number of slightly different conformations and conformation selection criteria that are sensitive to the environment lead to difficulty in obtaining cross-referenced corroborating data with multiple analytical techniques.[72]

## 3. Background theory

### 3.1 Introduction

The information from computational SF and experimental primary metal-air batteries incorporating SF studies will be utilised with the purpose of fabricating a computational SF model ($[Ala-Gly]_n$ crystal structure), as well as a unique silk-based primary Mg- and Zn-air battery. *B. mori* SF has been shown to play a key role at immobilising ILs (e.g. [Ch][$NO_3$]) via capillary action[1], consequently producing a composite material possessing ionic conductivity, this unique material would act as the PE for the proposed batteries. Because the biopolymer *B. mori* SF can be processed into materials with attractive properties (e.g. biocompatibility, biodegradability and ionic conductivity), it has seen application in a variety of industries.[10, 11, 12, 13, 14, 15, 16] The $(Ala-Gly)_n$ representation for SF is adopted because it has been shown that the lack of Ser in the model peptide $(Ala-Gly)_{15}$ does not affect the $^{13}C$ cross-polarisation magic angle spinning (CP-MAS) NMR chemical shifts of the Ala and Gly residues in the repeated sequence $(Ala-Gly-Ser-Gly-Ala-Gly)_n$ of native SF.[42, 75, 76] This indicates that the absence of Ser in the protein chain does not alter the protein structure. However, the introduction of water molecules around the protein chains has been shown to have an impact on the structural conformation of SF.[11] The subsequent application of both classical MD and electrochemical techniques would be

beneficial, because it offers a unique insight into SF-based materials which would in turn lead to improved device designs (e.g. TIMBs) and combat the E-waste crisis.

## 3.2 Methodological approaches to computational studies

### 3.2.1 Atomistic simulations

Atomistic simulation is a computer simulation method for analysing the physical movements of atoms and molecules. The atoms and molecules are allowed to interact for a period of time, giving a view of the dynamic evolution of the system. Over the last few decades all fields of science have seen an increasing utilisation of computational techniques to the point where these methods stand alongside theoretical and experimental techniques in value.[77] The growth within the computational simulation techniques can be attributed to the advancement in technology and that computing machines are becoming more powerful every year.[78] This has spurred the development of methods and code interfaces, widening the potential of simulations to tackle a wide range of scientific issues and placing tools in the hands of a wider group of scientists.[77] As a result, computer simulations can provide a beneficial insight into the behaviour of atoms or molecules on a scale not easily accessible by traditional experimental investigations. The scale and length of a computational simulation rely upon what behaviour is to be investigated which determines what computational technique should be employed.

Quantum mechanical calculations, also known as *ab initio* calculations, attempt to solve the many-body Schrödinger equation[79] which provides information about the electronic structure of a system. The fundamental laws for a quantum mechanical description of atomistic systems up to the nanoscale are well established.[80] However, there are many challenges related to the quantum mechanical treatment of larger systems. In most cases, scientists struggle to solve the fundamental Schrödinger equation for systems of realistic sizes in such a way that the results satisfy universal requirements of accuracy, precision, and especially predictability. The problems are not only related to the computational complexity needed to solve the equations of quantum mechanics but there are also intrinsic obstacles (e.g. not knowing all necessary conditions).[80] However, in 1964 and 1965, Kohn, Hohenberg, and Sham further reduced the complexity by showing that the electronic density is in a one-to-one correspondence with the ground state energy of a system of interacting electrons, and that such an interacting system can be replaced by a mean-field problem of $N$ non-interacting fermions that provide the same distribution of the density. These are the fundamental ideas of density functional theory (DFT).[80, 81, 82]

Conversely, during MD simulations the time evolution of a set of interacting particles is developed via the solution of Newton's equation for motion, represented in equation (8), where $r_i(t) = \big(x_i(t),\ y_i(t),\ z_i(t)\big)$ is the position vector of the $i$th particle:

$$F_i = m_i \frac{d^2 r_i(t)}{dr^2} \tag{8}$$

the $F_i$ is the force acting upon the $i$th particle at time $t$ and with the particular mass of the particle, $m_i$. Here, the particles typically refer to atoms, although they may represent distinct chemical groups, which may be conveniently described in terms of a certain interaction law.[48] To integrate the second order differential equations, the instantaneous forces acting on the particles and their initial positions and velocities need to be specified. Due to the many-bodied nature of the problem, the equations of motion are discretised and solved numerically. The MD trajectories are defined by both position and velocity vectors, and they describe the time evolution of the system in phase space. Accordingly, the positions and velocities are propagated with a finite time interval using numerical integrators, for instance, the Verlet algorithm.[51] The position and velocity of each particle in space is defined by $r_i(t)$, whereas the velocities $v_i(t)$ determine the kinetic energy and temperature of the system. As the particles move, their trajectories can be displayed and analysed, providing averaged properties.

An atomic force field is used to describe a physical system as a collection of atoms that are held together by interatomic forces. Specifically, chemical bonds result from the specific interactions between atoms that form a molecule. The interaction law is specified by the potential $U(r_1, \dots, r_N)$, which represents the potential energy of $N$ interacting atoms as a function of their positions $r_i = (x_i, y_i, z_i)$.[52] Given the potential, the force acting upon $i$th atom is determined by the gradient (vector of first derivatives) with respect to atomic displacements, as shown in equation (9):

$$F_i = -\nabla_{r_i} U(r_1, \dots, r_N) = -\left(\frac{\delta U}{\partial x_i}, \frac{\partial U}{\partial y_i}, \frac{\partial U}{\delta z_i}\right) \tag{9}$$

the notion of atoms in molecules approximates the quantum-mechanical picture, in which molecules are composed of interacting electrons and nuclei. Electrons are to a certain extent delocalised and shared by many nuclei and the resulting electronic cloud determines chemical bonding. However,

based on the difference in mass between nuclei and electrons and the adiabatic Born-Oppenheimer approximation, the electronic and nuclei problems can be separated.[48] The electron cloud equilibrates quickly for each instantaneous (but quasi-static on the time scale of electron motions) configuration of the heavy nuclei. Thus, the nuclei move in the field of the averaged electron densities. Therefore, the notion of the potential energy surface is introduced, which determines the dynamics of the nuclei without taking explicit account of the electrons.[48] Given the potential energy surface, classical mechanics can be used to follow the motion of the nuclei. By identifying the nuclei with the centre of the atoms and the adiabatic potential energy surface with the implicit interaction law, a justification of the representation of a molecule in terms of interacting atoms is obtained.[48]

The separation of electronic and nuclei variables introduces a new strategy, where the effect of the electrons on the nuclei can be expressed by an empirical potential.[53] For instance, a typical force field used in the simulation of biosystems begin to take the form depicted as follows in equation (10):

$$U(r_1, \dots, r_N) = \sum_{bonds} \frac{a_i}{2}\left(l_i - l_{i_0}\right)^2 + \sum_{angles} \frac{b_i}{2}\left(\theta_i - \theta_{i_0}\right)^2 \tag{10}$$

$$+ \sum_{torsion} \frac{c_i}{2}[l + cos(n\omega_i - \gamma_i)]$$

$$+ \sum_{atom\ pairs} 4\varepsilon_{ij}\left[\left(\frac{\sigma_{ij}}{r_{ij}}\right)^{12} - \left(\frac{\sigma_{ij}}{\Gamma_{ij}}\right)^6\right]$$

$$+ \sum_{atom\ pairs} k\frac{q_i q_j}{r_{ij}}$$

in the first three terms, the summation indices run over all the bonds, angles and torsion angles defined by the covalent structure of the system. Whereas, in the last two terms the summation indices run over all the pairs of atoms, separated by distances $r_{ij} = |r_i - r_j|$, and are not bonded chemically. Physically, the first two terms describe the energies of deformations of the bond lengths $l_i$ and bond angles $\theta_i$ from their corresponding equilibrium values $l_{i_0}$ and $\theta_{i_0}$, respectively. The system's structure is maintained and prevents chemical changes, such as bond breaking, via force constraints introduced in the harmonic form, $a_i$ and $b_i$. The third term describes rotations around the chemical bond, which

are characterised by periodic energy terms, with the periodicity determined by $n$ and heights of rotational barriers defined by $c_i$. The fourth term describes the Van der Waals (VdW) repulsive and attractive (dispersion) interatomic forces in the form of the Lennard-Jones 12-6 potential, and the last term being the Coulomb electrostatic potential. Some effects, due to specific environments, can be accounted for by properly adjusted partial charges $q_i$ (and an effective value of the constant $k$) as well as the VdW parameters $\varepsilon_{ij}$ and $\sigma_{ij}$.[48, 52]

The all-atom optimised potentials for liquid simulations (OPLS-AA) is a popular force field for simulating biomolecules (e.g. transient materials like silk).[54] The OPLS force field is where the total energy ($E_{tot}$) of a molecular system is evaluated as a sum of the following components, non-bonded energy ($E_{nb}$) equation (11), bond stretching and angle bending terms ($E_{bond}$ and $E_{angle}$, respectively) equation (12 and 13), and the torsional energy ($E_{torsion}$) equation (14).[55, 56] As above, the non-bonded term is computed as a sum of the Coulomb and Lennard-Jones contributions for pairwise intra and intermolecular interactions:

$$E_{nb} = \sum_{i<j} \left[ \frac{q_i q_j e^2}{r_{ij}} + 4\epsilon_{ij} \left( \frac{\sigma_{ij}^{12}}{r_{ij}^{12}} - \frac{\sigma_{ij}^{6}}{r_{ij}^{6}} \right) \right] f_{ij} \tag{11}$$

geometric combining rules for the Lennard-Jones coefficients were employed: $\sigma_{ij} = (\sigma_{ii} \sigma_{jj})^{1/2}$ and $\epsilon_{ij} = (\epsilon_{ii} \epsilon_{jj})^{1/2}$. The summation runs over all the pairs of atoms $i < j$ on molecules A and B or A and A for the intramolecular interactions. Moreover, in the latter case, the coefficient $f_{ij}$ is equal to 0.0 for any $i$ - $j$ pairs connected by a valence bond (1-2 pairs) or a valence bond angle (1-3 pairs). $f_{ij} = 0.5$ for 1,4 interactions (atoms separated by exactly three bonds) and $f_{ij} = 1.0$ for all the other cases. The $E_{bond}$ and $E_{angle}$ are reported as follows:

$$E_{bond} = \sum_{bonds} K_r (r - r_{eq})^2 \tag{12}$$

$$E_{angle} = \sum_{angles} K_\Theta (\Theta - \Theta_{eq})^2 \tag{13}$$

where $r_{eq}$ and $\Theta_{eq}$ are used to depict the equilibrium values of bond length and the angle, respectively, derived from experimental X-ray structural information. Whereas $K_r$ and $K_\Theta$ values are derived from linear interpolation between pure single and double bond values using the observed bond distances and vibrational analysis of a simple sp$^2$ atom containing fragments such as benzene and N-methyl acetamide, respectively. Finally, the torsional term is reported as:

$$E_{torsion} = \sum_i \frac{V_1^i}{2}[1 + cos(\phi_i)] + \frac{V_1^i}{2}[1 - cos(2\phi_i)] + \frac{V_3^i}{2}[1 + cos(3\phi_i)] \tag{14}$$

where, $\phi$ is the dihedral angle and $V_1$, $V_2$ and $V_3$ are the Fourier coefficients to be optimised.[55, 56]

When studying biomolecules such as proteins using MD simulations, the dihedral/torsion angle of a protein backbone is an integral aspect of understanding the structural rearrangements and confirmation. The torsion angle depicts the angle between two intersecting planes or half-planes. In chemistry, it is the clockwise angle between half-planes through two sets of three atoms, having two atoms in common, an example of a protein backbone's torsion angles is given in **Figure 10**.
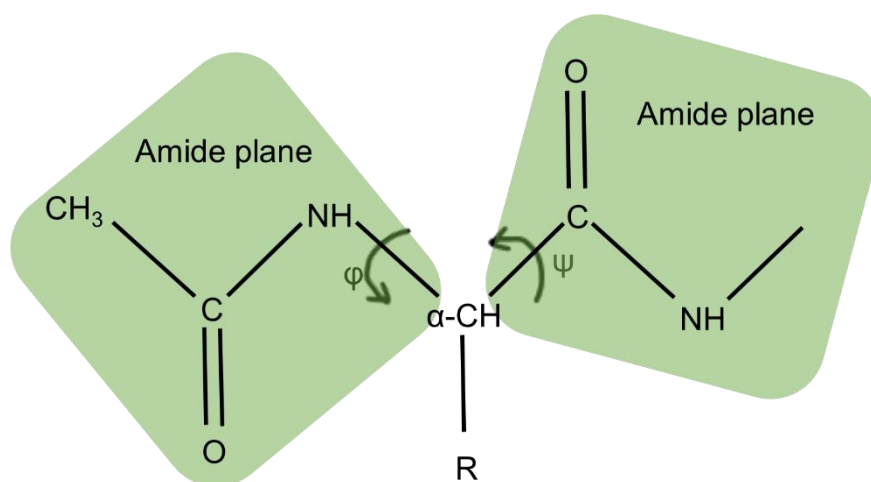
**Figure 10.** Illustration of a protein backbone's torsion angles represented by the phi ($\varphi$) and psi ($\psi$) angles in the amide planes adjacent to the alpha carbon ($\alpha$-C). The black arrows depict the $\varphi$ and $\psi$ angles with respect to the $\alpha$-C.

The torsional angle defines the relative orientation of four atoms in space and it is the angle between two planes (e.g. amide planes in **Figure 10**). Evaluating torsion angles can be advantageous for MD simulations because internal coordinates naturally provide a correct separation of internal and overall motion, which has been found to be essential for the construction and interpretation of the free energy landscape of a biomolecule undergoing large structural rearrangements.[57] Furthermore, knowing the torsion angles of a structure, like a protein, can be utilised in a Ramachandran plotting format. A Ramachandran plot can show the statistical distribution of the combinations of a protein backbone's torsion angles $\varphi$ and $\psi$. In theory, the allowed regions of the Ramachandran plot show which values of the $\varphi$/$\psi$ angles are possible for an amino acid.[58]

Moreover, the time step for MD simulations is an important component and should be dictated by how long the shortest event in the simulation takes to occur (e.g. in a protein structure MD simulation, this will likely be the C-H bond vibrations). The time step limits the length of the MD trajectory; utilising too large of a time step may result in the atoms moving too much between integrations, as a result, the simulation is likely to become unstable because the energy is increasing rapidly with time. There are certain parameters for a system used in simulations known as MD ensembles and a method of ensuring if the time step is suitable is to monitor if there is any drift in energy during a constant energy simulation, utilising the microcanonical ensemble (NVE). In addition to NVE, there are also the MD ensembles canonical ensemble (NVT) and the isothermal-isobaric ensemble (NPT), where N represents the constant number of moles/particles, E the constant energy, V the constant volume, T the constant temperature and P the constant pressure. The ensembles should be employed to best fit the information you want to understand and the link with statistical mechanics.

In nature, it is common to see water molecules participating within biomolecular systems (e.g. structure and function of proteins), although, the experimental properties of water around protein structures are not well understood. Generally, water around proteins can be divided into three categories: bulk water that surrounds the protein molecule, individually bound water that forms hydrogen bonds with charged or polar protein atoms in cavities inside the protein and hydration water at the protein surface with direct interactions with the protein. The three categories have different functions, where bulk water is free to move and assists in protein diffusion relative to the other interacting molecules by random movement in solution. Individually bound water has multiple contacts that stabilize the protein structure

and hydration water forms water networks around the protein surface to keep protein in solution. Computationally, the water can be classified by the separation from the protein surface into bulk water and hydration water. Hydration water interacts closely with the protein and contributes to protein folding, stability and dynamics, as well as interacting with the bulk water. Water potential functions are often parameterised to fit bulk water properties because of the limited experimental data for hydration water. Hereby, a water model is used to simulate and thermodynamically calculate water clusters, liquid water, and aqueous solutions with explicit solvents. The models are determined from quantum mechanics, molecular mechanics, experimental results, and as a combination of these. To imitate a specific nature of molecules, many types of models have been developed, such as transferrable intermolecular potentials: TIPS2, TIP3P and TIP4P; SCP/E and TIP4P/2005.[59, 60, 61, 62] In general, these can be classified by the following three points; the number of interaction points called sites, whether the model is rigid or flexible and whether the model includes polarisation effects. Rigid models are considered the simplest water models and rely on non-bonded interactions. In these models, bonding interactions are implicitly treated by holonomic constraints. The electrostatic interaction is modelled using Coulomb's law, and the dispersion and repulsion forces using the Lennard-Jones potential. The potential for models such as TIP3P (transferable intermolecular potential with three points) possesses three interaction points corresponding to the three atoms of the water molecule; each site has a point charge, $q$ for electrons and an $A$ and $C$ Lennard-Jones parameters, as given by equation (15):[63]

$$\Delta E(12 - 6 - 1) = \sum_a^{in\ A} \sum_b^{in\ B} \left( \frac{q_a q_b e^2}{r_{ab}} + \frac{A_a A_b}{r_{ab}^{12}} - \frac{C_a C_b}{r_{ab}^6} \right) \tag{15}$$

the 12-6-1 (Coulomb plus Lennard-Jones) form has been adopted since it is consistent with earlier work.[53, 64] Nevertheless, 12-6-1 and 9-6-1 functions were developed for water and were found to yield results of similar quality for the liquid.[63]

In accordance with statistical mechanics, physical quantities are represented by averages over microscopic states or configurations of a system distributed within a certain statistical ensemble. For example, NVE in which only the different states corresponding to a specific energy have non-zero probability of occurring. However, in NVT, the temperature and volume are constant, but the energy can be exchanged with the surroundings (e.g. a thermal bath) and the distribution of states is given by the Boltzmann function. Unlike NVT, in NPT, the pressure is constant.[64] In essence, a physical quantity

can be measured by MD simulation by taking an arithmetic average over instantaneous values of that quantity obtained from the trajectories. In the limit of infinite simulation time, such averages converge to the true value of the measured thermodynamic properties.[48] However, it is important to be aware of the limitations of MD in order to make reasonable use of it. For instance, the results from MD simulations will be realistic only if the potential energy function mimics the forces experienced in reality. Despite MD simulation being a useful tool for conformational sampling, it may only yield average structural and thermodynamic properties due to possible errors with numerical integration. Although, sampling many possible configurations can be utilised as an optimisation method. Furthermore, the complexity and accuracy (with respect to reality) of the structural model used for MD simulation experiments should be considered, because this would affect the time and scale of the experiment. Larger or more complex systems become more computationally demanding, because each integration step takes longer when investigating slower changes within a system (e.g. the conformational change of a protein or the degradation of a transient material). Hereby, investigating the transience of materials, used in transient electronic devices, pushes the frontier and development of MD simulations. In addition, it may build a stronger connection between experiment and theory.

Classical calculations employ an empirical force field that is fitted to reproduce the intra and intermolecular interactions between atoms/ions in the system. The form of the interaction potentials is based on considerations of the electronic structure; however, the parameterisation remains fixed during the simulation and therefore, they are unable to represent processes, such as, charge transfer, bond breaking and formation. On the other hand, this loss of electronic flexibility significantly reduces required computer power allowing the simulation of thousands, and in some cases millions of atoms over longer timescales (e.g. nanoseconds) enabling analysis of the secondary structure and the examination of bulk water transport around protein chains, for example. Therefore, classical MD is utilised in this work, with the aim of investigating SF protein structure and interactions within a hydrated system, the details of which will be discussed later in this work.

### 3.2.2 Classical molecular dynamics for the silk fibroin model

Classical MD calculates the time dependent behaviour of a molecular system (e.g. atoms within a supercell) by integrating their equations of motion as given by equation (16):

$$a = \frac{F}{m} \tag{16}$$

where $a$ is the acceleration vector, $F$ is the force vector, and $m$ is the mass of the atom. The crystal lattice is represented by using the supercell which is formed by repeated unit cells where periodic boundary conditions are often applied to approximate an infinite system. Lattice parameters refer to the physical dimension of unit cells in a crystal lattice, generally, the units are represented in Ångströms (Å). Lattices in three dimensions generally have three lattice constants, referred to as *a*, *b*, and *c*. The lattice parameters *a*, *b*, and *c* compose the length (in their respective dimension) of the unit cell while α, β, and γ are their respective angles. When an object (e.g. an atom) passes through one side of a unit cell (when periodic conditions are applied), it re-appears on the opposite side with the same velocity. Therefore, when utilising periodic boundary conditions, the structural characteristics computed are not compromised so that properties of bulk gasses, liquids, crystals, or mixtures etc. could be calculated.[83, 84]

MD simulations generate information at the microscopic level, involving atomic positions, velocities, and forces. The conversion of this microscopic information to macroscopic observables such as pressure, stress tensor, strain tensor, energy, heat capacities, etc. requires theories and strategies developed in the realm of statistical mechanics. Statistical mechanics is fundamental to the study of many different atomistic systems and integrating the equations of motion have led to algorithms for the $N$-body problem. The velocity Verlet algorithm is a numerical method used to integrate Newton's equations of motion and it is frequently used to calculate the trajectories of particles in MD simulations given by equation (17):

$$x(t + \Delta t) = 2x(t) - x(t - \Delta t) + \frac{F(t)}{m}\Delta t^2 \tag{17}$$

where $x$ is the atom position and $t$ is the time.[51, 85]

Furthermore, there are also algorithms to control the temperature, pressure, stress etc. of a system (e.g. Nose-Hoover) enabling the ensembles NVE, NVT and NPT for MD simulations.[86, 87] Most calculations in statistical mechanics use the NVE[67] representing a thermodynamically isolated system. Alternatively, when the system is linked to a thermal bath maintaining a constant temperature, the NVT is used. However, when the system is experiencing constant temperature and pressure the NPT is used.

Studying peptides and proteins using MD is dominated by three classes of all-atom MD force fields for biomolecular simulations: Optimised Potentials for Liquid Simulations (OPLS), Chemistry at Harvard Macromolecular Mechanics (CHARMM), and Assisted Model Building with Energy Refinement (AMBER). The use of these force fields is typically combined with various water models: TIPS2, TIP3P and TIP4P; SCP/E and the more recent TIP4P/2005 water model.[59, 60, 61, 63] In this work, the OPLS-AA[56, 88] force field was implemented for the interactions between the ions in the (Ala-Gly)$_n$ chains in the SF (specifically of *B. mori* SF) crystal model. In addition, the TIP3P[62, 63] water model was utilised to represent the interactions between water molecules and the silk chains when hydrating the supercell of the SF crystal model. These parameters have already seen wide use for many applications in MD simulations,[55, 81] because the parameterisation for the force field OPLS-AA was initially based on experimental information[55, 59, 81] and the three-site models of water achieve high computational efficiency. Furthermore, studies evaluating the performance of various force fields have generally found that OPLS-AA perform well,[89, 90] particularly for quantities that are dependent upon non-bonded parameters. However, some studies have noted weaknesses in the ability of the force fields to reproduce properties that are heavily dependent upon torsional energetics.[91, 92] The implementation of classical MD simulating the structural confirmation of an appropriate SF model in conjunction with experimental data (e.g. lattice parameters derived from XRD for the amino acid residues), would provide additional insight into these materials and possibly highlight conformational intermediates and provide a dynamic view of the structural conformation at various temperatures over nanoseconds.

The Ramachandran plot is a graphical illustration used for visualising protein backbone energetic position in terms of torsion angles.[58] The Ramachandran plot is one of the best methods of representing protein structure with minimal discrepancy between experiments and simulations. The concept is based on the rigidity of the N-C peptide bond, in which the torsion angle φ and ψ, representing X-N-Cα-X and X-Cα-C-O bonded atoms, are restricted by sterically unfavourable structure conformation due to collision between non-bonded atoms. These physical limits are embedded with conformation information and evaluating the data provides essential insight for the protein structure. The essence of Ramachandran plot remains unchanged since it was developed, but its reliability has been significantly improved in recent years.[93, 94 , 95] An example Ramachandran plot of a polypeptide is shown in **Figure 11**.
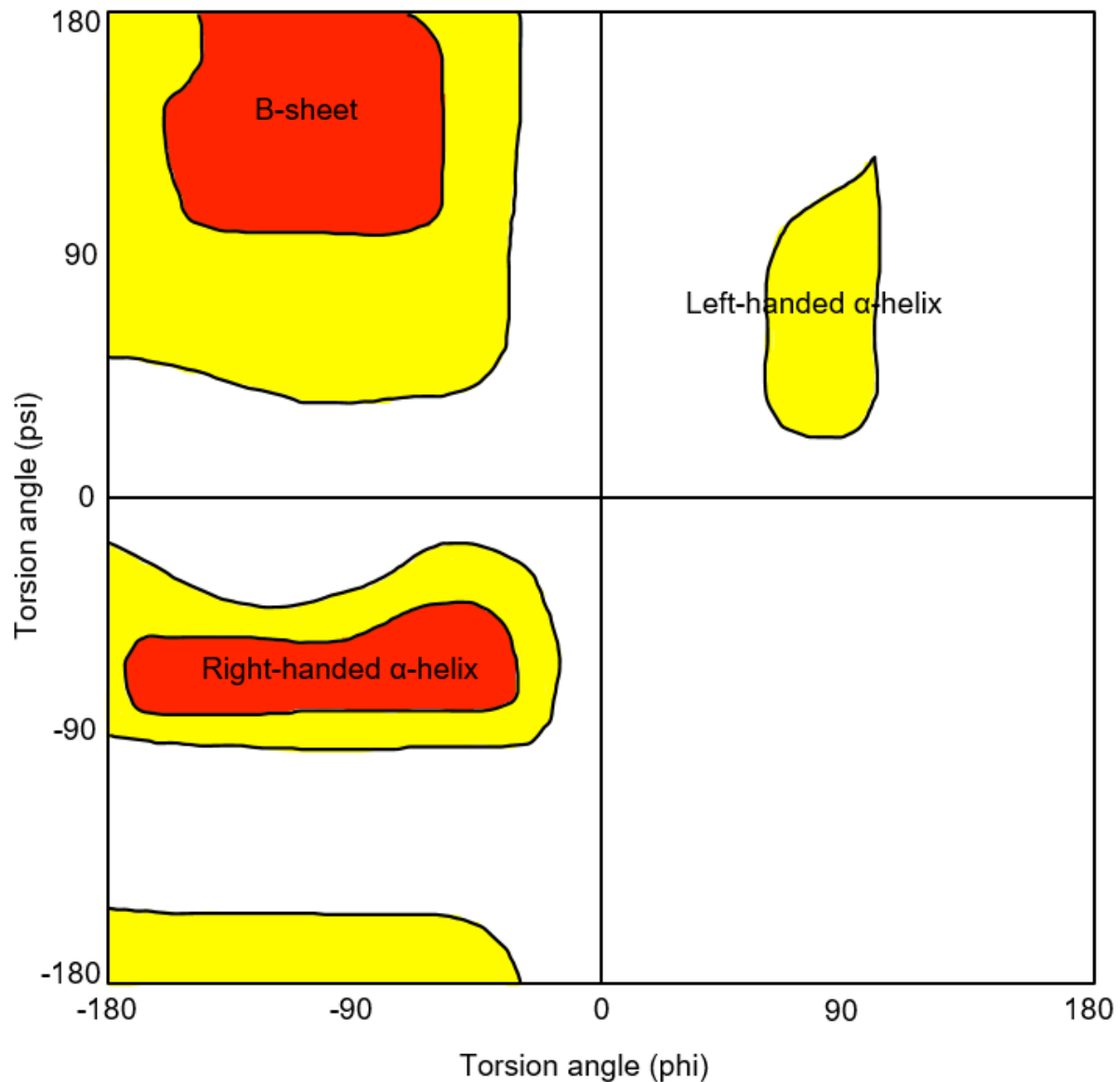
**Figure 11.** Example illustration of a Ramachandran plot of a polypeptide. The white areas in the plot signify regions sterically disallowed for all amino acids except Gly which is unique in that it lacks a side chain. The yellow regions signify regions of allowed confirmation, however, may experience steric hinderance. The red regions correspond to conformations where there are no steric clashes, i.e. these are the allowed regions, namely the right-handed α-helical and β-sheet conformations.

For MD simulations it can also be beneficial to evaluate the mean squared displacement (MSD) of atoms within the system. In statistical mechanics, MSD is a measure of the deviation of the position of the atom with respect to a reference position over time, $t$. It is the most common measure of the spatial extent of random motion.[96, 97] The linear relationship between the MSD and time $t$ allows for graphical methods to determine the diffusivity ($D$) of atoms of interest within a system. Diffusion is defined by the process by which atoms move in a material, for instance, the diffusivity of water or ions within a SF

crystal model. Many reactions in gases, solids and liquids are diffusion dependent. There are diffusion related reactions humans rely upon, for example, oxygen and carbon dioxide dissolved in water, are exchanged by diffusion in the lungs. Fick's second law,[98] predicts how diffusion causes the concentration to change with respect to time and is given by equation (18):

$$\frac{\partial \varphi}{\partial t} = D \Delta \varphi \tag{18}$$

where $\varphi$ is the concentration of the substance in the system's dimensions, $t$ the time and $D$ the diffusion coefficient in the dimensions of the system.

Moreover, the diffusion process is governed by its activation energy, this diffusion activation energy equals the value of the potential barrier that must be overcome by an atom to take a new position in the system. Atoms in gases, solids and liquids move constantly at any given temperature, they are subject to a thermal displacement from their average positions. This displacement is particularly important in the case of liquids. Theoretical calculations of activation energy can be difficult,[99] however the Arrhenius equation (19) can be used to estimate the energy of a diffusion processes:[100]

$$\Lambda = \Lambda_0 \, exp\left(-\frac{E_a}{RT}\right) \tag{19}$$

where $\Lambda$ is the coefficient of diffusion, $\Lambda_0$ the pre-exponential factor, $E_a$ the activation energy of diffusion, $R$ the gas constant and $T$ the temperature.

Atomic displacement does not follow a simple trajectory and the collisions with other atoms render their trajectories quite complex shaped in space. The trajectory followed by an atom in a liquid resembles that of a pedestrian random walk. Mathematically, this represents a sequence of steps done one after another where each step follows a random direction which does not depend on the one of the previous steps (Markov's chain of events).[100] Therefore, MSD also contains information on the diffusion of atoms. If the system is solid (frozen) then MSD saturate, and the kinetic energy is not sufficient to reach a diffusive behaviour. Nevertheless, if the system is not frozen (e.g. liquid) then the MSD will increase linearly in time. In such a case, it is possible to investigate the behaviour of the system by evaluating

the gradient of the MSD in time. The slope of the MSD or otherwise described as the diffusivity is defined by equation (20):

$$D = \lim_{t \to \infty} \frac{1}{6} \langle x^2(t) \rangle \qquad (20)$$

where $x$ is the mean distance from the starting point that a molecule will have diffused in time, $t$. The MSD at time $t$ is defined as an ensemble average depicted by equation (21):

$$MSD \equiv \langle |x(t) - x_0|^2 \rangle = \frac{1}{N} \sum_{i=1}^{N} \left| x^{(i)}(t) - x^{(i)}(0) \right|^2 \qquad (21)$$

where, $N$ is the number of particles to be averaged, vector $x^{(i)}(0) = x_0^{(i)}$ is the reference position of the $i$-th particle and vector $x^{(i)}(t)$ is the position of the $i$-th particle at time $t$.[12] Therefore, the relationship represented by equation (22) is generally valid:

$$\langle x^2 \rangle = q_i D t \qquad (22)$$

where $\langle x^2 \rangle$ is the MSD, $q_i$ is the numerical constant which depends on dimensionality: $q_i$ = 2, 4, or 6, for one-, two-, or three-dimensional diffusion. The interaction of water ions (and other ions from the IL e.g. nitrate) with SF would affect the SF's secondary structure and would alter the mechanical characteristics of the biopolymer. As a result, this would affect the performance of the PE, specifically, how SF immobilises the IL and the ionic conductivity of the PE, impacting the performance of its application (in this case a primary air battery). Understanding the diffusivity of water or ions through materials such as SF, could lead to the improvement of transient devices (e.g. **Figure 7**) functionality.

### 3.3 Methodological approaches to experimental studies

### 3.3.1 Silk fibroin and choline nitrate polymer electrolyte

A battery has three important components: anode, cathode and the electrolyte which separates the anode and cathode terminals. Therefore, the electrolyte possesses a vital role for the functionality of the battery. The electrolyte is a compound which allows an electrical charge to pass between the two terminals, therefore converting stored energy within the device into useable energy, providing power to a connected device (e.g. biomedical sensors).[32] Different types of batteries rely on different types of chemical reactions and consequentially different electrolytes. For example, a lead-acid battery usually uses sulfuric acid to achieve the intended chemical reactions,[101] whereas a Mg- or Zn-air battery relies on oxidising Mg and Zn with oxygen for the ORR, respectively.[1, 102] Since the electrolyte of the battery is responsible for allowing an electrical charge to pass between the two terminals, it is important to distinguish how this can be achieved. For instance, this is due to the electrolyte's conductivity; electronic conduction and ionic conduction are two forms of energy transferring methods which are categorised based on the medium of conduction. The key difference between electronic and ionic conduction is that electronic conduction is the movement of electrons from one place to another, whereas ionic conduction is the movement of ions from one place to another. Specifically, electronic conduction involves free electrons (carrying a negative charge) from the orbital of one atom to an orbital of an adjacent atom, whereas ionic conduction involves ions (carrying either a negative or positive charge) from one defect to another in a crystal lattice in a solid or through an aqueous solution. In addition, the electronic conductivity typically decreases with increase of temperature, whereas the ionic conductivity typically increases with increase of temperature.[103]

With regards to solid-state ionic conductivity, it was first recognised by Faraday who observed the electrical conductivity of solid lead fluoride at high temperature.[104, 105] The conductivity in this case was due to the motion of fluoride anions within the structure. This type of conductivity in solids has long been of fundamental interest as well as being applied in the interpretation of corrosion.[106] More recently, applications have been found in energy conversion devices[107] and chemical sensors.[105, 108] PEs are examples of solid-state electrolytes, comprising of a polymer matrix capable of ionic conduction.[109] Much like other types of electrolyte (e.g. ILs), PEs aid the movement of electrical charge between the anode and cathode terminals within an electrochemical cell.[109, 110, 111] The use of polymers as an electrolyte was first demonstrated using dye-sensitised solar cells.[112] The utilisation of PEs has since expanded and is now often implemented during the development and application of batteries, fuel cells, membranes and TIMBs.[1, 112, 113, 114, 115] In this work, the [Ch][NO$_3$] IL is immobilised by *B. mori* SF, as reported in literature, yielding a solid-state ionically conductive PE film.[1, 116]

SF is a naturally occurring biodegradable protein used to produce fibres used in cocoon production by silkworms, and a promising candidate for implantation in animals/humans.[117, 118] Proteins such as

regenerated SF can entrap/stabilise chemically/biologically active molecules, allowing the addition of a new function to materials loaded with them.[1, 119] ILs are molten salts at ambient temperature that have seen use as solvents and additives for biopolymers. When used as electrolytes they can possess the following advantages: a wide and stable electrochemical potential window, high ionic conductivity, negligible vapor pressure, low flammability, and in some cases good biocompatibility.[1, 120] However, non-covalent interactions between *B. mori* SF and [Ch][NO$_3$] IL may affect the hydrogen bond interactions in SF and consequently its secondary structure. Thereby, the inclusion of ILs weakening the hydrogen bond interactions between amino acids (e.g. Gly and Ala) in the crystalline region of SF enhances segmental motion, increasing the overall flexibility of the material.[121] The plasticising effect was also observed upon the addition of glycerol to SF-based materials because of the formation of hydrogen bonds between the hydroxyl O-H group of glycerol and hydrogen bond donors/acceptors in the protein.[122] Nevertheless, the incorporation of SF and IL leads to the formation of a PE harnessing both the biological activity from SF and ionic conductivity from the IL. Since the IL [Ch][NO$_3$] is also biocompatible,[123] this enables future potential applications of which this PE electrolyte could be utilised for powering devices (e.g. TIMBs).

After the preparation of the SF:IL PE, it is important to determine that the characteristics of the SF and IL in the new composite PE material, and that it is functional (i.e. ionically conductive).

SF can be processed using a variety of aqueous or organic solvent processing methods to generate SF-based biomaterials for a range of applications.[124, 125, 126] The properties of the SF-matrix in naturally spun fibres are controlled by a combination of the chemistry and the spinning process, which directly affect the activity and stability of the protein. Chemistry, such as ion concentration, type of ion, and solution pH can affect the mechanical properties of naturally spun SF-fibres. In addition, spinning conditions, such as temperature, drawing rate, time, and specific type of silkworm can modulate the biomaterial's features.[126] SF fibres, isolated from *B. mori* SF cocoons, are insoluble in water and in most organic solvents. However, the SF dissolves in concentrated acid solutions and in concentrated salt solutions, and certain organic liquids.[127] Those solutions that contain a high concentration of salts need to be dialysed to remove the salt and produce SF-based materials (e.g. hydrogels and films).[128, 129] The SF solution after dialysis is metastable (predominance of silk I) and it can easily convert to a more stable form, by a conformational transition to silk II. The rate of salt removal via dialysis can influence SF conformational transition since the salt is responsible for SF solvation and stabilisation in solution. If the necessary amount of salt is not removed during dialysis, SF-based materials are not easily prepared due to the strong salt solvation. On the contrary, the more salt is removed, the more rapid the gelation process is.[129, 130] The preparation of the aqueous SF solution in this work was

reproduced following the literature[126] and detailed in the *Preparation of silk fibroin, choline nitrate and the polymer electrolyte film* chapter.

Choline-based ILs have attracted widespread attention in recent years because they possess useful properties, such as low toxicity/biocompatibility and biodegradability. For instance, these ILs have seen extensive application in the field of pharmaceuticals and green sustainable chemistry.[123, 131] Choline is a naturally occurring cation and nutrient and is essential for many animals, including humans,[132] additionally, choline is assigned to the family of water-soluble quaternary ammonium compounds.[133] The preparation of choline-based ILs is generally carried out via the neutralisation reaction of the corresponding acid with choline hydroxide, thereby, the [Ch][NO$_3$] IL in this work was prepared as described in the literature.[1, 134]

PEs represent a broad class of materials with long polymeric chains and relatively high ion concentrations. Interest in these materials has a long history due to their potential applications in current and future technologies,[135] for instance, TIMBs and energy storage devices (e.g., regular and flow batteries).[1, 109, 136, 137, 138, 139] As a result, a large portion of PE research is related to their use in batteries.[135] Many current batteries are based on the utilisation of organic liquid electrolytes, but these can be flammable and toxic, and have a limited electrochemical stability window with little or no resistance to dendrite growth.[140, 141, 142] Whereas, solid-state electrolytes (e.g. PEs) can mitigate most of these problems making them materials of particular interest.[143] However, PEs do come with their own disadvantages, for example, they can have low ionic conductivity, have poor contact with electrodes and often fail after a few charge/discharge cycles.[142, 144, 145] Despite several decades of study, the conductivity of dry PEs struggle to satisfy the level required for many applications (ca. $10^{-3}$ S cm$^{-1}$), which strongly limits the battery power, and as a consequence, limits potential applications.[109, 142, 146] Through combining the aqueous SF solution and [Ch][NO$_3$] IL, following the literature,[1, 116] an SF:IL PE film was prepared, detailed in the *Preparation of silk fibroin, choline nitrate and the polymer electrolyte film* chapter. The effectiveness of the PE when incorporated in this work's batteries is discussed later in the *Polymer electrolyte utilised in primary magnesium-air battery* and *Polymer electrolyte utilised in primary zinc-air battery* chapters.

The first technique utilised in this work to characterise the materials prepared (i.e. the SF:IL PE films) is Fourier-transform infrared spectroscopy (FTIR). FTIR spectroscopy is a technique used to obtain an infrared spectrum of absorption or emission of a solid, liquid or gas. Infrared spectroscopy is based on molecular vibrations, the chemical bonds in the sample undergo various forms of vibrations, such as stretching, bending, and rotating. The energy of most molecular vibrations corresponds to that of the

infrared region of the electromagnetic spectrum. Many of the vibrations can be localised to specific bonds or groupings, such as the C-O and O-H groups. This has led to the concept of characteristic group frequencies. Although, there are vibrational modes that do not represent a single type of bond oscillation but are strongly coupled to neighbouring bonds, for example, the infrared spectrum of a protein is characterised by a set of absorption regions known as the amide modes. With the developments made in FTIR instrumentation, it is possible to obtain high quality spectra from dilute protein solutions in water.[147, 148] As a result, FTIR spectroscopy is a very useful tool to identify different chemical bonds (i.e. functional groups) present within a sample. The wavelength of light absorbed is characteristic of the chemical bond, which can be distinguished in the spectrum. By interpreting the infrared absorption spectrum, the functional groups present in the molecule/material can be ascertained.

The characteristic vibration bands of SF are well reported,[1, 72, 126] and the vibration bands around 1620 $cm^{-1}$ are assigned to the absorption peak of the peptide backbone of amide I (C = O stretching), bands around 1513 $cm^{-1}$ to amide II (N-H bending), the bands around 1230 and 1444 $cm^{-1}$ to amide III (C-N stretching),[149] and 694 $cm^{-1}$ to amide IV.[150, 151] All these characteristic absorbance peaks indicate the existence of a hydrogen bonded N-H group.[152] The molecular conformation of *B. mori* SF is characterised by β-sheet absorption peaks around 1630, 1530 and 1240 $cm^{-1}$, random coil conformation absorption peaks at 1650 or 1645, 1550 and 1230 $cm^{-1}$, and an α-helix absorption peak around 1655 $cm^{-1}$.[149, 153] Moreover, the characteristic vibration bands around 1330 $cm^{-1}$ and 954 $cm^{-1}$ are assigned to the absorption peaks for vibrations of $NO_3^-$ and C-C-OH, respectively, which are indicative of the [Ch][NO_3] IL.[1, 154]

Sometimes FTIR spectroscopy is not sufficient to conclusively determine the molecular confirmations within a sample. Therefore, X-ray crystallography can be utilised as it is a technique used for determining the atomic and molecular structure of a material, in which the morphology of the sample may cause a beam of incident X-rays to diffract into many specific directions (e.g. determining whether a polymer is amorphous or semi-crystalline). Two kinds of crystalline modifications, silk I and silk II, as well as the random coil form, exist as dimorphs of SF from *B. mori* in the solid state, depending on the sample preparation conditions. Extensive XRD studies have confirmed that the conformation for silk II as the antiparallel β-sheet form,[155, 156] however, the conformation for silk I is not as well defined as silk II.[157] The XRD measurements of untreated SF films exhibit a broad peak at 20 ° (2-θ), which is a typical characteristic pattern for an amorphous silk material. The peaks associated for the silk I form are: 2-θ = 9, 12, 19.8, 24 and 29 °, whereas for the silk II form they are 2-θ = 16.2 and 22.5 °.[126, 158, 159] Because the materials of interest in this work is a composite of *B. mori* SF and [Ch][NO_3] IL, it is

very possible to see X-ray diffractograms possessing augmented results due to the presence of the IL. In any case, the information from the literature will facilitate identifying the SF activity within the PE films.

As aforementioned, different types of batteries rely on different types of chemical reactions and in this work, Mg- and Zn-air batteries rely on oxidising Mg and Zn with oxygen for the ORR. In addition, water (within the PE films) will act as a proton source to support the ORR at the cathode.[160] To deduce the amount of water content within the PE films, thermogravimetric analysis (TGA) is used. TGA is a method of thermal analysis that evaluates the change in mass of a sample as a function of temperature. This measurement provides information about physical phenomena, such as phase transitions, absorption, adsorption, and desorption; as well as chemical phenomena including chemisorption, thermal decomposition, and solid-gas reactions (e.g. oxidation or reduction).[161] TGA studies of SF films have shown that when SF films undergo a heating cycle (e.g. 5 °C min$^{-1}$) the intermolecular water evaporates from the silk film into the air continuously.[162] In addition, the silk film typically begin to release the water molecules into the air when temperatures reach ca. 35 °C. Consequently, the overall mass of SF films will decrease as temperature increases. At ca. 160 °C, it was observed that there is no more intermolecular water in the SF film (i.e. water strongly bound in the hydration layer/shell has evaporated) and there was no observable mass change with increasing temperature after ca. 160 °C (until decomposition at ca. 260 °C).[162, 163] With this information, it is possible to suggest a working temperature range for the SF:IL PE used in this work. Since water acts as a proton source for the ORR at the cathode[160] once assembled in a battery, it is advisable to limit how much water evaporates from the PE film. Therefore, if operating open to air, temperatures below ca. 35 °C would be preferable, or indeed implanted within the animal/human body (at ca. 37 °C) due to the inherently hydrated conditions.

After confirmation of the presence of SF and IL in the PE films it is important to confirm the PE film's ionic conductivity. This is typically achieved by electrical impedance spectroscopy (EIS) analysis and mathematically correlating EIS experimental data, the resistance of a system can be approximated, which in turn can be used to estimate the conductivity of the PE. The resistance of a given material is proportional to the resistivity and length, but inversely proportional to the cross-sectional area. Hence, the resistance is defined by equation (23):[164, 165]

$$R = \rho \frac{l}{A} \tag{23}$$

where $R$ is the resistance (Ω), $\rho$ the resistivity (Ω·m), $l$ the length and $A$ the cross-sectional area. The conductivity is the inverse of resistivity shown in equation (24):

$$\sigma = \frac{1}{\rho} \tag{24}$$

where $\sigma$ is the conductivity (S m$^{-1}$).[164, 165]

EIS concerns the study of a system's response to sinusoidal electrical perturbation, this electrical perturbation can be a perturbation of the potential (PEIS) or a perturbation of the current (GEIS), and the response is a current or a potential, respectively. Furthermore, EIS has been extensively used to characterise the performance of electrical energy storage and conversion devices, including electrochemical capacitors,[166] batteries,[167] and fuel cells.[168, 169] Broadly speaking, EIS consists of imposing a time harmonic oscillating electric potential $\psi_s(t)$ of small oscillation amplitude (e.g. 10 mV) around a time-independent "direct current (DC) potential" at the electrode surfaces and measuring the resulting harmonic current density $j_s(t)$.[169, 170, 171, 172] Using complex notations, the imposed electric potential $\psi_s(t)$ and the resulting current density $j_s(t)$ can be expressed as shown in equation (25):

$$\psi_s(t) = \psi_{dc} + \psi_0 e^{i2\pi ft} \text{ and } j_s(t) = j_{dc} + j_0 e^{i[2\pi ft - \phi(f)]} \tag{25}$$

where $\psi_{dc}$ is the time-independent DC potential, $\psi_0$ the amplitude of the oscillating potential at frequency $f$, $j_{dc}$ the time-independent DC current density, $j_0$ the amplitude of the oscillating current density, and $\phi(f)$ the frequency-dependent phase angle between the imposed potential $\psi_s(t)$ and the measured current density $j_s(t)$. Then, the electrochemical impedance $Z$ can be defined as shown in equation (26):[172, 173, 174, 175]

$$Z = \frac{\psi_s(t) - \psi_{dc}}{j_s(t) - j_{dc}} = \frac{\psi_0}{j_0} e^{i\phi} = Z_{re} + iZ_{im} \tag{26}$$

where $Z_{re}$ and $Z_{im}$ ($\Omega$ m$^2$) are the real and imaginary parts of the complex impedance, respectively.[169]

With regards to solid-state PEs, the ionic conductivity can be investigated with the assistance of impedance spectroscopy. During impedance measurements, the sinusoidal potential is applied, and the impedance and phase shift of the current measured.[176] As a result, a Nyquist impedance plot ($Z'$ [X-axis] versus $Z''$ [Y-axis] plot, real and imaginary impedance, respectively) can be used to determine the appropriate equivalent circuit and estimate the values of the circuit parameters which reflect the carrier transport properties and the reaction in the electrode interface.[176] Using Nyquist impedance plots, the bulk resistance of polymeric films can be obtained.[116, 177, 178] The real ($Z'$) and imaginary ($Z''$) impedance of a PE sandwiched between two blocking electrodes for impedance measurements can be represented by the following equations (27 and 28):[179, 180]

$$Z_{re} = \frac{R}{1 + (\omega RC)^2} \tag{27}$$

and

$$Z_{im} = \frac{\omega R^2 C}{1 + (\omega RC)^2} + \frac{2}{\omega C_e} \tag{28}$$

where $\omega$ is the angular frequency, $C_e$ the electrical double layer (EDL) capacitance, $C$ the bulk geometrical capacitance and $R$ the bulk resistance of the PE.[178, 179, 180] The form of equations (27) and (28) implies that the Nyquist plot consists of a semicircle with its centre on the real ($Z'$) impedance axis and a vertical spike. The spike is represented by the second term on the right-hand side of equation (28) and implies a perfect capacitor. The factor 2 on the right-hand side of equation (28) considers the two EDLs formed on both sides of the electrolyte, which are in contact with the electrodes. The EDL is formed when ions accumulate at the electrode/electrolyte interfaces and these parameters are given by equations (29, 30 and 31):

$$C_e = \frac{\varepsilon_r \varepsilon_0 A}{\lambda} \tag{29}$$

$$C = \frac{\varepsilon_r \varepsilon_0 A}{2d} \qquad (30)$$

and

$$R = \frac{2d}{\sigma A} \qquad (31)$$

where $\varepsilon_r$ is the dielectric constant of the electrolyte, $\varepsilon_0$ the vacuum permittivity ($8.85 \times 10^{-14}$ F cm$^{-1}$), $\lambda$ the thickness of the EDL, $d$ the half thickness of the PE and $A$ the electrode/electrolyte contact area.[178, 179, 180] **Figure 12** has been illustrated to depict a typical Nyquist plot for a PE.[178, 181]



$Z'$ ($\Omega$ m$^2$)
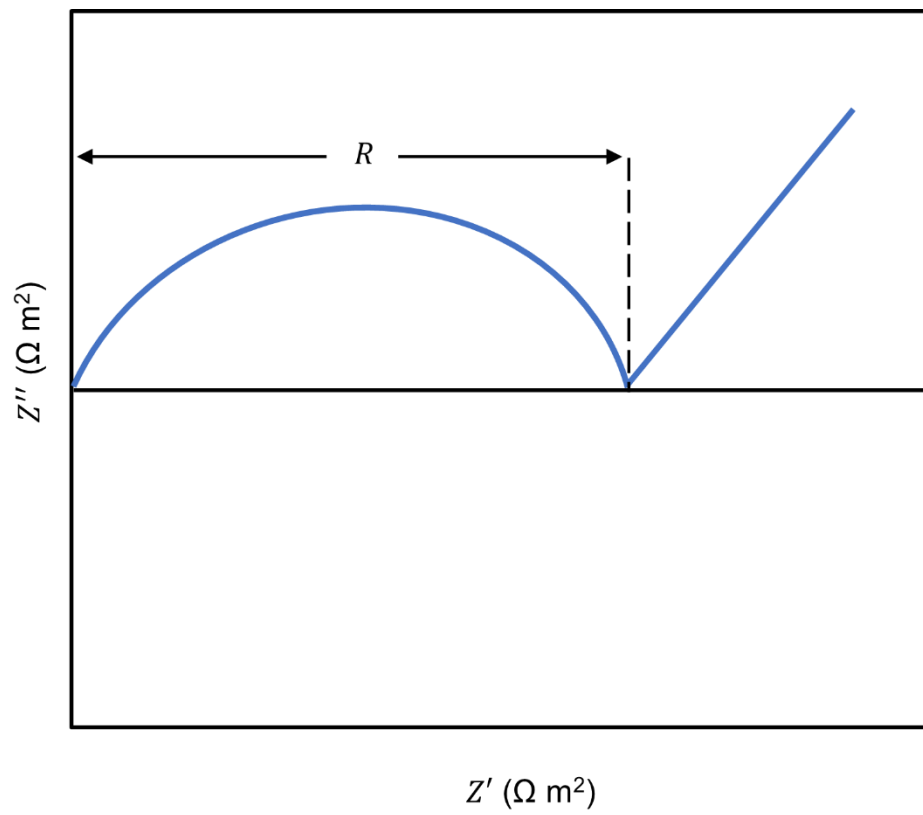
**Figure 12.** Illustration of a typical Nyquist plot for a PE, where the blue line depicts the impedance data measurements plotted for the X-axis ($Z_{re}$) and Y-axis ($Z_{im}$). The $R$ represents the resistance for the PE.

Therefore, the estimation for the ionic conductivity of PEs via impedance spectroscopy can be conducted using the following equation (32):

$$\sigma = \frac{d}{RA} \tag{32}$$

where $\sigma$ is the conductivity, $d$ the thickness of the PE material (e.g. film), $R$ is the bulk resistance obtained from the first intercept on the X-axis of the complex plane, and $A$ is the electrode/electrolyte contact area. [1, 116]

### 3.3.2 Prototype battery and magnesium- and zinc-air batteries

Once the components for the battery are ready for assembly, it is then required to evaluate the performance of the battery using electrochemical techniques. A comprehensive assessment of a battery and its materials includes energy/power density, conversion efficiency, and functional lifespan. The determination of these features involves characteristic parameters such as voltage, current, capacity, and testing duration that can be directly collected from electrochemical measurements. Voltammetry (e.g. linear sweep voltammetry [LSV]) and chronopotentiometry are the two most popular testing techniques, in addition, EIS is also often utilised (discussed previously).

In general, voltammetry involves the effects of the applied potential and the behaviour of the redox current. The applied potential controls the concentrations of the redox species at the electrode surface ($c_O^0$ and $c_R^0$) and the rate of the reaction ($k^0$), as described by the Nernst and Butler-Volmer equations, respectively.[182, 183] In the cases where diffusion plays a controlling part, the current resulting from the redox process (Faradaic current) is related to the material flux at the electrode-solution interface and is described by Fick's first law.[98] The interplay between these processes is responsible for the characteristic features observed in the voltammograms of various techniques. For a reversible electrochemical reaction (wherein a reaction is so fast that equilibrium is always re-established as soon as changes are made), can be described by $O + ne^- \longleftrightarrow R$, the application of a potential $E$ forces the respective concentrations of $O$ and $R$ at the surface of the electrode (that is, $c_O^0$ and $c_R^0$) to a ratio in compliance with the Nernst equation (33):

$$E = E^0 - \frac{RT}{nF} ln \frac{c_R^0}{c_O^0} \tag{33}$$

where $R$ is the molar gas constant (8.3144 J mol$^{-1}$ K$^{-1}$), $T$ the temperature (K), $n$ the number of electrons transferred, $F$ the Faraday constant (96,485 C mol$^{-1}$) and $E^0$ the standard reduction potential of the redox couple. If the potential is made more negative the ratio becomes larger ($O$ is reduced), whereas if the potential is made more positive the ratio becomes smaller ($R$ is oxidised). Furthermore, it is sometimes useful to use the relationship which links the variables for current, potential, and concentration for some techniques (i.e. the Butler-Volmer equation) (34):

$$\frac{i}{nFA} = k^0 \{c_O^0 \, exp[-a\theta] - c_R^0 \, exp[(1-a)\theta]\} \tag{34}$$

where $\theta = nF(E - E^0) / RT$, $k^0$ is the heterogenous rate constant, $a$ the transfer coefficient and $A$ the area of the electrode. Therefore, allowing for the values of parameters $k^0$ and $i$ to be obtained analytically. Lastly, the current flow also depends on the flux of material to the electrode surface. When new $O$ or $R$ is created at the surface, the increased concentration provides the force for its diffusion toward the bulk of the solution. Likewise, when $O$ or $R$ is removed, the decreased concentration promotes the diffusion of new material from the bulk solution. The resulting concentration gradient and mass transport is described by Fick's first law, which states that the flux of matter ($\phi$) is directly proportional to the concentration gradient, depicted in equation (35):

$$\phi = -AD_O(\partial c_0 / \partial c_x) \tag{35}$$

where $D_O$ is the diffusivity of $O$ and $x$ the distance from the electrode surface. An analogous equation can be written with respect for $R$. The flux of $O$ or $R$ at the electrode surface controls the rate of reaction, and thus the faradaic current flowing in the cell. In the bulk solution, concentration gradients are generally small and ionic migration carries most of the current. The current is a quantitative measure of how fast a species is being reduced or oxidised at the electrode surface. The actual value of this

current is affected by many additional factors, most importantly the concentration of the redox species, size, shape, and material of the electrode itself, the solution resistance, the cell volume, and the number of electrons transferred.[184] In addition to diffusion, mass transport can also occur by convection or migration. Convection is the movement of the electroactive species by thermal currents, density gradients present in the solution, stirring the solution or rotating the electrode. Whereas migration is the movement of a charged ion in the presence of an electric field. In voltammetry, the use of a supporting electrolyte at concentrations 100 times that of the species being determined eliminates the effect of migration.

Hence, voltammetry is an important technique for electrochemical measurements, and LSV are the most typical mode. In the case of batteries, we are dealing with a complex situation which involves solid-liquid interfaces, ion diffusion in an electrolyte and electrode, and multiple reactions in/on the electrode.[184] Furthermore, cyclic voltammetry (CV) is becoming more widely used when dealing with solid electrolytes.[185, 186] Nevertheless, there are many complex equations in the theory of voltammetric techniques that go beyond the scope of this thesis, but in practice, it is common with just identifying specific values collected from voltammograms that are useful to understand the electrode reactions.[1, 185] Since batteries, even though they deliver reversible faradic capacity, are generally not reversible systems (e.g. primary air batteries), the focus shifts more on the numerical meaning of the voltage and current. Voltage is corelated with specific electrode reactions defining the electrochemical window, while current is relevant to faradic capacity. In LSV measurements the current response is plotted as a function of voltage rather than time and the scan begins from the left-hand side of the current/voltage plot where no current flows. As the voltage is swept further to the right (to more reductive values) a current begins to flow and eventually reaches a peak before dropping. To rationalise this behaviour, the influence of voltage on the equilibrium established at the electrode surface needs to be considered. As an example, if we consider the electrochemical reduction of iron III to iron II, the rate of electron transfer is fast in comparison to the voltage sweep rate. Therefore, at the electrode surface an equilibrium is established identical to that predicted by thermodynamics. So as the voltage is swept from V1 (initial voltage) to V2 (final voltage) the equilibrium position shifts from no conversion at V1 to full conversion at V2 of the reactant at the electrode surface. The exact form of the voltammogram can be rationalised by considering the voltage and mass transport effects. As the voltage is initially swept from V1, the equilibrium at the surface begins to alter and the current begins to flow. The current rises as the voltage is swept further from its initial value as the equilibrium position is shifted further to the right-hand side, thus converting more reactant. The peak occurs because at some point the diffusion layer has grown sufficiently above the electrode so that the flux of reactant to the electrode is not fast

enough to satisfy that required by the Nernst equation. In this situation the current begins to drop. Furthermore, the scan rate can also affect the curves observed in LSV. This can be rationalised by considering the size of the diffusion layer and the time taken to record the scan. Since the LSV will take longer to record as the scan rate is decreased the size of the diffusion layer above the electrode surface will be different. In a slow voltage scan the diffusion layer will grow further from the electrode in comparison to a fast scan. Consequently, the flux to the electrode surface is considerably smaller at slow scan rates than it is at faster rates. As the current is proportional to the flux towards the electrode, the magnitude of the current will be lower at slow scan rates and higher at high rates. Lastly, for slower electron transfer processes, the voltage applied will not result in the generation of the concentrations at the electrode surface predicted by the Nernst equation. This occurs if the kinetics of the reaction are slow and thus the equilibria are not established rapidly. In this situation, unlike a reversible reaction, the position of the current maximum shifts depending upon the reduction rate constant (and the voltage scan rate). This occurs because the current takes more time to respond to the applied voltage than in the reversible case.

The final electrochemical technique to be addressed is that which is ubiquitous with batteries. Chronopotentiometry or galvanostatic charge-discharge is a robust and more straightforward electrochemical testing technique.[185] Simply speaking, galvanostatic charge-discharge measurements record the voltage response under a constant applied current. It is a practical technique to assess the capacity, reversibility, stability, and rate capability of electrode materials. Consequently, this technique is commonly used when evaluating the performance of a battery.[1, 185] In this work, primary air batteries are utilised and therefore not intended for recharge. Once a primary air battery becomes fully discharged (at ca. 0 V) it is no longer considered functionally useful and is either discarded or harmlessly degrades into the environment.[1, 24] Thus, only the galvanostatic discharge curves of the battery is of significance in this case. These measurements yield information pertaining to the battery's capacity, operation window, stability, and power capabilities. For instance, the specific volumetric power density of a battery can be obtained by using equation (36):

$$P = \frac{UI}{V} \tag{36}$$

where $P$ is the volumetric power density (W L$^{-1}$), $U$ depicts the plateau voltage (V) of the discharge curve, $I$ the discharge current (A), and $V$ the working device volume (L).[1]

## 4. Methods

### 4.1 Preparation of the computational silk fibroin model for classical molecular dynamic simulations

Construction of the (Ala-Gly)$_n$ SF unit cell followed the methodology described by Yamane *et al*, [11] the initial lattice parameters of the unit cell are orthorhombic: $a$ = 17.8 Å, $b$ = 15.7558 Å, $c$ = 11.4904 Å. The initial unit cell was created by arranging four Ala-Gly chains with repeated β-turns according to information from experimental and computational experiments on SF.[11, 42, 44, 45, 47, 187, 188] To simulate the bulk system of the repeated polymer chains, a periodic boundary condition was implemented, where nitrogen and carbon-termini were connected to mirror images of themselves. The hydrated SF supercells were created by introducing ca. 7.5 wt % of water molecules, mimicking experimentally reproduced SF films.[158, 189] Water molecules were placed randomly within the supercells, while ensuring that no water molecules were placed within 1.7 Å of the silk. The SF crystal structure is illustrated in **Figure 13**.
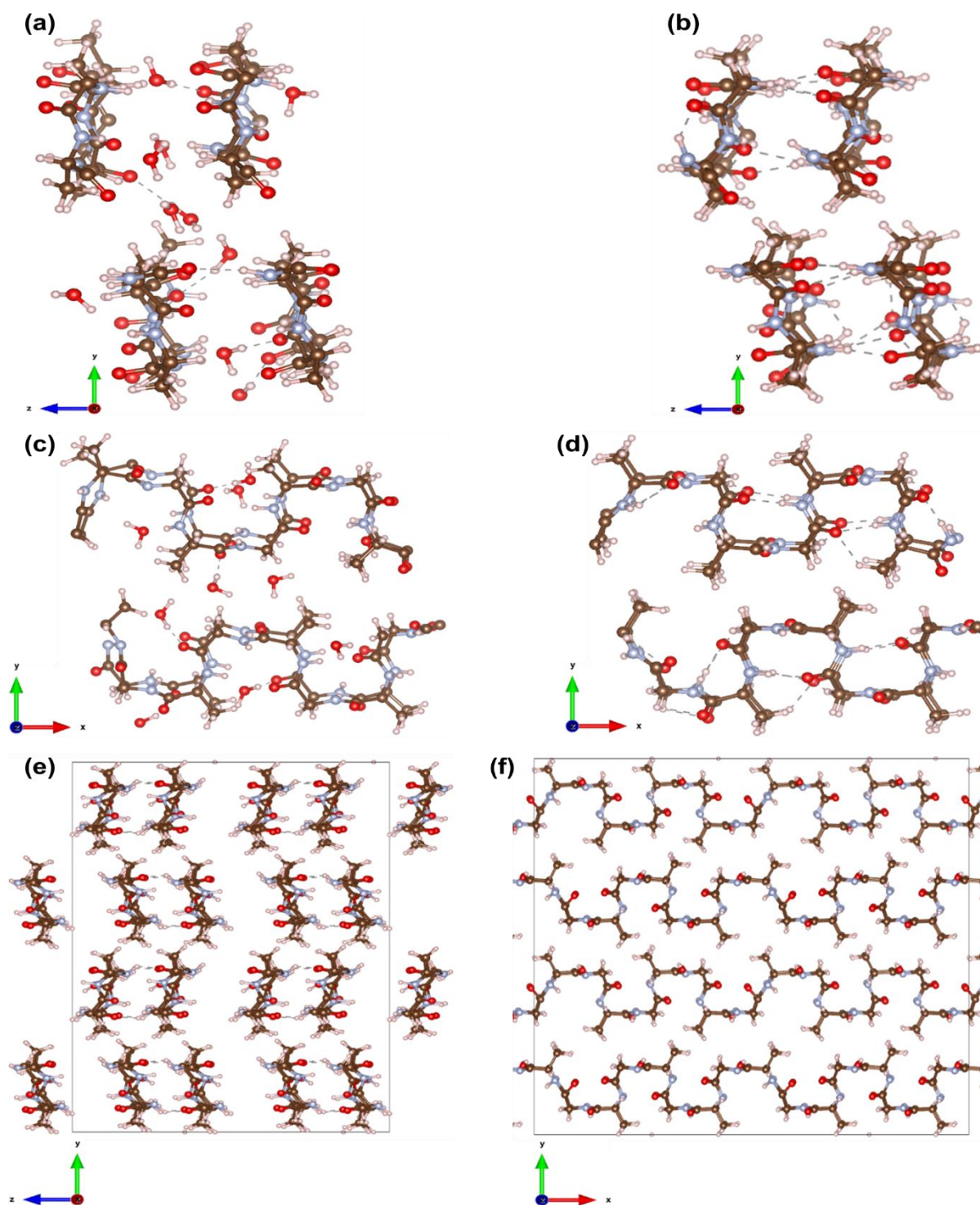
**Figure 13.** Visualisation of the initial crystal structure of *B. mori* SF in a silk I form. (a) Is a snapshot of the hydrated crystal structure (repeated β-turn type II conformation) from along the X-axis, (b) non-hydrated from along the X-axis, (c) hydrated from along the Z-axis and (d) non-hydrated from along the Z-axis. (e) Is another snapshot of a non-hydrated 2x2x2 periodic unit cell of *B. mori*. SF crystal structure from along the X-axis and (f) non-hydrated 2x2x2 periodic unit cell of *B. mori*. SF crystal

structure from along the Z-axis, wherein both (e) and (f), the grey box depicts the periodic boundary. A visual representation of the repeated β-turn type II conformation where the brown ball and sticks depict carbon atoms, light grey the hydrogen atoms, red the oxygen atoms and pale blue the nitrogen atoms. The initial lattice parameters of the unit cell shown in **Figure 13** are orthorhombic: $a$ = 17.8 Å, $b$ = 15.7558 Å, $c$ = 11.4904 Å. The grey dashed lines between atoms (shown in [a-d]) represent the hydrogen bond interactions. Figure created using VESTA.[206, 207]

The classical MD simulations utilised a range of supercells, ranging from 2×2×2 to 4×4×4 repetitions of the unit cell containing 2,176 and 17,408 atoms (2,377 and 19,022 atoms when hydrated). In each case, the DL_FIELD package was used to create the input files for the DL_POLY_4 simulation package.[55, 190, 191, 192] In addition, the periodic (Ala-Gly)$_n$ crystals were visualised using the visual molecular dynamics (VMD) programme.[193] The hydrated SF crystal structures of 2x2x2 and 4x4x4 supercells is illustrated in **Figure 14**.

**(a)**
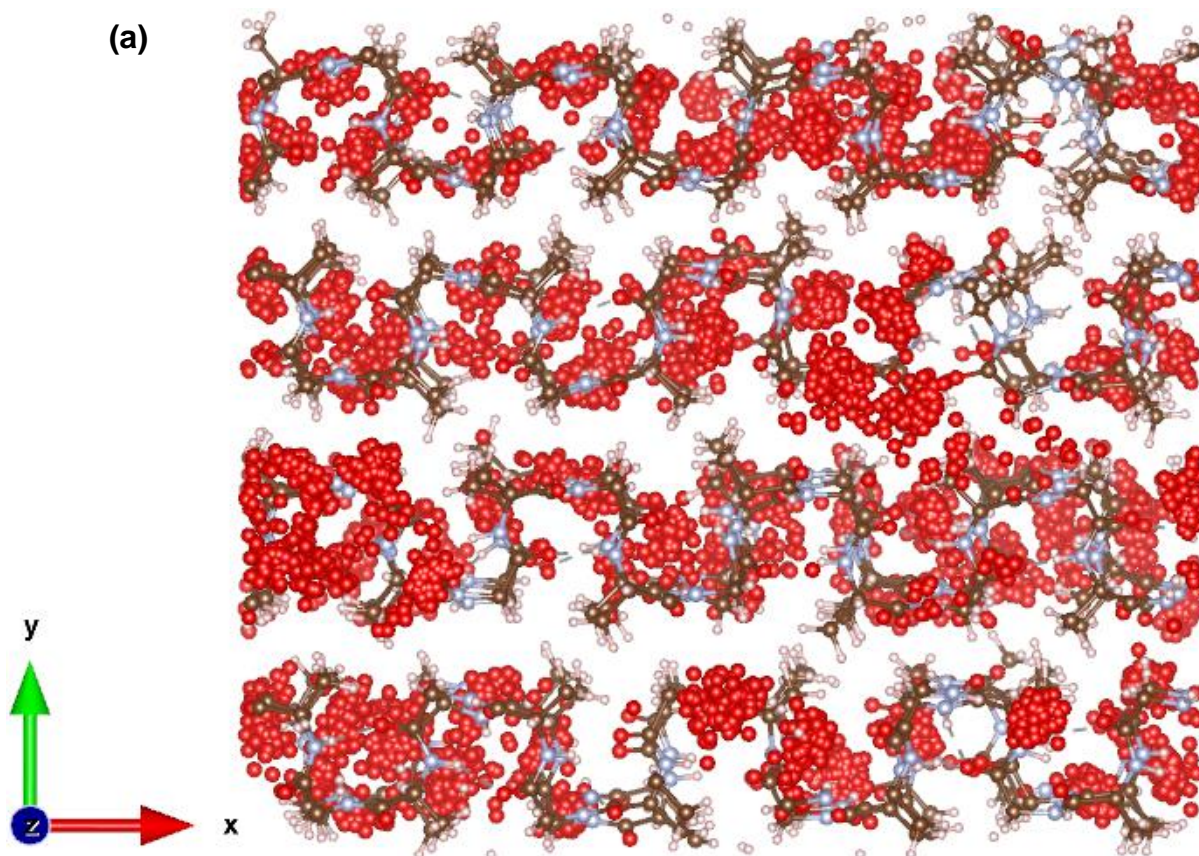
**(b)**
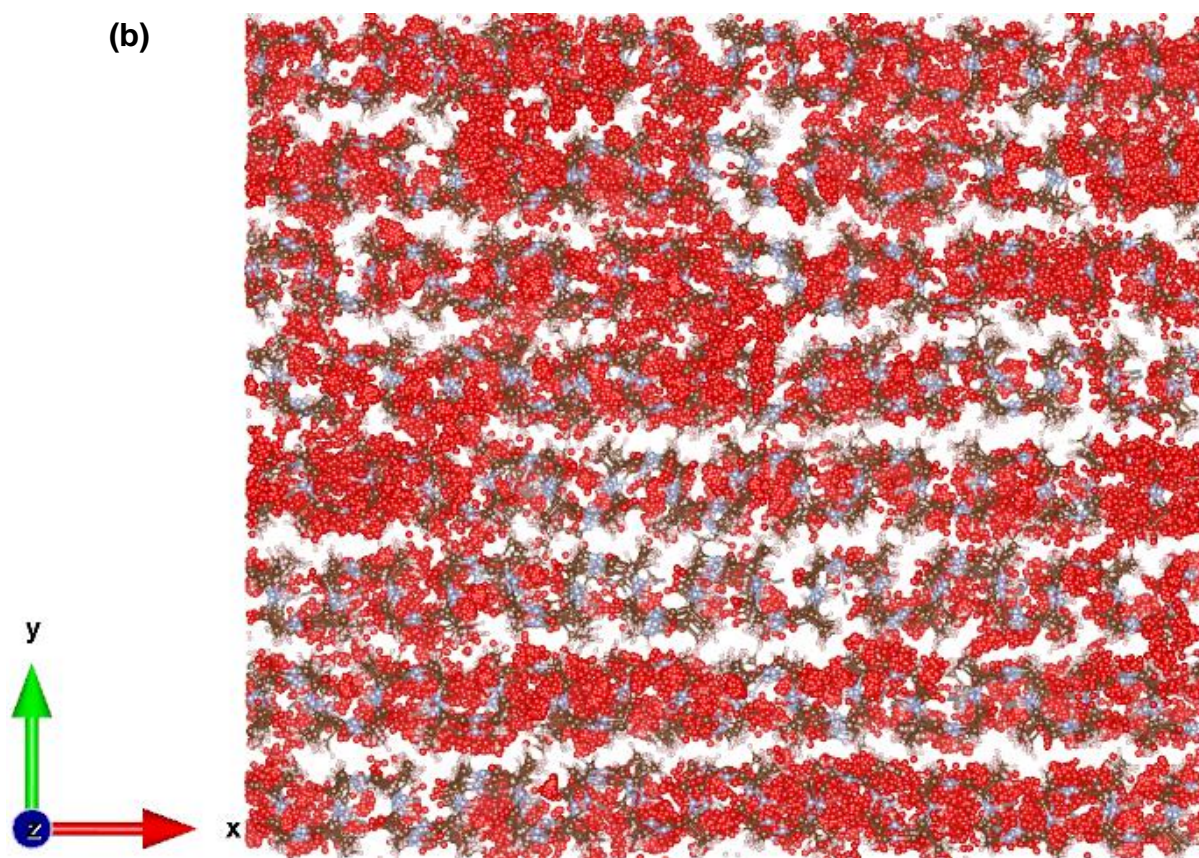
**Figure 14.** Visualisation of the hydrated crystal structure of *B. Mori* SF in 2x2x2 and 4x4x4 supercells at 298 K. (a) Is a snapshot of the hydrated SF crystal structure 2x2x2 supercell from along the Z-axis. (b) Is a snapshot of the hydrated SF crystal structure 4x4x4 supercell from along the Z-axis. A visual representation of the hydrated SF supercells where the brown ball and sticks depict carbon atoms, light grey the hydrogen atoms, red the oxygen atoms and pale blue the nitrogen atoms. In both (a) and (b) only the final position of the SF chain (after 2 ns sampling time, discussed later) at 298 K is shown, while all the positions of the water molecules (only the oxygen ions from the water molecules are shown for clarity) from each frame is shown to indicate how pervasive the water molecules are in the SF crystal structure supercells.

Interactions between the ions in the (Ala-Gly)$_n$ chains were represented using the OPLS-AA[56] force field where the $E_{tot}$ of a molecular system is evaluated as a sum of the components as depicted in equations (9, 10, 11 and 12). [55, 88, 194] To represent interactions between water molecules and the silk chains the three-site transferrable intermolecular potential TIP3P force field was employed.[62, 63]

The MD simulations were carried out by using DL_POLY and DL_FIELD[191] to construct the force field models and the necessary input files for DL_POLY.[190] The VdW and coulombic real space cut-off were set to 12 Å. The coulombic interactions were treated by means of smooth particle mesh Ewald (SPME).[194]

During the equilibration and sampling processes in the NVT and NPT ensembles, all the temperatures and pressures were maintained by using the Nose-Hoover formalism with the coupling constants set to 0.05 ps and 0.1 ps, respectively at atmospheric pressure. A fixed time step of 0.5 fs was used to update the trajectories.

The initial system configurations (both the non-hydrated and the hydrated ones) were optimised at a low temperature of 10 K within the NVE for 50 ps. After that, the system was equilibrated under NVT conditions at target temperatures of 10, 150, 273, 298, 310, 373 and 473 K, with each successive starting configuration obtained from the previously equilibrated configurations at the lower temperatures. These independent systems each with a target temperature, as mentioned above, were equilibrated for 100 ps and then the system ensembles were changed to the NPT and the systems were further equilibrated for 100 ps at each temperature, mentioned previously. Following this, the sampling runs were performed, and the atomic configurations were recorded every 1,000 steps (0.5 ps) for a total of 2 ns. Torsion angles were then calculated using the DL_ANALYSER[192] package enabling the creation of Ramachandran plots. Using the torsion angles of the Ala and Gly residues

(water molecules are excluded), Ramachandran plots were prepared for the purpose of comparison with Ramachandran plots of SF/Ala and Gly.[195, 58, 196]

Lastly, in order to examine the mobility of water around the SF, the MSD of the oxygen ions in the water molecule were determined. The simulation for the MSD of water molecules within the hydrated supercells were conducted in a similar manner as previously stated, however, the simulation progressed for a total of 1 ns.

## 4.2 Preparation of silk fibroin, choline nitrate and the polymer electrolyte film

SF (degummed fibres, throwsters waste from Etsy) was dissolved in a calcium chloride, ethanol and water mixture (1:2:8 mol ratio).[1] The ratio of the silk fibres and solution was 1:20 w/v.[1] The mixture was heated using a thermal bath at 65 °C while being stirred, the silk fibres completely dissolved within 1 h. The solution was passed through a glass frit to remove any particulates. The filtered mixture was dialysed for 5 days against deionised water using Pur-A-Lyzer Mega dialysis tubes of 3.5 kDa molecular weight cut-off (MWCO), purchased and used as received from Sigma-Aldrich. The solution was centrifuged at 4 °C at 5,000 RPM for 27.5 minutes, centrifugation was completed twice to optimise the removal of impurities.

The aqueous SF solution underwent up-concentration via dialysis (3.5 kDa MWCO) against a solution of 10 % w/v PEG 10k Mw in deionized water for 48 hrs. Dry weight analysis using 500 μL samples of the up-concentrated aqueous SF solution was conducted (ca. 7 wt % SF content), agreeing with literature values.[1]

Choline-based ILs are generally prepared by the neutralisation reaction of the corresponding acid with choline hydroxide.[11, 134] In this study, [Ch][NO$_3$] was prepared by the neutralisation reaction of nitric acid (70 %) with choline hydroxide (46 % wt. in water). The procedure is as follows: 25 mL of choline hydroxide (46 % wt. in water) was added dropwise into 6.5 mL of nitric acid (70 %) in an ice bath. The reaction solution was stirred at room temperature for 24 hrs. The solvent was removed by distillation and the product was vacuum dried at room temperature for 24 hrs. A deep yellow-orange solution of [Ch][NO$_3$] was obtained with ca. 98 % yield.

The polymer electrolyte composite films were prepared by adding the [Ch][NO$_3$] IL into the ca. 7 % SF solution with weight ratios of 1:1 and 1:3 (SF to IL). The mixtures were stirred continuously for 4 h and 0.1 mL samples were drop cast onto a Teflon mould, followed by drying in air for 24 h. The PE composite films possessed an average film thickness of ca. 0.05 cm and surface area of ca. 0.79 cm$^2$.

Pictures of the components (e.g. SF solution, IL and PE) utilised in this work (and detailed above) are shown in **Figure 15**.
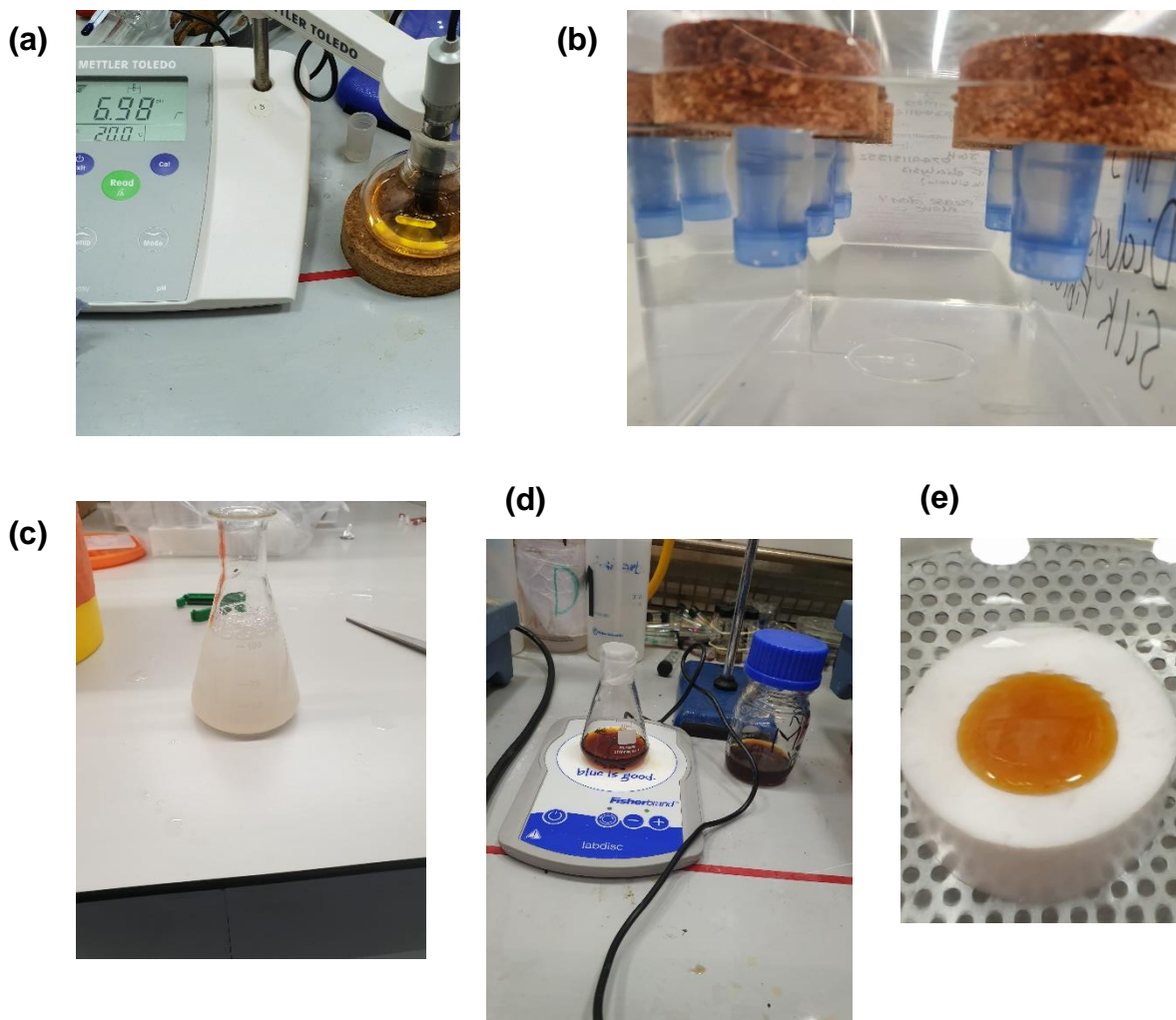


**Figure 15.** (a) Picture of the [Ch][NO$_3$] IL after distillation and showcasing its pH. (b) Picture of the SF solution undergoing up-concentration via dialysis against a solution of 10 % w/v PEG 10k Mw in deionized water. (c) Picture of the SF solution after dialysis, ca. 7 wt % SF content, determined via dry weight analysis of SF films. (d) Picture of the 1:1 weight mixture of SF:IL PE. (e) Picture of 0.1 mL PE sample drop cast onto a Teflon mould.

### 4.3 Fourier-transform infrared spectroscopy of the silk fibroin and polymer electrolyte film

The attenuate total reflectance FTIR spectra of the SF film, [Ch][NO$_3$] liquid and PE 1:1 and 1:3 composite films were recorded on an Agilent Technologies Cary 630 FTIR from 500 to 4000 cm$^{-1}$, at a

resolution of 4 cm$^{-1}$. Lint free tissue (purchased and used as received from Sigma-Aldrich) was wet with methanol and used to clean the crystal lens before each test.

## 4.4 X-ray diffraction of the polymer electrolyte

The XRD of the PEs samples in its solid-state (films) and liquid state were loaded onto an off-cut piece of Si(911) single crystal wafer. The samples were mounted on a Rigaku SmartLab 9kW diffractometer equipped with a germanium (Ge) (220) 2-bounce monochromator using a parallel beam geometry, and a D/teX 250 Ultra 1D detector. The samples were analysed by a $\theta/2\text{-}\theta$ scan with a step size of 0.01 °, and a scanning rate of 3 ° min$^{-1}$.

## 4.5 Thermogravimetric analysis of the polymer electrolyte films

TGA curves for the PE 1:1 and 1:3 composite films were determined using a NETZSCH STA 449 F3 TGA under a nitrogen atmosphere within the temperature range of 20 to 400 °C at a heating rate of 5 °C min$^{-1}$.

## 4.6 Potentiostatic electrical impedance spectroscopy of the polymer electrolyte films

The pre-discharge ionic conductivity of the PE 1:1 and 1:3 composite films assembled in the final batteries (two-electrode electrochemical cell) were deduced by conducting PEIS using a Biologic SP-300 potentiostat, with an alternating current (AC), an amplitude of 10 mV and the frequency range set at 100,000 to 0.1 Hz, OCV.

## 4.7 Preparation of the prototype battery and electrochemical experimentation

A prototype battery design, **Figure 16**, was initially prepared and underwent electrochemical experimentation before a final battery was designed and utilised. The purpose of this was to become familiar with the materials which would be used for a final iteration of the battery and streamline this experimental process. The initial metal-air prototype battery utilises a 25 mL glass beaker to house the working components of the battery: [Ch][NO$_3$] IL electrolyte, Mg AZ31 foil anode, Au coiled wire cathode, silver-silver chloride (Ag-AgCl) leak-free reference electrode and syringe needle for the oxygen inlet. Approximately 5 mL of the prepared IL was inside the 25 mL glass beaker, and submerged within the IL electrolyte was a Mg AZ31 alloy foil, 96 % Mg, 3 % Al and 1 % Zn purchased from GoodFellow with a foil thickness of 0.05 cm. The alloy's surface was polished before application by using a coarse (50) grit sandpaper followed by a fine (120) grit sandpaper and subsequently used as the anode. The surface area of the anode submerged within the electrolyte was calculated to be at 2 cm$^2$. In addition, a 99.997 % Au, 1 mm diameter wire was purchased from Sigma-Aldrich and coiled before use to optimise current density. The surface area of the cathode within the electrolyte was

approximated to take the shape of a cylinder, as a result, the Au wire was determined to possess a surface area of ca. 1.59 cm$^2$. Lastly, a leakless miniature Ag-AgCl reference electrode, ET072-1, was utilised, purchased from eDAQ. To provide oxygen for the ORR, an oxygen gas cannister was attached to an inlet with a syringe needle submerged within the IL electrolyte, 2 L min$^{-1}$ of oxygen was bubbled into the electrolyte to ensure an excess of oxygen was supplied for the ORR.
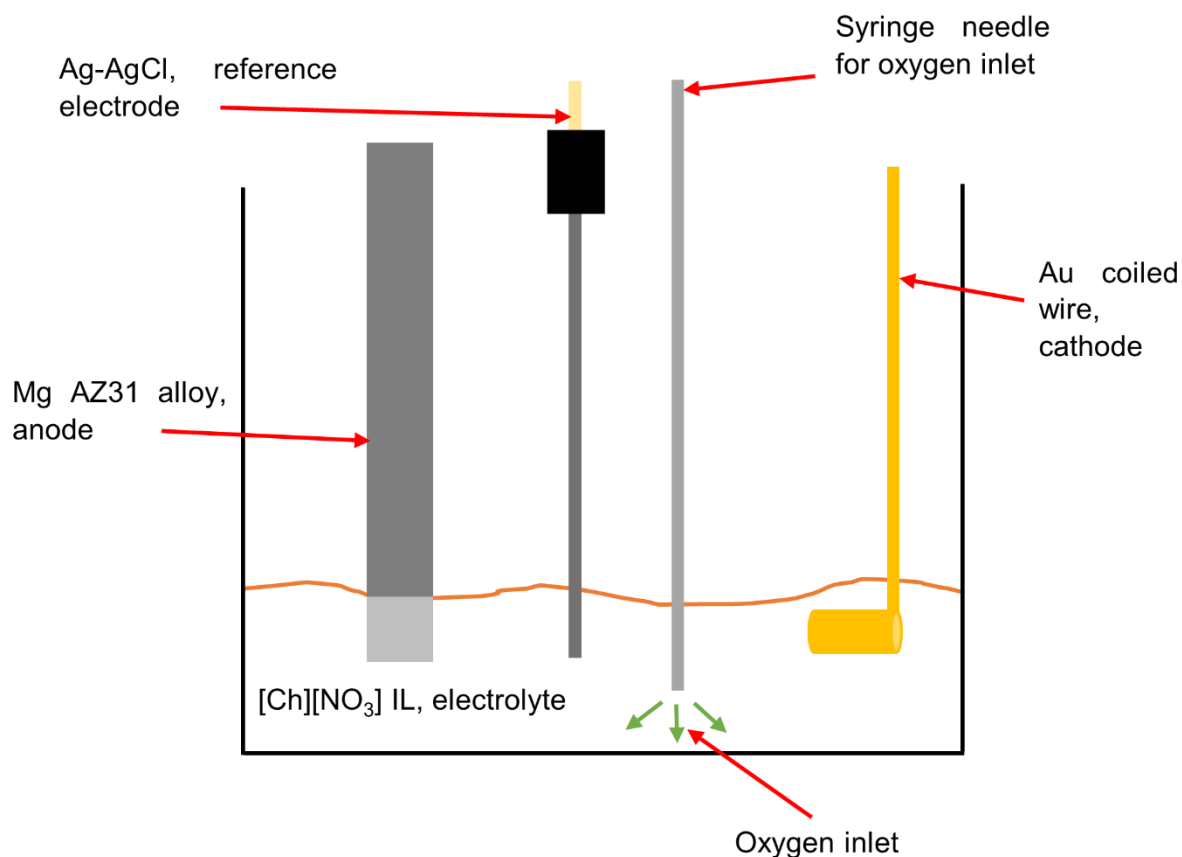


**Figure 16.** Illustrated design for the metal-air prototype battery utilising a 25 mL glass beaker (represented by the outer black lines) to house the working components. Labelled correspondingly by the red arrows.

The OCV, LSV and chronopotentiometry of the prototype battery illustrated in **Figure 16** was conducted on the Ivium-n-Stat with the sModule 2.5A/10V. The oxygen inlet was activated at 500 seconds into the initial OCV measurements to ensure sufficient oxygen was within the electrolyte to feed the ORR for the prototype battery (three-electrode electrochemical cell). Oxygen was subsequently bubbled through the electrolyte between experiments and the inlet deactivated before

measurements were conducted. The voltammograms were conducted over five cycles at a scan rate of 10 mV s$^{-1}$ with the voltage range from - 1.8 to 0 V. The chronopotentiometry was measured at five different currents initially beginning with 2 µA for 10 seconds then increasing to 10 µA for 10 seconds, then increased as follows: 20 µA, 40 µA and finally 100 µA for 10 seconds. This process was then repeated a further three more times and the voltage discrepancies from the initial and the final cycle were compared.

## 4.8 Preparation of the primary magnesium- and zinc-air batteries and electrochemical experimentation

The final battery design was prepared with the goal of possible implantation within the human body, as is the application for TIMBs. Therefore, the fundamental design for the battery needed to be biocompatible yet robust enough to remain functional after a surgical procedure. As a result, the final battery design in this work is a solid-state metal-air battery employing special use of *B. mori* SF solution and [Ch][NO$_3$] IL to produce an ionically conductive film to act as the battery's electrolyte. Represented by **Figure 17** is the final battery design.
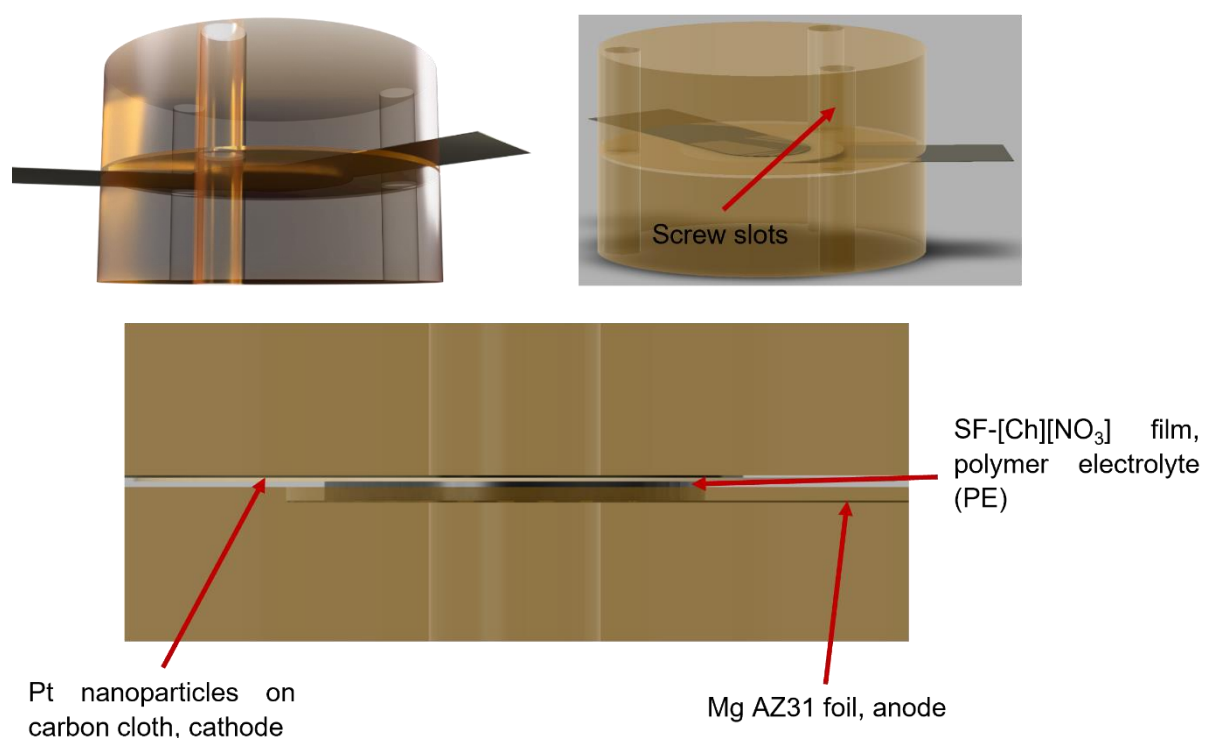


**Figure 17.** Computed aided design (CAD) illustrating the solid-state metal-air battery. Labelled correspondingly by the red arrows.

The final battery design utilises a stereolithography 3-D printed casing, generated from CAD Fusion 360, and printed using the SLA-type 3-D printer from FormLabs using the clear resin V2 and print layer resolution of 50 μm. This casing was employed to mechanically stabilise and protect the battery and ensure there was appropriate contact between the working components within the battery casing. A Mg AZ31 alloy foil, 96 % Mg, 3 % Al and 1 % Zn was purchased from GoodFellow with a foil thickness of 0.05 cm. The alloy's surface was polished before application by using a coarse (50) grit sandpaper followed by a fine (120) grit sandpaper and subsequently used as the anode. The contact surface area of the anode assembled within the Mg air battery was calculated to be at 0.79 cm$^2$. In addition, a Zn 99.994 % foil was purchased from Alfa Aesar with a foil thickness of 0.025 cm and was polished, as mentioned previously, before application and subsequently used as an alternative anode. The contact surface area of the alternative anode assembled within the Zn air battery was also calculated to be at 0.79 cm$^2$. Moreover, a 2 mg/cm$^2$ Pt black carbon cloth electrode was purchased from FuelCellStore with a cloth thickness of 0.0365 cm and used as the cathode for the ORR and the contact surface area of the cathode assembled within the batteries was calculated to be at 0.79 cm$^2$. The PEs 1:1 and 1:3 SF:IL composite films were assembled inside of independent batteries using Mg AZ31 alloy foil or Zn foil as the anode.

The galvanostatic discharge performance of the batteries (two-electrode electrochemical cell) was evaluated using the Biologic SP-300 potentiostat. The experiments involved two different techniques while the OCV was measured for the first 10 minutes beforehand to ensure that the batteries were operating as expected. The first experiment performed was a continuous discharge with a constant current of 20 μA being applied and proceeded until the minimum voltage cut-off (0 V) was reached. The second test involved an increasing current discharge with each new current applied persisting for 1 hr before the next. The experiment began with a 5 μA current being applied, then increased to 10 μA after 1 hr, then 20 μA, then increments of 10 μA until 80 μA was reached, then 100 μA and finally having the current applied reduced back to 5 μA for the final 1 hr.

The post discharge ionic conductivity of the PE 1:1 and 1:3 composite films assembled in the batteries (two-electrode electrochemical cell) were deduced by conducting PEIS using Biologic SP-300 potentiostat, with an amplitude of 10 mV with the frequency range set at 100,000 to 0.1 Hz, OCV.

## 5. Results and discussion: Computational studies

### 5.1 Introduction

Computational study is a rapidly growing field that uses advanced computing systems to understand or solve complex problems. It is an area of science which spans many disciplines, but at its core, it

involves the development of models and simulations to understand natural systems. Using MD, it is possible to observe and evaluate the effects of water has on the structure of the SF crystal model produced in this work. The goal is to achieve a realistic representation of the SF utilised in the PE for the battery experimentations where water acts as a proton source for the ORR at the cathode[1] and SF is also responsible for the immobilisation of the [Ch][NO$_3$] IL via capillary action.[1] Thus, investigating the chemical structure of SF in the presence of water molecules would provide a unique insight into this material and provide further insight into the chemistry of the PE (i.e. diffusivity of ions and secondary structure changes). The information procured from MD simulations would yield insight not easily accessed via conventional experimentation.

The structural features of *B. mori* SF have been conveniently represented using the synthetic peptide, (Ala-Gly)$_n$, where $n$ is the number of repetitions of the Ala-Gly units, as a model for the crystalline regions.[43, 197] From X-ray and electron diffraction studies *B. mori* SF the periodic copolypeptide (Ala-Gly)$_n$, has been shown to have an orthorhombic crystal structure with unit cell dimensions, $a$ = 4.65 Å, $b$ = 14.24 Å, $c$ = 8.88 Å, though these values are not the only reported unit cell dimensions for SF.[42, 43, 47, 198]

Within the simplified (Ala-Gly)$_n$ model the repeat β-turn type II structure is stabilised by intramolecular hydrogen bond interactions. The overall planar sheets are held together by intermolecular hydrogen bonding interactions, involving the central amide-bond of the β-turn, perpendicular to intramolecular interactions. Although, such an (Ala-Gly)$_n$ structural model vastly simplifies the overall structure of *B. mori* silkworm's SF, it makes it convenient and less computationally demanding.

Prior to spinning the *B. mori*. SF fibres, the SF is stored in the middle silk gland (ca. 30 % in water) and undergoes conformational changes when exposed to changes in ionic composition of the spinning dope, mechanical stress and loss of water during the natural fibre spinning process.[11] The rate of degradation of SF is related to the content of secondary β-sheet crystalline structure present within the bulk material.[162, 187] The β-sheet content in materials made from regenerated SF can be modified through the use of various processing conditions (e.g. water content and drying methods).[162, 199] In addition, the differing content of secondary structures present in the material also impact the materials mechanical properties.[162, 187, 199] Therefore, the utilisation of MD to evaluate the (Ala-Gly)$_n$ structural model of SF, specifically, the torsion angle coordinates of Ala and Gly would yield pertinent information about the secondary structure content. Furthermore, MD could also elucidate the interactions and changes in the secondary structure when the (Ala-Gly)$_n$ structural model of SF is incorporated with water molecules and/or charged ions (e.g. nitrates from [Ch][NO$_3$] IL). These characteristics have a

direct impact on the functionality of the PE utilised in the batteries and thus the performance of the batteries.

Previously, MD simulation has been used to investigate the mechanical behaviour of *B. mori* SF[188] and the conformational change of its silk I form into silk II.[11] The transformation of silk I into silk II is brought on by either external forces in an aqueous environment (i.e. the silk gland and spinneret).[11] To simulate this structural change, a (Ala-Gly)$_n$ model (at 298 K) was stretched (application of both shear (ca. 0.5 GPa) and tensile (ca. 0.1 GPa) stress) and the torsion angles of the residues evaluated. The resulting secondary structures showed a good agreement with existing ssNMR information indicating the potential of atomistic simulation techniques. The computationally produced silk II structure possessed ca. 75 % β-sheet and ca. 25 % β-turn content, which is comparable with experimental values of 73 % β-sheet and 27 % β-turn content.[11]

Although the primary structure of *B. mori* SF has been determined to be predominately (Ala-Gly)$_n$,[198] the SF can exist in either silk I or silk II form and their structural confirmations are less clear. It is generally accepted[155, 200, 201] that silk II contains regions rich in orderly packed antiparallel β-sheets, however, the precise content varies between studies which is in part caused by variations in experimental approaches/conditions and the variation of properties in natural materials.[202, 203] As for silk I, the structural parameters remain unclear because this conformation is less stable and susceptible to transformation into the silk II conformation, leading to difficulty in performing analysis (e.g. XRD experiments). As a result, multiple models exist for the silk I form (e.g. crankshaft model with Ala and Gly residues close to β-sheet and α-helix confirmations,[76] a loose 4-fold helical confirmation[204] and a four-residue β-turn structure).[205]

In this study, non-hydrated and hydrated SF crystal structure models were studied using classical MD to understand how water is accommodated in the silk structures, what impact it has on the silk itself and how it moves in the protein matrix to provide a unique insight into SF material properties. Utilising MD techniques will highlight where water is orientated around the silk protein chains and the direction the water molecules diffuse throughout the structure at various temperatures; this is particularly interesting owing to the importance of water in the structure and degradation of silk-based materials used for various technical and medical applications[74] (e.g. SF utilised as a PE for energy storage devices).[1] Furthermore, this will facilitate future work that investigate the incorporation of other molecules (e.g. charged ions, such as, $Zn^{2+}$ or $Mg^+$) within the silk model, expanding the potential in how this material could be applied.

**5.2 Lattice parameters and secondary structure of the non-hydrated and hydrated silk model**

Lattice parameters provide the foundation for building a crystal model from periodic unit cells to supercells, representing a bulk material, such as SF. Fortunately, SF and its lattice parameters have been extensively evaluated,[11, 42, 44, 45, 47, 187, 188] which provide the necessary information for constructing the unit cell in this work. Once the SF crystal model has been fabricated and undergone equilibration, it is vital to next evaluate the secondary structure for the purpose of comparison/confirmation with the literature. Ramachandran plots are ubiquitous and reliable when evaluating a protein's (e.g. SF) secondary structure, thus, they have been used to evaluate the SF crystal model's secondary structure detailed in this work.[58, 93, 94, 95]

The hydrated SF supercells were created by introducing ca. 7.5 wt % of water molecules, mimicking experimentally reproduced SF films.[158, 189] Water molecules were placed randomly within the supercells, while ensuring that no water molecules were placed within the 1.7 Å cut-off with respect to the silk protein Ala-Gly chains. Presented in **Table 1** are the averaged lattice parameters for the silk structures, $(Ala-Gly)_{128}$ and $(Ala-Gly)_{1024}$, after equilibration at 298 K for both the non-hydrated and hydrated simulation supercells. In addition, the initial lattice parameters (after the construction of the SF crystal model) are included for comparison.

**Table 1.** Initial lattice parameters after construction of the SF crystal model and average lattice parameters for the hydrated and non-hydrated silk structures at 298 K.[207]

| Parameter | Initial | Hydrated | Non-hydrated |
|:---:|:---:|:---:|:---:|
| | | Classical MD | Classical MD |
| a/ Å | 17.80 | 17.20 | 17.42 |
| b/ Å | 15.76 | 15.22 | 15.42 |
| c/ Å | 11.49 | 11.10 | 11.25 |

From X-ray and electron diffraction studies of *B. mori* SF, the periodic copolypeptide $(Ala-Gly)_n$ silk I form, has been shown to have an orthorhombic crystal structure with unit cell dimensions, $a = 4.65$ Å, $b = 14.24$ Å, $c = 8.88$ Å, though these values are not the only reported unit cell dimensions for SF.[42, 43, 47, 198] In addition, the aforementioned unit cell dimensions have been reported to be inconsistent due the packing of the protein chains.[198] Therefore, **Table 1** reports new unit cell dimensions but for the computationally fabricated SF crystal structure, that depict the periodic copolypeptide $(Ala-Gly)_n$.

**Figure 18** show the Ramachandran plots of the initial (torsion angles of Ala and Gly at the start of simulation) and final (torsion angles of Ala and Gly at the end of the simulation) positions of the non-hydrated and hydrated (Ala-Gly)$_{128}$ SF crystal model, at the timescale of 2 ns. **Figure 19** show the Ramachandran plots of the initial and final positions of the non-hydrated and hydrated (Ala-Gly)$_{1024}$ SF crystal model, at the same timescale mentioned above (2 ns). Classical MD simulations were conducted to obtain the torsion angles for residues Ala and Gly required for plotting, for clarity; only the 298 K NPT ensemble experiments are depicted.
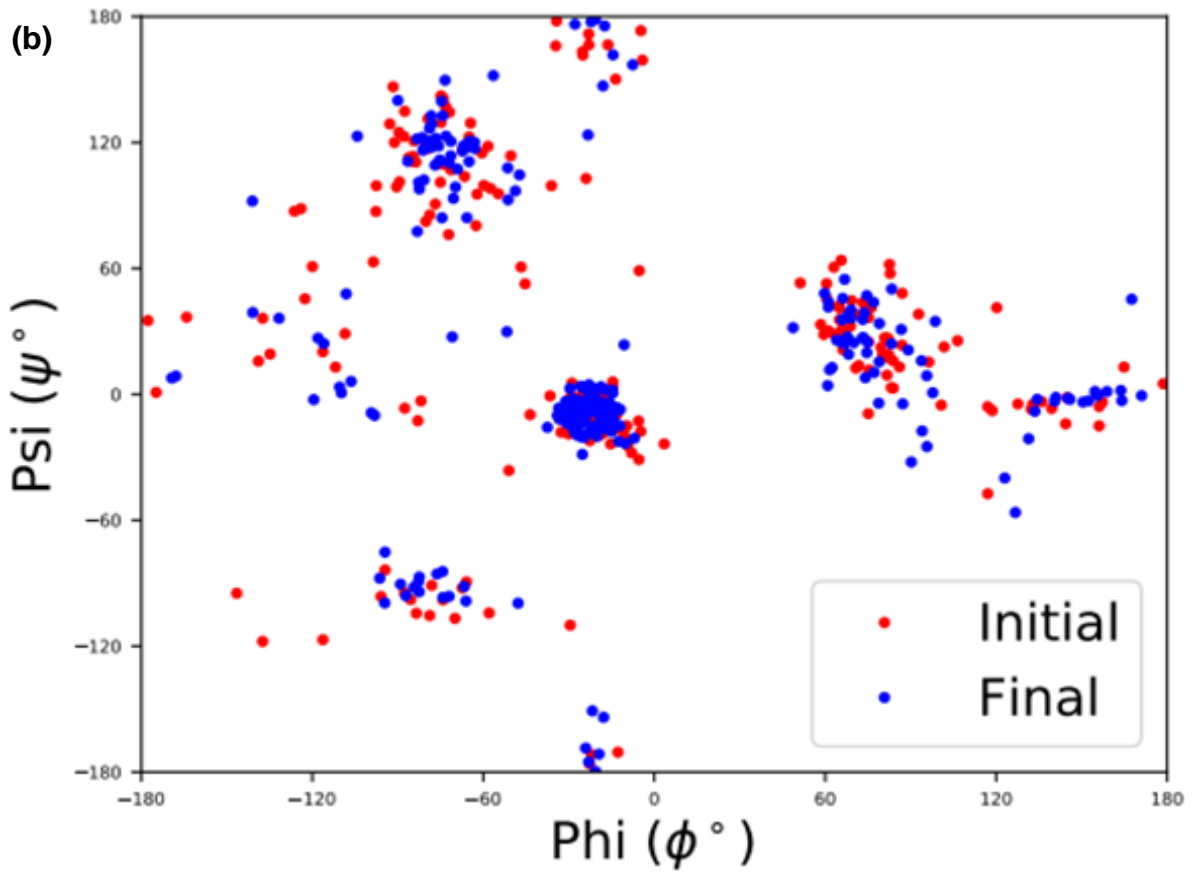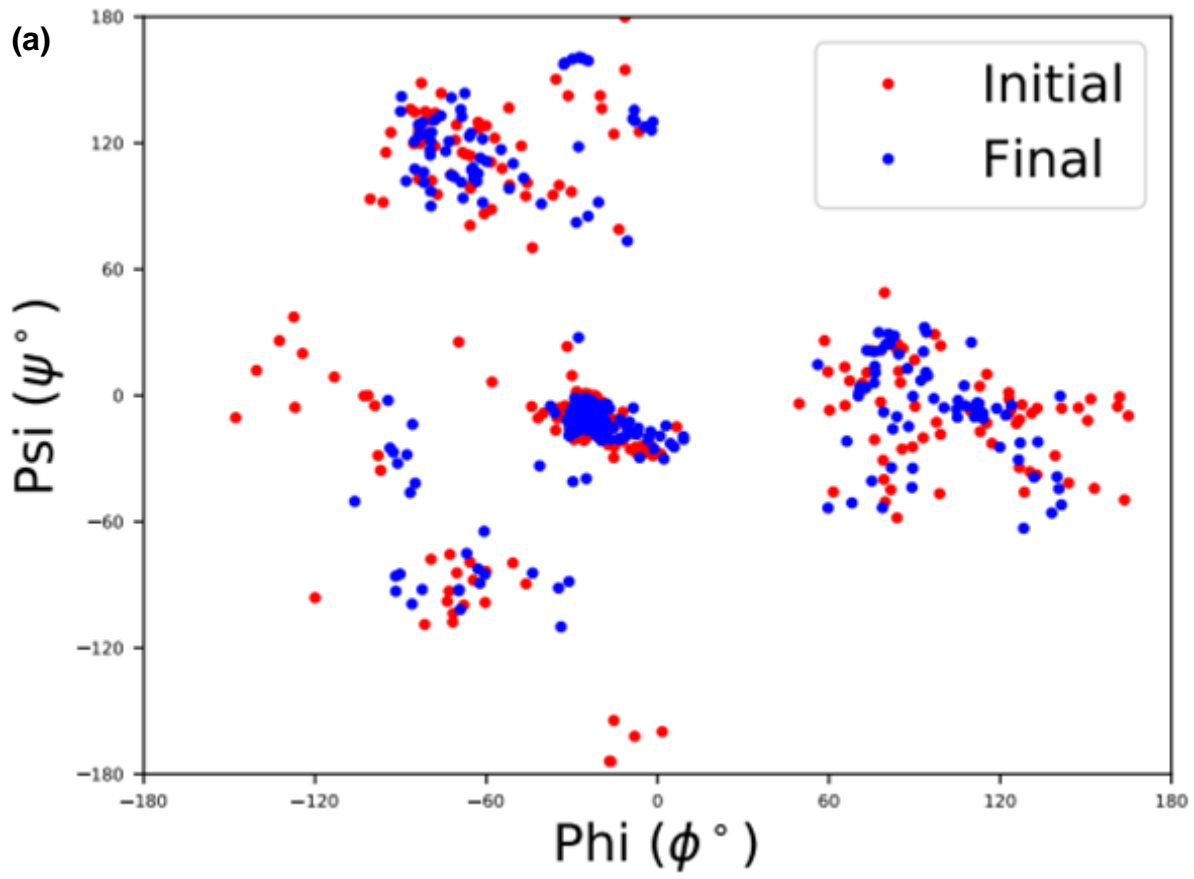
**Figure 18.** (a) Ramachandran plot at 298 K of the non-hydrated (Ala-Gly)$_{128}$ SF crystal. (b) Ramachandran plot at 298 K of the hydrated (Ala-Gly)$_{128}$ SF crystal. MD generated the torsion angles of the Ala and Gly residues from (Ala-Gly)$_{128}$. The legend depicts the initial (red dots) and final (blue dots) positions of the Ala and Gly residues at 2 ns sampling.
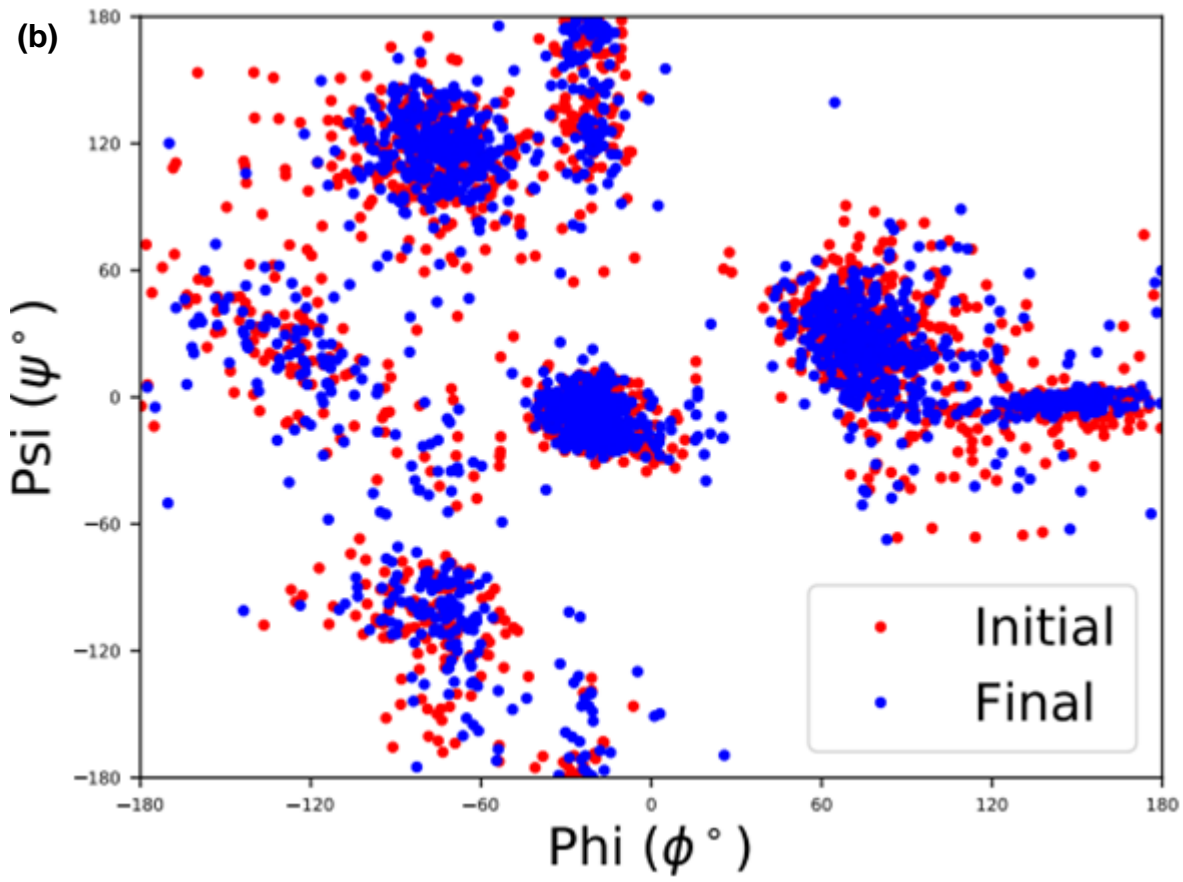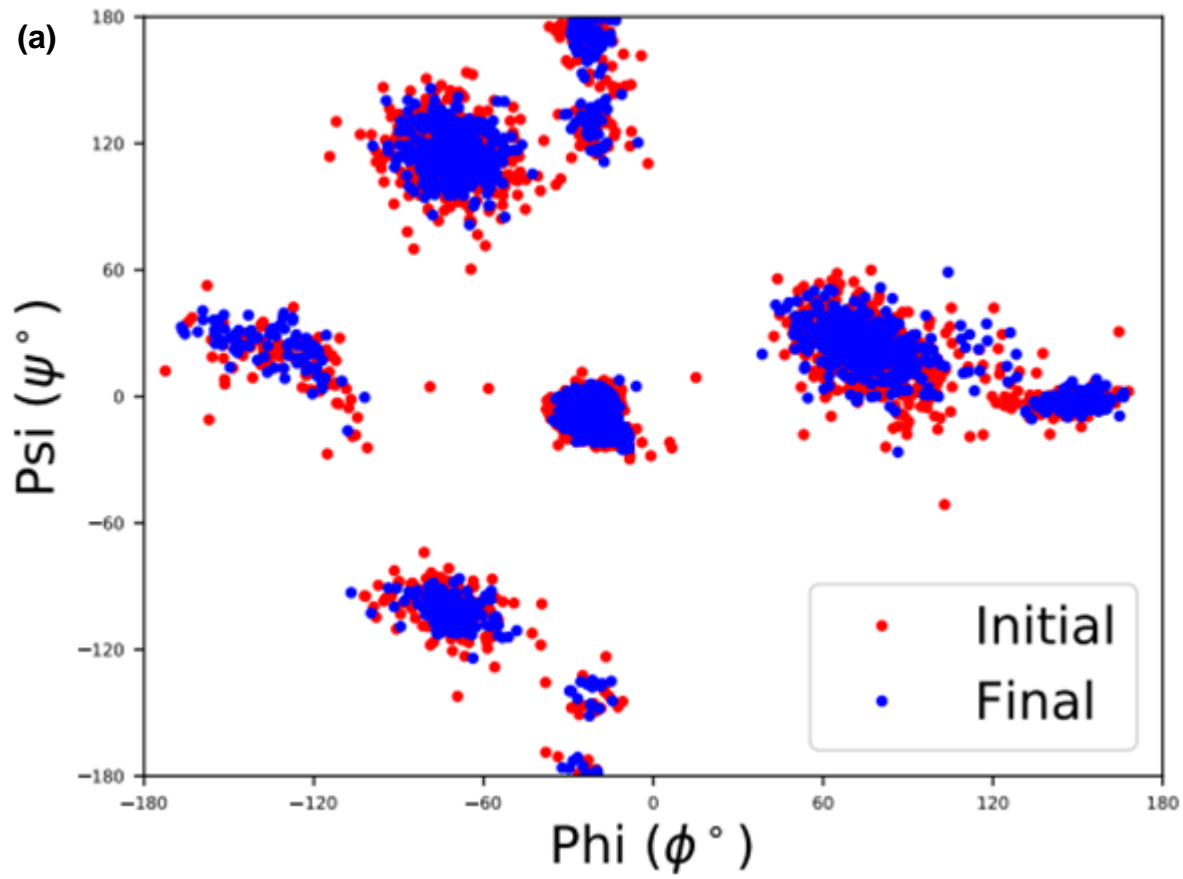
**Figure 19.** (a) Ramachandran plot at 298 K of the non-hydrated $(Ala-Gly)_{1024}$ SF crystal. (b) Ramachandran plot at 298 K of the hydrated $(Ala-Gly)_{1024}$ SF crystal. MD generated the torsion angles of the Ala and Gly residues from $(Ala-Gly)_{1024}$. The legend depicts the initial (red dots) and final (blue dots) positions of the Ala and Gly residues at 2 ns sampling.

**Figure 18** and **19** highlight the initial and final positions of the residues Ala and Gly during the 2 ns MD simulations. It is observed that the initial and final residue positions are not dramatically different after the timescale of 2 ns. This is especially true for the $(Ala-Gly)_{1024}$ SF crystal model, likely due to the statistical difference between each system. However, it appears that when the SF crystal models have water molecules incorporated (**Figure 18(b)** and **19(b)**), the positions of the Ala and Gly residues are more sparsely distributed when compared to their respective non-hydrated SF crystal models (**Figure 18(a)** and **19(a)**). The incorporation of water molecules introduces new hydrogen bond interactions (i.e. the protein backbone with the water molecule). This information implies that the incorporation of water molecules disrupts typical protein backbone hydrogen bond interactions, thus, allowing a greater degree of movement. $^{13}C$ NMR techniques have also been utilised to observe the effects of water on the structure and dynamics of SF. It has been reported that hydrated (immersed in water overnight) SF sponges, films and fibres indicated a shift towards silk I form and showed an enhancement in the random coil conformation, resulting in a high degree of mobility of the protein backbone.[208] Therefore, the classical MD of the SF crystal models in this work indicate an agreement with experimentally determined information from the literature.

Moreover, the information from **Figure 18** and **19** is difficult to digest on its own. Hence, Ramachandran contour plots were fabricated from averaged over the 2 ns of torsional angle information generated from MD. **Figure 20** shows the Ramachandran contour plots of the non-hydrated and hydrated $(Ala-Gly)_{128}$, and **21** for the $(Ala-Gly)_{1024}$ SF crystal models. Classical MD simulations were conducted to obtain the torsion angles for residues Ala and Gly required for plotting, for clarity; only the 298 K NPT ensemble experiments are depicted.
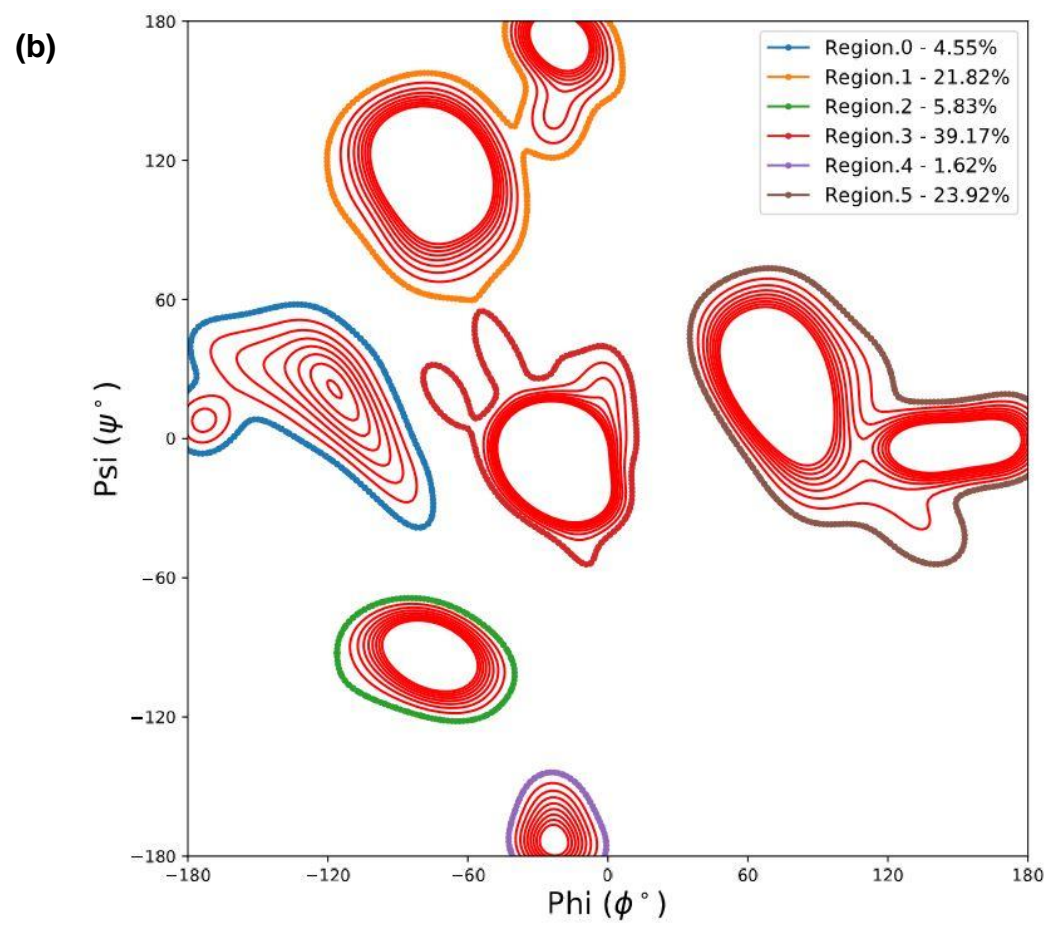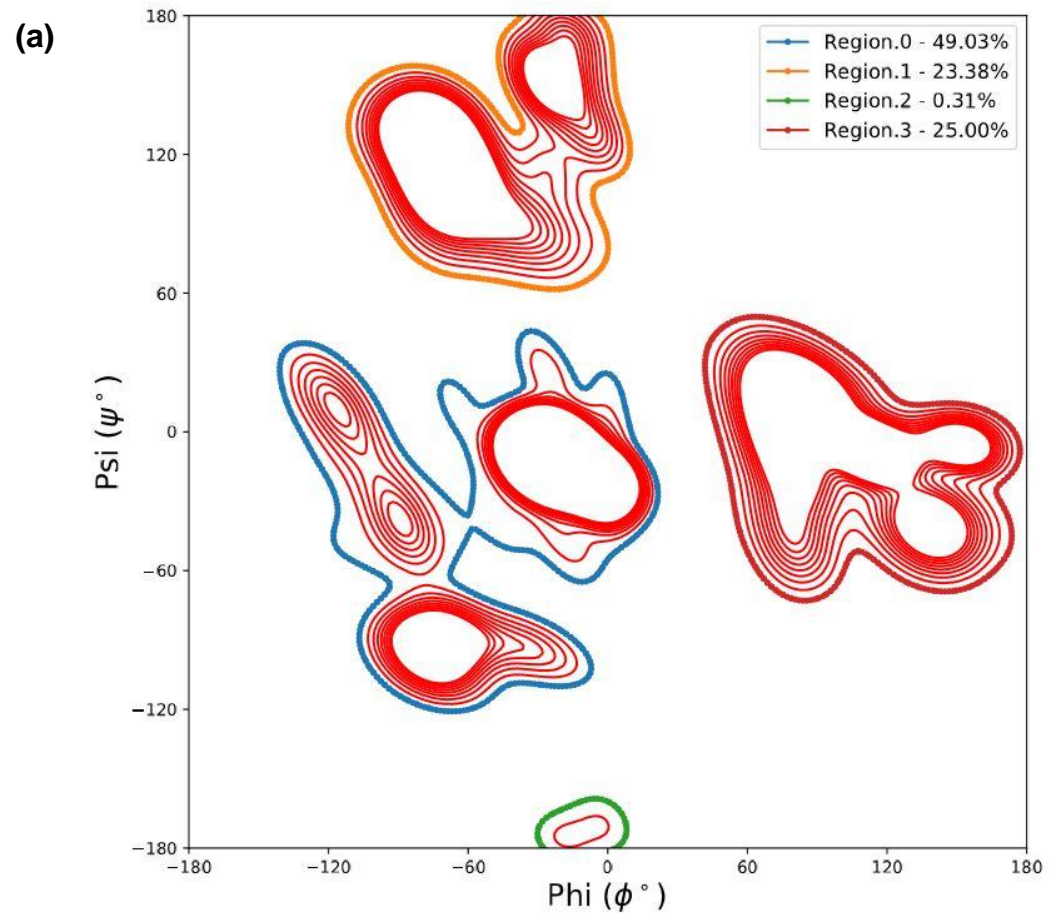
**Figure 20.** (a) Ramachandran contour plot at 298 K of the non-hydrated (Ala-Gly)$_{128}$ SF crystal. (b) Ramachandran contour plot at 298 K of the hydrated (Ala-Gly)$_{128}$ SF crystal. MD generated the torsion angles of the Ala and Gly residues from (Ala-Gly)$_{128}$. The legend depicts the percentage of the residues (averaged over 2 ns) within each region.[207]
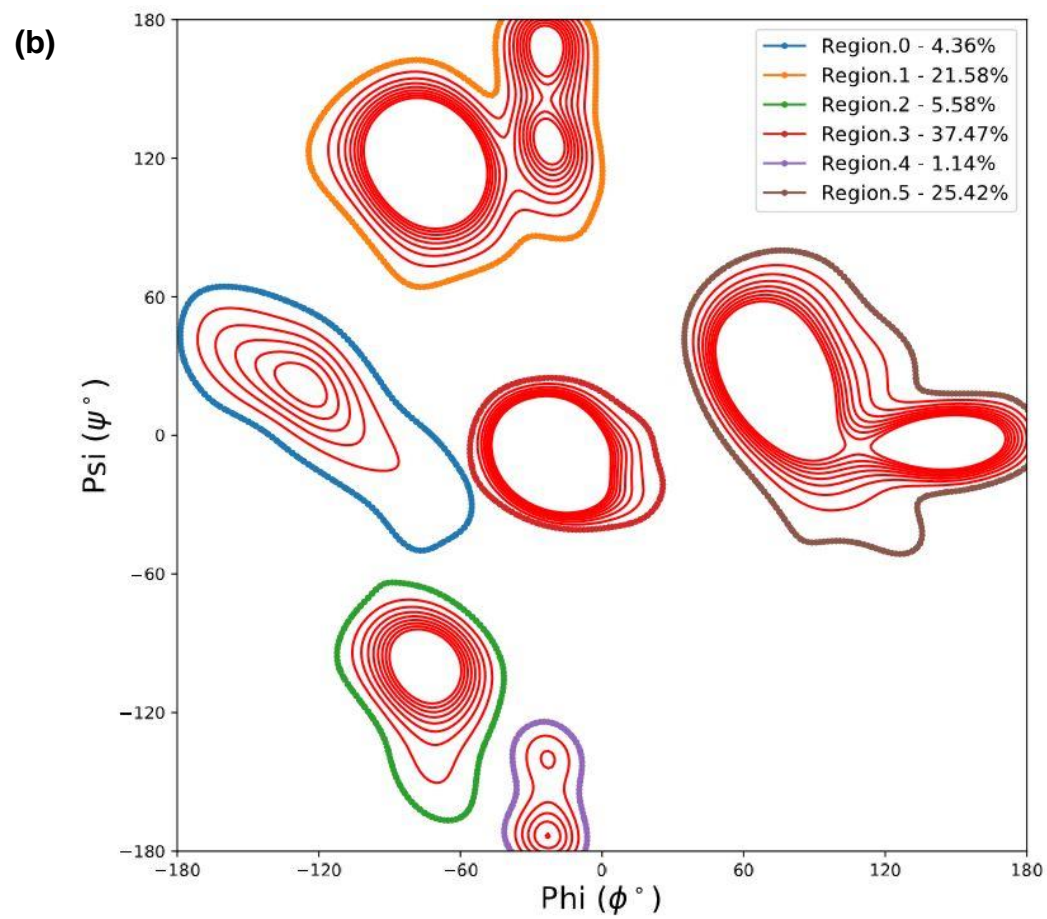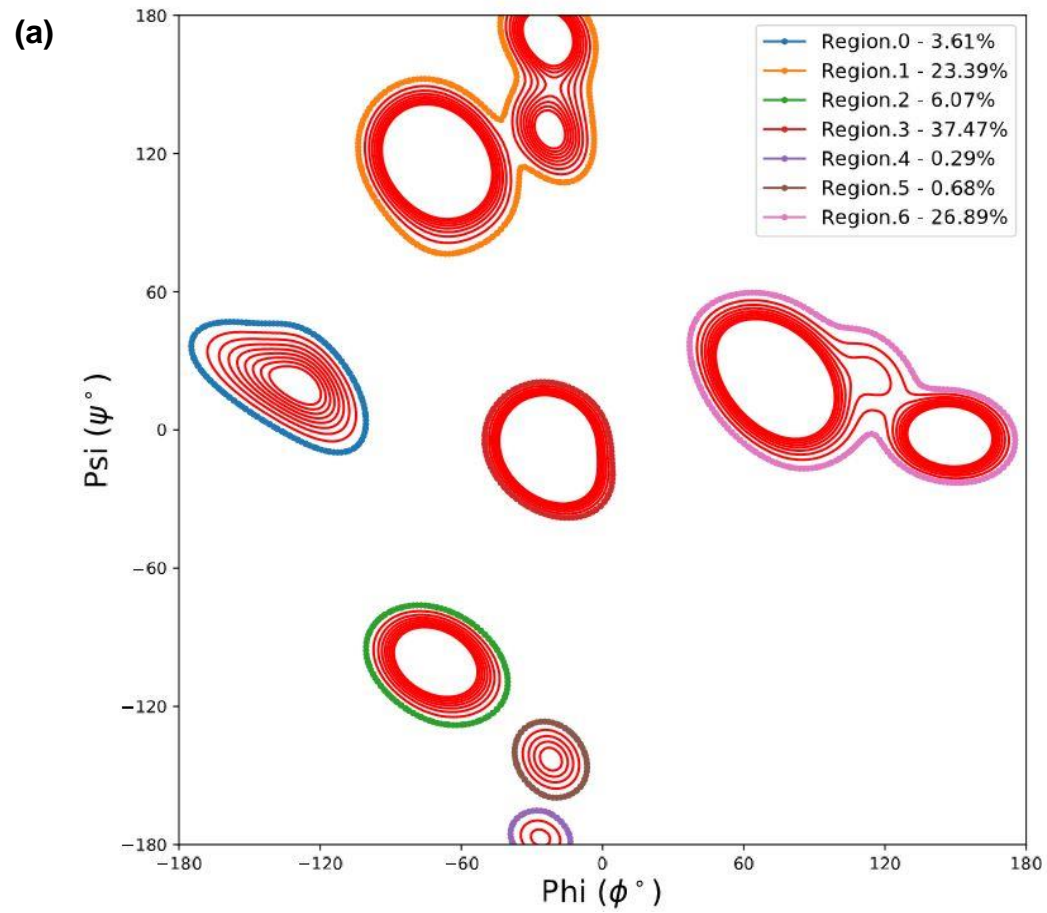
**Figure 21.** (a) Ramachandran contour plot at 298 K of the non-hydrated (Ala-Gly)$_{1024}$ SF crystal. (b) Ramachandran contour plot at 298 K of the hydrated (Ala-Gly)$_{1024}$ SF crystal. MD generated the torsion angles of the Ala and Gly residues from (Ala-Gly)$_{1024}$. The legend depicts the percentage of the residues (averaged over 2 ns) within each region.[207]

The Ramachandran contour plots in **Figure 20** and **21** possess regions that lie within $<\varphi>$ = - 60 ° and $<\psi>$ = 130 ° and $<\varphi>$ = 70 ° and $<\psi>$ = 10 °, which is characteristic of the Ala and Gly residues, respectively, as reported in the literature.[11, 68, 69, 70, 71, 72] Hereby, implying the SF model utilised in this work, possesses qualities that have been experimentally observed. In addition, **Figure 20** and **21** indicate that the SF crystal models possesses a heterogeneous structure, evidenced by a left-handed α-helix, 3$_{10}$-helix, β-sheet (ca. $<\varphi>$ = 70 ° and $<\psi>$ = 10 °, ca. $<\varphi>$ = - 40 ° and $<\psi>$ = - 30 °, ca. $<\varphi>$ = - 60 ° and $<\psi>$ = 130 °, respectively) and random coil structures. Furthermore, the (Ala-Gly)$_n$ SF crystal structure is to be considered in the silk I form (i.e. repeated β-turn type II conformation), because β-sheets are not the predominant secondary structure, instead, the 3$_{10}$-helix is the predominant secondary structure (ca. 37 %), in agreement with the literature.[11, 42, 43, 45, 46, 68, 69, 70, 71, 72, 158, 187, 188, 209]

On the other hand, by comparing the non-hydrated state of the (Ala-Gly)$_n$ SF crystal model (**Figure 20(a)** and **21(a)**) with the hydrated state (**Figure 20(b)** and **21(b)**), the torsion angle regions for the Ala and Gly residues appear in slightly different locations. This is likely due to the flexibility of the SF model's protein backbone (Ala and Gly) chains, caused by the introduction of new hydrogen bond interactions, mentioned previously. In addition, a lower number of hydrogen bond interactions between polymer chains within a system could hinder the reorganisation of the system. As might be anticipated, as the temperature increases, the protein backbone chains can move more freely, resulting in a broadening of the Ala and Gly residue's positions. With the introduction of more hydrogen bond interactions from residues and/or water molecules (e.g. between protein backbone chains), impacts the potential flexibility of the (Ala-Gly)$_n$ SF crystal model.

Moreover, the regions for the Ala and Gly residue positions for the non-hydrated and hydrated states of the larger (Ala-Gly)$_{1024}$ SF crystal model (**Figure 21**) are more defined compared to the (Ala-Gly)$_{128}$ SF crystal model (**Figure 20**). For instance, **Figure 20(a)** regions 0, 1 and 3 are distorted when compared to **Figure 21(a)** regions 1, 3 and 6. This could be due to a statistical difference between each system, as mentioned previously, (Ala-Gly)$_{1024}$ possesses a greater number of torsion angles, therefore, outliers are less likely to affect overall residue region position/shape. In addition, the hydrated states in **Figure 20(b)** and **Figure 21(b)** show many more similarities, which supports that the idea

that the introduction of water molecules influence the positions of the Ala and Gly residues and their potential positions.

Furthermore, a previous SF structure study using DFT chemical shift calculation, reported that the torsion angle ranges for Ala and Gly are $<\varphi> = -143 \pm 6\,°$, $<\psi> = 142 \pm 5\,°$. In addition, the torsion angle range of $<\varphi> = -143 \pm 6\,°$, $<\psi> = 142 \pm 5\,°$ is within the characteristic range for antiparallel β-sheets.[11, 210] In this work (**Figure 20** and **21**), the hydrated (Ala-Gly)$_{128}$ and (Ala-Gly)$_{1024}$ cells have achieved similar torsion angle values for Ala and Gly residues supporting the validity of the SF crystal model; as the two different computational techniques predict similar secondary structures that also agrees with the literature.[11, 76, 155, 158, 200, 201, 202, 203, 204, 210]

The average lattice parameters for the hydrated SF crystal models reported in this work using classical MD are $a = 17.20$ Å, $b = 15.22$ Å, $c = 11.10$ Å. Furthermore, the SF crystal model possess ca. 7.5 % water by weight. The literature has disputed the exact values for SF lattice parameters depending on the macrostructure (i.e. if it is a film or fibre or in silk I or silk II form). This is attributed by the highly flexible conformation an Aly-Gly-based structure can have due to very minimal side chain interactions. Therefore, by evaluating the Ramachandran plots and contour plots, it was found that the SF crystal models detailed in this work strongly agree with the literature. Specifically, the SF crystal models have a predominance for a silk I form as the $3_{10}$-helix is the predominant secondary structure (ca. 37 %).

### 5.3 Diffusion and trajectory of water in the silk model

In this work the diffusion capabilities of SF are quintessential for its ultimate use as an electrolyte for batteries. Therefore, using classical MD, it is possible to not only determine the diffusivity of water through silk but also its trajectory and direction over a given timeframe. After having investigated the structure of the silk model and its hydrated state, we now examine the mobility of the water molecules around the hydrated silk. In order to obtain sufficient water diffusion to provide adequate statistics, the MSD calculations were performed using classical MD simulations of the largest 4x4x4 simulation supercells. The MSDs for the oxygen ions in the water molecule at the temperature range of 273, 293, 298, 303 and 310 K are reported in **Figure 22**.
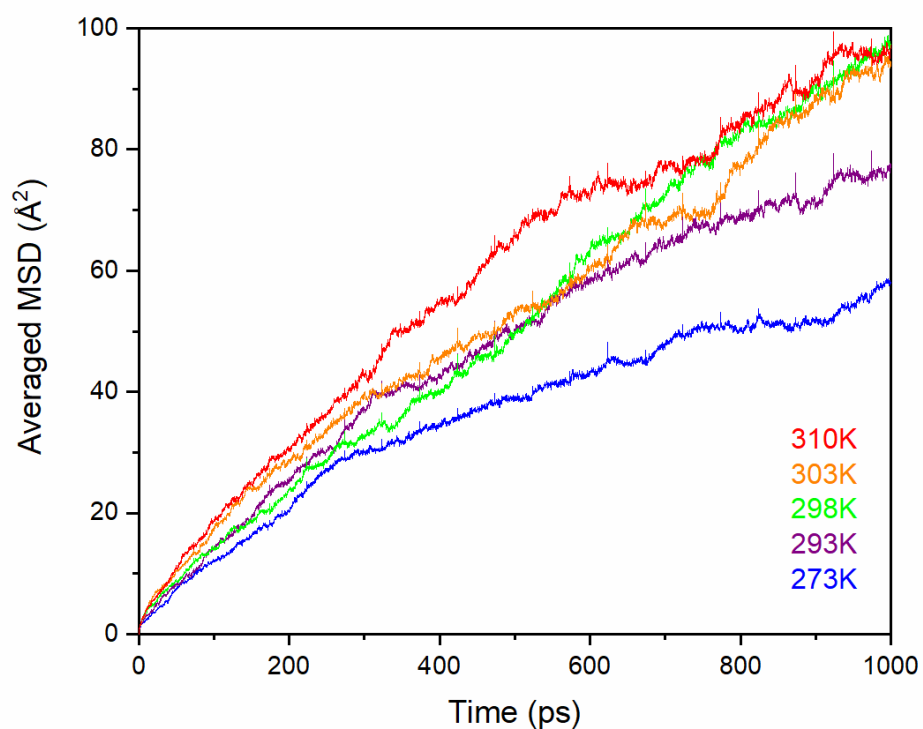
**Figure 22.** MSD of the oxygen ions from the water molecules (in $\text{Å}^2$) in the hydrated SF crystal model $(Ala\text{-}Gly)_{1024}$. The legend depicts the temperature (in K).[207]

From **Figure 22**, it shows that as the temperature increases the MSD for the oxygen ions in the water molecules increase linearly with time, indicating that the water molecules are free to diffuse around the polymer chains, even at very modest temperatures. By taking the gradient of the MSDs and plotting against 1/Temperature, it is possible to create an Arrhenius[211] plot, as shown in **Figure 23**.
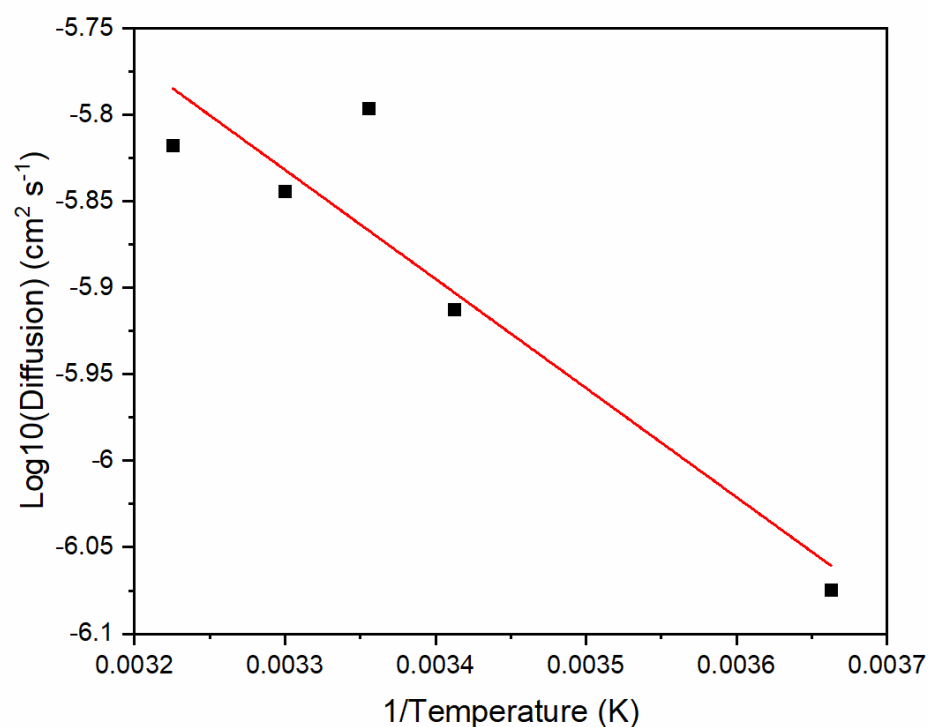
**Figure 23.** Arrhenius[211] plot of the hydrated (Ala-Gly)$_{1024}$ SF crystal at the temperature range of 273 to 310 K. By using equation (19) and the gradient of the slope in the Arrhenius plot, the calculated activation energy for water diffusion in the SF crystal is determined as 12.07 kJ mol$^{-1}$.[207]

From the Arrhenius[211] plot it is clear that the data can be fitted using a straight line, yielding an activation energy of 12.07 kJ mol$^{-1}$ and maximal diffusivity ($D_0$) of 1.78x10$^{-4}$ cm$^2$ s$^{-1}$. Moreover, a previous study on SF as an edible coating for perishable food preservation reported that their experimentally obtained diffusivity, at room temperature, was 1.05x10$^{-6}$ cm$^2$ s$^{-1}$ at 58 % β-sheet content, 3.21x10$^{-6}$ cm$^2$ s$^{-1}$ at 48 % β-sheet content and 5.79x10$^{-6}$ cm$^2$ s$^{-1}$ at 36 % β-sheet content.[212] Looking at room temperature (298 K), the diffusivity predicted from **Figure 23** is 1.60x10$^{-6}$ cm$^2$ s$^{-1}$, which is similar to the experimental results. As mentioned above, the experimental samples had β-sheet contents greater than 36 %, while the sample studied here has a lower β-sheet content (ca. 26 %) that does appear to have an impact on the diffusivity.

Finally, we explore the dynamic motions of the water molecules to elucidate the diffusion mechanism around the polymer chains. Shown in **Figure 24** are the trajectories of the water molecules around the silk from the classical MD simulations at 298 K over 1 ns. From the trajectories depicted in **Figure 24**, the red isosurface represents the regions explored by the water molecules. The isosurface indicates

that while there is a connected region that water can explore extending in the X direction, there appears to be significantly less diffusion evident in the Y direction (indicated by the lack of connected isosurface in this direction). To explore this further a plot for the directional MSD of the oxygen ions from the water molecules in the hydrated SF crystal model (Ala-Gly)$_{1024}$ at 298 K over 1 ns is presented by **Figure 25**. This figure illustrates the highly anisotropic diffusion of water in the SF crystal model. While water is clearly free to diffuse along the chains in the X direction, there is little movement of water across the chains in the Y direction and even less in the Z direction. Therefore, indicating a high degree of anisotropy, as the water molecules tend to diffuse through the free space between the chains rather than crossing the chains.
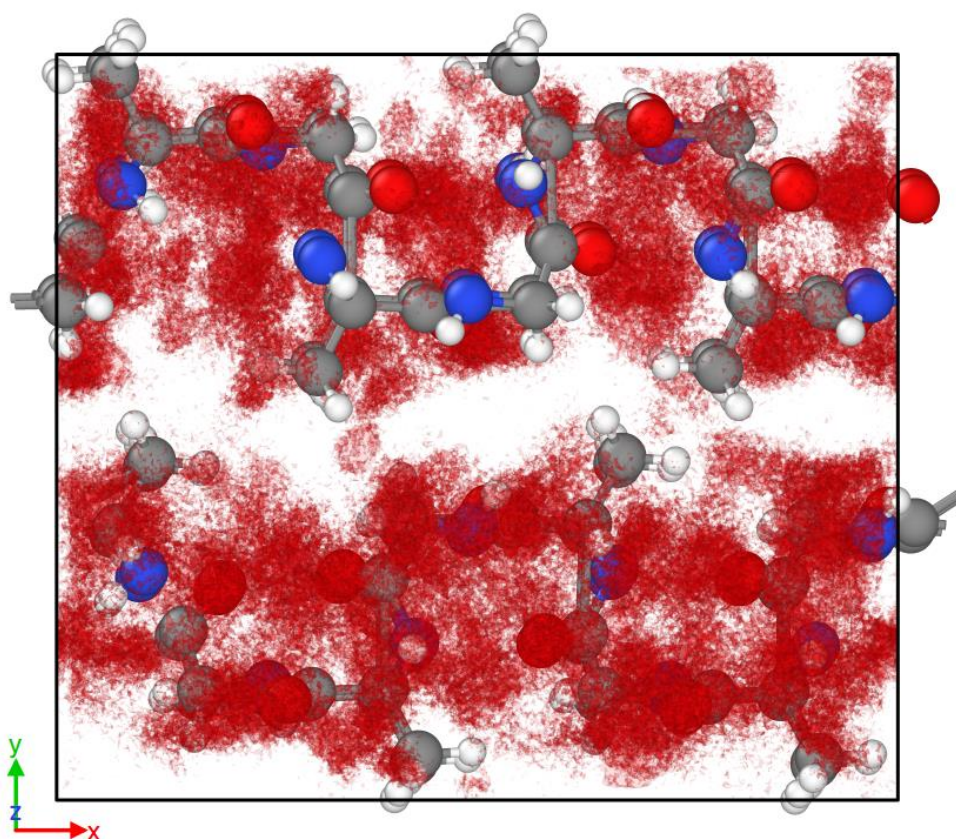


**Figure 24.** A VESTA[206] visualisation of the water trajectory of the hydrated (Ala-Gly)$_{1024}$ SF crystal at 298 K over 1 ns. The dark grey ball and sticks depict the carbon atoms, white the hydrogen atoms, red the oxygen atoms and blue the nitrogen atoms. For the water molecules, only their oxygen atoms are used to depict their locations and the red isosurface represents the water density around the silk chains. In addition, the water density displayed represents from the initial and final frame, whereas, the Ala-Gly protein chain depicts only the final frame position of the residues.[207]
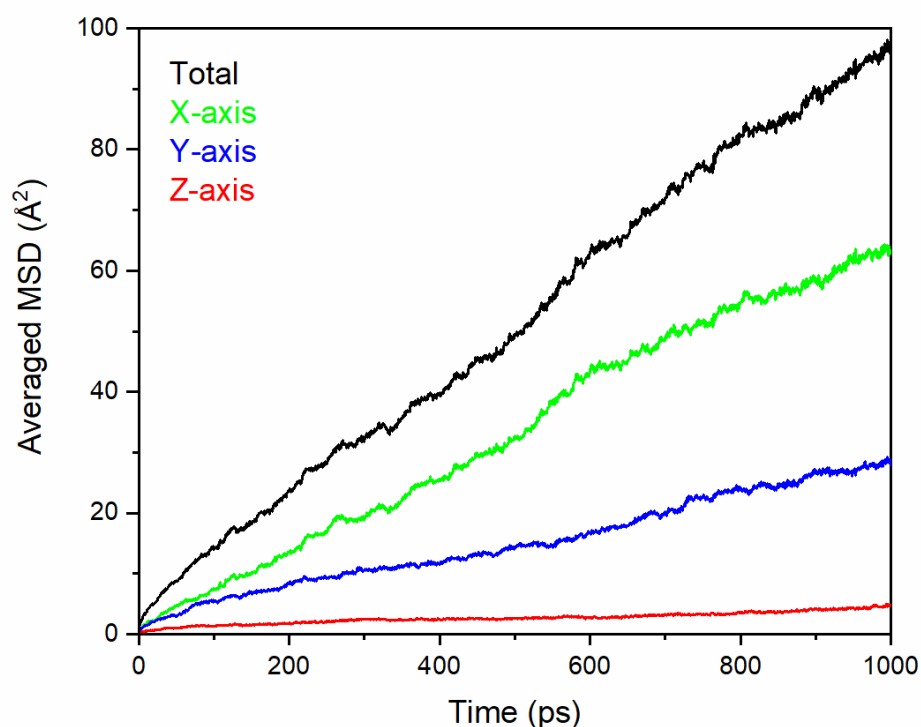
**Figure 25.** The directional MSD of the oxygen ions from the water molecules (in Å$^2$) in the hydrated SF crystal model (Ala-Gly)$_{1024}$ at 298 K. The total MSD of the oxygen ions from the water molecules is represented by the black line, MSD of the oxygen ions from the water molecules along the X-axis is represented by the green line, along the Y-axis is represented by the blue line and along the Z-axis is represented by the red line.[207]

As seen from **Figure 24**, numerous water molecules populate the areas across the protein chains; however, the water molecules mostly diffuse through the spaces between the protein chains (along the X-axis direction, as seen from **Figure 25**). Therefore, **Figure 24** and **25** highlights the potential positions for water molecules incorporated in the SF crystal structure and their diffusivity. As a result, this opens an interesting avenue for further research, for instance, how the water molecule positions/diffusivity change with change in the proteins secondary structure. In addition, what impacts/behaviour other species (e.g. charged ions and ILs) have when incorporated into the SF model. Ultimately, better understanding these aspects will improve upon the applications this material could be applied to.

The activation energy for water diffusion in the SF model, reported in this work, has been calculated to be 12.07 kJ mol$^{-1}$ for the temperature range of 273 to 310 K, indicating water molecules have relatively

free motion/diffusion within the SF model. In addition, the diffusivity of water incorporated in the SF crystal model at 298 K was calculated to be $1.60 \times 10^{-6}$ $cm^2$ $s^{-1}$. This is very similar to the diffusivity of water in SF films determined experimentally. Therefore, classical MD of the SF crystal models in this work show signs of confidence, because it has reproduced results like that of published experimental studies of similar materials. Furthermore, MD has also allowed for the study of the trajectory of the water molecules diffusing in the SF crystal model. It is reported in this work, that water diffusion in the SF crystal model is predominantly anisotropic, favouring diffusion along the X-axis or along the protein chains. It could then be implied that the diffusion of species other than water (e.g. charged ions) may adopt a similar trajectory and this could impact the future applications for SF.

## 6. Results and discussion: Experimental studies

### 6.1 Introduction

Previously reported in this work, classical MD was utilised to provide a unique insight into the material of SF to supplement experimental information. The approach for investigating the SF material now takes an experimental approach. Since SF is a biopolymer with promising characteristic properties, it will be harnessed and applied into batteries. Specifically, immobilising the [Ch][NO$_3$] IL to produce a PE for batteries. The goal of fabricating a transient and biocompatible battery combats our current E-waste crisis, additionally, these batteries would then be a promising device to power TIMBs.

SF from the *B. mori* silkworm is an Ala-Gly-rich protein, which is spun from aqueous solution to produce strong fibres.[11, 213] Furthermore, SF has excellent biocompatibility, making it a popular component of biomaterials.[3, 4] Many attempts have been made to mimic the natural process of producing robust silk filament under mild experimental conditions.[214, 215, 216, 217] However, this has proven challenging and many of the resultant fibres have been weaker than natural silk.[209] Therefore, a greater understanding of the chemistry and properties of natural silk fibres, such as *B. mori* SF, is essential, because this can help optimise the utilisation of silk for various technical, electrochemical and biomedical applications.[11, 36, 37, 38, 39, 40, 41]

SF has seen application in transient technology and TIMBs (e.g. encapsulation materials and food preservation).[1, 3, 212] Encapsulation materials can be vital for protecting a transient device, like a biocompatible and biodegradable battery or implantable medical device,[5] from premature degradation or controlling the transient characteristic of the device when first exposed to a stimulus (e.g. aqueous solutions of enzymes).[1] In addition, food quality and safety are important factors in the economics underpinning food value chains. Many perishable fruit and vegetables possess high metabolic activity and suffer from the possibility of microbial contamination, resulting in a short shelf-life, fungal decay,

colour change, and off-flavour.[212] Interestingly, SF has been shown to be a beneficial coating applied to foodstuffs.[1, 212]

Transient technology is a flourishing area of research aimed at designing materials and devices that undergo controlled degradation processes after a period of stable and reliable operation. Transient energy storage systems, such as biodegradable and biocompatible batteries, may enable fully autonomous and self-sufficient transient electronic devices (e.g. TIMBs) that do not rely on external power sources. To date, there are very few examples of transient batteries in the literature. The main challenges are the deficit of suitable soluble materials, fabrication schemes, and battery designs that must fulfil completely different requirements than for traditional batteries. Nevertheless, transient batteries have the potential to reduce the environmental footprint caused by inadequate disposal of used batteries (i.e. ca. 50 million tons a year of E-waste).[4] Therefore, these batteries/devices fulfil a significant role in powering our future technologies. As a result, it is crucial to improve and develop their potency because some solid-state electrolytes (e.g. PEs) do struggle to satisfy the level required for many applications (ca. $10^{-3}$ S cm$^{-1}$), limiting potential applications.[109, 142, 146]

The focus of this thesis is the development of a silk-based primary Mg- or Zn-air batteries. The batteries utilised a PE composite, consisting of *B. mori* SF and [Ch][NO$_3$] IL. This design makes use of SF in the development of biocompatible and biodegradable PEs, wherein the SF immobilises the IL creating an ion conducting separator between the electrodes. In the future, the case housing the electrochemical components may be substituted with SF, to generate completely transient devices. The efficiency of the PEs was demonstrated when deployed in the batteries and their discharge profiles over prolonged periods were evaluated. However, before this could be implemented, a prototype battery design was fabricated to evaluate the working components which would later be utilised in the final iteration of the batteries.

## 6.2 Prototype battery

A prototype is an early sample, model, or release of a product built to test a concept or process, in this case a battery. A prototype is typically utilised to evaluate a design to enhance/streamline product fabrication and eventual experimentation. Therefore, the prototype battery in this work details the initial chemistry of how the primary air battery works and the evolution of this experimental process toward a final concept. In addition, the prototype battery was fabricated to gain familiarity with how the electrochemical system behaves (e.g. if the battery lacks oxygen from the air and requires a supplementary source).

A prototype battery design was fabricated to observe how the materials utilised for the battery behave/operate. Furthermore, it would provide initial results for the basis of reference and comparison with future battery iterations. See in **Figure 26** the initial prototype battery assembly utilising Mg AZ31 alloy as the anode, coiled Au wire as the cathode, Ag-AgCl leak-free as the reference electrode and [Ch][NO$_3$] IL as the electrolyte. The Mg AZ31 alloy is utilised due to its biocompatibility but also its agreeable degradation/corrosion rates (4.0 mg cm$^{-1}$ day$^{-1}$ in 3.5 wt % NaCl solution at 25 °C and 1.5 mm year$^{-1}$ in whole blood when utilised as an implantable stent, respectively).[249, 250] Thus, Mg AZ31 is suitable for TIMB applications (i.e. implantable and degradable energy storage devices). In addition, [Ch][NO$_3$] IL is also utilised for its biocompatible properties, as well as its ionic conductivity. Lastly, the Au wire acts as the chosen cathode because it is biocompatible/bioinert, readily available and acts as a catalyst toward the ORR.[1]
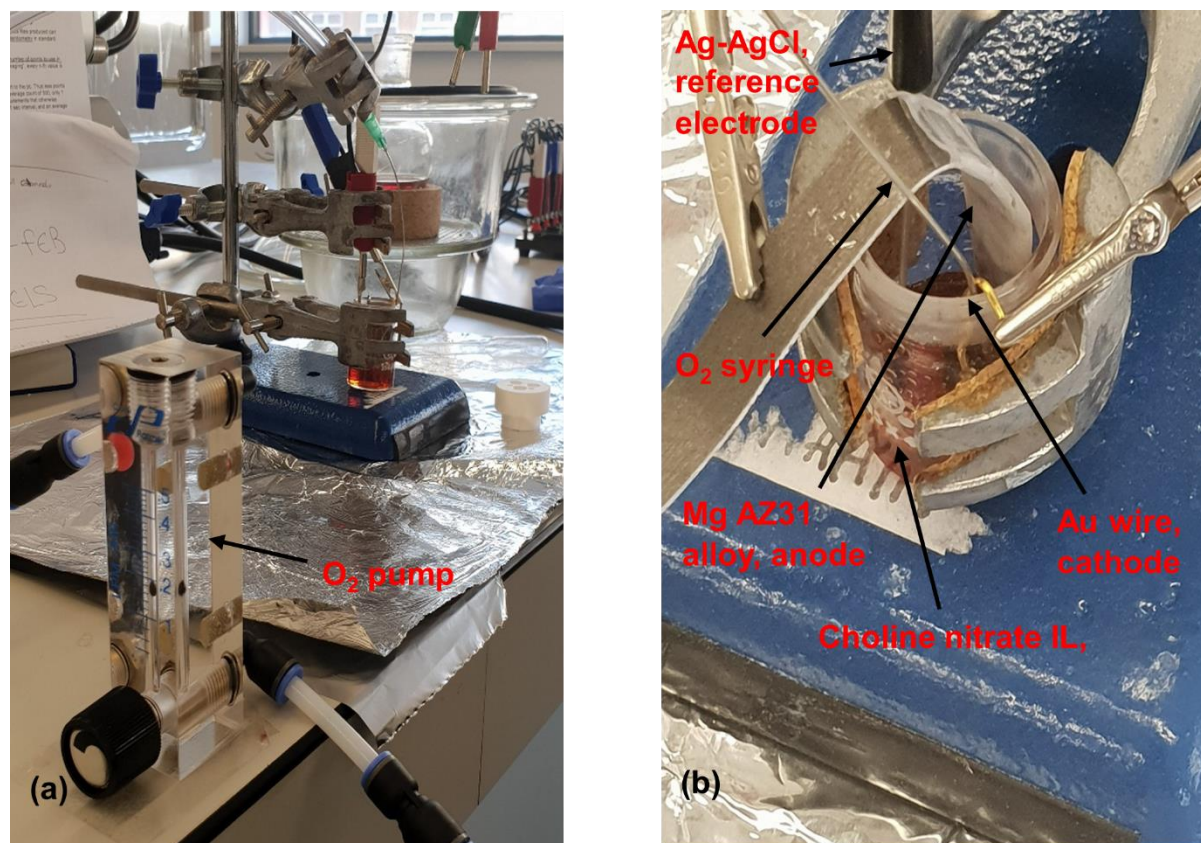


**Figure 26.** Pictures of the prototype battery. (a) Full picture of the prototype battery setup including the oxygen inlet (2 L min$^{-1}$) and (b) close-up picture of the prototype battery highlighting the working components. Labelled correspondingly by the black arrows and bold red text.

After the initial assembly of the prototype battery, the OCV of the prototype battery was measured and the resulting measurements are depicted by **Figure 27**.
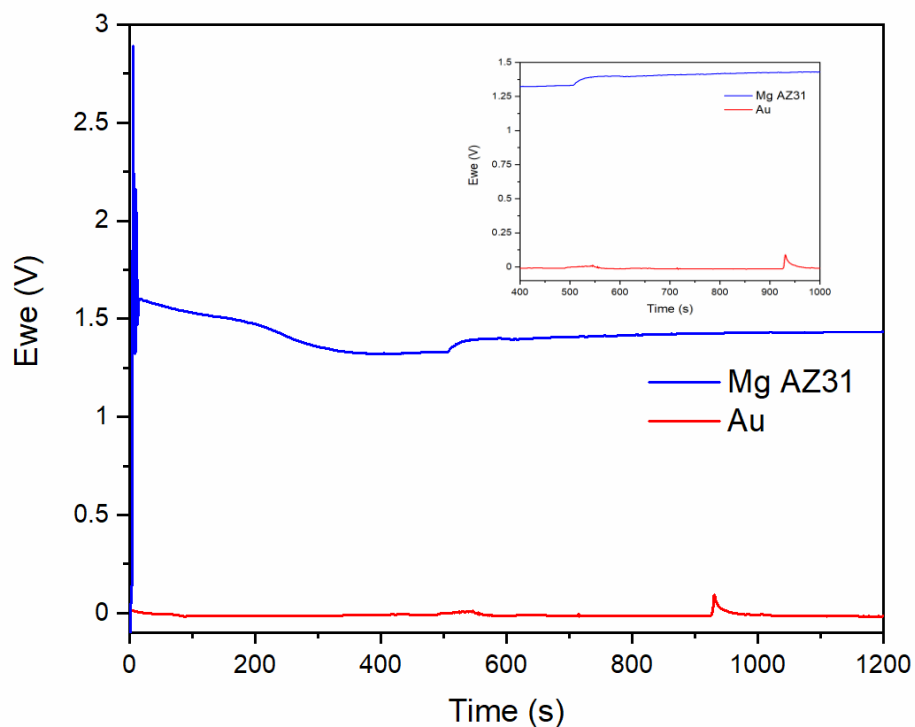


**Figure 27.** OCV of the prototype battery using an Ag-AgCl leak-free electrode as the reference electrode. The inset portrays an expanded view (400 to 1000 seconds) to highlight the region at which the oxygen inlet was activated at 500 seconds.

This battery system Mg-AZ31|[Ch][NO$_3$]|Au is a metal-air battery and the prototype battery achieved ca. 1.6 V OCV for 1,200 seconds. The main discharge reactions involved are as follows:[1]

Anode

$$2Mg_{(s)} + 4OH^-_{(aq)} \rightarrow 2Mg(OH)_{2(s)} + 4e^- \quad (E = -2.69 \text{ V})$$

Cathode

$$O_{2(g)} + 2H_2O_{(l)} + 4e^- \rightarrow 4OH^-_{(aq)} \quad (E = 0.40 \text{ V})$$

Overall reaction

$$2Mg_{(s)} + O_{2(g)} + 2H_2O_{(l)} \rightarrow 2Mg(OH)_{2(s)} \quad (E_{cell} = 3.09 \text{ V})$$
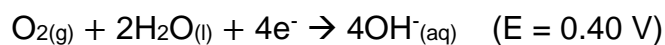
Therefore, oxygen (from the air) or in this case an oxygen gas cannister, has an important role in the overall reaction of this battery system and can already be seen to impact the behaviour of the battery, as evidenced by **Figure 27**. After the oxygen inlet was switched on (at 500 seconds) the potential of the battery slightly increased and plateaued for the duration of the measurement.

The LSV of the prototype battery was then conducted because LSV is a powerful and popular electrochemical technique commonly employed to investigate the reduction and oxidation processes of molecular species. LSV is also invaluable for studying electron transfer-initiated chemical reactions, including catalysis.[218] Therefore, the LSV of the prototype battery first depicted by **Figure 26**, is represented in **Figure 28**.
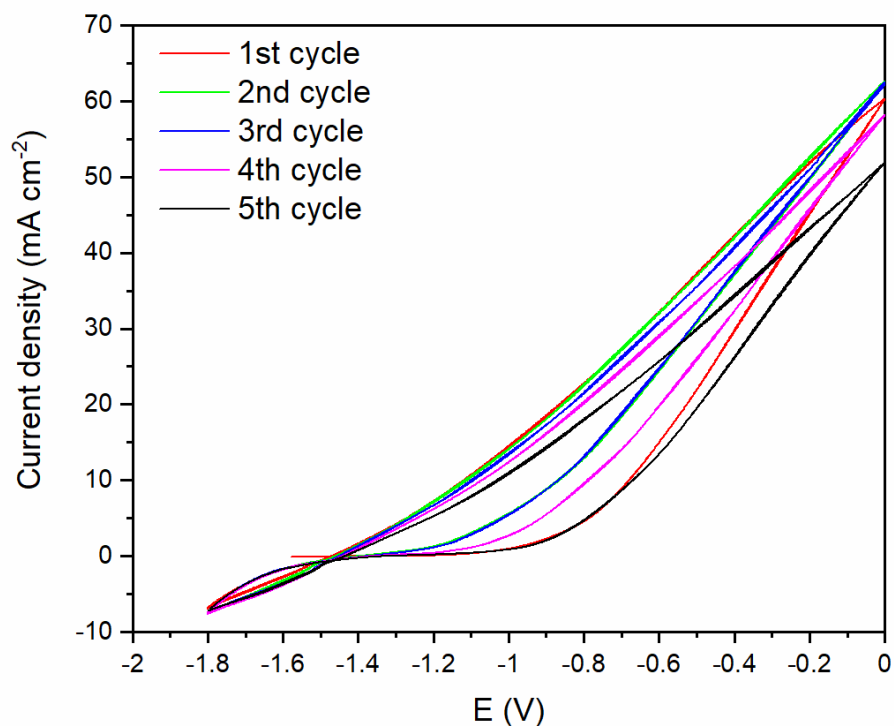


**Figure 28.** Linear sweep voltammogram of the prototype battery where the working electrode is the Mg AZ31 alloy, reference electrode the Ag-AgCl and counter electrode the coiled Au wire. Five cycles, coloured correspondingly, were taken at a slow scan rate of 10 mV S$^{-1}$.

The voltammogram of the prototype battery indicated by **Figure 28** highlight the processes occurring at the Mg AZ31 alloy electrode. Firstly, that the current density of the Mg electrode during the 1st cycle is lower than that of subsequent cycles (e.g. 2nd, 3rd and 4th cycles). Since this is the case, we can assume that the Mg electrode was being activated likely due to an increase in surface area from the stripping and deposition of Mg. However, this trend did not continue as subsequent sweeps of the battery indicate a decrease in current density after the 2nd sweep, until the final 5th sweep had a current density lower than that of the initial 1st sweep. Therefore, the surface of the Mg electrode is slowly being deactivated, likely due to Mg ions at the surface reaching saturation limits and beginning to precipitate into thin films on the surface or that a passivation layer is gradually forming on the surface of the electrode. When the Mg electrode's surface becomes passivated the internal resistance of the battery enhances, the passivation layer is electronically insulating and usually cannot be avoided, instead mitigated (e.g. design morphology of the electrode).

Moreover, after each cycle the forward and reverse sweeps of the voltammogram take on slightly different positions, indicating hysteresis. Paying attention to the 5th sweep, during the forward scan (anodic sweep) zero current density is observed between ca. − 1.4 and − 1 V, therefore, an overpotential of ca. 0.4 V is required before the reaction starts. This suggests sluggish kinetics possibly due to intermediate products, for instance magnesium nitrate[1] being forming when scanning negative (- 1.4 V) and removed when scanning positive (- 1 V).

Finally, the chronopotentiometry of the prototype battery was then investigated to observe the chemical kinetics at different current densities over multiple cycles and measure the decrease in voltage for the battery, furthermore, the inlet of oxygen was activated before experimentation to ensure that the prototype metal-air battery had a sufficient oxygen supply but deactivated when measurements were to be taken. Therefore, this would indicate the operational efficiency for the battery which would enable the results to then be compared with literature values, specifically the current density to power density relationship. **Table 2** summarises the final plateau voltage readings of the prototype battery at different current densities during its 1st cycle and the final 4th cycle. The current density of the prototype battery was approximated using the surface area from the Mg AZ31 alloy and Au coiled wire electrodes.

**Table 2.** A comparison of the voltage at different current densities from the 1st and 4th discharging cycle of the prototype battery.

| 1ˢᵗ Cycle | | 4ᵗʰ Cycle | |
|---|---|---|---|
| Current density (μA cm⁻²) | Voltage (V) | Current density (μA cm⁻²) | Voltage (V) |
| 0.56 | 1.432 | 0.56 | 1.325 |
| 2.79 | 1.392 | 2.79 | 1.269 |
| 5.57 | 1.352 | 5.57 | 1.214 |
| 11.14 | 1.299 | 11.14 | 1.142 |
| 27.86 | 1.177 | 27.86 | 1.045 |

At each current density the discharging of the prototype battery proceeded for 10 seconds before increasing in current density, after discharging at the current density of 27.86 μA cm⁻², the process was then repeated and the subsequent cycles started. Using the information from **Table 2** and then by following the equation (36):

$$P = \frac{UI}{V}$$
(36)

where $P$ is the volumetric power density (μW cm⁻³), $U$ depicts the plateau voltage (V) of the discharge curve, $I$ the discharge current (μA), and $V$ the working device volume (cm⁻³).[1] The current versus power density plot can be produced and is portrayed in **Figure 29**. Since the exact working device volume $V$ is unknown, the volume used were that of each electrode combined. In the case for the Au coiled wire, the calculation of the volume calculation assumed it was a cylinder. The approximated $V$ for the prototype battery is 0.168 cm³.

**(a)**

**(b)**
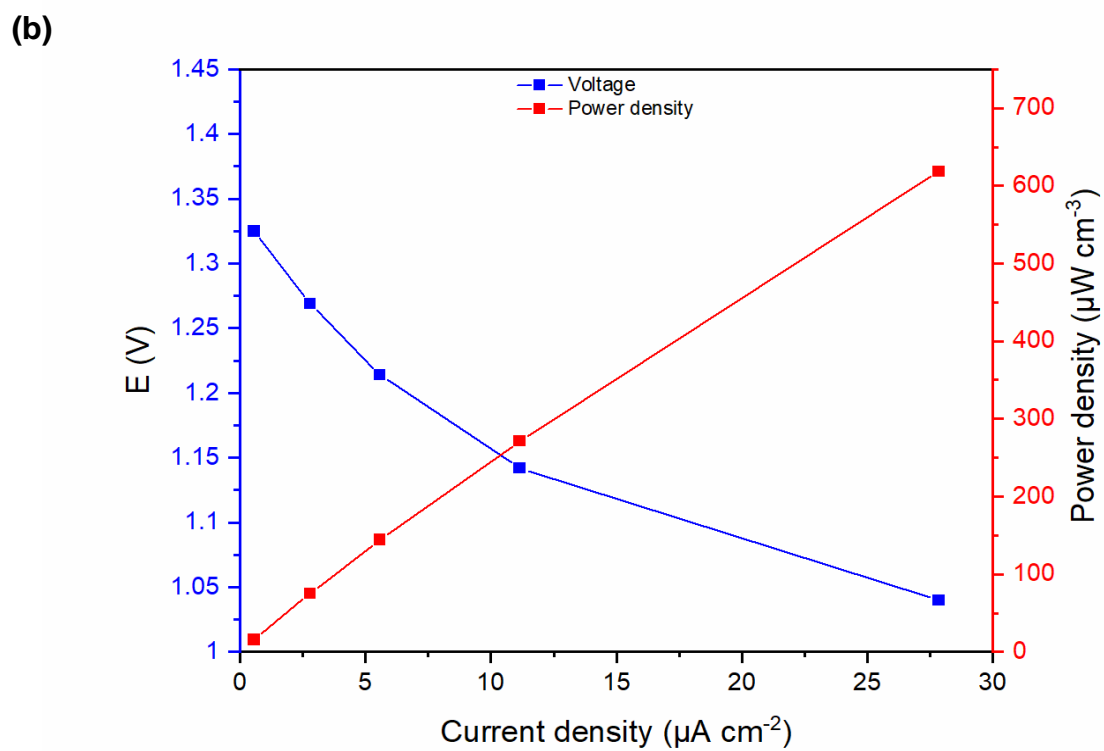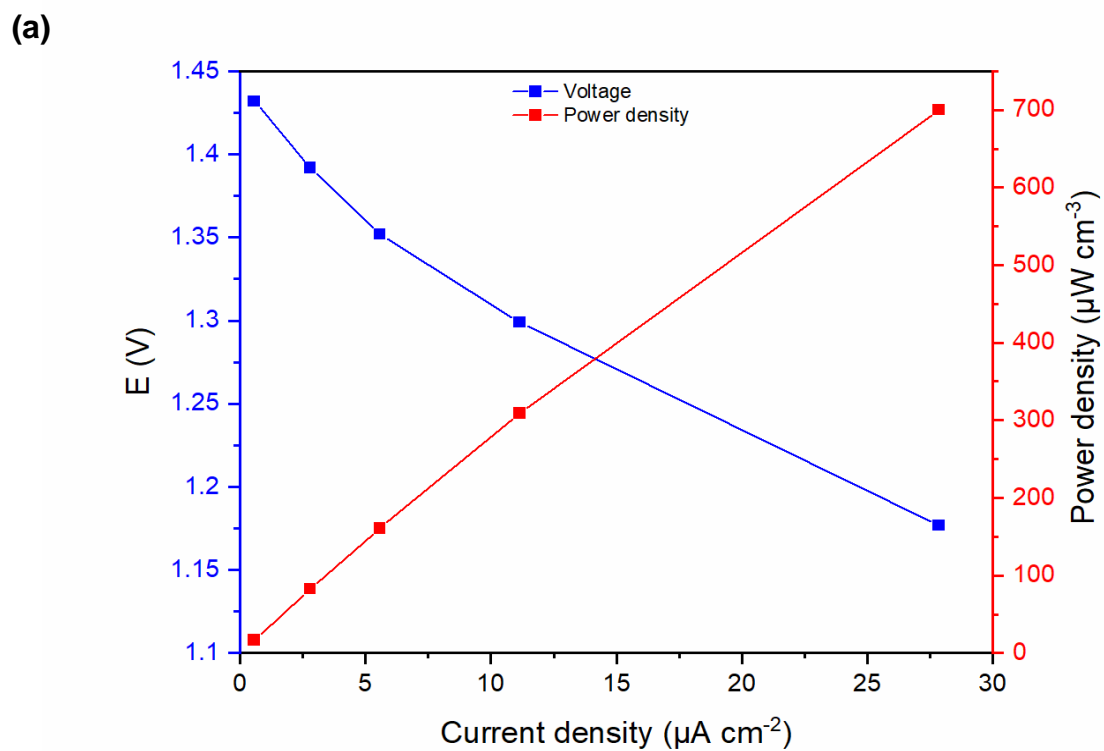
**Figure 29.** Prototype Mg-air battery's current versus power density. (a) depicts the 1st cycle and (b) depicts the 4th cycle, while the voltage Y-axis and plot are coloured blue and power density Y-axis and plot are coloured red.

From **Figure 29**, as the prototype battery undergoes discharge the overall voltage and power density both decrease concurrently. This characteristic is expected as it agrees with the literature, for instance, a battery which also utilises a Mg AZ31 alloy as the anode, however, polypyrrole−*para*(toluene sulfonic acid) (PPy-pTS) as the cathode and chitosan-[Ch][NO$_3$] as the polymer electrolyte reported similar findings.[116] The prototype battery fabricated here assisted with the consolidation toward the final battery design (discussed later in this work). The specific changes made from the prototype was the phase state of the electrolyte switching from liquid to solid, as the aim for this project is to reproduce potential TIMB devices, therefore, it must be possible for implantation within the human body and a solid-state battery can practically achieve this. In addition, the cathode (Au coiled wire) being replaced with a readily available Pt nanoparticle carbon cloth electrode for two primary reasons: to increase the surface area of the anode and because Pt is a better catalyst for the ORR. Pt is specifically optimal for metal-air batteries due to its low binding energy of O$_2$, optimising the kinetics within the electrochemical cell as established within the literature and portrayed by ORR volcano plots.[219, 220, 221] Furthermore, the Pt nanoparticle carbon cloth is also biocompatible (bioinert, like Au) so its use over Au is motivated by a performance rationality. Thus, the focus shifts on to the electrolyte which must possess electroactivity, biocompatibility and be robust enough to be considered for implantation within a human body.

The prototype battery provided experience of how the components of the battery operate. Although, an oxygen pump was incorporated and was shown to have a slight impact on the prototype battery's potential, it was likely unnecessary as there was sufficient access for oxygen (from the air) to diffuse into the IL. The OCV of the battery is at ca. 1.6 V and would provide the initial reference for comparison after the fabrication of the final battery is achieved. Additionally, the values for current and power density in **Figure 29** are like that of batteries utilising similar materials reported in the literature. The chronopotentiometry of the prototype battery highlights the depreciation of the battery when increasing current over multiple cycles, which also indicates the stability of the cell. Furthermore, after experimentation of the prototype battery, it became apparent utilising a coiled Au wire would not be ideal as a cathode for a battery powering TIMBs, due to its poor surface area. Thus, it was decided to replace the cathode material with a 2 mg/cm$^2$ Pt nanoparticle carbon cloth.

### 6.3 Polymer electrolyte

The PE film utilised in this work will act as the ion conducting separator between the two electrode terminals for the final battery design. The ion conducting separator's function is to prevent electrical short circuits while also allowing the transport of ionic charge carriers (e.g. choline and OH$^-$) that are

needed to close the circuit during the passage of current in an electrochemical cell. Since the PE involves the combination of SF and [Ch][NO$_3$] IL, experimental techniques will be used to confirm the characteristics of the materials involved and provide verification of the applicability of the PE film for use in batteries. It is well-known SF and [Ch][NO$_3$] IL is biocompatible,[11, 222, 223] thus *in vitro* and *in vivo* experiments were not concluded, and experimentation instead focused on SF immobilising the IL to produce ionically conductive films to behave as a PE. The reason for this is because the PE is an integral component for the purpose and functionality of the batteries used in this study. Therefore, the characterisation of the SF, IL and consequently the PE is important.

Firstly, the FTIR spectroscopy of SF, IL and PE have been conducted and portrayed in **Figure 30** and **31**, with variants of the PE utilised (1:1 wt ratio of SF:IL and a 1:3 wt ratio of SF:IL) to understand the importance of variations in the ratio of the components.
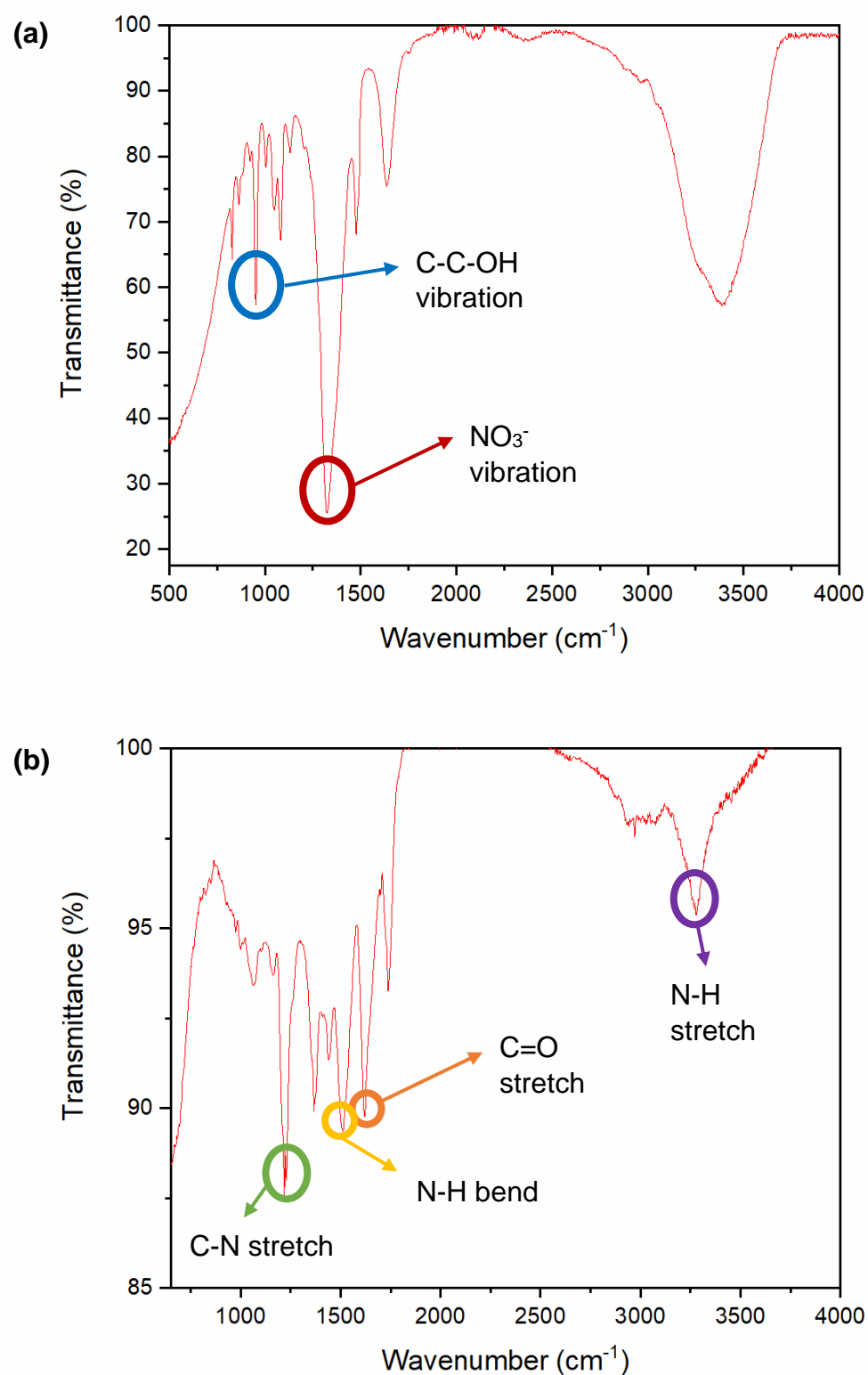
**Figure 30.** (a) FTIR spectroscopy of the [Ch][NO$_3$] IL solution. Strong band at 1330 cm$^{-1}$ for vibrations of NO$_3^-$ and 954 cm$^{-1}$ for vibrations of C-C-OH, characteristic of the IL.[1, 154] (b) FTIR spectroscopy of

the *B. mori* SF film. Peaks observed with wavelengths of 1625 to 1690 cm$^{-1}$ depict a C=O stretch, 1520 to 1550 cm$^{-1}$ N-H deformation, 1219 to 1313 cm$^{-1}$ C-N stretch and 3250 to 3300 cm$^{-1}$ a N-H stretch, are characteristic of *B. mori* SF.[1, 224, 225]
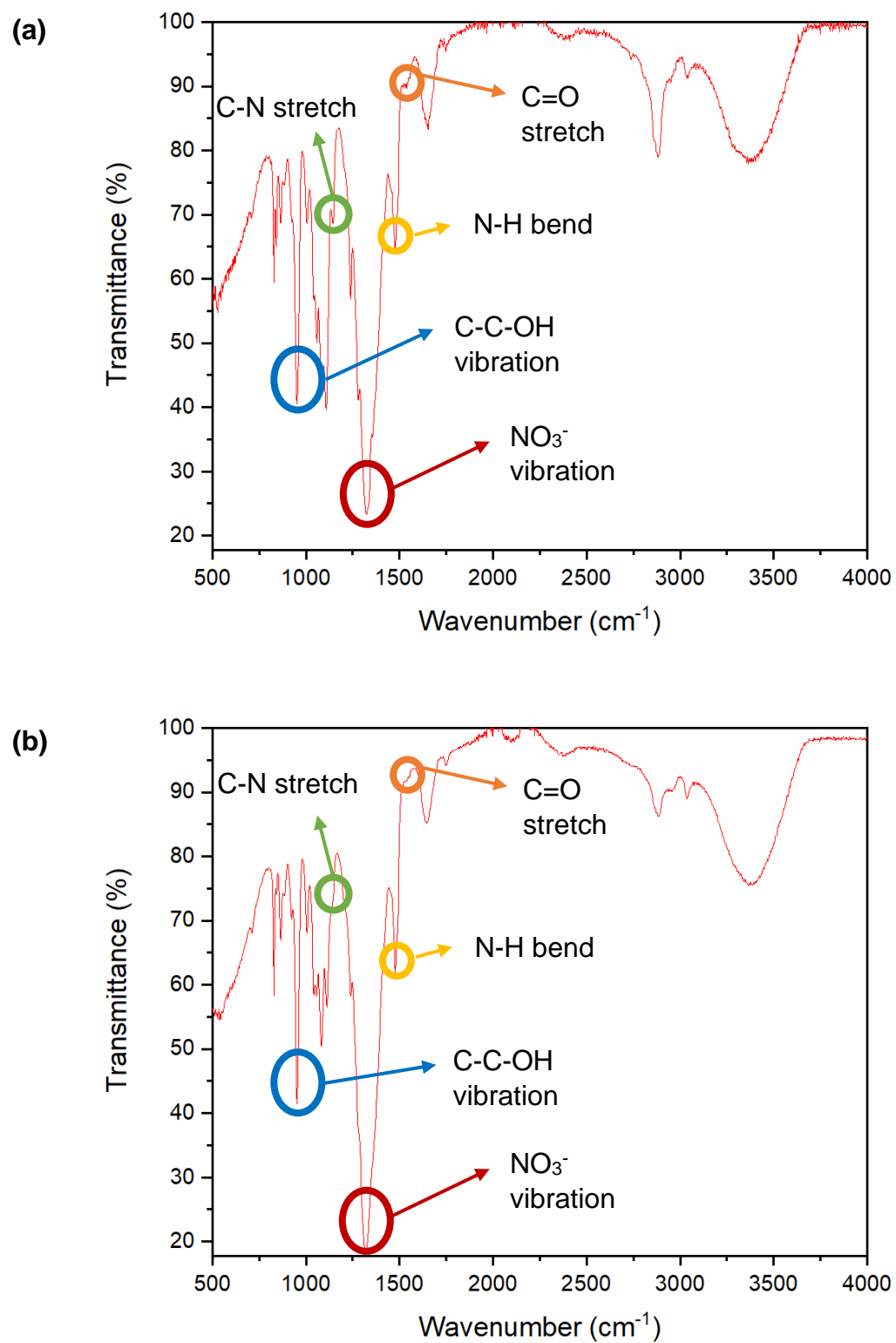
**Figure 31.** (a) FTIR spectroscopy of the 1:1 wt ratio of SF:IL PE film. The absorbance bands characteristic of the IL are clearly observed at 1330 cm$^{-1}$ for vibrations of $NO_3^-$ and 954 cm$^{-1}$ for

vibrations of C-C-OH. In addition, there is evidence of peaks at 1625 to 1690 cm$^{-1}$ characteristic of a C=O stretch, 1520 to 1550 cm$^{-1}$ N-H bending and 1219 to 1313 cm$^{-1}$ C-N stretch, which are characteristic of *B. mori* SF.[1] (b) FTIR spectroscopy of the 1:3 wt ratio of SF:IL PE film. Similar to **Figure 31(a)**, the absorbance bands indicative of the IL are clearly observed at 1330 cm$^{-1}$ for vibrations of NO$_3^-$ and 954 cm$^{-1}$ for vibrations of C-C-OH. However, the evidence for peaks at 1625 to 1690 cm$^{-1}$ are characteristic of a C=O stretch, 1520 to 1550 cm$^{-1}$ N-H bending and 1219 to 1313 cm$^{-1}$ C-N stretch, which are characteristic of *B. mori* SF, are less obvious from the plot.[1]

From **Figure 30** and **31** depicting the FTIR spectra of the SF, IL and PEs (1:1 and 1:3 wt ratio), it is clear that the samples possess the desired characteristic functional groups of the individual components from the IL and SF. SF is a complex macromolecule and, as discussed earlier, exhibits a range of different conformations (e.g. α-helix, β-sheet, β-turns, random coils and 3$_{10}$-helix),[224] which can affect the proteins properties (e.g. its solubility, stability and tensile strength) and the FTIR spectra alone would not conclusively determine the molecular conformations adopted in the PE material.[11, 212] Therefore, the XRD of the PE in its liquid state and solid (film) state were conducted, the results of which are depicted in **Figure 32** and **33**.
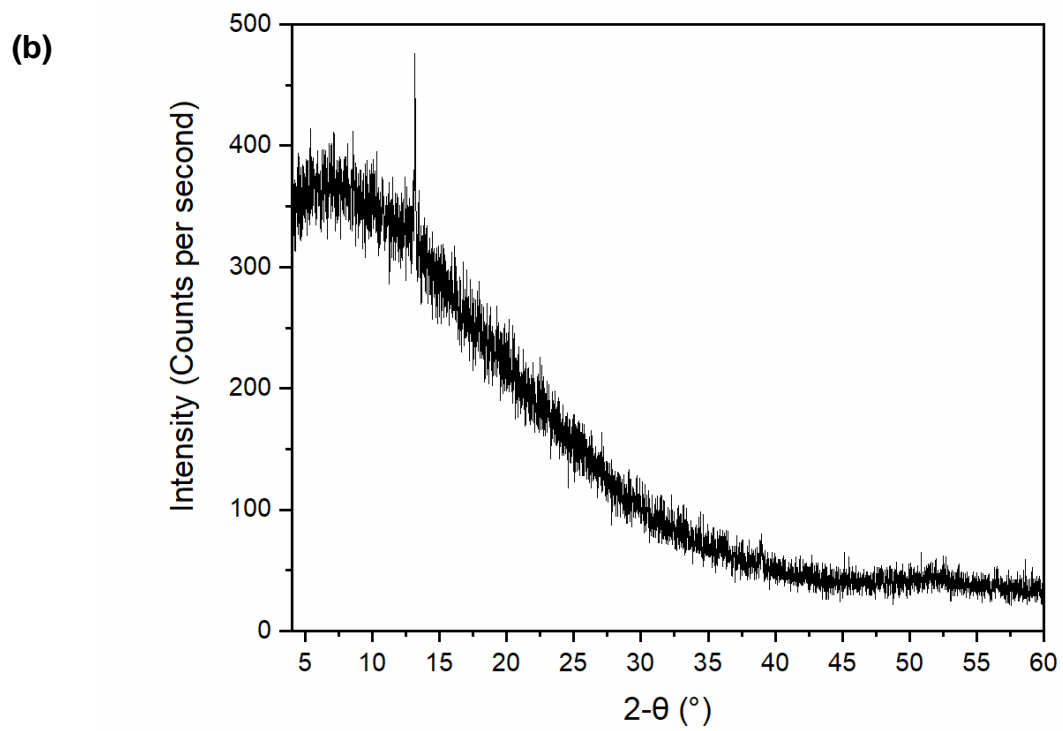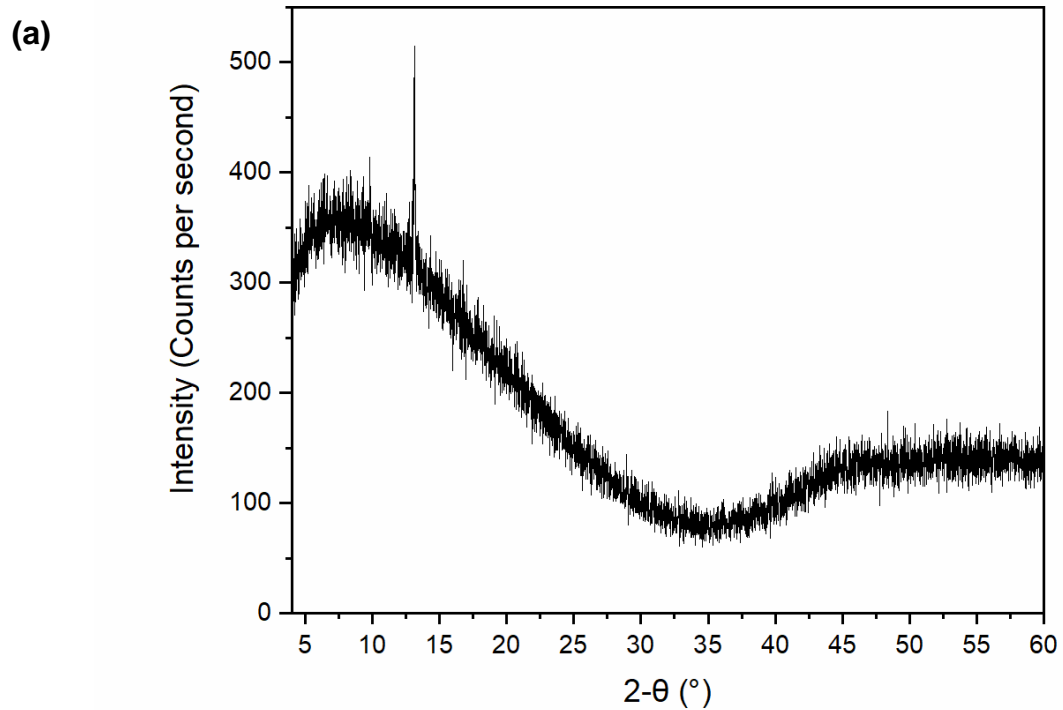
**Figure 32**. (a) XRD of the 1:1 SF:IL PE in the liquid state. The diffractogram indicates a broad peak at ca. 8 ° 2-θ and a sharp peak at ca. 13 ° 2-θ, indicative of amorphous β-sheets and a crystalline β-turn

conformation, respectively.[159, 225, 226] Furthermore, the presence of these peaks suggest evidence for silk I (13 ° 2-θ) and a silk II (8 ° 2-θ) structure.[227] (b) XRD of the 1:1 SF:IL PE in the solid (film) state. Like **Figure 32(a)**, the diffractogram indicates a broad peak at ca. 8 ° 2-θ and a sharp peak at ca. 13 ° 2-θ, indicative of amorphous β-sheets and a crystalline β-turn conformation, respectively.[159, 225, 226] In addition, there also appears to be a depression in the observed peaks between 40 to 60 ° 2-θ, suggesting that the [Ch][NO$_3$] IL contributes to the peaks (within the same range) observed in **Figure 32(a)**.
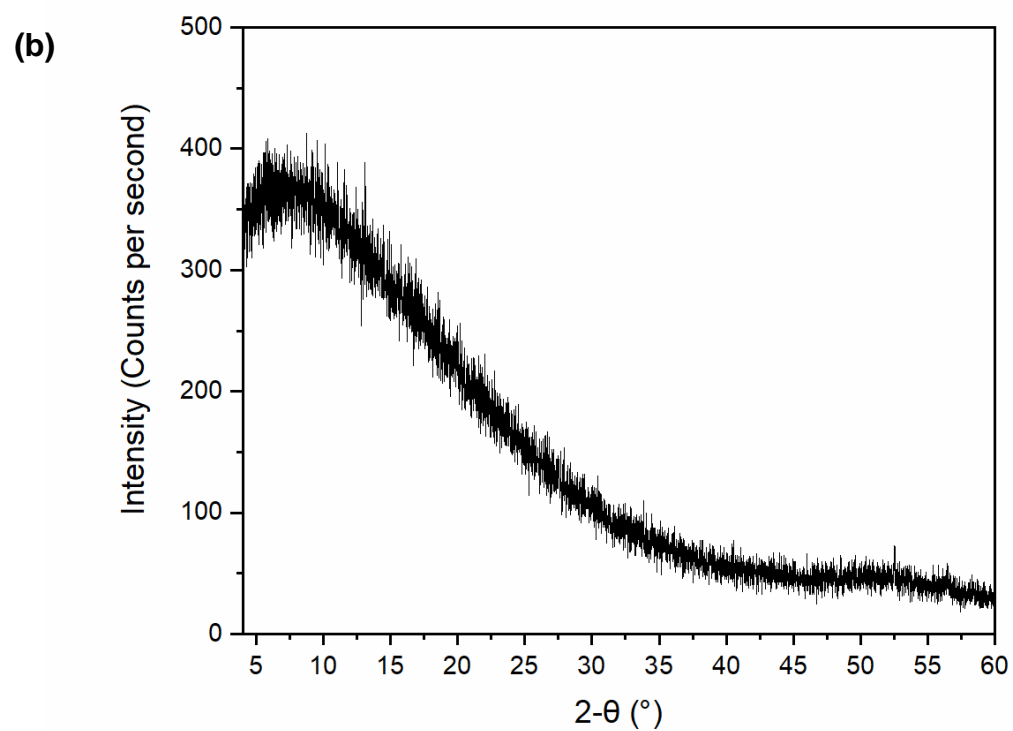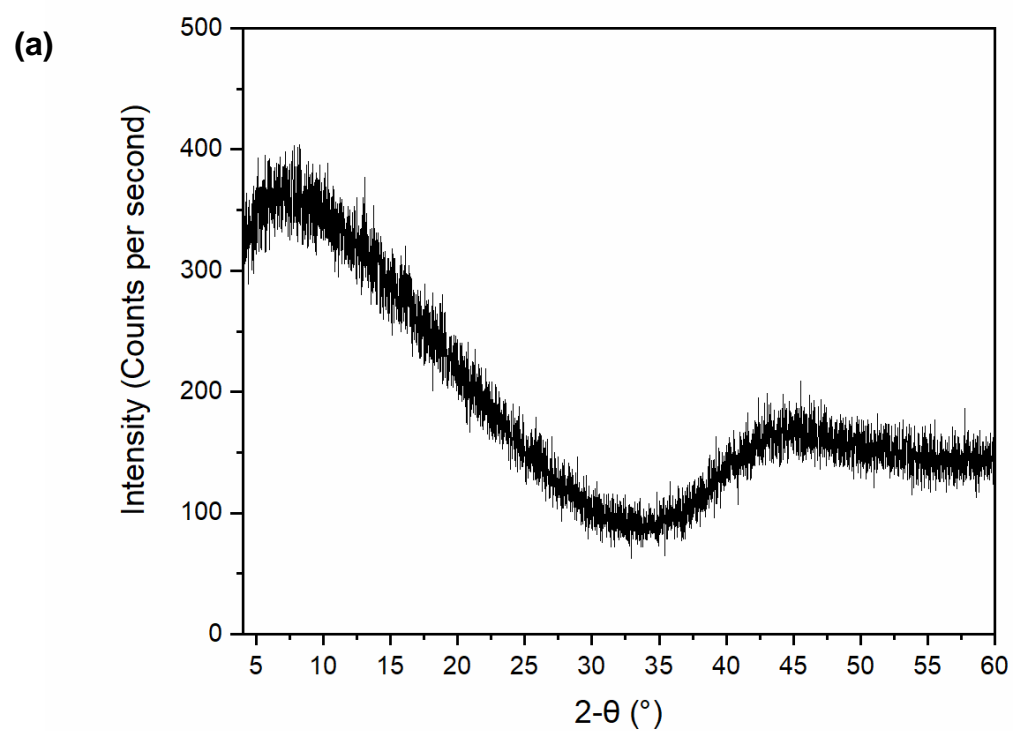
**Figure 33**. (a) XRD of the 1:3 SF:IL PE in the liquid state. The diffractogram indicates a broad peak at ca. 8 ° 2-θ, indicative of amorphous β-sheets.[159, 225, 226] However, there appears to be no obvious 13 °

2-θ peak. Furthermore, the peaks between 40 to 60 ° 2-θ appear more intense compared to the peaks (within the same range) first observed in **Figure 32(a)** which may be indicative to the IL presence since there is a greater concentration of IL in the 1:3 SF:IL PE versus the 1:1 SF:IL PE. (b) XRD of the 1:3 SF:IL PE in the solid (film) state. Like **Figure 33(a)**, the diffractogram indicates a broad peak at ca. 8 ° 2-θ, indicative of amorphous β-sheets.[159, 225, 226] In addition, there appears to be no obvious 13 ° 2-θ peak. However, there appears to be a depression in the observed peaks between 40 to 60 ° 2-θ, also observed in **Figure 32(b)**.

XRD is a useful method to determine the crystallographic structure of a material. Here, XRD was conducted to confirm the conformational information with the assistance of FTIR spectroscopy, depicting the present functional groups. The XRD diffractograms indicate peaks at ca. 8 ° 2-θ and at ca. 13 ° 2-θ, commonly found in silk I and silk II, signifying it is heterogeneous.[159, 225, 226, 227] The FTIR spectroscopy of the SF:IL PE film possesses peaks with wavelengths of 1625 to 1690 cm$^{-1}$ indicative of amide I, 1520 to 1550 cm$^{-1}$ amide II, 1219 to 1313 cm$^{-1}$ amide III and 3250 to 3300 cm$^{-1}$ fluctuations due to hydrogen bonds.[227, 228] Consequently, these FTIR peaks are for β-turns and β-sheets, α-helices and random coils, supported by the XRD diffractograms possessing the indicative peaks at 8 ° 2-θ and 13 ° 2-θ, which are characteristic for the silk I and silk II form.[159, 224, 225, 226, 227, 228]

Moreover, **Figure 32(a)** and **33(a)** indicate peaks not normally found in regenerated SF, specifically, in the range of 40 to 60 ° 2-θ. Since the XRDs were conducted for the PEs, it can be inferred using information from the literature that these peaks are not from the SF and that the IL contributed to these peaks. Since these peaks are not present when the PEs are in the solid (film) state (**Figure 32(b)** and **33(b)**), the loss/reduction of the IL also portrays the reduction of these peaks. Previous XD studies of chitosan and SF composites have shown diffractograms possessing the indicative peaks of each component,[229, 230] therefore, this is likely to be what is observed in **Figure 32** and **33**.

In the diffractograms of the 1:3 SF:IL PEs in **Figure 33**, the sharp peak at ca. 13 ° 2-θ previously observed (**Figure 32**) is no longer obviously present, implying that no crystalline β-turn conformations are present. However, the noise of the lines plotted in **Figure 32** and **33** makes it difficult to distinguish subtle peaks, and therefore the disappearance or reduction of this peak could be attributed to the addition of more [Ch][NO$_3$] IL, affecting the SF secondary structure, or simply masking the peak. Untreated SF films also exhibit a broad peak at 20 ° 2-θ which is a typical characteristic pattern of an amorphous silk material,[159] however, this broad peak at 20 ° 2-θ is not observable in **Figure 32** and **33**, suggesting the ILs affect the XRD diffractograms of materials after mixing in line with the literature.[231]

Understanding how the bulk material properties change in specific environmental conditions, (such as exposure to ILs or water) is important for various applications of the materials. SF possess both hydrophobic and hydrophilic regions with a block copolymer-like structure,[232] and solvents like water interact with the SF protein structure. Water molecules can potentially cause a plasticising effect on SF-based materials, altering molecular interactions and impacting the mechanical properties of the material.[188, 233] In addition, previous work has shown that when silk films are treated with methanol, there is a significant increase in β-sheet content.[234] Consequently, it is important to understand how silk film material properties change with respect to this change in β-sheet content. For instance, this information is important for the design of silk-based devices destined for *in vivo* applications, such as TIMBs and biocompatible and biodegradable batteries.[1] Therefore, understanding how the water content and organisation of SF secondary structure contributes to changes in material properties, and in our case, how the water content affects the PE films.

The PE films, 1:1 SF:IL and 1:3 SF:IL, had their water content determined via TGA because the water content confined within the PE composites can act as a proton source to support the ORR at the cathode.[160] The averaged (from three repeated experiments) TGA curves are represented in **Figure 34**.
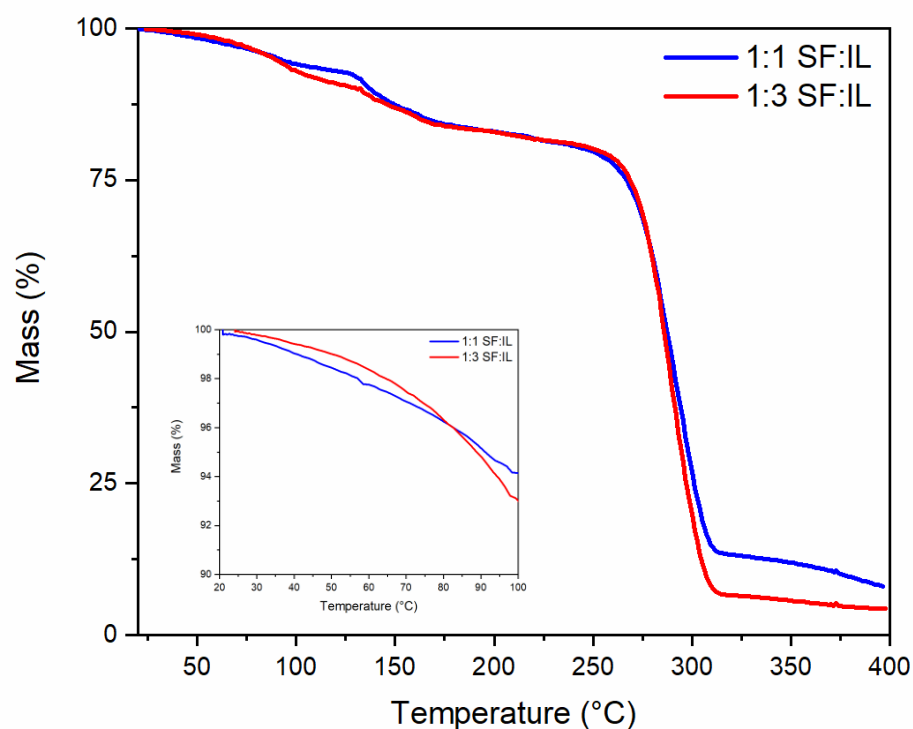
**Figure 34.** Averaged TGA curves for the PE 1:1 and 1:3 films, blue and red lines, respectively. The heating was conducted under a nitrogen atmosphere at a rate of 5 °C min^{-1}. The inset portrays the expanded view (20 to 100 °C) of the averaged TGA curves for PE 1:1 and 1:3, blue and red lines, respectively.

From **Figure 34**, the approximate water content confined within the PE composites is 6 % by weight for the 1:1 PE film and 7 % by weight for the 1:3 PE film. This is approximated by assuming the weight loss up to 100 °C is entirely water. The water content obtained is consistent with similar materials reported in the literature.[1, 116] The information from **Figure 34** is particularly important, because it validates the computational model of SF in its hydrated state possessing ca. 7.5 wt % water, mentioned previously. Furthermore, the thermal decomposition of silk I crystals have been reported to occur at ca. 260 °C, whereas silk II begins thermal decomposition at ca. 286 °C.[163] Paying attention to the TGA curves conducted on the PE films, specifically at around 260 °C, the PE material begins significant weight loss (thermal decomposition), therefore indicating silk I form characteristic which is in agreement with the literature and the SF crystal models reported previously in this work.

Finally, the PE composites assembled for the batteries (primary Mg- or Zn-air battery) initially underwent PEIS, and their averaged (from three repeated experiments) Nyquist plots are depicted in

**Figure 35** and **36**. The ionic conductivity of the PE composite films were then estimated using the following equation (32):

$$\sigma = \frac{d}{RA} \tag{32}$$

where $\sigma$ is the conductivity (S cm$^{-1}$), $d$ the thickness of the film (cm), $R$ is the bulk resistance ($\Omega$) obtained from the first intercept on the X-axis of the complex plane, and $A$ is the contact area (cm$^2$).[116] Where the measurements never intercepts the X-axis, the $R$ values were approximated via extrapolation as they would not likely deviate much from a linear slope for the missing datapoints.[116]
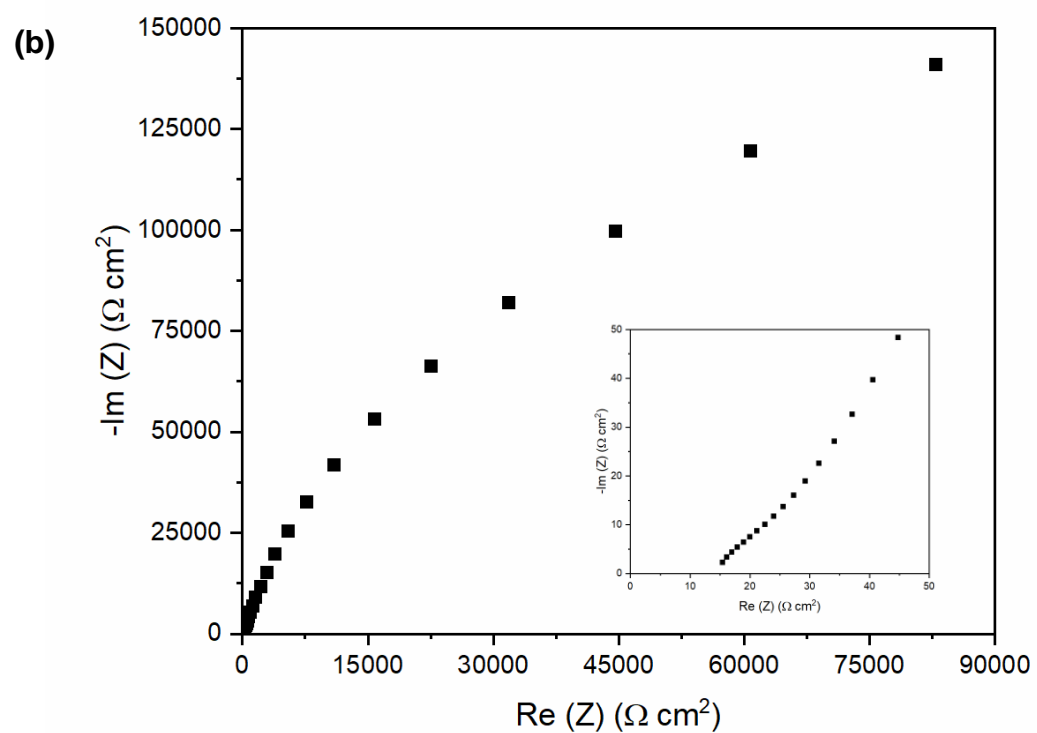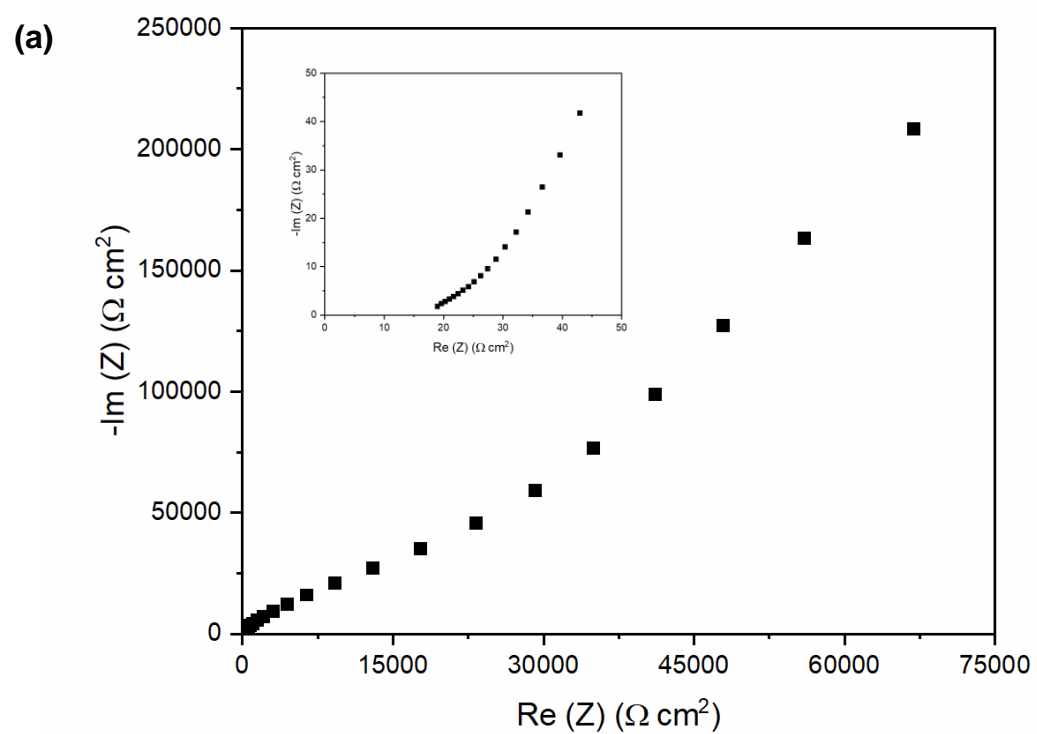
**Figure 35.** (a) PEIS spectra of the 1:1 PE assembled in the primary Mg-air battery. The inset portrays the spectra in an expanded view of the high frequency region. (b) PEIS spectra of the 1:3 PE

assembled in the primary Mg-air battery. The inset portrays the spectra in an expanded view of the high frequency region.
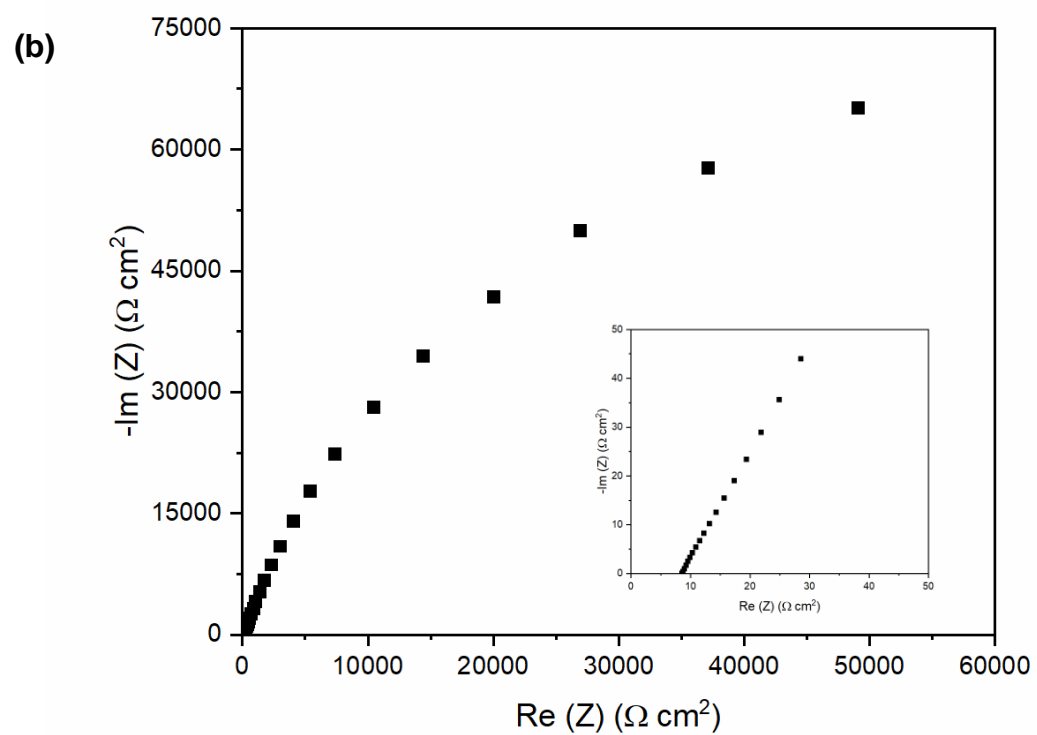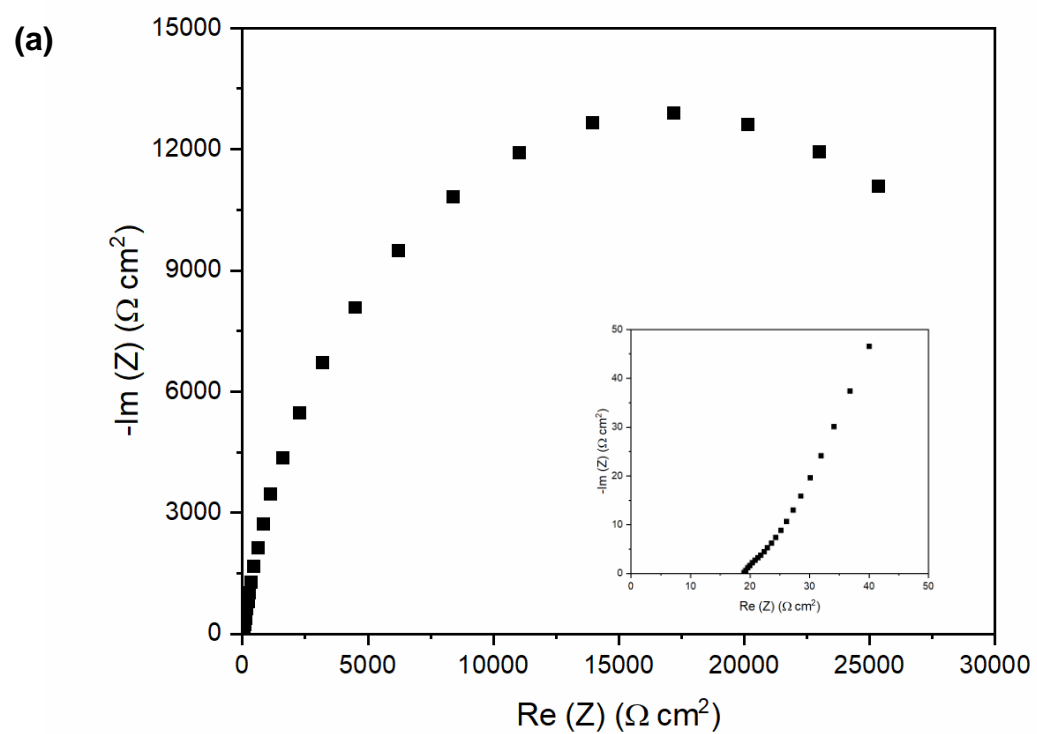
**Figure 36.** (a) PEIS spectra of the 1:1 PE assembled in the primary Zn-air battery. The inset portrays the spectra in an expanded view of the high frequency region. (b) PEIS spectra of the 1:3 PE

assembled in the primary Zn-air battery. The inset portrays the spectra in an expanded view of the high frequency region.

The average thickness of the PE composites used to interpret the spectra portrayed in **Figure 35** and **36** is ca. 0.05 cm and the contact surface area for the electrodes and PEs is ca. 0.79 cm$^2$. By using equation (32) and the information from **Figure 35** and **36**, the average ionic conductivity for the 1:1 PE film is 3.55 mS cm$^{-1}$ (3.74 mS cm$^{-1}$ for the Mg anode battery and 3.35 mS cm$^{-1}$ for the Zn anode battery) and for the 1:3 PE film it is 6.43 mS cm$^{-1}$ (4.90 mS cm$^{-1}$ for the Mg anode battery and 7.96 mS cm$^{-1}$ for the Zn anode battery). The conductivity values for the PE composites are in agreement with the literature (3.4 mS cm$^{-1}$ of a similar PE reported in the literature)[1] and would satisfy the conductivity requirements for many battery applications.[1, 116]

The presence of SF and IL in the PE films have been confirmed via FTIR and XRD spectroscopy. Due to TGA, the water content of the PE films was found to be averaged at 6 and 7 % for the 1:1 and 1:3 PE films, respectively, which is similar to the water content incorporated into the SF crystal model for computational studies. In addition, TGA also showed the presence of silk I form for the PE films. Lastly, PEIS was conducted on the batteries assembled with the PE films and using equation (32) it was determined that the average ionic conductivity of the 1:1 SF:IL PE film was 3.55 mS cm$^{-1}$ and for the 1:3 SF:IL PE film 6.43 mS cm$^{-1}$. Once the ionic conductivity of the PE composites was confirmed, the films were assembled in batteries with Mg or Zn foil anodes, and their discharge profiles were recorded and compared with the literature.

### 6.4 Polymer electrolyte utilised in primary magnesium-air battery

Metal-air batteries (e.g. Mg-air) have received much attention recently[235] because of their advantageous electrochemical properties. For instance, Mg possesses a high theoretical volumetric capacity of 3,833 mAh cm$^{-3}$ and low reduction potential of - 2.37 V versus the SHE.[235] In addition, Mg-based-air batteries possesses a theoretical energy density of 6.80 kW h kg$^{-1}$.[235, 236, 237] Furthermore, Mg is biocompatible and Mg$^{2+}$ ions can be absorbed by the body.[238] However, Mg-air batteries can suffer from high polarisation and low coulombic efficiency, typically caused by corrosion arising from the reaction of Mg and the electrolyte and the sluggish kinetics of the ORR on the Pt cathode.[239] Mg deposition and dissolution processes in polar organic electrolytes may lead to the formation of a passivation film with an insulating effect towards Mg$^{2+}$ ions.[239] Nevertheless, the alloy Mg AZ31, was chosen as the Mg anode material in this study's battery due to its favourable biocompatibility and biodegradability.[1, 240]

A photograph of the SF:IL PE film fabricated and prepared for utilisation within the battery is depicted in **Figure 37**. In addition, a photograph of the final battery assembly is depicted by **Figure 38**. Furthermore, the 1 mm drilled air holes seen in **Figure 37** and **38** were not initially incorporated within the final battery design (**Figure 17**) but were later added to optimise the oxygen from the air reaching the working components within the battery once assembled.
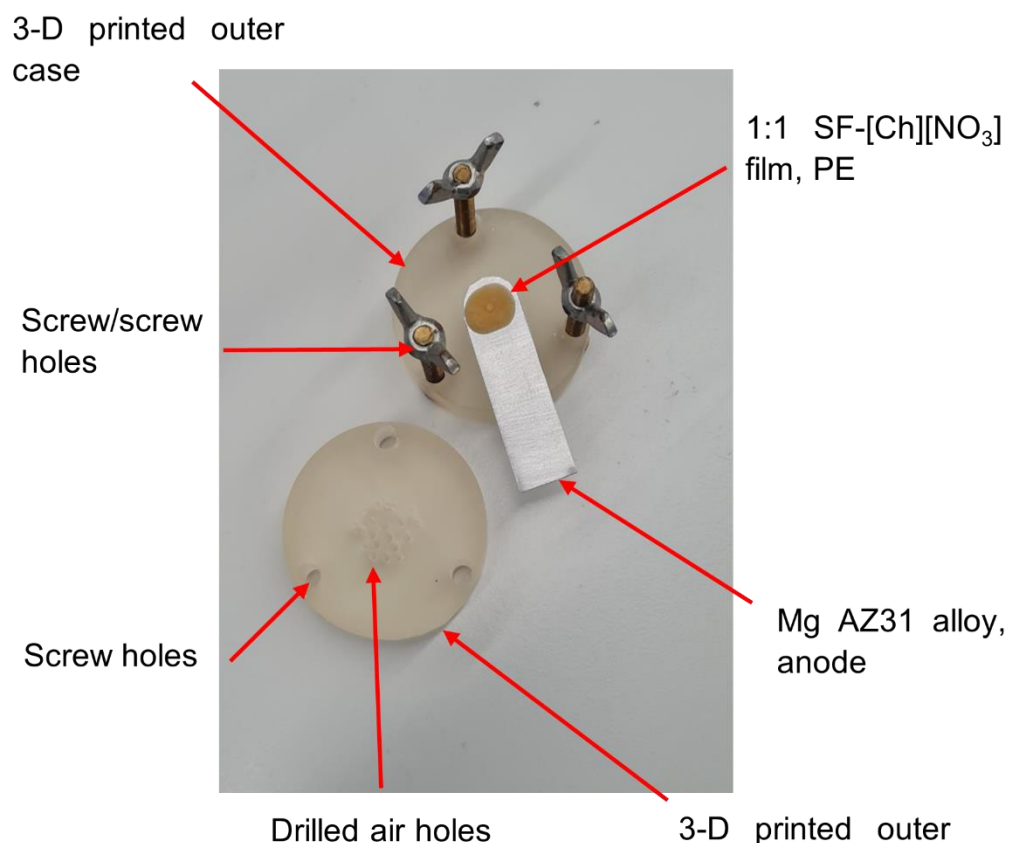


**Figure 37.** Picture of the 1:1 SF:IL PE film on top of the Mg AZ31 alloy as the anode. Labelled correspondingly by the red arrows.

Before the measurements were taken via experimentation of the battery, areas of the anode foil around the PE film were taped using clear Sellotape, preventing the two terminals (anode and cathode) from contacting one another.
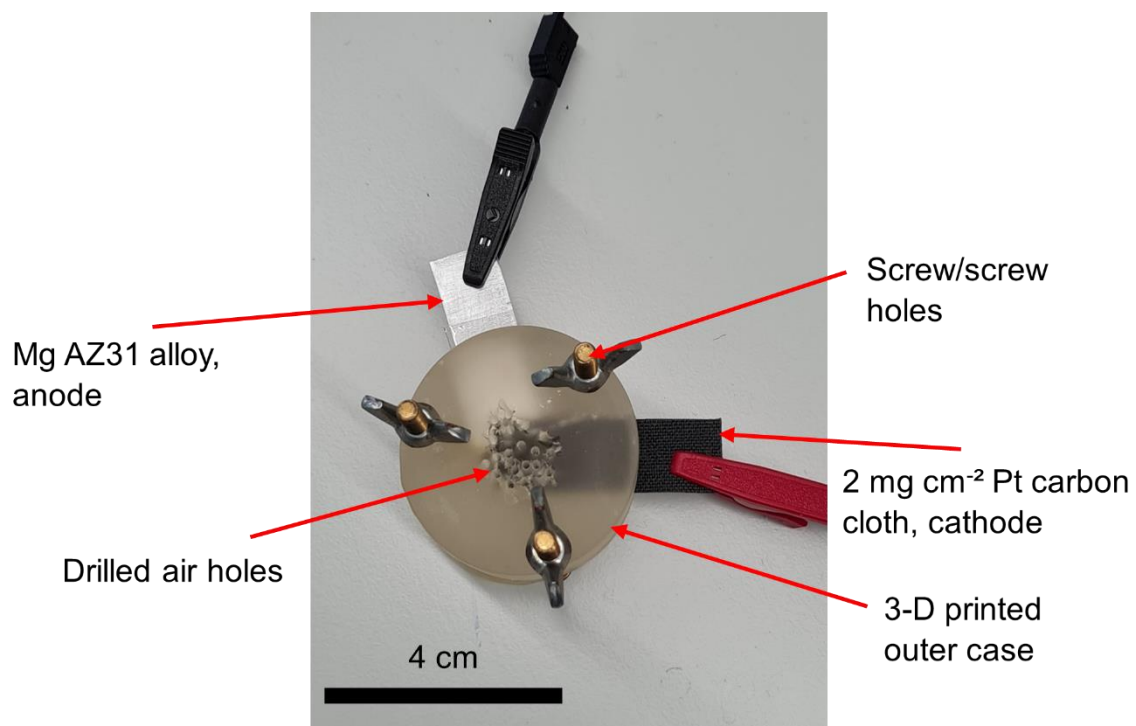
**Figure 38.** Picture of a final battery assembled utilising Mg AZ31 alloy as the anode with the PE sandwiched between the anode and cathode. The outer case protects the working components of the battery secured by the screws in the screw holes. Labelled correspondingly by the red arrows.

The averaged (from three repeated experiments) discharge performance of the primary Mg-air battery, utilising the [Ch][NO$_3$] IL immobilised by SF as electrolyte, is represented in **Figure 39**.
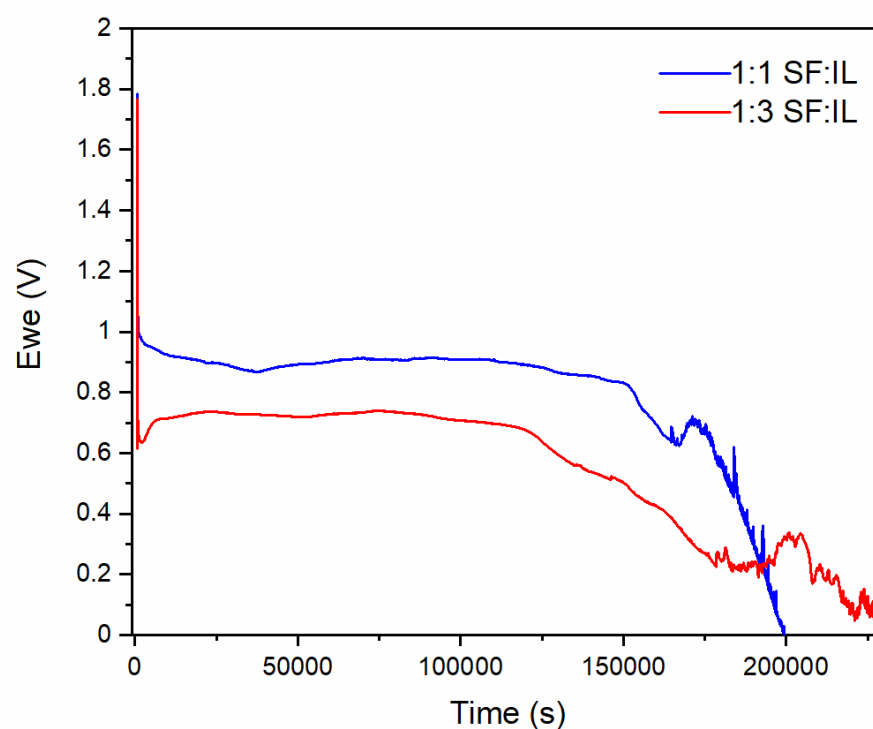
**Figure 39.** Discharge performance of the primary Mg-air battery using the 1:1 SF:IL PE (blue line) and the 1:3 SF:IL PE (red line) at a current density of ca. 25 µA cm$^{-2}$.

The OCV (V) for the Mg 1:1 SF:IL and 1:3 SF:IL batteries were in the range of 1.8 and 1.7 V just after fabrication. The cell voltage decreased immediately when a discharge current was applied, likely due to the battery's internal resistance, and soon reached a plateau. At a current density of ca. 25 µA cm$^{-2}$ the 1:1 SF:IL battery displayed a capacity of 0.84 mAh cm$^{-2}$, whereas the 1:3 SF:IL battery displayed a capacity of 0.68 mAh cm$^{-2}$. The plateau voltage (approximately the middle point of the discharge curve) for the 1:1 SF:IL battery was ca. 0.9 V and for the 1:3 SF:IL battery was ca. 0.7 V. The specific volumetric power density of the batteries were calculated from the discharge curves in **Figure 39** using equation (36):

$$P = \frac{UI}{V} \tag{36}$$

where $P$ is the volumetric power density (W L$^{-1}$), $U$ depicts the plateau voltage (V) of the discharge curve, $I$ the discharge current (A), and $V$ the working device volume (L).[1] The $V$ of the SF:IL Mg-air battery is $1.065 \times 10^{-4}$ L.

The 1:1 SF:IL battery could deliver a volumetric power density of 0.17 W L$^{-1}$ and an energy density of 7.18 Wh L$^{-1}$. As for the 1:3 SF:IL battery, it could deliver a volumetric power density of 0.14 W L$^{-1}$ and an energy density of 4.66 Wh L$^{-1}$. When compared to the literature, these batteries demonstrated similar capacities but at greater current densities. For instance, an unsealed primary Mg-air battery using nanoparticles of Au as the cathode instead of Pt and with similar electrolyte, reported a capacity of 1.43 mAh cm$^{-2}$ at a current density of 10 µA cm$^{-2}$.[1] The 1:1 SF:IL and 1:3 SF:IL batteries reported here demonstrated capacities of 0.84 mAh cm$^{-2}$ and 0.68 mAh cm$^{-2}$, respectively, at a current density of ca. 25 µA cm$^{-2}$. Furthermore, the power offered from the 1:1 SF:IL PE battery at 23.33 µW cm$^{-2}$ and from the 1:3 SF:IL PE battery at 18.72 µW cm$^{-2}$ may fulfil the requirements for average consumption of published implantable biomedical devices (e.g. wireless implantable sensing systems).[35, 240]

To further investigate and evaluate the performance of the 1:1 and 1:3 SF:IL PEs utilised in these batteries, the averaged (from three repeated experiments) discharge performance of the batteries with varying current applied was conducted and reported in **Figure 40**.
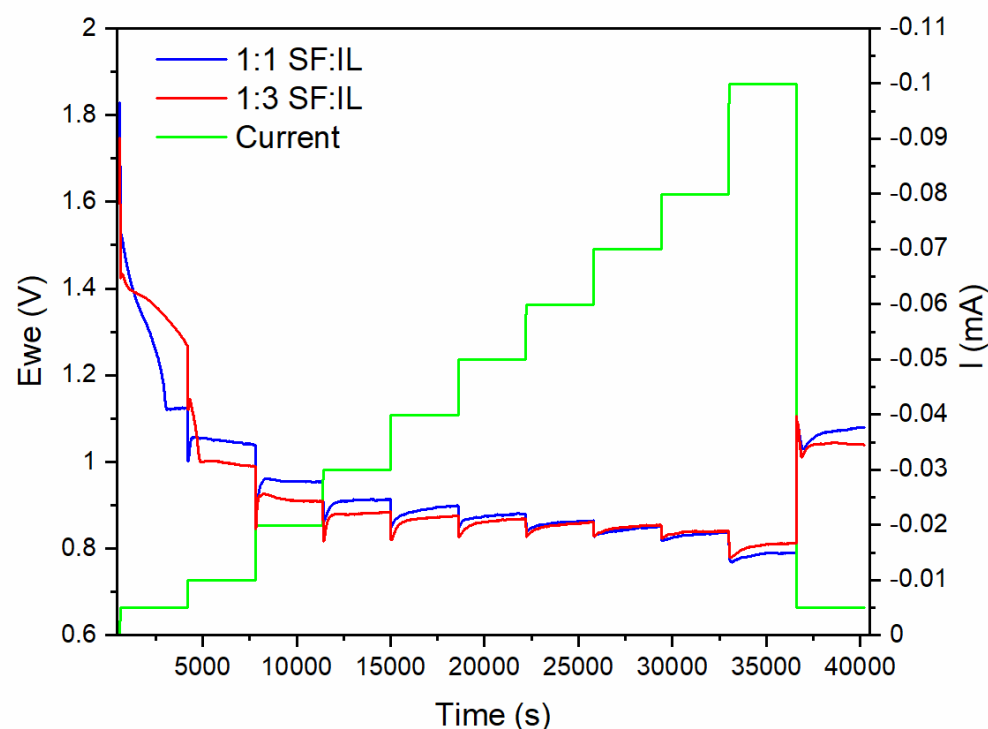
**Figure 40.** Discharge performance of the primary Mg-air battery using the 1:1 SF:IL PE (blue line) and the 1:3 SF:IL PE (red line) at varying current (green line) applied.

From **Figure 40** the performance of each battery with 1:1 SF:IL or 1:3 SF:IL as electrolyte is similar within the current range of 0 to 100 µA in the time frame of ca. 11 hours. Therefore, using the **Figure 39** and **40** it is suggested the main difference between 1:1 SF:IL and 1:3 SF:IL as a PE in these batteries is the capacity, with the 1:1 SF:IL PE battery possessing a greater capacity. In addition, the ionic conductivity of the 1:3 SF:IL PE is greater than that of the 1:1 SF:IL PE just after battery assembly, as previously mentioned. As a result, it could be determined that with greater concentration of the [Ch][NO$_3$] IL in the PE film, you can expect a more ionic conductive material but a battery using this as an electrolyte could possess lower capacity than that with a PE with a lower concentration. Furthermore, higher concentrations of [Ch][NO$_3$] IL could result in the IL separating from the PE that would impact the PEs performance within the battery.[1] The electrolyte must be able to solvate and move Mg or Zn ions away from electrode surface, otherwise the ions will accumulate above the electrode surface and precipitate as Mg or Zn salts/oxides.

Lastly, the ionic conductivity of the PE films post discharge was investigated in order to compare them with the initial PEIS spectra to highlight the stability of the PE films. The averaged Nyquist plot for the

batteries utilising the 1:1 SF:IL and 1:3 SF:IL composite films post discharge are depicted in **Figure 41**. The ionic conductivity of the PE composites was also estimated using equation (32).
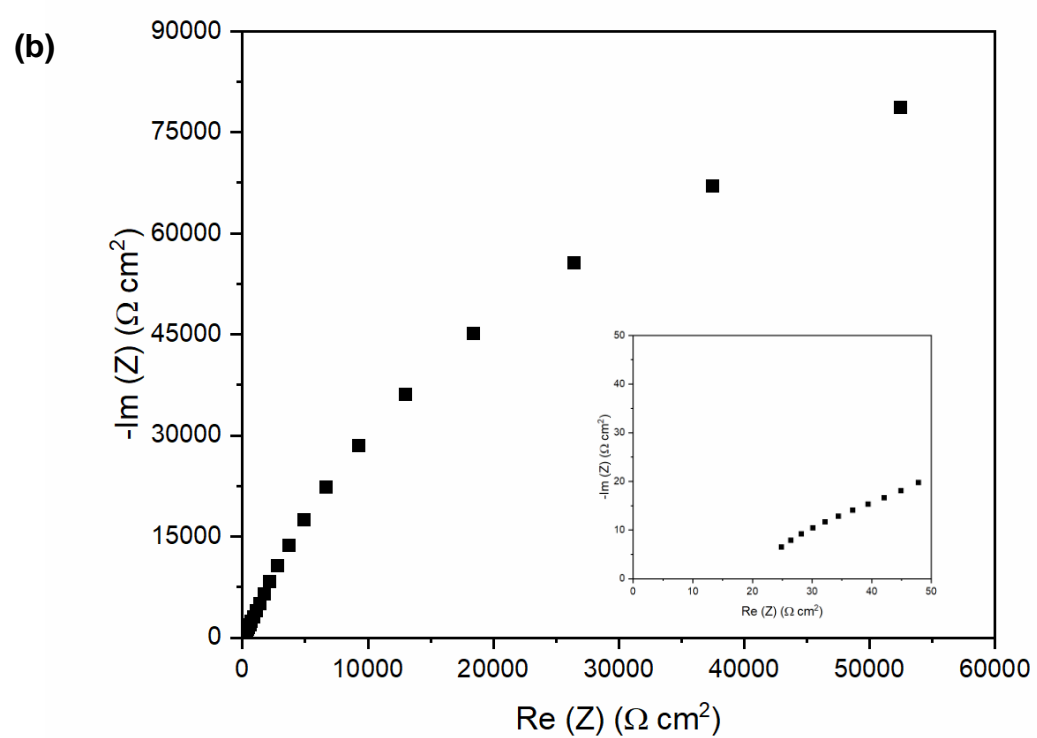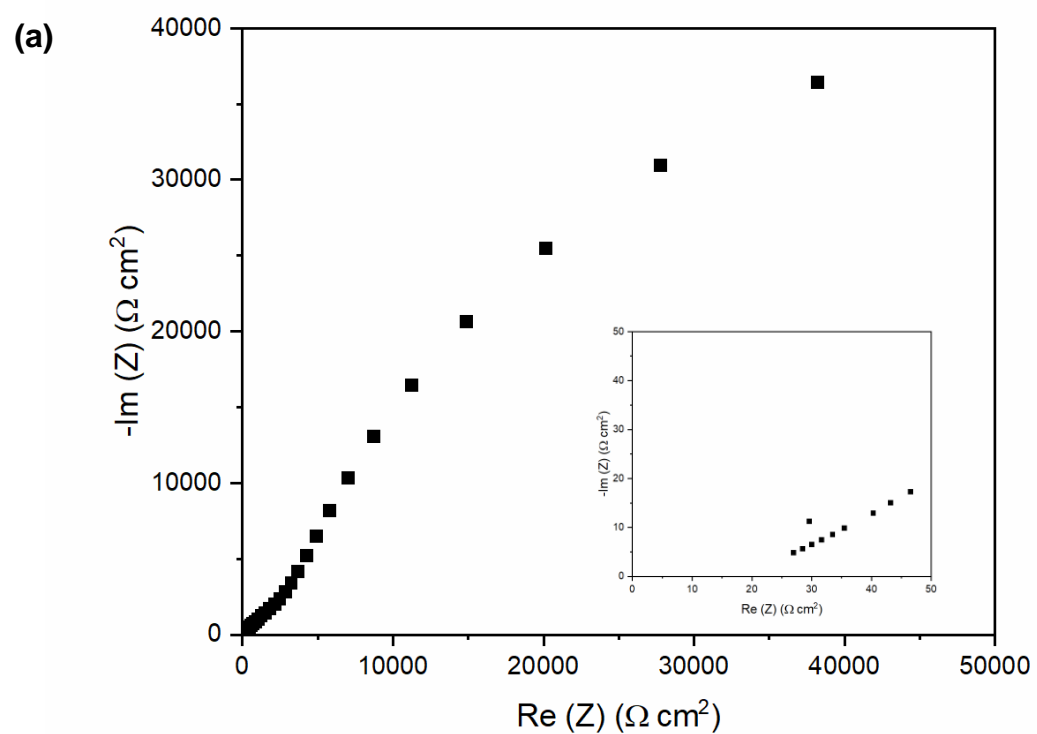
**Figure 41.** (a) PEIS spectra of the 1:1 PE assembled in the primary Mg-air battery post discharge. The inset portrays the spectra in an expanded view of the high frequency region. (b) PEIS spectra of the

1:3 PE assembled in the primary Mg-air battery post discharge. The inset portrays the spectra in an expanded view of the high frequency region.

By using equation (32) and the information from **Figure 41**, the average ionic conductivity post discharge for the 1:1 PE film is 3.18 mS cm$^{-1}$ and for the 1:3 PE film it is 3.54 mS cm$^{-1}$. Comparing the ionic conductivity of the PE composite films before and after electrochemical experimentation, the 1:1 SF:IL PE ionic conductivity is less by a factor of 1.18, whereas the 1:3 SF:IL PE ionic conductivity is less by a factor of 1.38. Hereby, with the ionic conductivity of the 1:3 SF:IL PE decreasing more than the 1:1 SF:IL PE, suggest that the 1:3 SF:IL PE composite is less stable under the same experimental conditions. In addition, we can imply that the IL from the 1:3 SF:IL PE is prone to separating due to the lower concentration of SF present and decreased capacity within the battery, as demonstrated in **Figure 39**. Therefore, highlighting SFs ability to immobilise the IL as an integral aspect of the functionality of the PE composite films. A better understanding of the chemistry involving the interactions between SF and the IL could lead to improved designs for energy storage devices utilising this material as the electrolyte/ionic conducting separator.

### 6.5 Polymer electrolyte utilised in primary zinc-air battery

Like Mg-air batteries, Zn-air batteries have received much attention recently[235] because of their advantageous electrochemical properties. Zn possesses a high theoretical volumetric capacity of 5,855 mAh cm$^{-3}$ and low reduction potential of - 0.76 V versus the SHE.[241] In addition, Zn-based-air batteries possesses a theoretical energy density of 1.65 kW h kg$^{-1}$.[235] Furthermore, as an essential nutrient Zn and its Zn$^{2+}$ ions has many important biological functions, such as, the development and sustenance of bones.[242] Therefore, Zn is identified as a promising biocompatible and biodegradable metal alongside Mg.[237, 243] However, Zn-air batteries can also suffer from issues such as, passivation, dendrite growth and hydrogen evolution from the hydrogen evolution reaction (HER) during the use of the battery, limiting the practical applications by weakening the discharge performance of Zn-air batteries.[244] Nevertheless, Zn was chosen as the Zn anode material in this study's battery due to its favourable biocompatibility and degradability. In addition, Zn was also chosen to investigate how the SF:IL PE incorporated battery performs when using a different degradable and biocompatible anode material.

The assembly of the Zn-air battery was the same as that of the Mg-air battery depicted in **Figure 37** and **38**, the difference only being is the anode utilised. Furthermore, before the measurements were taken via experimentation of the battery, areas of the anode foil around the PE film were again taped using clear Sellotape, preventing the two terminals (anode and cathode) from contacting one another.

The averaged (from three repeated experiments) discharge performance of the primary Zn-air battery, utilising the [Ch][NO$_3$] IL immobilised by SF as electrolyte, is represented in **Figure 42**.
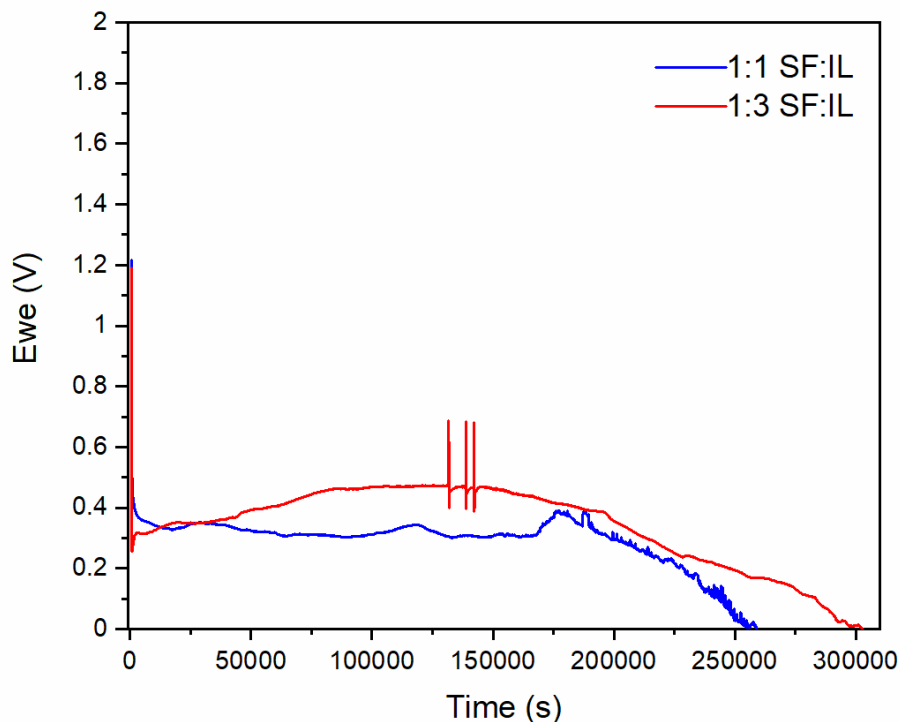


**Figure 42.** Discharge performance of the primary Zn-air battery using the 1:1 SF:IL PE (blue line) and the 1:3 SF:IL PE (red line) at a current density of ca. 25 μA cm$^{-2}$.

The OCV (V) for the Zn 1:1 SF:IL and 1:3 SF:IL batteries were in the range of 1.3 and 1.2 V just after fabrication. The cell voltage again decreased immediately when a discharge current was applied, likely due to the battery's internal resistance, and soon reached a plateau. The large voltage drop observed for the batteries at the start of discharge is probably due to the Pt black carbon cloth cathode. Therefore, fabrication of future batteries could be optimised to mitigate this voltage drop from ca. 0.8 V to ca. 0.4 V, for instance, using Au nanoparticles deposited onto a crystalised SF film as the cathode.[1]

At a current density of ca. 25 μA cm$^{-2}$ the 1:1 SF:IL battery displayed a capacity of 0.96 mAh cm$^{-2}$. Regarding the 1:3 SF:IL batteries, each discharge experiment conducted showed these oscillation signals (ca. 131,000 seconds or 35 hrs into the experiment). In addition, these oscillation signals persisted for varying time lengths, some seemingly indefinite (e.g. over 360,000 seconds or 100 hrs) and others only for a couple hours after first observation. The average of those discharge experiments depicting this oscillation occurring then disappearing after a few hours were used for **Figure 42**.

Henceforth, the capacity for the 1:3 SF:IL battery was determined using the information up until these oscillating signals are observed. As a result, the 1:3 SF:IL battery displayed a capacity of 0.72 mAh cm$^{-2}$.

It is unclear what causes these oscillating signals in **Figure 42** for the 1:3 SF:IL PE battery, because these signals were not observed for the 1:1 SF:IL battery. However, it is plausible that this phenomenon is due to the Zn reacting with the water within the PE to form excess hydrogen which may disrupt the battery's discharge performance. The excess hydrogen potentially formed after Zn reacts with the water within the PE and its ability to escape, could explain the oscillating signals and with various time lengths observed. As previously discussed, the implication that the IL in the 1:3 SF:IL PE is prone to separating and with its greater water content, previously determined by **Figure 34**, support this prediction. For potential future work at investigating this explanation, a differential electrochemical mass spectroscopy (DEMS) setup with the 1:3 SF:IL PE Zn-air battery could elucidate whether excess hydrogen is being formed ca. 35 hrs into the discharge experiment.

The specific volumetric power density of the batteries were calculated following the same method first used for the Mg-air batteries, using equation (36). The $V$ of the SF:IL Zn-air battery is 8.697x10$^{-5}$ L. The 1:1 SF:IL battery could deliver a volumetric power density of 0.08 W L$^{-1}$ and an energy density of 3.86 Wh L$^{-1}$. As for the 1:3 SF:IL battery, it could deliver a volumetric power density of 0.11 W L$^{-1}$ and an energy density of 3.89 Wh L$^{-1}$. Reported here, the 1:1 SF:IL and 1:3 SF:IL batteries demonstrated capacities of 0.96 mAh cm$^{-2}$ and 0.72 mAh cm$^{-2}$, respectively, at a current density of ca. 25 μA cm$^{-2}$. Furthermore, the power offered from the 1:1 SF:IL PE battery at 8.97 μW cm$^{-2}$ and from the 1:3 SF:IL PE battery at 12.05 μW cm$^{-2}$ may still fulfil the requirements for average consumption of published implantable biomedical devices (e.g. wireless implantable sensing systems).[35, 240]

When comparing the information gathered for the Mg-air batteries and the Zn-air batteries, we begin to see the effects the SF:IL PE has for each of the batteries. For the Mg-air batteries, the 1:1 SF:IL PE battery provided greater power and energy density when compared to the 1:3 SF:IL PE battery. However, the opposite is true when the Mg AZ31 anode material is swapped for Zn. Furthermore, the 1:3 SF:IL from the Zn-air battery possessed a different discharge profile to that of the 1:3 SF:IL Mg-air battery. Therefore, this indicates that increasing the content of the IL impacts the discharge performance for each battery differently. This may imply that the [Ch][NO$_3$] IL increases the rate of discharge and/or corrosion rate of the Mg anode material for Mg-air batteries, whereas for a Zn-air battery this may not necessarily be the case. To further investigate and evaluate the performance of the 1:1 and 1:3 SF:IL PEs utilised in the Zn-air batteries, the averaged (from three repeated

experiments) discharge performance of the batteries with varying current applied was conducted and reported in **Figure 43**.
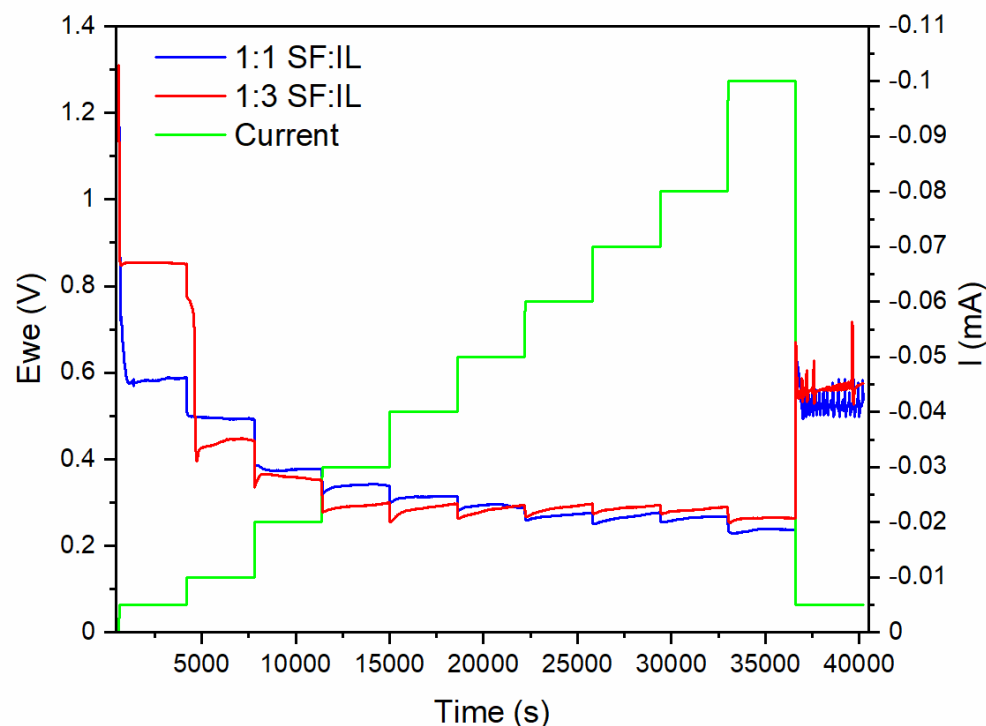


**Figure 43.** Discharge performance of the primary Zn-air battery using the 1:1 SF:IL PE (blue line) and the 1:3 SF:IL PE (red line) at varying current (green line) applied.

From **Figure 43** the performance of each battery with 1:1 SF:IL or 1:3 SF:IL as electrolyte is similar within the current range of 20 to 100 µA in the time frame of ca. 11 hours. However, when each battery experiences a low current of 5 and 10 µA, the 1:3 SF:IL PE battery retains a noticeably greater potential versus the 1:1 SF:IL PE battery. This observation was less pronounced when the anode material was Mg AZ31. In addition, after the batteries experienced 100 µA and then had the current reduced back to 5 µA, both the 1:1 SF:IL and 1:3 SF:IL batteries demonstrated these oscillating signals which persisted for ca. 1 hour, the full duration of the final current application step. This was the first time we observe the 1:1 SF:IL PE battery with Zn anode depict these oscillating signals, therefore, it is suggested the current application could affect the discharge performance of the primary Zn-air battery. As a result, from the experiments using Mg AZ31 and Zn foil as an anode material we can conclude Mg AZ31 would likely be most suitable over the current range of 5 to 100 µA due to its apparent stability

and superior power offered. However, the Zn batteries did possess higher capacities, although, this did not seem to provide many benefits, possibly due to the interfering chemistries (e.g. HER) impacting the primary Zn-air batteries to a greater extent than the Mg AZ31. On the other hand, the physical appearance of the Mg AZ31 anode after experimentation was considerably blackened (**Supplementary Information** [**SI**] **Figure 1**), likely caused by corrosion of the Mg material which could indicate why the Mg batteries possessed lower capacities during the discharge performance experiments.

Finally, the ionic conductivity of the PE films post discharge was investigated in order to compare them with the initial PEIS spectra to further showcase the stability of the PE films assembled within the batteries. The averaged Nyquist plot for the batteries utilising the 1:1 SF:IL and 1:3 SF:IL composite films post discharge are depicted in **Figure 44**. The ionic conductivity of the PE composites was also estimated using equation (32).
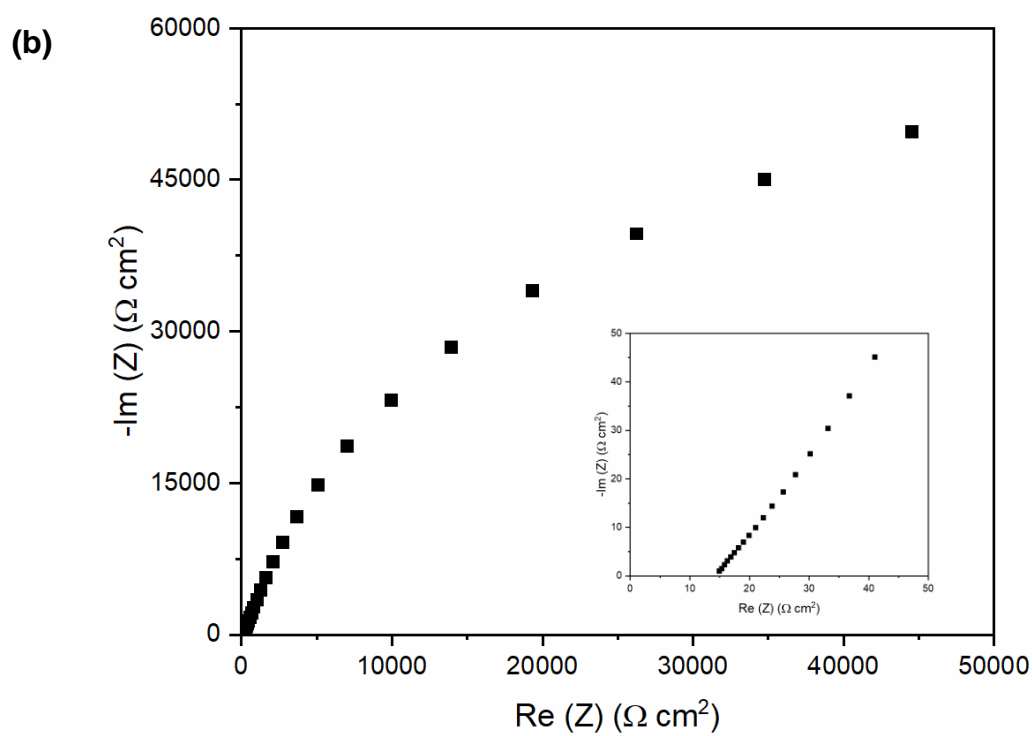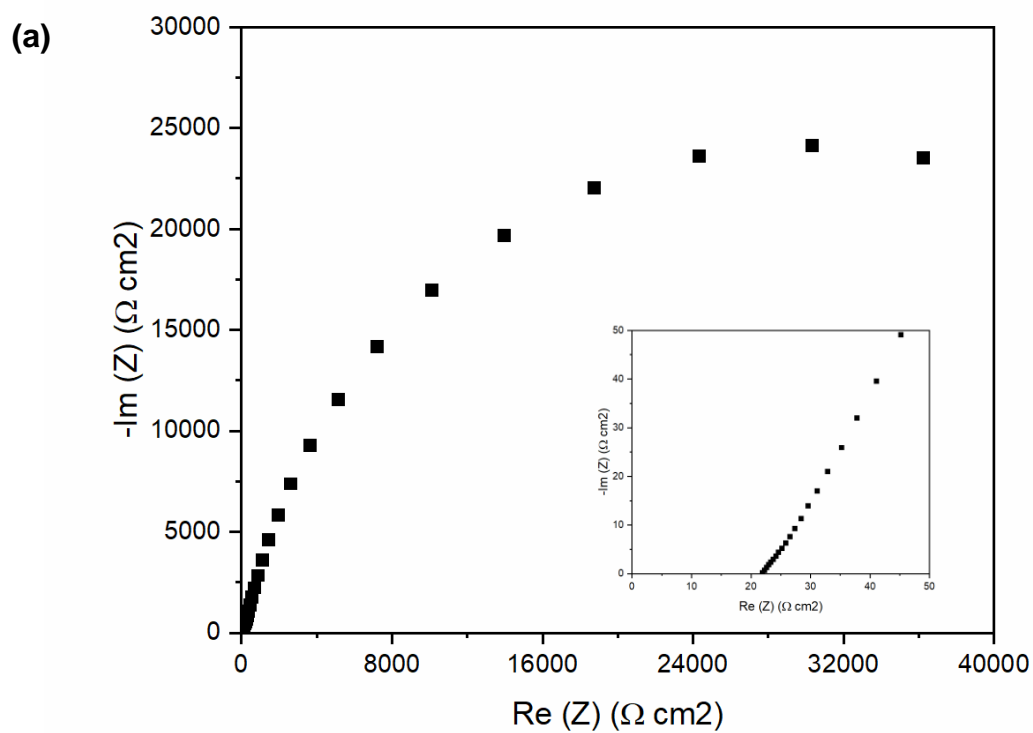
**Figure 44.** (a) PEIS spectra of the 1:1 PE assembled in the primary Zn-air battery post discharge. The inset portrays the spectra in an expanded view of the high frequency region. (b) PEIS spectra of the

1:3 PE assembled in the primary Zn-air battery post discharge. The inset portrays the spectra in an expanded view of the high frequency region.

By using equation (32) and the information from **Figure 44**, the average ionic conductivity post discharge for the 1:1 PE film is 3.03 mS cm$^{-1}$ and for the 1:3 PE film it is 4.55 mS cm$^{-1}$. Comparing the ionic conductivity of the PE composite films before and after electrochemical experimentation, the 1:1 SF:IL PE ionic conductivity is less by a factor of 1.11, whereas the 1:3 SF:IL PE ionic conductivity is less by a factor of 1.75. As a result, with the ionic conductivity of the 1:3 SF:IL PE decreasing more than the 1:1 SF:IL PE, supports the previous statement that the 1:3 SF:IL PE composite is less stable under the same experimental conditions and that with greater IL content present, the discharge performance of each battery (Mg and Zn) is impacted differently. For instance, the ionic conductivity of the 1:3 SF:IL PE assembled in the Zn anode battery decreased by more than that of the 1:3 SF:IL PE assembled in the Mg anode battery, a reduction factor of 1.75 compared to pre-discharge for Zn batteries and 1.38 compared to pre-discharge for the Mg batteries. In addition, the anion (the nitrate) from the PE may also participate in the reaction with the anodes forming magnesium nitrate or zinc nitrate, respectively, and results in decreased conductivity after discharge.

What we can discern from these electrochemical tests using different anode materials and concoctions of the electrolyte is that when using 1:1 SF:IL PE, the performance of the batteries and stability of the films (retention of ionic conductivity after discharging) are similar with respect to their outcomes. Most notably, when the IL content is increased in the SF films, we start to see the performance of the Mg and Zn batteries impacted and how exactly this is impacted seems more determined by the anode material specifically and its interactions with the constituents of the PE throughout the experiment (e.g. solvating ability of the Mg or Zn ions). Therefore, SFs role of immobilising the IL seems vital and demonstrated to maintain the functional lifetime of the battery. As seen from **Figure 42**, oscillating signals are observed ca. 35 hrs into the 1:3 SF:IL discharge experiment when using Zn as the anode. However, this was not observed for the Mg anode battery experiments (**Figure 39** and **40**) and only observed for the 1:1 SF:IL Zn anode batteries after 100 µA current was applied (**Figure 42**). Therefore, it is anticipated that the tailoring of silk composites utilised for energy storage devices can further modulate the discharge performance of batteries and lead to enhanced TIMB applications.

### 7. Summary comments

The average lattice parameters for the non-hydrated (Ala-Gly)$_n$ SF crystal model (after equilibration) are $a = 17.42$ Å, $b = 15.42$ Å, $c = 11.25$ Å and hydrated are $a = 17.20$ Å, $b = 15.22$ Å, $c = 11.10$ Å. After 2 ns sampling time at 298 K, the (Ala-Gly)$_n$ SF crystal model possess Ala and Gly residues in regions

indicative of a heterogeneous structure, evidenced by a left-handed α-helix, $3_{10}$-helix, β-sheet (ca. $\langle\varphi\rangle$ = 70 ° and $\langle\psi\rangle$ = 10 °, ca. $\langle\varphi\rangle$ = - 40 ° and $\langle\psi\rangle$ = - 30 °, ca. $\langle\varphi\rangle$ = - 60 ° and $\langle\psi\rangle$ = 130 °, respectively) and random coil structures. In addition, the $(Ala-Gly)_n$ SF crystal structure is to be considered in the silk I form (i.e. repeated β-turn type II conformation), because β-sheets are not the predominant secondary structure, instead, the $3_{10}$-helix is the predominant secondary structure (ca. 37 %).

When the $(Ala-Gly)_{1024}$ SF crystal model had water molecules incorporated within its system (ca. 7.5 wt %), the activation energy for the diffusion of the water molecules was calculated to be at 12.07 kJ $mol^{-1}$. Furthermore, the diffusivity of the water molecules incorporated within the system was calculated to be at $1.60 \times 10^{-6}$ $cm^2$ $s^{-1}$ at 298 K. Lastly, it was observed that the diffusion of water within the system was anisotropic and that the water molecules were predominantly found to be in positions in the free space between the Ala-Gly chains, thus preferred diffusion along the X-axis direction of the supercell.

After fabrication of the PE film, the PE film SF:IL 1:1 possessed ca. 6 wt % water while the PE film SF:IL 1:3 possessed ca. 7 wt % water. In addition, once assembled within the batteries (before discharge experiments) the 1:1 PE film possessed an ionic conductivity of 3.55 mS $cm^{-1}$ whereas the 1:3 PE film possessed an ionic conductivity of 6.43 mS $cm^{-1}$.

The assembled primary Mg-air battery utilising the SF:IL 1:1 PE film, could deliver a volumetric power density of 0.17 W $L^{-1}$ and an energy density of 7.18 Wh $L^{-1}$. When utilising the SF:IL 1:3 PE film SF:IL 1:3 as electrolyte for the battery, it could deliver a volumetric power density of 0.14 W $L^{-1}$ and an energy density of 4.66 Wh $L^{-1}$. In addition, the batteries utilising the 1:1 SF:IL and 1:3 SF:IL PE films demonstrated capacities of 0.84 mAh $cm^{-2}$ and 0.68 mAh $cm^{-2}$, respectively, at a current density of ca. 25 μA $cm^{-2}$. Furthermore, the power offered from the 1:1 SF:IL PE battery at 23.33 μW $cm^{-2}$ and from the 1:3 SF:IL PE battery at 18.72 μW $cm^{-2}$ may fulfil the requirements for average consumption of published implantable biomedical devices.[35, 240] Lastly, the average ionic conductivity post discharge for the 1:1 PE film is 3.18 mS $cm^{-1}$ and for the 1:3 PE film it is 3.54 mS $cm^{-1}$.

The assembled primary Zn-air battery utilising the SF:IL 1:1 PE film, could deliver a volumetric power density of 0.08 W $L^{-1}$ and an energy density of 3.86 Wh $L^{-1}$. When utilising the SF:IL 1:3 PE film SF:IL 1:3 as electrolyte for the battery, it could deliver a volumetric power density of 0.11 W $L^{-1}$ and an energy density of 3.89 Wh $L^{-1}$. In addition, the batteries utilising the 1:1 SF:IL and 1:3 SF:IL PE films demonstrated capacities of 0.96 mAh $cm^{-2}$ and 0.72 mAh $cm^{-2}$, respectively, at a current density of ca. 25 μA $cm^{-2}$. Furthermore, the power offered from the 1:1 SF:IL PE battery at 8.97 μW $cm^{-2}$ and from the 1:3 SF:IL PE battery at 12.05 μW $cm^{-2}$ may still fulfil the requirements for average consumption of

published implantable biomedical devices.[35, 240] Finally, the average ionic conductivity post discharge for the 1:1 PE film is 3.03 mS cm$^{-1}$ and for the 1:3 PE film it is 4.55 mS cm$^{-1}$.

## 8. Conclusion

This thesis has explored the use of silk-based PE for application in biodegradable batteries to power implantable electronic devices. By employing a combination of theoretical and experimental approach, this study has demonstrated the feasibility of silk-based biodegradable batteries and provided unique insight into the structure of the silk and important information pertaining to their degradation characteristics (e.g. water incorporation and diffusion of water ions).

The utilisation of classical MD has provided a unique insight into SF-based biomaterials. The secondary structure was evaluated by comparing to information available in the literature and demonstrating the efficacy of the simulation models that predicted the characteristic torsion angles for residues Ala and Gly. The Ramachandran contour plots provided insight for the β-sheet region residues, and the MD simulations enabled calculation of the percentages of the residues detailing the predominant secondary structures for both hydrated and non-hydrated materials, improving our understanding of the impact of water on the structure of the underlying silk. The simulations also provided insight into how the presence of the silk chains impacted the mobility of the water molecules. It was found that the water moved in the regions in between the chains, however, it was reluctant to cross the chains. The result was that most of the water's movement was parallel to the polymer chains with very little movement perpendicular to the chain. This significant anisotropy in the mobility of the water in silk may be exploitable in future applications.

The design, fabrication, and experimentation of the primary Mg- and Zn-air batteries utilising a SF:IL-based film as PE have highlighted the challenges faced when investigating transient and biocompatible energy storage devices. Nevertheless, the promising characteristics (biocompatibility and transiency) make it worthwhile to study and develop such devices for future technological applications. The PEIS of the batteries were conducted to estimate the ionic conductivity of the PEs before and after galvanostatic discharging. The discharge experiments portray the batteries' performance capabilities and highlight the batteries' response to varying current.

In this work, two separate techniques have been utilised to investigate the SF material and the incorporation of SF for energy storage devices. The aim was to achieve an improved understanding of the science underpinning the chemistry of the materials used in these devices, as a result, a greater control over these devices could be achieved. Showcased in this work, the PE can be incorporated into batteries utilising Mg and Zn anode materials, indicating the PE material's design application

versatility. Furthermore, the anisotropic water diffusion of SF signifies an interesting characteristic that could be exploited by modifying the protein's secondary structure, perhaps effecting diffusion of ions or solvent in similar devices. Ultimately, this may lead to tailored performance and degradation rates for future devices making use of similar materials. Moreover, an appreciation for combining different techniques to investigate materials was obtained.

## 9. Future work

The information reported in this work could be expanded upon for future work. With continued investigation into materials like SF it is believed that a greater understanding of their properties and key aspects/interactions can be achieved; positively impacting the applications of materials produced using SF and silk-inspired polymers and proteins.[245, 246]

The MD exploration of SF discussed in this work can be easily expanded upon. For instance, using the $(Ala-Gly)_n$ SF crystal model, species other than water molecules could be incorporated within the system and their diffusivity investigated (e.g. charged ions, such as $Mg^{2+}$). Investigating the diffusivity of charged ions through silk could showcase the effectiveness of silk acting as an ionic conducting separator and lead to the capability of predicting the degradation and performance of such batteries. Furthermore. the modelling of incorporated choline compounds would take substantial computing power and work but would provide a hugely insightful explanation on how SF interacts with the choline compound and what affects it has on the secondary structure of SF. In addition, the mechanical stress of the system could also be evaluated and compared with the literature of other SF computational models. Lastly, in this work, the transportation/diffusivity of bulk water is measured but a variety of structural and dynamical properties of the protein hydration water can be reviewed and compared with those of bulk and with the corresponding experimental results. In particular, the accessibility to the protein medium, the hydrogen bond networking capability, the residence times, the relaxation behaviour, and the inelastic vibrational features of hydration water could be analysed in framework of the peculiar interactions of water at the protein surface. All these features, which can be traced back to the complexity of the overall protein-solvent energy landscape, can be investigated in connection with the role played by hydration water in the biological functionality of SF.

The design and implementation of the batteries detailed in this work could also be expanded upon since the materials themselves possess desirable characteristics. To achieve full transiency of the batteries reported in this work, different cases must be utilised. For instance, an encapsulation material of SF films could be suitable, as this would enable the battery to become completely biocompatible and biodegradable, thus achieving full transiency. Furthermore, to improve upon the capabilities of the

batteries, greater surface area electrodes would yield greater energy densities. Akin to the Pt nanoparticle carbon cloth cathode, nanoparticles of Mg AZ31 on a SF film could be a viable anode material, although, it is suspected that this could also create greater internal resistance within the battery. Furthermore, the applicability to utilise SF and similar PE designs for different energy storage devices (e.g. fuel cells), the thickness of the PE films could be investigated and what impact that has on the performance and stability of the destined application and compare this with existing polymeric ion conducting membranes (e.g. Nafions).

Therefore, it is anticipated that the combination of MD investigating the materials described in this work and the tailoring of the designs and materials utilised for energy storage devices can further modulate the performance of devices destined for TIMB applications.

## References

1. X. Jia, C. Wang, V. Ranganathan, B. Napoer, C. Yu, Y. Chao, M. Forsyth, F. G. Omenetto, D. R. MacFarlane and G. G. Wallace, "A Biodegradable Thin-Film Magnesium Primary Battery Using Silk Fibroin−Ionic Liquid Polymer Electrolyte", *ACS Energy Letters*, **2017**, 2, 831-836.
2. S. Hwang, H. Tao, D. Kim, H. Cheng, J. Song, E. Rill, M. A. Brenckle, B. Panilaitis, S. M. Won, Y. Kim, Y. M. Song, K. J. Yu, A. Ameen, R. Li, Y. Su, M. Yang and  D. L. Kaplan, "A Physically Transient Form of Silicon Electronics", *SCIENCE*, **2012**, 337, 1640-1644.
3. K. K. Fu, Z. Wang, J. Dai, M. Carter and L. Hu, "Transient Electronics: Materials and Devices", *Chem. Mater.* **2016**, 28, 3527-3539.
4. S. Sthiannopkao and M. H. Wong, "Handling e-waste in developed and developing countries: Initiatives", *Science of the Total Environment*, **2013**, 463-464, 1147-1153.
5. X. Huang, D. Wang, Z. Yuan, W. Xie, Y. Wu, R. Li, Y. Zhao, D. Luo, L. Cen, B. Chen, H. Wu, H. Xu, X. Sheng, M. Zhang, L. Zhao and L. Yin, "A Fully Biodegradable Battery for Self-Powered Transient Implants", *Small*, **2018**, 14, 1800994.
6. 10993-1, ISO, "Biological Evaluation of Medical Devices - Part 1: Evaluation and Testing within a Risk Management Process", **2018**, 5, 1-41.
7. R. Li, L. Wang, D. Kong and L. Yin, "Recent progress on biodegradable materials and transient electronics", *Bioactive Materials*, **2018**, 3, 322-333.
8. F. R. Salsbury Jr. "Molecular dynamics simulations of protein dynamics and their relevance to drug discovery", *Curr. opin. Pharmacol.* **2010**, 10, 738-744.
9. B. J. Alder and T. E. Wainwright, "Studies in Molecular Dynamics. I. General Method", *J. Chem. Phys.* **1959**, 31, 459-466.

10. A. Rahman, "Correlations in the Motion of Atoms in Liquid Argon", *Physical review*, **1964**, 136, 405-411.

11. T. Yamane, K. Umemura, Y. Nakazawa and T. Asakura, "Molecular Dynamics Simulation of Conformational Change of Poly(Ala-Gly) from Silk I to Silk II in Relation to Fiber Formation Mechanism of Bombyx mori Silk Fibroin", *Macromolecules*, **2003**, 36, 6766-6772.

12. D. Frenkel and B. Smit, "Understanding molecular simulation: from algorithms to applications", *Academic Press*, **2007**, San Diego.

13. H. L. Hernandez, S. Kang, O. P. Lee, S. Hwang, J. A. Kaitz, B. Inci, C. W. Park, S. Chung, N. R. Sottos, J. S. Moore, J. A. Rogers and S. R. White, "Triggered Transience of Metastable Poly(phthalaldehyde) for Transient Electronics", *Advanced Materials*, **2014**, 26, 7637-7642.

14. C. W. Park, S. Kang, H. L. Hernandez, J. A. Kaitz, D. S. Wie, J. Shin, O. P. Lee, N. R. Sottos, J. S. Moore, J. A. Rogers and S. R. White, "Thermally Triggered Degradation of Transient Electronic Devices", *Advanced Materials*, **2015**, 27, 3783-3788.

15. L. Yin, H. Cheng, S. Mao, R. Haasch, Y. Liu, X. Xie, S. Hwang, H. Jain, S. Kang, Y. Su, R. Li, Y. Huang, and J. A. Rogers, "Dissolvable Metals for Transient Electronics", *Advanced Functional Materials*, **2014**, 24, 645-658.

16. S. H. Jin, J. Shin, I. Cho, S. Y. Han, D. J. Lee, C. H. Lee, J. Lee and J. A. Rogers, "Solution-processed single-walled carbon nanotube field effect transistors and bootstrapped inverters for disintegratable, transient electronics", *Applied Physics Letters*, **2014**, 105, 013506-1-4.

17. H. Acar, S. Çınar, M. Thunga, M. R. Kessler, N. Hashemi and R. Montazami, "Study of Physically Transient Insulating Materials as a Potential Platform for Transient Electronics and Bioelectronics", *Advanced Functional Materials*, **2014**, 24, 4135-4143.

18. S. Hwang, D. Kim, H. Tao, T. Kim, S. Kim, K. J. Yu, B. Panilaitis, J. Jeong, J. Song, F. G. Omenetto and J. A. Rogers, "Materials and Fabrication Processes for Transient and Bioresorbable High-Performance Electronics", *Advanced Functional Materials*, **2013**, 23, 4087-4093.

19. Y. H. Jung, T. Chang, H. Zhang, C. Yao, Q. Zheng, V. W. Yang, H. Mi, M. Kim, S. J. Cho, D. Park, H. Jiang, J. Lee, Y. Qiu, W. Zhou, Z. Cai, S. Gong and Z. Ma, "High-performance green flexible electronics based on biodegradable cellulose nanofibril paper", *Nature Communications*, **2015**, 6, 7170, 1-11.

20. S. Hwang, G. Park, C. Edwards, E. A. Corbin, S. Kang, H. Cheng, J. Song, J. Kim, S. Yu, J. Ng, J. E. Lee, J. Kim, C. Yee, B. Bhaduri, Y. Su, F. G. Omennetto, Y. Huang, R. Bashir, L. Goddard, G. Popescu, K. Lee and J. A. Rogers, "Dissolution Chemistry and Biocompatibility of Single-

Crystalline Silicon Nanomembranes and Associated Materials for Transient Electronics", *ACS NANO*, **2014**, 8, 5841-5851.

21. R. S. Khurmi and R. S. Sedha, "Materials Science", *S. Chand & Company Ltd*, **2014**, New Delhi.

22. J. N. Spencer, G. M. Bodner and L. H. Rickard, "Chemistry: Structure and Dynamics, 5th Edition", *John Wiley & Sons*, **2010**, New Jersey.

23. Battery University: Will Secondary Batteries replace Primaries?, https://batteryuniversity.com/learn/archive/will_secondary_batteries_replace_primaries, (accessed: April 9th 2019).

24. Everyday-Green: Batteries, http://everyday-green.com/html/batteries.html, (accessed: April 14th 2019).

25. I. A. de Castro, R. S. Datta, J. Z. Ou, A. Castellanos-Gomez, Sharath Sriram, T. Daeneke and K. Kalantar-zadeh, "Molybdenum Oxides-From Fundamentals to Functionality", *Advanced Materials*, **2017**, 29, 1701619, 1-31.

26. X. Wei and J. Liu, "Power sources and electrical recharging strategies for implantable medical devices", *Frontiers of Energy and Power Engineering in China*, **2008**, 2, (1), 1-13.

27. M. Luo, C. Song, F. Herrault and M. G. Allen, "A Microfabricated Wireless RF Pressure Sensor Made Completely of Biodegradable Materials", *Journal of Microelectromechanical Systems*, **2014**, 23, 4-14.

28. M. Tsang, A. Armutlulu, F. Herrault, R. H. Shafer, S. A. B. Allen, and M. G. Allen, "Development of Electroplated Magnesium Microstructures for Biodegradable Devices and Energy Sources", *J. Microelectrochemical Systems*. **2014**, 23, (6), 1281-1289.

29. M. Moravej and D. Mantovani, "Biodegradable Metals for Cardiovascular Stent Application: Interests and New Opportunities", *International Journal of Molecular Sciences*, **2011**, 12, 4250-4270.

30. F. Witte, "The history of biodegradable magnesium implants: A review", *Acta Biomaterialia*, **2010**, 6, (5), 1680-1692.

31. D. Xue, Y. Yun, Z. Tan, Z. Dong and M. J. Schulz, "I*n Vivo* and In Vitro Degradation Behavior of Magnesium Alloys as Biomaterials", *Journal of Materials Science & Technology*, **2012**, 28, (3), 261-267.

32. M. Tsang, A. Armutlulu, A. W. Martinez, S. A. B. Allen and M. G. Allen, "Biodegradable magnesium/iron batteries with polycaprolactone encapsulation: A microfabricated power source for transient implantable devices", *Microsystems and Nanoengineering*, **2015**, 1, 15024, 1-10.

33. D. Noviana, D. Paramitha, M. F. Ulum and H. Hermawan, "The effect of hydrogen gas evolution of magnesium implant on the postimplantation mortaility of rats", *Journal of Orthopaedic Translation*, **2016**, 5, 9-15.

34. Z. Rong, P. Xiao, M. Liu, W. Huang, D. C. Hannah, W. Scullin, K. A. Perssonbd and G. Ceder, "Fast $Mg^{2+}$ diffusion in Mo3(PO$_4$)3O for Mg batteries", *Chem. Comm.* **2017**, 53, 7998-8001.

35. Y. Lee, S. Bang, I. Lee, Y. Kim, G. Kim, M. H. Ghaed, P. Pannuto, P. Dutta, D. Sylvester, D. A. Blaauw, "A Modular 1 mm$^3$ Die-Stacked Sensing Platform With Low Power I$^2$ C Inter-Die Communication and Multi-Modal Energy Harvesting", *IEEE J. of Solid-State Circuits*, **2013**, 48, (1), 229-243.

36. S. Aznar-Cervantes, M. I. Roca, J. G. Martinez, L. Meseguer-Olmo, J. L. Cenis, J. M. Moraleda and T. F. Otero, "Fabrication of conductive electrospun silk fibroin scaffolds by coating with polypyrrole for biomedical applications", *Bioelectrochemistry*, **2012**, 85, 36–43.

37. J. G. Hardy, L. M. Romer and T. R. Scheibel, "Polymeric materials based on silk proteins", *Polymer,* **2008**, 49, 4309-4327.

38. J. G. Hardy and T. R. Scheibel, "Composite materials based on silk proteins", *Progress in Polymer Sci.* **2010**, 35, 1093-1115.

39. C. Vepari and D. L. Kaplan, "Silk as a biomaterial", *Progress in Polymer Sci.* **2007**, 32, 991-1007.

40. Y. Qi , H. Wang, K. Wei, Y. Yang, R. Zheng, I. S. Kim and K. Zhang, "A Review of Structure Construction of Silk Fibroin Biomaterials from Single Structures to Multi-Level Structures", *Mol. Sci.* **2017**, 18, 1-15.

41. C. Holland, K. Numata, J. Rnjak-Kovacina, and F. P. Seib, "The Biomedical Use of Silk: Past, Present, Future", *Adv. Healthcare Mater.* **2019**, 8, 1-22.

42. T. Asakura, Y. Suzuki, Y. Nakazawa, G. P. Holland and J. L. Yarger, "Elucidating silk structure using solid-state NMR", *Soft Matter*, **2013**, 9, 11440-11450.

43. B. Lotz and F. C. Cesari, "The chemical structure and the crystalline structures of Bombyx mori silk fibroin", *Biochimie*, **1979**, 61, 205-214.

44. C. Z. Zhou, F. Confalonieri, M. Jacquet, R. Perasso, Z. G. Li and J. Janin, "Silk fibroin: structural implications of a remarkable amino acid sequence", *Proteins Struct. Funct. Genet.* **2001**, 44, 119–122.

45. C. Z. Zhou, F. Confalonieri, N. Medina, Y. Zivanovic, C. Esnault, T. Yang, M. Jacquet, J. Janin, M. Duguet, R. Perasso and Z. G. Li, "Fine organization of Bombyx mori fibroin heavy chain gene", *Nucleic Acids Res.* **2000**, 15;28 (12), 2413-9.

46. S. Inoue, K. Tanaka, F. Arisaka, S. Kimura, K. Ohtomo and S. Mizuno, "Silk fibroin of Bombyx mori is secreted, assembling a high molecular mass elementary unit consisting of H-chain, L-chain and P25 with a 6: 6: 1 molar ratio", *J. Biol. Chem.* **2000**, 275, 40517-40528.

47. J. O. Warwicker, "The Crystal Structure of Silk Fibroin", *Acta. Cryst.* **1954**, 7, 565-573.

48. J. Meller, "Molecular Dynamics", *Encyclopaedia of life sciences*, **2001**, 1-8.

49. S. A. Hollingsworth and R. O. Dror, "Molecular Dynamics Simulation for All", *Neuron*, **2018**, 99, 1129-1143.

50. K. El Hage, F. Hedin, P. K. Gupta, M. Meuwly and M. Karplus, "Valid molecular dynamics simulations of human hemoglobin require a surprisingly large box size", *Structural Biology and Molecular Biophysics*, **2018**, 1-16.

51. L. Verlet, "Computer "Experiments" on Classical Fluids. I. Thermodynamical Properties of Lennard-Jones Molecules", *Physical Review*, **1967**, 159, (1), 98-103.

52. A. K. Rappé, C. J. Casewit, K. S. Colwell, W. A. Goddard III and W. M. Skif, "UFF, a Full Periodic Table Force Field for Molecular Mechanics and Molecular Dynamics Simulations", *Journal of American Chemical Society*, **1992**, 114, (25), 10024-10035.

53. B. R. Brooks, R. E. Bruccoleri, B. D. Olafson, D. J. States, S. Swaminathan and M. Karplus, "CHARMM: A program for macromolecular energy, minimization, and dynamics calculations", *Journal of Computational Chemistry*, **1983**, 4, (2), 187-217.

54. S. W. I. Siu, K. Pluhackova and R. A. Böckmann, "Optimization of the OPLS-AA Force Field for Long Hydrocarbons", *J. Chem. Theory Comput.* **2012**, 8, 1459-1470.

55. G. A. Kaminski, R. A. Friesner, J. Tirado-Rives and W. L. Jorgensen, "Evaluation and Reparameterization of the OPLS-AA Force Field for Proteins via Comparison with Accurate Quantum Chemical Calculations on Peptides", *J. Phys. Chem. B*, **2001**, 105, 6474−6487.

56. M. J. Robertson, J. Tirado-Rives and W. L. Jorgensen, "Improved Peptide and Protein Torsional Energetics with the OPLS-AA Force Field", *J. Chem. Theory Comput.* **2015**, 11, 7, 3499-3509.

57. A. Altis, P. H. Nguyen, R. Hegger and G. Stock, "Dihedral angle principle component analysis of molecular dynamics simulations", J. Chem. Phys. **2007**, 126, 2441111, 1-10.

58. G. N. Ramachandran and V. Sasisekharan, "Conformation of polypeptides and proteins", *Adv. Protein Chem.* **1968**, 23, 283-437.

59. S. Zhang, R. Schweitzer-Stenner and B. Urbanc, "Do Molecular Dynamics Force Fields Capture Conformational Dynamics of Alanine in Water?", *J. Chem. Theory Comput.* **2020**, 16, (1), 510-527.

60. H. J. C. Berendsen, J. R. Grigera and T. P. Straatsma, "The missing term in effective pair potentials", *J. Phys. Chem.* **1987**, 91, 6269-6271.

61. J. L. F. Abascal and C. Vega, "A general purpose model for the condensed phases of water: TIP4P/2005", *J. Chem. Phys.* **2005**, 123, 234505.

62. W. L. Jorgensen, "Transferable Intermolecular Potential Functions for Water, Alcohols, and Ethers. Application to Liquid Water", *J. Am. Chem. Soc.* **1981**, 103, 335-340.

63. W. L. Jorgensen, J. Chandrasekhar, J. D. Madura, R. W. Impey and M. L. Klein, "Comparison of simple potential functions for simulating liquid water", *J. Chem. Phys.* **1983**, 79, 926.

64. I. G. Tironi, R. Sperb, P. E. Smith and W. F. van Gunsteren, "A generalized reaction field method for molecular dynamics simulations", *American Institute of Physics the Journal of Chemical Physics*, **1995**, 102, (13), 5451-5459.

65. H. Zhang, X. Lu, Y. Leng, L. Feng, S. Qu, B. Feng, J. Weng and J. Wang, "Molecular dynamics simulations on the interaction between polymers and hydroxyapatitie with and without coupling agents", *Acta Biomaterialia*, **2008**, 1169-1181.

66. T. Asakura, Y. Watanabe and T. Itoh, "NMR of Silk Fibroin. 3. Assignment of Carbonyl Carbon Resonances and Their Dependence on Sequence and Conformation in Bombyx mori Silk Fibroin Using Selective Isotopic Labelling", *Macromolecules*, **1984**, 17, (11), 2421-2426.

67. H. C. Andersen, "Molecular dynamics simulations at constant pressure and/or temperature", *American Institute of Physics the Journal of Chemical Physics*, **1980**, 72, (4), 2384-2393.

68. K. Okuyama, K. Takanashi, Y. Nakajima and Y. Hasegawa, "Analysis of Silk I structure by X-ray and electron diffraction methods", *Journal of Sericultural Science of Japan*, **1988**, 57, (1), 23-30.

69. T. Asakura, J. Yao, T. Yamane, K. Umemura and A. S. Ulrich, "Heterogeneous Structure of Silk Fibers from Bombyx mori Resolved by 13C Solid-State NMR Spectroscopy", *Journal of the American Chemical Society*, **2002**, 124, (30), 8794-8795.

70. S. Piana, J. L. Klepeis and D. E. Shaw, "Assessing the accuracy of physical models used in protein-folding simulations: quantitative evidence from long molecular dynamics simulations", *Curr. Opin. Struct. Biol.* **2014**, 24, 98-105.

71. R. B. Best, N. V. Buchete and G. Hummer, "Are current molecular dynamics force fields too helical?", *J. Biophys.* **2008**, 95, 7-9.

72. D. Wilson, R. Valluzzi and D. Kaplan, "Conformational Transitions in Model Silk Peptides", *J. Biophys.* **2000**, 78, 2690-2701.

73. R. Valluzzia, S. P. Gido, W. Muller and D. L. Kaplan, "Orientation of silk III at the air-water interface", *International Journal of Biological Macromolecules*, **1999**, 24, (2-3), 237-242.

74. P. Taddei, V. Chiono, A. Anghileri, G. Vozzi, G. Freddi and G. Ciardelli, "Silk Fibroin/Gelatin Blend Films Crosslinked with Enzymes for Biomedical Applications", *Macromolecular Bioscience*, **2013**, 13, (11), 1492-1510.

75. J. M. Yao, K. Ohgo, R. Sugino, R. Kishore and T. Asakura, "Structural analysis of Bombyx mori silk fibroin peptides with formic acid treatment using high-resolution solid-state ^{13}C NMR spectroscopy", *Biomacromolecules*, **2004**, 5, 1763-1769.

76. T. Asakura, K. Ohgo, T. Ishida, P. Taddei, P. Monti and R. Kishore, "Possible Implications of Serine and Tyrosine Residues and Intermolecular Interactions on the Appearance of Silk I Structure of Bombyx mori Silk Fibroin-Derived Synthetic Peptides: High-Resolution [13]C Cross-Polarization/Magic-Angle Spinning NMR Study", *Biomacromolecules*, **2005**, 6, 468-474.

77. M. T. Dove, "An introduction to atomistic simulation methods", *Seminarios de la SEM*, **2007**, 4, 7-37.

78. W. M. Browna, T. D. Nguyen, M. Fuentes-Cabrera, J. D. Fowlkes, P. D. Rack, M. Berger and A. S. Bland, "An Evaluation of Molecular Dynamics Performance on the Hybrid Cray XK6 Supercomputer", *Procedia Computer Science*. **2012**, 9, 186-195.

79. E. Schrodinger, "An Undulatory Theory of the Mechanics of Atoms and Molecules", *Phys. Rev.***1926**, 28, 1049-1070.

80. L. E. Ratcliff, S. Mohr, G. Huhs, T. Deutsch, M. Masella and L. Genovese, "Challenges in large scale quantum mechanical calculations", *Comput. Mol. Sci.* **2017**, 7, 1-24.

81. W. Kohn and P. Hohenberg, "Inhomogenous electron gas" *Phys. Rev.* **1964**, 136, 1-8.

82. L. J. Sham and W. Kohn, "Self-Consistent Equations Including Exchange and Correlation Effects", *Phys. Rev.* **1965**, 140, 1-6.

83. W. Wu, J. Owino, A. Al-Ostaz and L. Cai, "Applying Periodic Boundary Conditions in Finite Element Analysis", *SIMULIA Community Conference*, **2014**, 707-714.

84. M. C. Payne and G. Makov, "Periodic boundary conditions in ab initio calculations", *Phys. Rev. B*, **1995**, 51, (7), 4014-4022.

85. W. C. Swope, . H. C. Andersen, P. H. Berens and K. R. Wilson, "A computer simulation method for the calculation of equilibrium constants for the formation of physical clusters of molecules: Application to small water clusters", *J. Chem. Phys.* **1982**, 76, (1), 637-649.

86. S. Nosé, "A unified formulation of the constant temperature molecular dynamics methods", *J. Chem. Phys.* **1984**, 81, 511-519.

87. W. G. Hoover, "Canonical dynamics: Equilibrium phase-space distributions", *Phys. Rev A*, **1985**, 31, 1695-1697.

88. W. L. Jorgensen, D. S. Maxwell and J. Tirado-Rives, "Development and Testing of the OPLS All-Atom Force Field on Conformational Energetics and Properties of Organic Liquids", *J. Am. Chem. Soc.* **1996**, 118, 11225-11236.

89. A. T. Tzanov, M. A. Cuendet and M. E. Tuckerman, "How Accurately Do Current Force Fields Predict Experimental Peptide Confirmations? An Adiabatic Free Energy Dynamics Study", *J. Phys. Chem. B*, **2014**, 118, 6539-6552.

90. M. R. Shirts, J. W. Pitera, W. C. Swope and V. S. Pande, "Extremely precise free energy calculations of amino acid side chain analogs: Comparison of common molecular mechanics force fields for proteins", *J. Chem. Phys.* **2003**, 119, 5740-5761.

91. K. A. Beaucamp, Y. Lin, R. Das and V. S. Pande, "Are Protein Force Fields Getting Better? A Systematic Benchmark on 524 Diverse NMR Measurements", *J. Chem. Theory Comput.* **2012**, 8, 1409-1414.

92. K. Lindorff-Larson, P. Maragakis, S. Piana, M. P. Eastwood, R. O. Dror and D. E. Shaw, "Systematic Validation of Protein Force Fields against Experimental Data", *PLoS One*, **2012**, 1-7.

93. B. Tam, S. Sinha and S. M. Wang, "Combining Ramachandran plot and molecular dynamics simulationfor structural-based variant classification: Using TP53 variants as model", *Computational and Structural Biotechnology Journal*, **2020**, 18, 4033-4039.

94. M. C. Vega, L. Serrano and J. C. Martínez, "Thermodynamic and structural characterization of Asn and Ala residues in the disallowed II′ region of the Ramachandran plot", *Protein Sci.* **2000**, 9, (12), 2322-2328.

95. A. M. Nip and D. S. Wishart, "Protein chemical shift analysis: a practical guide", *Biochem. Cell Biol.* **1998**, 76 (2-3), 153-163.

96. N. Bernstein, J. L. Feldman and D. J. Singh, "Calculations of dynamical properties of skutterudites: Thermal conductivity, thermal expansivity, and atomic mean-square displacement", *Phys. Rev. B*, **2010**, 81, 1-11.

97. G. G.Naumis and H. M. Flores-Ruiz, "Mean-square-displacement distribution in crystals and glasses: An analysis of the intrabasin dynamics", *Phys. Rev. E*, **2012**, 85,1-8.

98. A. Fick, "Ueber Diffusion", *Annalen der Physik*. **1855**, 170, (1), 59-86.

99. G. A. Korablev, "Calculation of Activation Energy of Diffusion and Self-Diffusion", *Eur. Chem. Bull.* **2018**, 7, (1), 23-29.

100. P. A. Gagniuc, "Markov Chains: From Theory to Implementation and Experimentation", *John Wiley & Sons.* **2017**, USA, NJ.

101.     G. J. May, A. Davidson and B. Monahov, "Lead batteries for utility energy storage: A review", *Journal of Energy Storage*, **2018**, 15, 145-157.

102.     H. Dai and Y. Li, "Recent advances in zinc-air batteries", *Chem. Soc. Rev.* **2014**, 43, 5257-5275.

103.     A. E. Javier, S. N. Patel, D. T. Hallinan Jr., V. Srinivasan and N. P. Balsara, "Simultaneous Electronic and Ionic Conduction in a Block Copolymer: Application in Lithium Battery Electrodes", *Angew. Chem. Int. Ed.* **2011**, 50, 9848-9851.

104.     M. Faraday, "Experimental Researches in Electricity", *Art. 1339, Taylor and Francis*, **1839**, 1-12.

105.     J. Owen, "Comprehensive Polymer Science and Supplements", *Elsevier Ltd.* **1989**, UK, Salford.

106.     Y. Zhou, J. Hu, P. He, Y. Zhang, J. Xu and X. Wu, "Corrosion Suppression of Aluminum Metal by Optimizing Lithium Salt Concentration in Solid-State Imide Salt-Based Polymer Plastic Crystal Electrolyte Membrane", *ACS Appl. Energy Mater.* **2018**, 1, 7022-7027.

107.     Y. Shi, A. H. Bork, S. Schweiger and J. L. M. Rupp, "The effect of mechanical twisting on oxygen ionic transport in solid-state energy conversion membranes", *Nat. Mater.* **2015**, 14, 721-727.

108.     J. W. Fergus, "The application of solid fluoride electrolytes in chemical sensors", *Sensors and Actuators B.* **1997**, 42, 119-130.

109.     N. P. Balsara and D. T. Hallinan, "Polymer Electrolytes", *Annu. Rev. Mater. Res.* **2013**, 43, 503-525.

110.     S. B. Aziz, T. J.Woo, M. F. Z. Kadir and H. M. Ahmed, "A conceptual review on polymer electrolytes and ion transport models", *Journal of Science: Advanced Materials and Devices*, **2018**, 3, (1), 1-17.

111.     L. Long, S. Wang, M. Xiao and Y. Meng, "Polymer electrolytes for lithium polymer batteries", *J. Mater. Chem. A.* **2016**, 4, 10038-10069.

112.     A. Hagfeldt, G. Boschloo, L. Sun, L. Kloo and H. Pettersson, "Dye-Sensitized Solar Cells", *Chem. Rev.* **2010**, 110, 6595-6663.

113.     K. Xu, "Electrolytes and Interphases in Li-Ion Batteries and Beyond", *Chem. Rev.* **2014**, 114, 11503-11618.

114.     S. Muench, A. Wild, C. Friebe, B. Haupler, T. Janoschka and U. S. Schubert, "Polymer-Based Organic Batteries" *Chem. Rev.* **2016**, 116, 9438-9484.

115.     X. Jia, C. Wang, C. Y. Lee, C. Yu, and G. G. Wallace, "Energy materials for transient power sources", *MRS Bulletin*, **2020**, 45, (2), 121-128.

116.    X. Jia, Y. Yang, C. Wang, C. Zhao, R. Vijayaraghavan, D. R. MacFarlane, M. Forsyth and G. G. Wallace, "Biocompatible Ionic Liquid-Biopolymer Electrolyte-Enabled Thin and Compact Magnesium-Air Batteries", *ACS Appl. Mater. Interfaces*, **2014**, 6, 21110-21117.

117.    H. Tao, D. L. Kaplan and F. G. Omenetto, "Silk materials-a road to sustainable high technology", *Adv. Mater.* **2012**, 24, 2824-2837.

118.    D. L. Kaplan and F. G. Omenetto, "New opportunities for an ancient material", *Science*, **2010**, 329, 528-531.

119.    E. M. Pritchard, P. B. Dennis, F. Omenetto, R. R. Naik and D. L. Kaplan, "Physical and chemical aspects of stabilization of compounds in silk", *Biopolymers*, **2012**, 97, 479-498.

120.    T. Ueki, and M. Watanabe, "Macromolecules in ionic liquids: progress, challenges, and opportunities", *Macromolecules*, **2008**, 41, 3739-3749.

121.    J. Lu, F. Yan and J. Texter, "Advanced applications of ionic liquids in polymer science", *Prog. Polym. Sci.* **2009**, 34, 431-448.

122.    S. Lu, X. Wang, Q. Lu, X. Zhang, J. A. Kluge, N. Uppal, F. Omenetto and D. L. Kaplan, "Insoluble and flexible silk films containing glycerol", *Biomacromolecules*, **2010**, 11, 143-150.

123.    K. D. Weaver, H. J. Kim, J. Sun, D. R. MacFarlane and G. D. Elliott, "Cyto-toxicity and biocompatibility of a family of choline phosphate ionic liquids designed for pharmaceutical applications", *Green Chem.* **2010**, 12, 507-513.

124.    D. N. Rockwood, R. C. Preda, T. Yücel, X. Wang, M. L. Lovett and D. L. Kaplan, "Materials Fabrication from Bombyx mori Silk Fibroin", *Nat Protoc.***2011**, 6, (10), 1-43.

125.    Z. H. Zhu, K. Ohgo and T. Asakura, "Preparation and characterization of regenerated Bombyx mori silk fibroin fiber with high strength", *Polymer Letters*, **2008**, 2, (12), 885-889.

126.    H. Zhang, L. L. Li, F. Y. Dai, H. H. Zhang, B. Ni, W. Zhou, X. Yang and Y. Z. Wu "Preparation and characterization of silk fibroin as a biomaterial with potential for drug delivery", *Journal of Translational Medicine*, **2012**, 10, (117), 1-9.

127.    E. S. Sashina, A. M. Bochek, N. P. Novoselov and D. A. Kirichenko, "Structure and solubility of natural silk fibroin", *Russ. J. Appl. Chem.* **2006**, 79, 869-876.

128.    M. Agostini de Moraes, G. M. Nogueira, R. F. Weska and M. M. Beppu, "Preparation and Characterization of Insoluble Silk Fibroin/Chitosan Blend Films", *Polymers*, **2010**, 2, 719-727.

129.    G. M. Nogueira, M. Agostini de Moraes, A. C. D. Rodas, O. Z. Higa and M. M. Beppu, "Hydrogels from silk fibroin metastable solution: Formation and characterization from a biomaterial perspective", *Materials Science and Engineering C*, **2011**, 31, 997-100.

130.    M. Ribeiro, M. A de Moraes, M. M. Beppu, F. J. Monteiro and M. P Ferraz, "The role of dialysis and freezing on structural conformation, thermal properties and morphology of silk fibroin hydrogels", *Biomatter.* **2014**, 4, 1-7.

131.    S. Sekar, M. Surianarayanan, V. Ranganathan, D. R. MacFarlane and A. B. Manda, "Choline-Based Ionic Liquids-Enhanced Biodegradation of Azo Dyes", *Environ. Sci. Technol.* **2012**, 46, 4902-4908.

132.    S. H. Zeisel, "Choline and Human Nutrition" *Ann, Rev. Nutr.* **1994**, 14, 269-296.

133.    A. M. A. Dias, A. R. Cortez, M. M. Barsan, J. B. Santos, C. M. A. Brett and H. C. Sousa, "Development of Greener Multi-Responsive Chitosan Biomaterials Doped with Biocompatible Ammonium Ionic Liquids", *ACS Sustainable Chem. Eng.* **2013**, 1, 1480-1492.

134.    O. Winther-Jensen, R. Vijayaraghavan, J. Sun, B. Winther-Jensen and D. R. MacFarlane, "Self polymerising ionic liquid gel", *Chem. Commun.* **2009**, 3041-3043.

135.    A. P. Sokolov and V. Bocharova, "Perspectives for Polymer Electrolytes: A View from Fundamentals of Ionic Conductivity", *Macromolecules*, **2020**, 53, 4141-4157.

136.    S. J. Tan, X. X. Zeng, Q. Ma, X. W. Wu, and Y. G. Guo, "Recent Advancements in Polymer-Based Composite Electrolytes for Rechargeable Lithium Batteries", *Electrochemical Energy Reviews*, **2018**, 1, 113-138.

137.    X. Cheng, J. Pan, Y. Zhao, M. Liao and H. Peng, "Polymer Electrolytes for Electrochemical Energy Storage", *Adv. Energy Mater.* **2018**, 8, 1-16.

138.    F. Croce, G. B. Appetecchi, L. Persi and B. Scrosati, "Nanocomposite Polymer Electrolytes for Lithium Batteries", *Nature*, **1998**, 394-456.

139.    L. Fan, S. Wei, S. Li, Q. Li and Y. Lu, "Recent Progress of the Solid-State Electrolytes for High-Energy Metal-Based Batteries", *Adv. Energy Mater.* **2018**, 8, 1-31.

140.    J. M. Tarascon and M. Armand, "Issues and challenges facing rechargeable lithium batteries", *Nature*, **2001**, 414, 359-367.

141.    P. Mustarelli and E. Quartarone, "Electrolytes for solid-state lithium rechargeable batteries: recent advances and perspectives", *Chem. Soc. Rev.* **2011**, 40, 2525-2540.

142.    A. Manthiram, X. Yu and S. Wang, "Lithium battery chemistries enabled by solid-state electrolytes", *Nat. Rev. Mater.* **2017**, 2, 16103.

143.    T. Famprikis, P. Canepa, J. A. Dawson, M. S. Islam, and C. Masquelier, "Fundamentals of inorganic solid-state electrolytes for batteries", *Nat. Mater.* **2019**, 18, 1278-1291.

144.    K. C. Santosh, R. C. Longo, K. Xiong and K. Cho, "Electrode-Electrolyte Interface for Solid State Li-Ion Batteries: Point Defects and Mechanical Strain", *J. Electrochem. Soc.* **2014**, 161, 3104-3110.

145.     M. Ebner, F. Marone, M. Stampanoni and V. Wood, *"*Visualization and Quantification of Electrochemical and Mechanical Degradation in Li Ion Batteries", *Science*, **2013**, 342, 716-720.

146.     P. M. Vereecken and X. Chen, "Solid and Solid-Like Composite Electrolyte for Lithium Ion Batteries: Engineering the Ion Conductivity at Interfaces", *Adv. Mater. Interfaces*, **2019**, 6, 1-31.

147.     F. Severcan and P. I. Haris, "FTIR spectroscopic characterization of protein structure inaqueous and non-aqueous media", *Journal of Molecular Catalysis B: Enzymatic*, **1999**, 7, 207-221.

148.     D. Chapman and P. I. Haris, "Does Fourier-transform infrared spectroscopy provide useful information on protein structures?", *Trends in Biochemical Sciences*, **1992**, 17, (9), 328-333.

149.     S. W. Ha, A. E. Tonelli and S. M. Hudson, "Structural studies of Bombyx mori silk fibroin during regeneration from solutions and wet fiber spinning", *Biomacromolecules*, **2005**, 6, 1722-1731.

150.     K. H. Liang and  X. Chuan, "Improvements of the physical properties of fibroin membranes with sodium alginate", *J. Appl. Polym. Sci.* **1992**, 45, 1937-1943.

151.     A. T. Anshu Bagga Mathur, T. Rathke and S. Hudson, "The dissolution and characterization of Bombyx mori silk fibroin in calcium nitrate-methanol solution and the regeneration of films", *Biopolymers*, **1997**, 42, 61-74.

152.     G. Freddi, G. Pessina and M. Tsukada, "Swelling and dissolution of silk fibroin (Bombyx mori) in N-methyl morpholine N-oxide", *Int. J. Biol. Macromol.* **1999**, 24, 251-263.

153.     L. Meinel, S. Hofmann, V. Karageorgiou, C. Kirker-Head, J. McCool, G. Gronowicz, L. Zichner, R. Langer, G. Vunjak-Novakovic and D. L. Kaplan, "The inflammatory responses to silk films in vitro and in vivo", *Biomaterials*, **2005**, 26, 147-155.

154.     V. H. Paschoal, L. F. O. Faria and M. C. C. Ribeiro, "Vibrational Spectroscopy of Ionic Liquids", *Chem. Rev.* **2017**, 117, 7053-7112.

155.     R. E. Marsh, R. B. Corey and L. Pauling, "An investigation of the structure of silk fibroin", *Biochim. Biophys. Acta*, **1955**, 16, 1-34.

156.     M. G. Dobb, R. D. B. Fraser and T. P. Macrae, "The Fine Structure of Silk Fibroin", *J. Cell. Biol.* **1967**, 32, (2), 289-295.

157.     T. Asakura, A. Kuzuhara, R. Tabeta and H. Saito, "Conformation Characterization of Bombyx mori Silk Fibroin in the Solid State by High-Frequency 13C Cross Polarization-Magic Angle Spinning NMR, X-ray Diffraction, and Infrared Spectroscopy", *Macromolecules*, **1985**, 18, (10), 1841-1845.

158. Q. Lu, X. Hu, X. Wang, J. A. Kluge, S. Lu, P. Cebe and D. L. Kaplan, "Water-insoluble silk films with silk I structure", *Acta Biomater.* **2010**, 6, 1380-1387.

159. N. Jaramillo-Quicenoa, C. Alvarez-Lopez and A. Restrepo-Osorio, "Structural and thermal properties of silk fibroin films obtained from cocoon and waste silk fibers as raw materials", *Proc. Eng.* **2017**, 200, 384-388.

160. D. R. MacFarlane, N. Tachikawa, M. Forsyth, J. M. Pringle, P. C. Howeltt, G. D. Elliott, J. H. Davis, M. Watanabe, P. Simon and C. A. Angell, "Energy applications of ionic liquids", *Energy Environ. Sci.* **2014**, 7, 232-250.

161. J. P Redfern and A. W. Coats, "Thermogravimetric Analysis: A Review", *Analyst*, **1963**, 88, 908-924.

162. X. Hu, D. Kaplan and P. Cebe, "Effect of water on the thermal properties of silk fibroin", *Thermochimica Acta*, **2007**, 461, 137-144.

163. M. Zhao, Z. Qi, X. Tao, C. Newkirk, X. Hu and S. Lu, "Chemical, Thermal, Time, and Enzymatic Stability of Silk Materials with Silk I Structure", *Int. J. Mol. Sci.* **2021**, 22, (4136), 1-16.

164. W. Lowrie, "Fundamentals of Geophysics", *Cambridge University Press*, **2007**, Cambridge, New York, Melbourne.

165. N. Kumar, "Comprehensive Physics for Class", *Laxmi Publications*, **2019**, India, New Delhi.

166. M. Carlen and R. Kötz, "Principles and Applications of Electrochemical Capacitors", Electrochem. Acta, **2000**, 45, 2483-2498

167. F. L. Mantia, J. Vetter and P. Novak, "Impedance Spectroscopy on Porous Materials: A General Model and Application to Graphite Electrodes of Lithium-Ion Batteries", *Electrochem. Acta*, **2008**, 53, 4109-4121.

168. F. Mansfeld and Z. He, "Exploring the Use of Electrochemical Impedance Spectroscopy (EIS) in Microbial Fuel Cell Studies", *Energy Environ. Sci.* **2009**, 2, 215-219

169. B. A. Mei, O. Munteshari, J. Lau, B. Dunn and L. Pilon, "Physical Interpretations of Nyquist Plots for EDLC Electrodes and Devices", *J. Phys. Chem. C*, **2018**, 122, 194-206.

170. M. Pech, D. Brunet, P. Durou, H. Huang, V. Mochalin, Y. Gogotsi, P. Taberna and P. Simon, "Ultrahigh-Power Micrometre-Sized Supercapacitors Based on Onion-like Carbon", *Nat. Nanotechnol.* **2010**, 5, 651-654.

171. H. Itoi, H. Nishihara, T. Kogure and T. Kyotani, "Three-Dimensionally Arrayed and Mutually Connected 1.2-nm Nanopores for High-performance Electric Double Layer", *J. Am. Chem. Soc.* **2011**, 133, 1165-1167.

172.     X. Z. Yuan, C. Song, H. Wang and J. Zhang, "Electrochemical Impedance Spectroscopy in PEM Fuel Cells: Fundamentals and Applications", *Springer-Verlag*, **2010**, UK, London.

173.     A. J. Bard, L. R. Faulkner, J. Leddy and C. G. Zoski, "Electrochemical Methods: Fundamentals and Applications", *John Wiley & Sons: Hoboken*, **1980**, USA, New Jersey.

174.     A. Lasia, B. E. Conway, J. O. M. Bockris and R. E. White, "In Modern Aspects of Electrochemistry", *Kluwer Academic*, **2002**, USA, New York.

175.     B. Tribollet and M. E. Orazem, "Electrochemical Impedance Spectroscopy", *John Wiley & Sons*, **2008**, USA, New Jersey.

176.     X. Qian, N. Gu, Z. Cheng, X. Yang, E. Wang and S. Dong, "Methods to study the ionic conductivity of polymer electrolytes using a.c. impedance spectroscopy", *J. Solid State Electrochem.* **2001**, 6, 8-15.

177.     J. H. Perez, J. Cardoso and O. Manero, "Mechanisms of ionic conductivity for zwitterionic polymers", *Polymer*, **1998**, 39, (26), 6969-6975.

178.     A. K. Arof, S. Amirudin, S. Z. Yusof and I. M. Noor, "A method based on impedance spectroscopy to determine transport properties of polymer electrolytes", *Phys. Chem.* **2014**, 16, 1856-1867.

179.     B. E. Mellander and T. M. W. J. Bandara, "Ionic Liquids: Theory, Properties, New Approaches", *A. Kokorin, InTech*, **2011**, Rijeka.

180.     T. M. W. J. Bandara, M. A. K. L. Dissanayake, I. Albinsson and B. E. Mellander, "Mobile charge carrier concentration and mobility of a polymer electrolyte containing PEO and Pr4N + I− using electrical and dielectric measurements", *Solid State Ionics*, **2011**, 189, 63-68.

181.     S. Nakamura, H. Nishikawa, T. Aoki and Y. Ogami, "The diffusion overpotential increase and appearance of overlapping arcs on the Nyquist plots in the low humidity temperature test conditions of polymer electrolyte fuel cell", *Journal of Power Sources*, **2009**, 186, 278-285.

182.     M. V. Orna and J. T Stock, "Electrochemistry, past and present", *American Chemical Society*, **1989**, USA. Washington DC.

183.     G. Hinds and E. J. F. Dickinson, "The Butler-Volmer Equation for Polymer Electrolyte Membrane Fuel Cell (PEMFC) Electrode Kinetics: A Critical Discussion", *Journal of The Electrochemical Society*, **2019**, 166, (4), 221-231.

184.     A. L. Rogach and X. Yang, "Electrochemical Techniques in Battery Research: A Tutorial for Non-electrochemists", *Advanced Energy Materials*, **2019**, 9, (25), 1-10.

185.     R. Knake, P. Jacquinot, A. W. E. Hodgson and P. C. Hauser, "Amperometric sensing in the gas-phase", *Analytica Chimica Acta*, **2005**, 549, (1-2), 1-9.

186.	G. Jasinski, P. Jasinski, A. Nowakowski and B. Chachulski, "Properties of a lithium solid electrolyte gas sensor based on reaction kinetics", *Meas. Sci. Technol.* **2006**, 17, 17-21.

187.	B. D. Lawrence, S. Wharram, J. A. Kluge, G. G. Leisk, F. G. Omenetto, M. I. Rosenblatt and D. L. Kaplan, "Effect of Hydration on Silk Film Material Properties", *Macromol. Biosci.* **2010**, 10, 4, 393-403.

188.	M. Patel, D. K. Dubey and S. P. Singh, "Phenomenological models of Bombyx mori silk fibroin and their mechanical behavior using molecular dynamics simulations", *Mater. Sci. and Eng.* **2020**, 108, 2-20.

189.	K. Yazawa, K. Ishida, H. Masunaga, T. Hikima and K. Numata, "Influence of Water Content on the β-Sheet Formation, Thermal Stability, Water Removal, and Mechanical Properties of Silk Materials", *Biomacromolecules*, **2016**, 17, 1057-1066.

190.	I. T. Todorov, W. Smith, K. Trachenko and M. T. Dove, "DL_POLY_3: new dimensions in molecular dynamics simulations via massive parallelism", *J. Mater. Chem.* **2006**, 16, 1911-1918.

191.	C. W. Yong, "Descriptions and Implementations of DL_F Notation: A Natural Chemical Expression System of Atom Types for Molecular Simulations", *J. Chem. Inf. Model.* **2016**, 56, 1405-1409.

192.	C. W. Yong and I. T. Todorov, "DL_ANALYSER Notation for Atomic Interactions (DANAI): A Natural Annotation System for Molecular Interactions, Using Ethanoic Acid Liquid as a Test Case", *Molecules*, **2018**, 23, 36.

193.	W. Humphrey, A. Dalke and K. Schulten, "VMD - Visual Molecular Dynamics", *J. Molec. Graphics*, **1996**, 14, 33-38.

194.	U. Essmann, L. Perera, M. L. Berkowitz, T. Darden, H. Lee and L. G. Pedersen, "A smooth particle mesh Ewald method", *J. Chem. Phys.* **1995**, 103, 8577-8593.

195.	A. L. Morris, M. W. MacArthur, E. G. Hutchinson and J. M. Thornton, "Stereochemical Quality of Protein-Structure Coordinates", *Proteins*, **1992**, 12, 345-364.

196.	T. E. Creighton, "Proteins: Structures and Molecular Properties", 2nd Ed. **1996**, 172-176, 183. New York: W. H. Freeman & Company.

197.	K. Okuyama, R. Somashekar, K. Noguchi and S. Ichimura, "Refined molecular and crystal structure of silk I based on Ala–Gly and (Ala–Gly)$_2$—Ser–Gly peptide sequence", *Biopolymers*, **2001**, 59, 310-319.

198.	B. Lotz and H. D. Keith, "Crystal structure of poly(l-Ala-Gly)II: A model for silk I", *J. of Molecular Bio.* **1971**, 61, 1, 201-202.

199.    K. Mita, S. Ichimura, M. Zama and T. C. James, "Specified codon usage pattern and its implications on the secondary structure of silk fibroin mRNA", *J. Mol. Biol.* **1988**, 203, 917-925.

200.    M. Demura, M. Minami, T. Asakura and T. A. Cross, "Structure of Bombyx mori Silk Fibroin Based on Solid-State NMR Orientational Constraints and Fiber Diffraction Unit Cell Parameters", *J. Am. Chem. Soc.* **1998**, 120, 1300-1308.

201.    R. D. B. Fraser, T. P. MacRae, F. H. C. Stewart and E. Suzuki, "Poly-L-alanylglycine", *J. Mol. Biol.* **1965**, 11, 706-712.

202.    Y. Takahashi, M. Gehoh and K. Yuzuriha, "Crystal structure of silk (bombyx mori)", *J. Polym. Sci. Polym. Phys.* **1991**, 29, 889-891.

203.    Y. Takahashi, M. Gehoh and K. Yuzuriha, "Structure refinement and diffuse streak scattering of silk (Bombyx mori)", *Int. J. Biol. Macromol.* **1999**, 24, 127-138.

204.    T. Konishi and M. Kurokawa, *Sen'i Gakkaishi*, "The structure of silk fibroin-α", **1968**, 24, 550-554.

205.    N. D. Lazo and D. T. Downing, "Crystalline Regions of Bombyx mori Silk Fibroin May Exhibit β-Turn and β-Helix Conformations", *Macromolecules*, **1999**, 32, 4700-4705.

206.    K. Momma and F. Izumi, "VESTA 3 for three-dimensional visualization of crystal, volumetric and morphology data," *J. Appl. Crystallogr.* **2011**, 44, 1272-1276.

207.    Mathew John Haskew, Benjamin Deacon, Chin Weng Yong, John George Hardy, Samuel Thomas Murphy, "Atomistic Simulation of Water Incorporation and Mobility in Bombyx mori Silk Fibroin", *ACS Omega*, **2021**, 6, (51), 35494-35504.

208.    A. Nishimura, H. Matsuda, Y. Tasei and T. Asakura, "Effect of Water on the Structure and Dynamics of Regenerated [3-13C] Ser, [3-13C] , and [3-13C] Ala-Bombyx mori Silk Fibroin Studied with $^{13}$C Solid-State Nuclear Magnetic Resonance", *Biomacromolecules*, **2018**, 19, 563-575.

209.    T. Asakura, K. Okushita and M. P. Williamson, "Analysis of the Structure of Bombyx mori Silk Fibroin by NMR", *Macromolecules*, **2015**, 48, 2345-2357.

210.    P. Zhou, G. Li, Z. Shao, X. Pan and T. Yu, "Structure of Bombyx mori Silk Fibroin Based on the DFT Chemical Shift Calculation", *J. Phys. Chem. B*, **2001**, 105, 12469-12476.

211.    S. A. Arrhenius, "Über die Dissociationswärme und den Einfluß der Temperatur auf den Dissociationsgrad der Elektrolyte", *Z. Phys. Chem.* **1889**, 4, 96-116.

212.    B. Marelli, M. A. Brenckle, D. L. Kaplan and F. G. Omenetto, "Silk Fibroin as Edible Coating for Perishable Food Preservation", *Sci. Rep.* **2016**, 6, 25263.

213.    J. P. O'Brien, S. R. Fahnestock, Y. Termonia and K. H. Gardner, "Nylons From Nature: Synthetic Analogs to Spider Silk", *Adv. Mater.* **1998**, 10, 1185-1195.

214.    D. Porter and F. Vollrath, "Silk as a Biomimetic Ideal for Structural Polymers", *Adv. Mater.* **2009**, 487−492.

215.    J. Yan, G. Zhou, D. P. Knight, Z. Shao and X. Chen, "Wet-Spinning of Regenerated Silk Fiber from Aqueous Silk Fibroin Solution: Discussion of Spinning Parameters", *Biomacromolecules*, **2010**, 11, 1−5.

216.    Y. Jin, Y. Hang, J. Luo, Y. Zhang, H. Shao and X. Hu, "In vitro studies on the structure and properties of silk fibroin aqueous solutions in silkworm", *Int. J. Biol. Macromol.* **2013**, 62, 162−166.

217.    B. Mortimer, J. Guan, C. Holland, D. Porter and F. Vollrath, "Linking naturally and unnaturally spun silks through the forced reeling of Bombyx mori", *Acta Biomater.* **2015**, 11, 247−255.

218.    N. Elgrishi, K. J. Rountree, B. D. McCarthy, E. S. Rountree, T. T. Eisenhart and J. L. Dempsey, "A Practical Beginner's Guide to Cyclic Voltammetry", *J. Chem. Educ.* **2018**, 95, 197-206.

219.    K. Sun, J. Xue, K. Tai and S. J. Dillon, "The Oxygen Reduction Reaction Rate of Metallic Nanoparticles during Catalyzed Oxidation", *Scientific Reports*, **2017**, 1-4.

220.    K. Zhang, W. Guo, Z. Liang and R. Zou, "Metal-organic framework based nanomaterials for electrocatalytic oxygen redox reaction", *Sci. China Chem.* **2019**, 1-12.

221.    J. K. Nørskov, J. Rossmeisl, A. Logadottir, L. Lindqvist, J. R. Kitchin, T. Bligaard and H. Jónsson, "Origin of the Overpotential for Oxygen Reduction at a Fuel-Cell Cathode", *J. Phys. Chem. B* **2004**, 108, 46, 17886-17892.

222.    G. H. Altman, F. Diaz, C. Jakuba, T. Calabro, R. L. Horan, J. Chen, H. Lu, J. Richmond and D. L. Kaplan, "Silk-based biomaterials", *Biomaterials*, **2003**, 24, 401−416.

223.    G. Gronau, S. T. Krishnaji, M. E. Kinahan, T. Giesa, J. Y. Wong, D. L. Kaplan and M. J. Buehler, "A review of combined experimental and computational procedures for assessing biopolymer structure-process-property relationships", *Biomaterials*, **2012**, 33, 8240−8255.

224.    E. Kamalha, Y. Zheng, Y. Zeng and M. N. Fredrick, "FTIR and WAXD Study of Regenerated Silk Fibroin", *Adv. Mater. Res.* **2013**, 677, 211-215.

225.    E. Kamalha, Y. Zheng and Y. Zeng, "Analysis of the secondary crystalline structure of regenerated Bombyx mori fibroin", *Res. Rev. BioSci.* **2013**, 7, (2), 76-83.

226.    In Chul Um, H. Kweon, Y. H. Park and S. Hudson, "Structural characteristics and properties of the regenerated silk fibroin prepared from formic acid", *International Journal of Biological Macromolecules*, **2001**, 29, (2), 91-97.

227.     X. Wu, X. Wu, M. Shao and B. Yang, "Structural changes of Bombyx mori fibroin from silk gland to fiber as evidenced by Terahertz spectroscopy and other methods", *International Journal of Biological Macromolecules*, **2017**, 102, 1202-1210.

228.     Y. Tang, C. Cao, X. Ma, C. Chen and H. Zhu, "Study on the preparation of collagen-modified silk fibroin films and their properties", *Biomed. Mater.* **2006**, 1, 242-246.

229.     S. B. Aziz, R. T. Abdulwahid, M. A. Rasheed, O. Gh. Abdullah and H. M. Ahmed, "Polymer Blending as a Novel Approach for Tuning the SPR Peaks of Silver Nanoparticles", *Polymers*, **2017**, 9, 486-498.

230.     Y. Zhang and H. Wang, "Processing and characterisation of a novel electropolymerized silk fibroin hydrogel membrane", *Sci. Rep.* **2014**, 4, 1-11.

231.     K. Vidanapathirana and K. Perera, "Impedance spectroscopy, DC polarization, XRD and SEM studies on anionic liquid based gel polymer electrolyte to be used for dyesensitized solar cells", *Materials Discovery*, **2017**, 7, 30-33.

232.     D. L. Kaplan and H. J. Jin, "Mechanism of silk processing in insects and spiders", *Nature*, **2003**, 28, 424, (6952),1057-61.

233.     A. Motta, L. Fambri and C. Migliaresi, "Regenerated silk fibroin films: Thermal and dynamic mechanical analysis", *Macromolecular Chemistry and Physics*, **2002**, 203, (10-11), 1658-1665.

234.     T. Chirila, Z. Barnard, Zainuddin, D. G. Harkin, I. R. Schwab and L. Hirst, "Bombyx mori silk fibroin membranes as potential substrata for epithelial constructs used in the management of ocular surface disorders", *Tissue Eng Part A.* **2008**, 4, (7),1203-11.

235.     F. Tong, X. Chen, Q. Wing, S. Wei and W. Gao, "Hypoeutectic Mg-Zn binary alloys as anode materials for magnesium-air batteries", *Journal of Alloys and Compounds*, **2021**, 1-10.

236.     F. Bella, S. De Luca, L. Fagiolari, D. Versaci, J. Amici, C. Francia and S. Bodoardo, "An Overview on Anodes for Magnesium Batteries: Challenges towards a Promising Storage Solution for Renewables", *Nanomaterials*, **2021**, 11, (810), 1-29.

237.     T. Zhang, Z. Tao and J. Chen, "Magnesium-air batteries: from principle to application", *Materials Horizons*, **2014**, 1, 196-206.

238.     A. Hahn and J. P. Schuchardt, "Intestinal Absorption and Factors Influencing Bioavailability of Magnesium-An Update", *Current Nutrition and Food Science*, **2017**, 13, 260-278.

239.     T. Monetta, A. Carangelo and A. Acquesta, "Durability of AZ31 magnesium biodegradable alloys polydopamine aided. Part 2: Aging in Hank's solution", *Journal of Magnesium and Alloys*, **2019**, 7, (2), 218-226.

240.     E. Sejdic and K. Bocan, "Adaptive Transcutaneous Power Transfer to Implantable Devices: A State of the Art Review", *Sensors*, **2016**, 16, (3), 1-23.

241.     W. Du, E. H. And, Y. Yang. Y. Zhang, M. Ye and C. C. Li, "Challenges in the material and structural design of zinc anode towards high-performance aqueous zinc ion batteries", *Energy and Environmental Science*, **2020**, 13, 3330-3360.

242.     M. B. Kannan, C. Moore, S. Saptarshi, S. Somasundaram, M. Rahuma and A. L. Lopata, "Biocompatibility and biodegradation studies of a commercial zinc alloy for temporary mini-implant applications", *Scientific Reports*, **2017**, 7, 1-11.

243.     J. J. D. Venezuela, S. Johnston and M. S. Dargusch, "The Prospects for Biodegradable Zinc in Wound Closure Applications", *Adv. Healthcare Mater.* **2019**, 8, 1-15.

244.     Z. Zhao, X. Fan, J. Ding, W. Hu, C. Zhong and J. Lu, "Challenges in Zinc Electrodes for Alkaline Zinc-Air batteries: Obstacles to commercialization", *ACS Energy Lett.* **2019**, 4, 2259-2270.

245.     J. G. Hardy and T. R. Scheibel, "Silk-inspired polymers and proteins", *Biochem. Soc. Trans.* **2009**, 37, 677-681.

246.     A. Sarkar, A. J. Connor, M. Koffas and R. H. Zha, "Chemical Synthesis of Silk-Mimetic Polymers", *Materials*, **2019**, 12, 1-18.

247.     M. H. Lee, J. Lee, S. K. Jung, D. Kang, M. S. Park, G. D. Cha, K. W. Cho, J. H. Song, S. Moon, Y. S. Yun, S. J. Kim, Y. W. Lim, D. H. Kim and K. Kang, "A Biodegradable Secondary Battery and its Biodegradation Mechanism for Eco-Friendly Energy-Storage Systems", *Adv. Mater.* **2021**, 33, 1-11.

248.     M. Prakash, T. Lemaire, D. Di Tommaso, N. de Leeuw, M. Lewerenz, M. Caruel and S. Naili, "Transport properties of water molecules confined between hydroxyapaptite surfaces: A Molecular dynamics simulation approach", *Applied Surface Science*, **2017**, 418, 296-301.

249.     M. Zhou, C. Liu, S. Xu, Y. Gao and S. Jiang, "Accelerated degradation rate of AZ31 magnesium alloy by copper additions", *Materials and Corrosion*, **2017**, 760-769.

250.     J. Wang, V. Giridharan, V. Shanov, Z. Xu, B. Collins, L. White, Y. Jang, J. Sankar, N. Huang and Y. Yun, "Flow-induced corrosion behavior of absorbable magnesium-based stents", *Acta Biomaterialia*, **2014**, 10, 5213-5223.

**Supplementary information**



Blackened Mg AZ31 alloy surface, post discharge

1:1 SF-[Ch][NO$_3$] film, PE

Clear Sellotape

2 mg cm$^{-2}$ Pt carbon cloth, cathode

Mg AZ31 alloy, anode
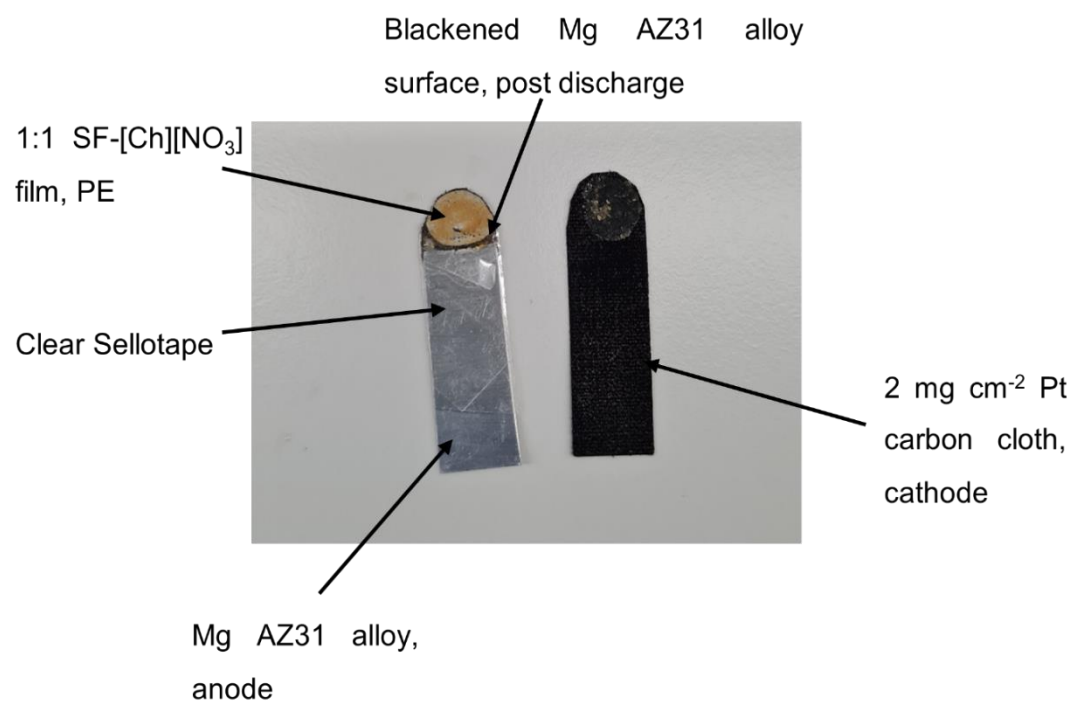
**SI Figure 1.** Picture of the Mg AZ31 anode and Pt carbon cloth cathode post discharge. The electrodes were taken from the primary Mg-air battery using the 1:1 SF:IL PE film after discharging at a current density of ca. 25 µA cm$^{-2}$.